GEOLOGY AND MINERAL DEPOSITS OF THE GALLINAS MOUNTAINS, LINCOLN AND TORRANCE COUNTIES, NEW MEXICO

Virginia T. McLemore, Shari Kelley, Matthew J. Zimmerer, Evan Owen, Ethan B. Haft, Tyler Cantrell, Alexander Gysi, Haley Dietz, Stellah Cherotich, and Amy Trivitt

New Mexico Bureau of Geology and Mineral Resources
New Mexico Institute of Mining and Technology
Socorro, NM 87801
virginia.mclemore@nmt.edu

Open-file Report 617
v.1

November 2021

This information is preliminary and has not been reviewed according to New Mexico Bureau of Geology and Mineral Resources (NMBGMR) standards. The content of this report should not be considered final and is subject to revision based upon new information. Any resource or reserve data are historical data and are provided for information purposes only and does not reflect Canadian National Instrument NI 43-101 requirements, unless specified as such. The views and conclusions contained in this document are those of the authors and should not be interpreted as representing the opinions or policies of the U.S. Geological Survey (USGS). Mention of trade names or commercial products does not constitute their endorsement by the USGS or NMBGMR.

ABSTRACT

Rare earth elements (REE) are a group of critical minerals that are essential in most modern electronic devices. In New Mexico, many REE deposits are found in the North American Cordilleran alkaline-igneous belt, a regional zone of Cenozoic alkaline igneous rocks and associated mineral deposits that extends from Canada, through the U.S., and into eastern Mexico. This zone has been explored and exploited for numerous types of mineral deposits, especially gold, silver, fluorite, and REE. The Gallinas Mountains in central New Mexico is one such district with established REE potential. A small amount of bastnäsite, a REE fluorocarbonate mineral, was recovered during historic processing for fluorite. In addition to fluorite production, lead, copper, zinc, silver, gold, and iron have been produced from the district.

Previous reports have examined the geology and evolution of the mineral deposits in the Gallinas Mountains, but few have thoroughly examined the mineral-resource potential for REE, nor has the area been comprehensively mapped in detail. Re-examination of the REE deposits in the Gallinas Mountains is warranted in light of the economic importance of REE. Therefore, the New Mexico Bureau of Geology and Mineral Resources (NMBGMR), largely funded by the U.S. Geological Survey (USGS) Earth Mapping Resource Initiative (MRI) program, updated the previous mapping and characterized the geology, alteration, and mineralization of the Gallinas Mountains REE-fluorite district and surrounding areas. A geologic map at a scale of 1:24,000, along with more detailed maps, accompanies this report. Detailed mapping, coupled with geochemistry, mineralogy, and geochronology, provides new insight into the geologic history of the region and particularly focuses on the extent and origin of alteration and mineralization.

Geologic mapping of the Gallinas Mountains was conducted by senior project personnel between 2019 and 2021. Prior published and unpublished geologic maps were used to guide map construction. The major intrusions of the Gallinas Mountains are generally poorly exposed and contacts are commonly covered with colluvium. However, outcrop and float mapping techniques differentiated the Cenozoic igneous rocks, unlike previous mapping. More than 20 intrusive units have been mapped. Additional faults have been mapped as well. Several altered areas were mapped.

Cougar Mountain, in the northeastern portion of the Gallinas Mountains, consists of a coarse-grained porphyritic syenite intrusion, possibly a laccolith. Exposed in the northern portion of the Gallinas Mountains is a crystal-poor, sparsely porphyritic rhyolite laccolith. The intrusions in the southern portion of the Gallinas Mountains consist of syenite (equigranular texture) to trachyte (trachytic texture) dikes and sills with different textures and compositions, as shown on the map. These metaluminous to peraluminous, alkaline igneous rocks have pervasively intruded the Permian Yeso and Abo formations. The Permian Glorieta Sandstone overlies most of the units.

New and published $^{40}Ar/^{39}Ar$ ages provide insight in the timing of magmatism, alteration, and mineralization in the Gallinas Mountains. Dating of the intrusions indicates at least two and possibly three periods of magmatic activity. Andesite dikes and sills, a small-volume monzonite, and possibly the Cougar Mountain syenite were emplaced during discontinuous magmatic activity between 38.5 and 29.3 Ma. The majority of the intrusions exposed in the Gallinas Mountains, which includes dikes, sills, and laccoliths of syenite, rhyolite, trachyte, and andesite were emplaced between 29 to 27 Ma, with most activity occurring at approximately 28.8 Ma. Dating of K-feldspar fenitization and richterite associated with alteration yield similar ages to intrusions of the alkaline flare-up, suggesting alteration and mineralization is genetically related

to the exposed intrusions. Magmatic activity and related alteration may have continued to as young as 25.8 to 24.4 Ma, but this pulse of magmatism is poorly constrained.

Four types of alteration are described in the Gallinas Mountains, all of which are related to the intrusions. Evidence for early non-mineralized regional silicification and brecciation of host rocks is preserved throughout most of the southern Gallinas Mountains, where the mineral deposits are located. This was followed by regional hematization and sericitization (liesegang banding). Dissolution and brecciation of gypsum and limestone followed to form carbonate breccias and calcite veins, which are locally enriched in REE. Metasomatic alteration (i.e. fenitization) followed. Na-fenitization occurred first, followed by K-fenitization, and both types are interpreted to be coeval with the intrusions (29 to 27 Ma). The fenites are not enriched in REE. Fenitization also is related to the skarns.

Seven types of mineral deposits are found in the district, distinguished by mineralogy, chemistry, form, and host rocks: (1) Fe skarn-contact replacement deposits, (2) hydrothermal breccia and fissure veins (mapped as Tv), (3) F replacements/disseminations, (4) magmatic intrusive breccia pipes (mapped as Tibx), (5) carbonate breccias, (6) hypogene oxidation, and (7) supergene oxidation. Economically, the most important REE deposits are the hydrothermal breccia and fissure vein deposits, which are further subdivided into eight chemical and mineralogical subtypes. Most precious and base metal sulfide deposits are associated with the predominant REE-F-Ba hydrothermal breccia and fissure vein deposits. The magmatic intrusive breccia pipes are also a potential economic source of REE. The origin of the mineralizing fluids is uncertain but geochemical analyses, mineralogy, texture, and field relationships from this study are consistent with previous conclusions that the REE deposits are derived from magmatic-hydrothermal fluids from either an alkaline magma, such as the trachyte and syenite exposed in the Gallinas Mountains or from a deep-seated, buried carbonatite.

The updated mapping reveals that many of the magmatic intrusive breccia pipes in Pinatosa Canyon and along Rattlesnake Ridge were emplaced along the margins of syenite intrusions, suggesting a connection between fluids associated with the intrusions and breccia pipe formation. The Sky High breccia pipe was emplaced along the contact of a trachyte dike. Furthermore, the mineralized hydrothermal breccia deposits at several larger mines appear to be circular in shape (not linear or vein-like), similar to the intrusive breccia pipes. These observations provide a focus for future research into the origin of intrusive breccia pipes in this part of the Gallinas Mountains.

In general, many exposed outcrops of hydrothermal breccias and fissure veins in the Gallinas Mountains are small and low grade, although samples with concentrations as high as 8% total REE are found in some hydrothermal breccias, fissure veins, and magmatic intrusive breccia pipes. Drilling is required to evaluate their potential. The hydrothermal breccia and vein deposits in the Gallinas Mountains are too low grade to be economic for Au, U, Th, and Nb in the current market. Drilling and subsurface sampling is suggested at the Pride vein, M and E breccia pipe, Red Cloud-Deadwood copper veins, Rio Tinto vein, Sky High-Big Ben veins, veins along the road to Rough Mountain, and Park breccia pipe to determine the REE mineral-resource potential.

TABLE OF CONTENTS

LIST OF FIGURES

LIST OF TABLES

INTRODUCTION

The growing market for alternative technologies like solar panels, wind turbines, batteries, electric cars, desalination plants, and carbon capture and storage require non-traditional elements for their manufacture. In December 2017, President Trump signed an executive order (U.S. Presidential Executive Order (EO) No. 13817) that required the Departments of Interior and Defense to develop a list of critical minerals. In May 2018, the U.S. Department of the Interior published its final list of 35 critical minerals. As defined by EO No. 13817, "*a critical mineral is a mineral (1) identified to be a nonfuel mineral or mineral material essential to the economic and national security of the United States, (2) from a supply chain that is vulnerable to disruption, and (3) that serves an essential function in the manufacturing of a product, the absence of which would have substantial consequences for the U.S. economy or national security*". Many critical minerals are 100% imported into the United States. These mineral resources are essential to our economy and have supply chains that may be disrupted (Committee on Critical Mineral Impacts of the U.S. Economy, 2008; Subcommittee on Critical and Strategic Mineral Supply Chains Committee on Environment, Natural Resources, and Sustainability, 2018).

Rare earth elements (REE) are one group of critical minerals that are essential in most of our electronic devices, such as cell phones, laptops, computer chips, wind turbines, hybrid/electric cars, etc. (Committee on Critical Mineral Impacts of the U.S. Economy, 2008; Long et al., 2010; McLemore, 2011, 2015b). Other developing technologies such as solar panels, water purification and desalination systems, magnetic refrigeration, and efficient light bulbs also require REE and other critical elements in their manufacture. Most of the current world production of REE comes from China, but the U.S. has significant REE resources that could be developed in the future. Established REE deposits are located in New Mexico (Long et al., 2010; McLemore, 2015b), such as those in the Gallinas Mountains, but they have not been important exploration targets in the past because demand has been met elsewhere. However, with the projected increase in demand and potential lack of available REE production from China, the New Mexico deposits are being re-evaluated for their potential, and several areas are undergoing current exploration.

Many REE deposits are common in carbonatites and alkaline igneous rocks and are associated with alkaline metasomatism, known as fenitization. Therefore, re-examination of the REE deposits in the Gallinas Mountains in northern Lincoln and southern Torrance Counties is warranted in light of today's potential economic importance of REE. A series of alkaline igneous rocks, including trachyte, syenite, andesite, and rhyolite laccoliths, sills, and dikes, have intruded Permian sedimentary rocks in the Gallinas Mountains and have potential for REE (Kelley et al., 1946; Kelley, 1949; Kelley, 1971, 1972; Perhac, 1961, 1970). A small amount of bastnäsite (671 short tons), a REE fluorocarbonate mineral, was recovered during historic processing for fluorite. Host rock alteration types recognized previously, are associated with the igneous intrusions, and include brecciation, silicification, and fenitization (Griswold, 1959; Perhac, 1961, 1970; Woodward and Fulp, 1991; Schreiner, 1993). Small skarns are found in limestones and sandstones within the Yeso Formation adjacent to the trachyte, syenite, and rhyolite (exoskarn) or within the trachyte (endoskarn).

Previous reports have examined the geology and evolution of the mineral deposits of the Gallinas Mountains, but few have examined the mineral-resource potential for REE. Only limited reconnaissance mapping has been completed before this study (Kelley et al., 1946; Kelley, 1949; Perhac, 1961, 1970; Kelley, 1971, 1972). More recently, additional geochemical

and geochronological studies have been conducted in the Gallinas Mountains (Williams-Jones et al., 2000; McLemore, 2010; Vance, 2013; Robison, 2017), but none of these included geologic mapping.

Previous studies (e.g., Robison, 2017) have posed several questions that have yet to be answered and new geologic mapping presented here (Plate 1) will help address some of these. McLemore (2010a) summarized additional studies needed, including: (1) detailed outcrop geologic mapping along with geochemical analyses, (2) defining the extent of the alteration and defining any alteration zonation, (3) additional geochemical studies, including isotopic studies, of igneous rocks, mineralization, and alteration, and (4) precise dating of the igneous rocks in the Gallinas Mountains to fully understand the temporal relationships of igneous activity and associated mineralization and alteration. The New Mexico Bureau of Geology and Mineral Resources (NMBGMR), partially funded by the U.S. Geological Survey (USGS) Earth Mapping Resource Initiative (MRI) program, updated the previous mapping of the geology, alteration, and mineral deposits of the Gallinas Mountains REE-fluorite district and surrounding areas. This report accompanies the new geologic map of the district (Plate 1) and aims to: (1) compile and interpret available published and unpublished data from the Gallinas Mountains, (2) support the new 1:24,000-scale geologic map (Plate 1) and present detailed map sections of mineralized and altered areas, (3) describe the geochemistry, geochronology, mineral-resource potential, and origin of the mineral deposits and alteration in the Gallinas Mountains, and (4) relate the Gallinas Mountains district to other REE mineral deposits in New Mexico and elsewhere. This report is organized by regional geologic setting, methods, historical data and previous work, descriptions, and geochronology, followed by discussion, conclusions, and recommendations. The descriptions of the rock units, structure, alteration, and mineralized deposits are generally organized by perceived age of deposits, oldest to youngest.

REGIONAL GEOLOGIC AND TECTONIC SETTING

Lindgren (1915, 1933) was one of the first geologists who noted that a belt of alkaline-igneous rocks extends from Alaska and British Columbia southward into eastern New Mexico, Trans-Pecos Texas, and eastern Mexico (Fig. 1) and that these rocks contain relatively large quantities of fluorine (F), zirconium (Zr), REE, gold (Au), and other commodities. Since then, the North American Cordilleran alkaline-igneous belt has been explored and exploited for numerous types of mineral deposits, especially gold and silver (Mutschler et al., 1985, 1991; Clark, 1989; Kelley and Ludington, 2002; Kelley and Spry, 2016), fluorite (Van Alstine, 1976), and REE (Woolley, 1987; McLemore, 2018). Economic mineral deposits found within this belt have produced nearly 13% of the total lode gold production in the U.S. and Canada (Mutschler et al., 1991). Consequently, numerous companies have examined the belt for additional mineral deposits, including those related to REE.

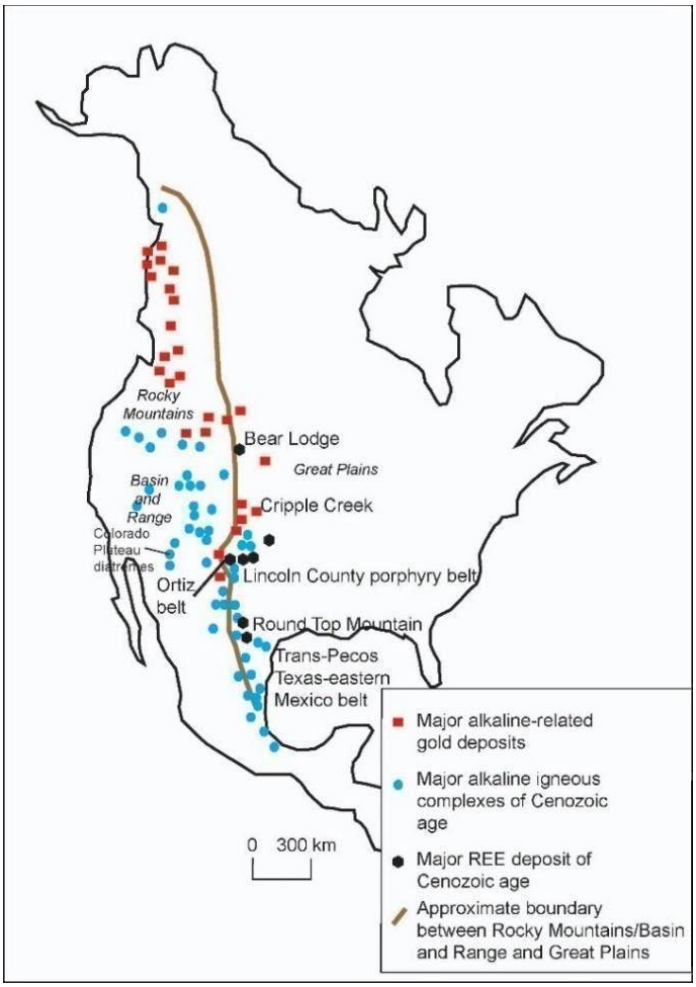

FIGURE 1. Simplified map showing the extent of the North American-Cordilleran alkaline igneous belt (modified from Mutschler et al., 1991; McLemore, 1996, 2015, 2018).

The North American Cordilleran alkaline-igneous belt in New Mexico coincides with exposures of alkaline intrusions and eastward lithospheric thickening, which follows the tectonic boundary between the stable Great Plains and the tectonically active Rocky Mountains and Basin and Range provinces from Colorado to Texas. The lithosphere of the Basin and Range and Southern Rocky Mountains is thinner, has a higher heat flow, and is more permeable, and more fractured than the lithosphere of the Great Plains (Eaton, 1980; Prodehl and Lipman, 1989; McLemore, 1996). The diversity of igneous rocks and associated mineral deposits within this belt (Mutschler et al., 1985, 1991; McLemore, 1996, 2018) suggests that the boundary between the Great Plains and Rocky Mountains/Basin and Range provinces is a region of highly fractionated and differentiated magmas (Thompson, 1991a, b; Allen and Foord, 1991).

In New Mexico, the North American Cordilleran alkaline-igneous belt extends from the Sangre de Cristo Mountains west of Raton, southward to the Cornudas Mountains, located to the east of El Paso, Texas (Fig. 2; North and McLemore, 1986, 1988; McLemore, 1996, 2001, 2018). Significant mineral production, especially gold and silver, has come from deposits spatially associated with Cenozoic alkaline-igneous rocks in the New Mexico portion of the alkaline-igneous belt (McLemore, 1996, 2001). These mineral deposits in New Mexico have been referred to as Great Plains Margin (GPM) deposits by North and McLemore (1986, 1988)

and McLemore (1996, 2001, 2018). Alternative classifications by other workers include alkalic-gold or alkaline-igneous related gold deposits (Fulp and Woodward, 1991; Thompson, 1991a, b; Bonham, 1988; Mutschler et al., 1985, 1991; Richards, 1995), porphyry gold deposits, and Rocky Mountain gold province. Low initial $^{87}Sr/^{86}Sr$ ratios suggest intrusive rocks associated with the GPM deposits are derived from upper mantle to lower crustal sources (Allen and Foord, 1991; McLemore, 1996, 2018).

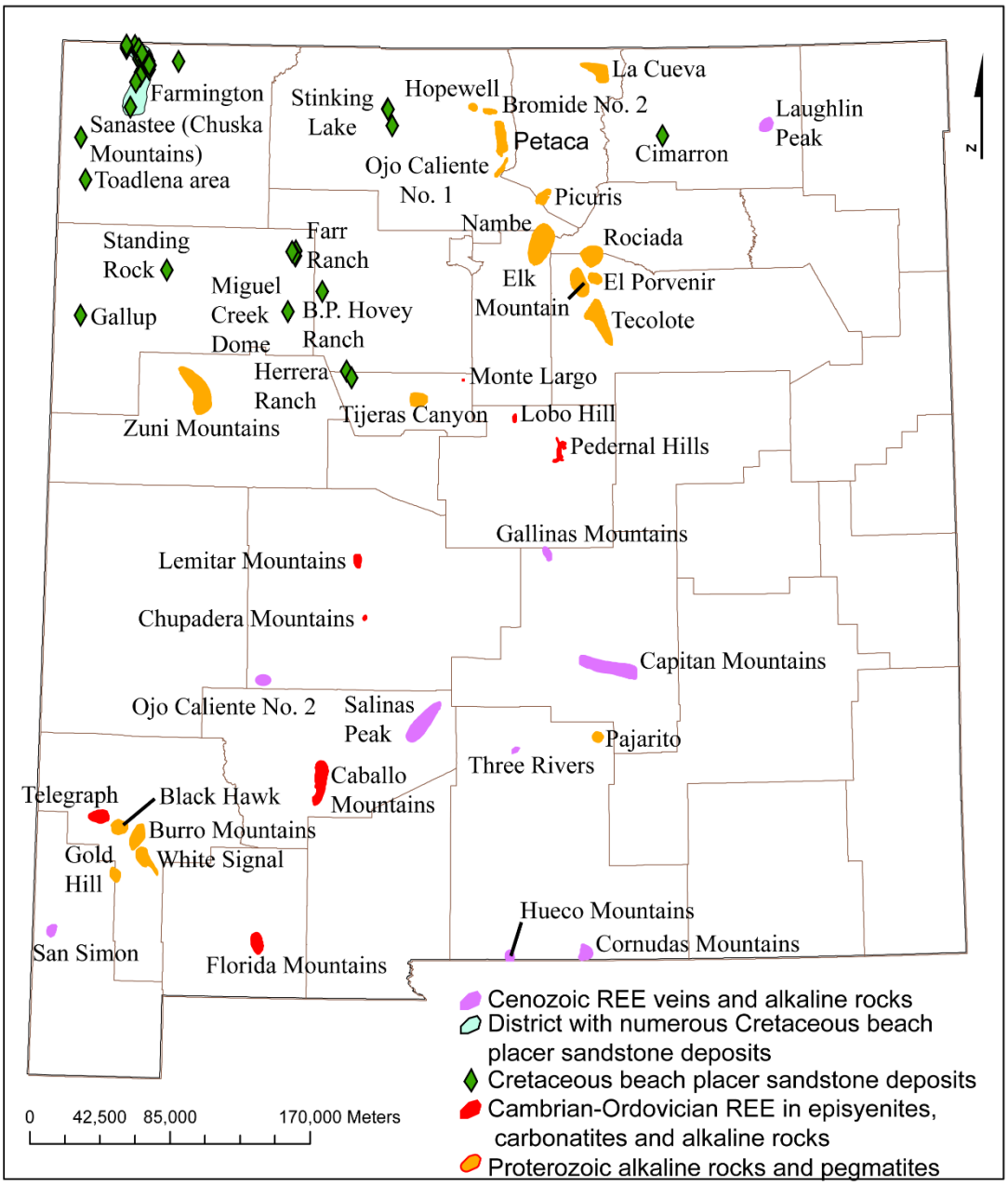

FIGURE 2. Mining districts and areas in New Mexico that contain REE deposits (modified from Adams, 1965; Northrop, 1996; McLemore et al., 1988a, b; 2005a).

The Gallinas Mountains are within the Lincoln County porphyry belt (LCPB) in central New Mexico, which is part of the North American Cordilleran alkaline-igneous belt located at the intersection of the north-trending Pedernal arch and the east-west-trending Capitan lineament (Fig. 3). The Pedernal arch and Capitan lineament appear to have localized magmatic and volcanic activity in the LCPB (Kelley and Thompson, 1964; Kelley, 1971; Allen and Foord, 1991; McLemore and Zimmerer, 2009). Alkaline to subalkaline igneous rocks are found in all districts in the LCPB, but mineralization is locally associated with silica-saturated (monzonite) or oversaturated (quartz monzonite) rocks (Seagerstrom and Ryberg, 1974; McLemore and Phillips, 1991; Thompson, 1991a, b). Prior K-Ar and $^{40}Ar/^{39}Ar$ dating studies (Fig. 4) suggests two stages of magmatism in the LCPB, including an early alkaline igneous suite emplaced along a north-south trend (Pedernal uplift) between 38 and 30 Ma and a younger bimodal suite emplaced along an east-west trend between 30 and 25 Ma (Fig. 2; Allen and Foord, 1991; McLemore, 2018). The GPM deposits in New Mexico consist of seven deposit types: (1) polymetallic, epithermal to mesothermal veins, (2) breccia pipes and quartz veins, (3) porphyry Cu-Mo-Au deposits, (4) Cu, Pb/Zn, and/or Au skarns or carbonate-hosted replacement deposits, (5) Fe skarns and replacement bodies, (6) placer Au, and (7) Th-REE-fluorite epithermal veins, breccias, and carbonatites. The GPM veins have high gold to base metal ratios and typically low Ag/Au ratios (North and McLemore, 1988; McLemore, 1996, 2001, 2017) in contrast to other high Ag/Au deposits in western New Mexico (McLemore, 2001, 2018).

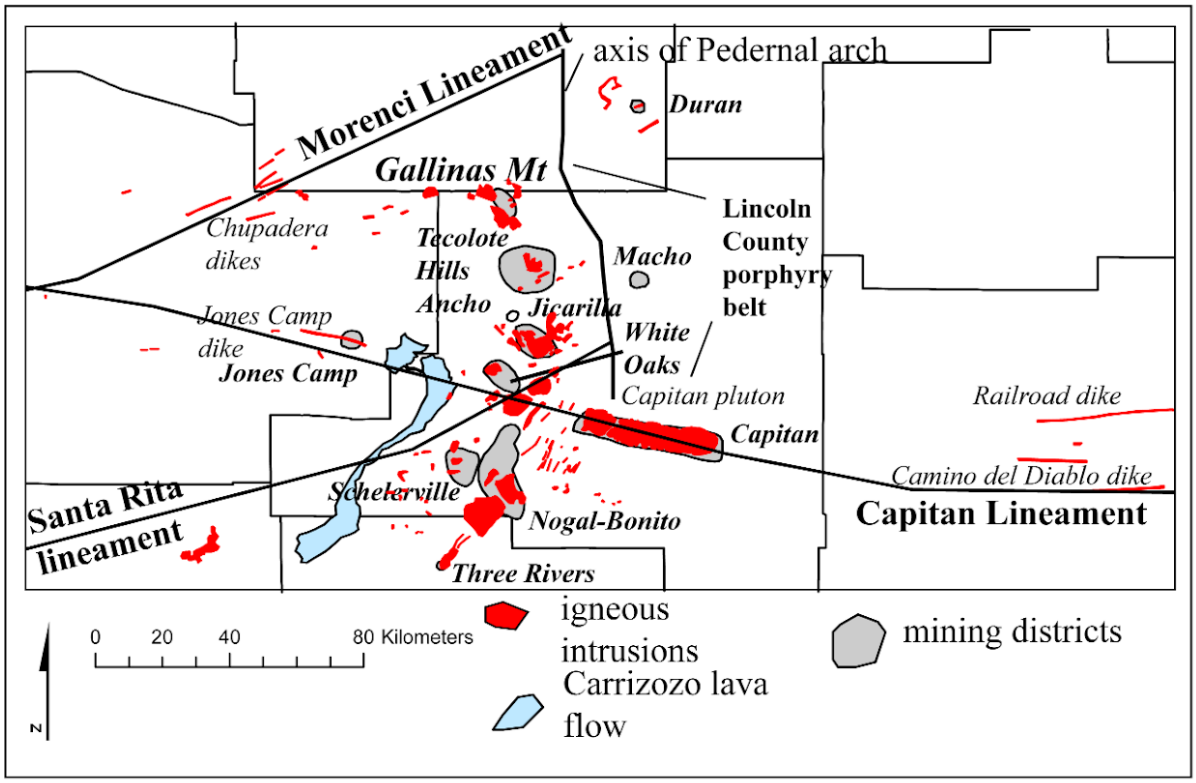

FIGURE 3. Mining districts and igneous intrusions forming the Lincoln County porphyry belt (LCPB) (modified from McLemore and Zimmerer, 2009). The mining districts are from the New Mexico Mines Database (McLemore et al., 2005a, b; McLemore, 2010b).

The genetic relationship between the identified mineral deposits and exposed igneous rocks of the LCPB is not fully understood. Observations supporting a magmatic origin of mineralization includes: (1) fluid inclusion, stable isotope, and age data from the Capitan REE-Th-bearing quartz veins (Phillips, 1990; Phillips et al., 1991; Campbell et al., 1995; Dunbar et al., 1996), (2) nature of stockwork molybdenum deposits at Sierra Blanca (Thompson, 1968, 1973), (3) close spatial association of mineralization with igneous rocks, (4) presence of skarn deposits along the contacts of igneous rocks, and (5) similarity to deposits at Cripple Creek, Colorado and elsewhere where a magmatic origin is favored (Thompson et al., 1985; Porter and Ripley, 1985; Thompson, 1992; Maynard et al., 1989, 1990; Kelley and Luddington, 2002). The co-occurrence of Au, Cu, Fe, Mo, F, W, and other elements is likely the result of several complex magmatic fractionation and differentiation events and tectonic sub-environments, which overlap near the Great Plains Margin. The association of lineaments and other major structures with igneous rocks and mineral deposits in New Mexico (Fig. 3, 4) suggests that deep-seated tectonic features likely provided ascent pathways for the magmas and related fluids. Once the magmas and fluids reached shallow levels, local structures and wall rock compositions determined the final character and distribution of intrusions and mineralization.

Evidence suggests that multiple magma intrusion events are needed to generate the fluids necessary to produce GPM mineral deposits (Thompson, 1991a, b, c; Allen and Foord, 1991; McLemore, 2017). The more productive districts, such as Nogal and White Oaks districts, occur in areas of protracted magma emplacement that lasted for more than 5 Ma. Many of these areas have older calc-alkaline rocks followed by younger alkaline intrusions (Fig. 4; Allen and Foord, 1991). In areas such as the Capitan Mountains, where intrusive activity occurred for less than 5 Ma, only localized minor Au, Ag, and REE occurrences are found (McLemore and Phillips, 1991). Additional age determinations are required to confirm these observations, especially in the Gallinas Mountains and nearby districts, including Jicarilla Mountains, White Oaks, Sierra Blanca (Three Rivers and Nogal-Bonito), and Tecolote districts (see Fig. 3 for the location of districts).

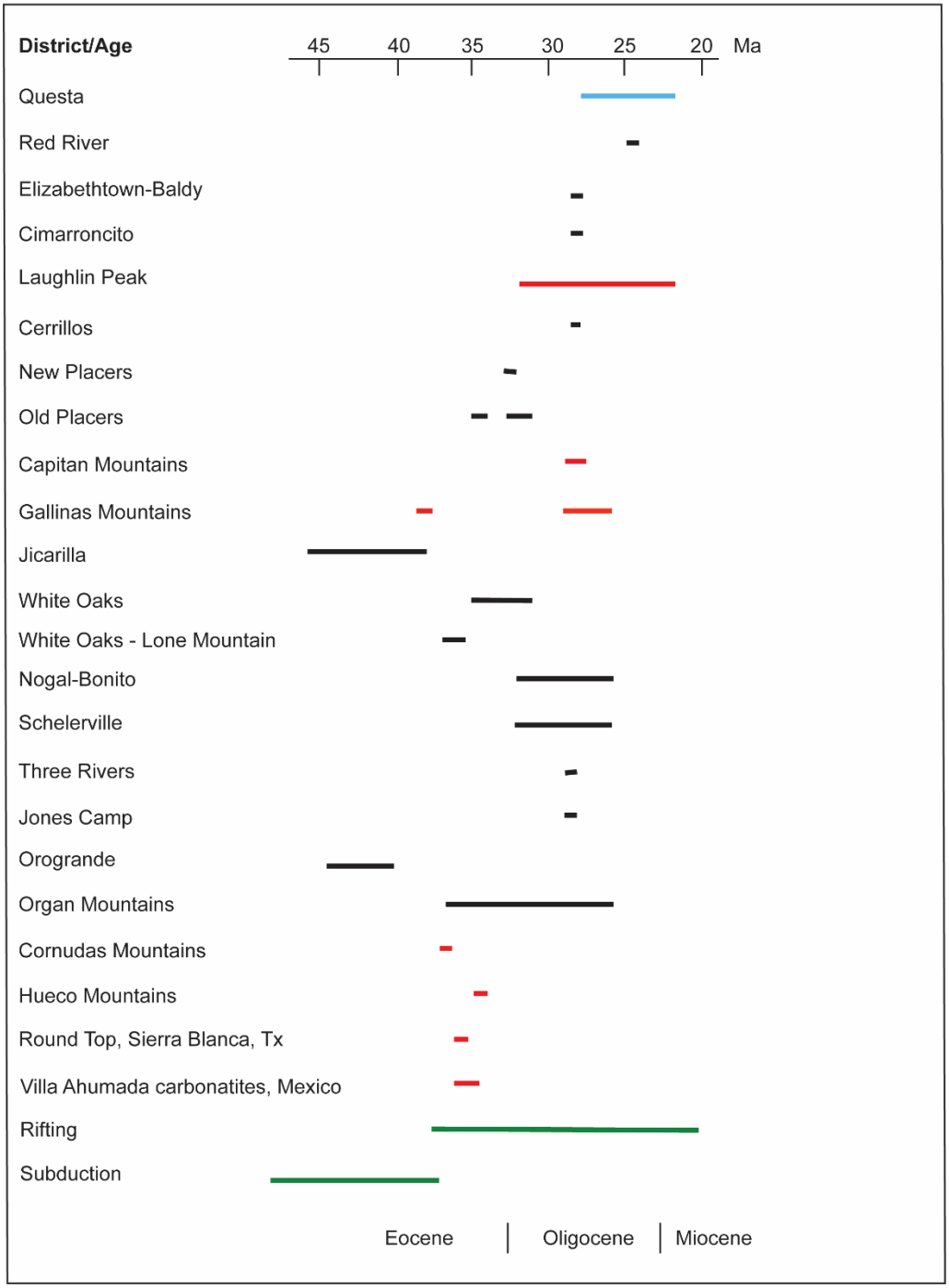

FIGURE 4. Ages of igneous rocks associated with GPM districts in New Mexico, Texas, and eastern Mexico, arranged from north to south (modified from McLemore, 2018). The blue line represents predominantly porphyry molybdenum deposits, black lines represent primary gold and base metals districts, and the red lines represent predominantly REE districts. The green lines, represent rifting and subduction, and are from McMillan et al. (2000) and Chapin et al. (2004). $^{40}Ar/^{39}Ar$ ages have been recalculated using the new monitor age 28.201 Ma from Kuiper et al. (2008). Published ages are listed in McLemore (2018) and include new unpublished ages by the senior author from Jicarilla Mountains and this report on White Oaks districts (Appendix 8). Locations are in Figures. 1, 2.

METHODS OF STUDY

Previous data

An important step in economic geology projects is to compile all published and unpublished data from existing mines and prospects within the Gallinas Mountains, including historical accounts from newspaper articles and older geologic reports. Mineral databases were examined, including the Mineral Resource Data System (MRDS) of the USGS (Mason and Arndt, 1996), the Minerals Industry Location System (MILS) of the U.S. Bureau of Mines (USBM) (U.S. Bureau of Mines, 1995), U.S. Forest Service Abandoned and Inactive Mines database, and AMLIS (U.S. Bureau of Land Management). Published and unpublished reports and files at the NMBGMR were also examined. Using these data resources, mineral occurrences, deposits, mines, prospects, and mills were identified, plotted, and entered in the NMBGMR New Mexico Mines Database (McLemore et al., 2005a, b; McLemore, 2010b). These data are located in Appendices 1 and 2. Appendix 1 is a synopsis of the mining history of the area (at the end of this document). The other appendices are separate files. Mines, prospects, and quarries in the Gallinas Mountains are identified by the unique mine identification number (NMLIxxxx, New Mexico Mines Database) throughout the report. Locational and other data are in the New Mexico Mines Database, summarized in Appendix 2.

Mineral production by commodity and year since the late 1880s is summarized in Tables 1 and 2 (below in Mining History). Mining and production records are generally poor, particularly for the earliest times, and many early records are conflicting. These production figures are the best data available (NMBGMR, file data). However, production figures are subject to change as new data is obtained in the future.

Geologic mapping

Geologic mapping of the Gallinas Mountains was conducted by senior project personnel (McLemore, Kelley, and Zimmerer) at scales ranging from 1:12,000 to 1:24,000 between 2019 and 2021 (Plate 1). Geologic maps were constructed onto U.S. Geological Survey topographic base maps. Prior geologic maps by Kelley et al. (1946), Perhac (1961, 1970), Kelley (1972), Fulp and Woodward (1991), and Schreiner (1993) and an unpublished geologic map by Molycorp geologists also were used to guide map construction. Geologic features could be determined in more detail than in previous mapping because of better outcrop exposures following a forest fire in 2004 and the additional use of handheld GPS units. Handheld GPS units were used to accurately locate geologic features. Because outcrop is limited throughout the Gallinas Mountains, many contacts were identified using float mapping techniques. Thus, many contacts are approximated on the geologic map. Data was compiled and digitized in ArcMap version 10.7.1 using the GeMS format. More than 30 units (22 intrusive) have been mapped. Additional faults have been recognized and mapped as well.

In addition to regional mapping of the Gallinas Mountains, detailed geologic mapping of selected areas of alteration and mineral deposits was conducted at scales of 1:1000 to 1:12,000 by McLemore (figures throughout this report). Numerous pits, trenches, shafts, and adits have exposed some of the mineralized areas. Mineralized linear zones, fractures, and faults were mapped as veins on Plate 1 (Tv), and distinguished separately from non-mineralized faults. Orientations of fractures, faults, dikes, veins, and bedding are recorded in the project ArcMap database. Chemical plots and rose diagrams were created using ioGAS-64 (ioGAS™ - REFLEX (reflexnow.com) and GCDkit (GCDkit, home).

Project database

Several databases were developed for this project. Initially, data were collected and stored in MS Access databases. During the course of the project, to increase reliability, efficiency and security, data were migrated to MS SQL Server (SQLS) and the Access "front end" forms were reworked to connect to the external database server. Mapping components and other spatial data are in ESRI ArcMap geodatabases (Plate 1). Some of the appendices are taken from the project databases. Locational and other information of photographs taken in the field, sawed samples, thin sections and hand samples are recorded in the SQLS database. These databases will be online and will be available to the public. Location and descriptions of samples referred to in this report are in the SQLS database.

Sample collection

Samples from outcrops, mine waste rock piles, mine workings and, rarely subcrop or float were collected by project personnel, analyzed, and used to supplement published and unpublished data (Appendices 3, 4). Appendix 5 is a summary of the quality assurance and quality control. Mineralized and altered areas were previously sampled and analyzed in 1980 and 2009-2010 by McLemore, in 1991-1992 by the USBM (Schreiner, 1993), in 2016 by A. Robison (2017), and in 2020 by Brian Alers. These data were used in the chemical interpretations. Since none of these samples were available for petrographic analyses, some sites were resampled for this study. Location, type of sample, and other descriptive data were entered into the project database. Most samples were composite samples (i.e. combination of individual samples over an outcrop, generally 0.3 cm in diameter), although select or chip (i.e. combination of individual samples over a specified length) samples of mineralized and altered areas were collected for specific analyses. Samples were sawed and scanned. Samples (slabbed samples, thin sections, hand samples, mineral separates, probe samples) are archived at NMBGMR for future examination.

Composite samples of waste rock piles were collected in order to evaluate potential environmental issues, especially acid-rock generation potential. Procedures developed by Munroe (1999) and the USGS (Smith et al., 2000; Smith, 2007; McLemore et al., 2014; Harrison et al., 2020) were used. Evenly spaced metal flagging pegs were positioned across an entire rock pile at each site, marking a subsample location. Approximately two shovels of material were collected from each marked location on the waste pile. Subsamples were collected with a small stainless steel hand trowel or shovel and sieved using 0.5 mm mesh into a 5-gallon bucket. Subsamples were then mixed thoroughly and stored in buckets or large plastic bags. Sampling equipment was cleaned after sampling each waste pile. A subsample of the homogenized, composite sample was split for petrographic, mineralogical, and geochemical analyses. Sample splits were examined for mineralogy, and submitted for chemical analyses and determination of paste pH (Harrison et al., 2020); data are in Appendix 3. Figure 5 is the flow chart used in collecting samples.

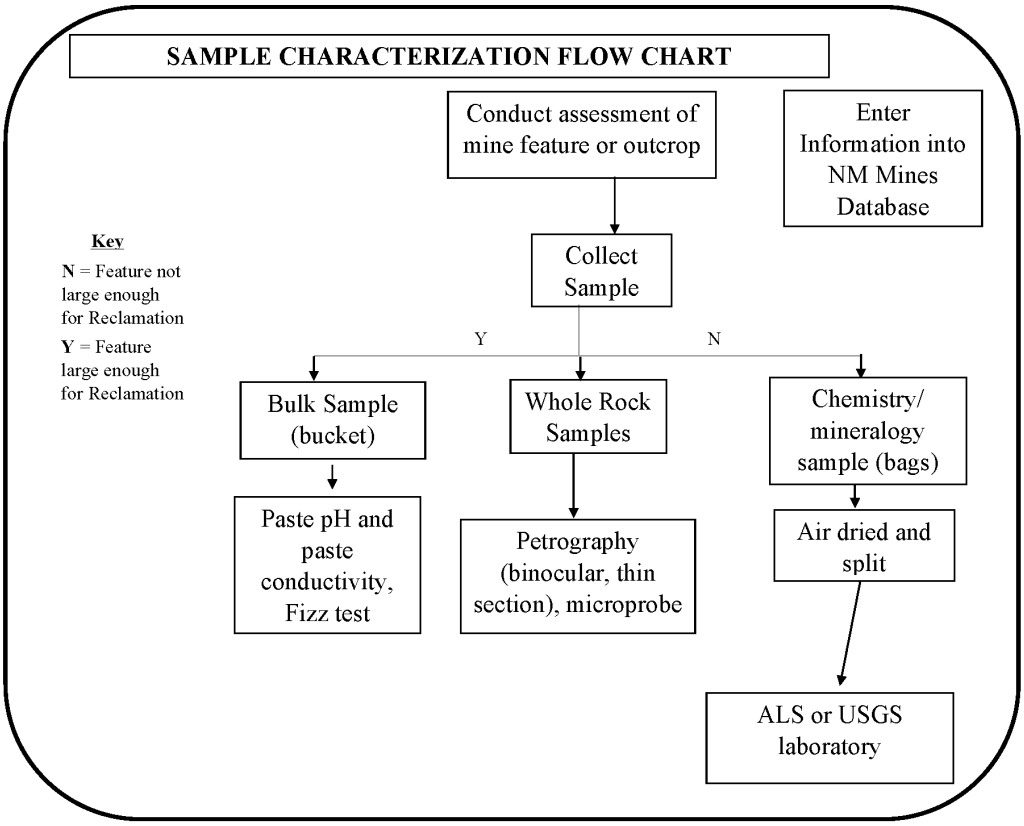

FIGURE 5. Sample characterization flow chart.

Petrography and mineralogy

Hand sample descriptions of both sawed samples and thin sections were entered into the project's SQLS database. Polished thin sections of selected samples of the igneous, altered, and mineralized rocks were made by Quality Thin Sections. Petrographic descriptions, including mineralogy and texture, of thin sections using plain, plane polarized and reflective light were entered into the SQLS database. Modal analyses were estimated by standard percentage charts (Walker and Cohen, 2009, section 6.2). Thin sections were scanned in both plane and plane polarized light, and selected photomicrographs were taken. Mineralogy of selected samples was determined by visual, petrographic methods, X-ray diffraction (XRD), and electron microprobe. Igneous rock lithologies were identified on the basis of mineralogy and chemistry as defined by Le Maitre (1989).

X-ray powder diffraction (XRD) analysis was performed on either whole rock or mineral separates performed on a PANalytical X- Pert PRO® diffractometer at the NMBGMR X-ray Diffraction Laboratory. Analyses were conducted using 45 kV X-ray beam tension and 40 mA X-ray beam current. XRD scans were identified using X'Pert HighScore Plus® software, which identifies intensity peaks and matches patterns to a Powder Diffraction File database. XRD data are in Appendix 6.

Geochemical analyses

Geochemical analyses of samples collected for this study were determined by the USGS laboratory and by ALS Laboratory (description of methods can be found at

https://www.alsglobal.com/en-us/?gclid=EAIaIQobChMI9rrc5an05gIVFq5kCh3n1AEBEAAYASAAEgLbY_D_BwE). Unweathered fist-sized samples or small chips were selected in the field specifically for chemical analyses. Weathered surfaces and organic material were removed. Samples were submitted to the laboratories where sample preparation occurred. Duplicate samples and standards were analyzed and uncertainty of analyses is generally <5%. Specific analytical methods for each element and additional quality control and quality assurance (QA/QC) are discussed in Appendix 5. Published geochemical analyses by Schreiner (1993), Korzeb and Kness (1992), McLemore (2010a), and Robison (2017) were incorporated with samples collected and analyzed by Brian Alers (unpublished) to form an extensive geochemical data set (Appendix 3).

Electron microprobe studies

Selected mineralized samples and host rocks were investigated using backscatter imaging (BSE) and qualitative wavelength dispersive spectrometer (WDS) analyses using a Cameca SX100 electron microprobe at NMBGMR to characterize compositional, chemical, and textural characteristics. Analyses were conducted with a spot size of 1μm, a 20 kV accelerating voltage and a 10 nA probe current. Samples for microprobe analysis were selected based on three criteria: (1) veins with elevated whole-rock concentrations of F, Ba, base metals, and REE, (2) types of alteration, and (3) unaltered host rocks. Samples of host rocks were selected from areas known to have undergone minimal alteration and are therefore representative of original host rock compositions and textures. Samples were initially cut to an appropriate size and then placed in 1 inch round sample mounting cups, set in Spurr Low Viscosity epoxy, and cured at approximately 80°C. Cured samples were cut to expose the surface to be analyzed and polished.

Several types of analyses were completed using the electron microprobe. Initial observations were made using BSE, which allowed observation of sample textures, and location of high mean atomic number (Z) phases that may contain REE, and other high Z elements. BSE observations were coupled with acquisition of WDS X-ray maps and/or qualitative element scans to identify different mineral phases.

Quantitative analyses focused on REE-bearing phases, feldspars, and amphiboles, and selected additional minerals. Analyses were made using a 15 kV accelerating voltage, 20 nA probe current and beam broadened to 10 um to avoid Na loss. Analytical results are being interpreted and will be presented in later reports.

$^{40}Ar/^{39}Ar$ Geochronology

K-feldspar, amphibole, biotite, and groundmass concentrates were prepared using standard separation techniques. Samples were crushed, sieved to a size range between 0.125 and 0.841 mm (20 to 60 mesh), and washed in deionized water to remove fines. Crushed material was passed through a Frantz magnetic separator and placed in heavy liquids to concentrate mineral phases. Altered grains were removed via handpicking using a binocular microscope. In addition, K-feldspar separates were picked in mineral oils to remove grains with melt inclusions, which are known to host excess ^{40}Ar (Esser et al., 1997; Kelley, 2002).

Eleven samples were dated using the $^{40}Ar/^{39}Ar$ method at the New Mexico Geochronology Research Laboratory. Samples were co-irradiated in a known geometry with the interlaboratory standard FC-2 equal to 28.201 Ma (Kuiper et al., 2008) using a decay constant of 5.463×10^{-10}/yr (Min et al., 2000). Single crystals of K-feldspar were step-heated using a focused 55-watt CO_2-laser. The step-heat experiments consist of between two and five steps, designed to

assess the presence of excess ^{40}Ar and/or ^{40}Ar loss. Amphibole, biotite, and groundmass concentrate were step-heated using an 810 nm diode laser. Released gases were cleaned in an all-metal automated extraction line shared between the two laser systems. Isotope ratios for K-feldspar were measured using the high-sensitivity multi-collector ARGUS VI mass spectrometer, whereas amphibole, biotite, and groundmass concentrate gases were measured using the high-resolution, multi-collector Helix MC Plus mass spectrometer. Blanks were measured before and after step-heat experiments. Atmospheric air ($^{40}Ar/^{36}Ar = 295.5$; Nier, 1950) and cocktails (an in-house reference gas with a $^{40}Ar/^{39}Ar$ values 6.71) were also measured before and after step-heat analyses to intercalibrate detectors and monitor machine drift. Data was reduced using PyChron software (Ross, 2014). Additional information regarding analytical procedures, instrumentation, and age calculations can be found in the footnotes of the data tables in Appendix 7.

MINING HISTORY AND PREVIOUS WORK IN THE GALLINAS MOUNTAINS DISTRICT

The Gallinas Mountains mining district is in the central Gallinas Mountains, in Lincoln and Torrance Counties (Fig. 3). Historical accounts also show it as being known as the Corona, Iron Mountain, Red Cloud, and Gallinas mining districts (File and Northrop, 1966; McLemore, 2017). The Gallinas Mountains were first examined about 1870 when a stamp mill was constructed, probably to recover gold and silver (Mellen and Olson, 1921). In 1881 the Red Cloud, Buckhorn, Deadwood, and Summit mining claims were established and patented from 1891 through 1952 (Table 1; mining claims, mines, and prospects are shown in Figure 6.). In 1882, the miners organized and wrote a mining district constitution (Daily New Mexico, 1882). Production started around 1885 for copper, silver, and lead (File and Northrop, 1966). Small quantities of ore were sent by ox-drawn wagons to Socorro for smelting (Jones, 1904), but there are no early production records available. Several small operations occurred before 1900 (Table 2; Appendix 1). A synopsis of the operational and production history of the district is in Appendix 1.

The first recorded production for base metals was in 1909, and production continued until 1956 (Table 2, 3). Lindgren et al. (1910) mentions the gold, copper, lead, and iron deposits in the Gallinas Mountains, but the authors do not provide a description because of the remoteness of the district at that time. In 1920 the ore was shipped to El Paso for refining at that smelter. In 1928, Darton (1928) interpreted a large stock intruding flat-lying sediments in the Gallinas Mountains. Iron ore was found in 1904 (Jones, 1904) and production occurred in 1942-1943 from the American (NMLI0003) and Rare Metals (NMLI0039) mines (Table 3; Kelley, 1949). In the late 1940's, mapping of the geology and iron resources was conducted (Kelley et al., 1946; Kelley, 1949). Harrer and Kelly (1963) also described the iron resources in the 1960's.

TABLE 1. Patented mining claims in the Gallinas Mountains mining district, Lincoln County, New Mexico. A single patent can contain several claims and more than one mine feature can be on each claim. Mining claims, mines, and prospects are shown in Figure 6.

Mine Id	Name	Mineral Survey	Patent No.	Date patented	Original Owner	Comments
NMLI0322, NMLI0310	Seventeen No. 2 (Park)	1680	669457	3/12/1919	Jesse Jenkins	
NMLI0326	White Oaks	1099	35920	10/2/1902	Jones Taliaferro	
NMLI0316	Hoosier Boy	1099	35920	10/2/1902	Jones Taliaferro	
NMLI0317	Eureka	1099	35920	10/2/1902	Jones Taliaferro	

Mine Id	Name	Mineral Survey	Patent No.	Date patented	Original Owner	Comments
NMLI0021	Hoosier Girl South	1099	35920	10/2/1902	Jones Taliaferro	
NMLI0308	Old Hickory	1099	35920	10/2/1902	Jones Taliaferro	
NMLI0725, NMLI0726	Hoosier Girl	1099	35920	10/2/1902	Jones Taliaferro	
NMLI0727, NMLI0728, NMLI0302	Buckhorn	1099	35920	10/2/1902	Jones Taliaferro	
NMLI0029	Little Wonder	487	25122	1/4/1895	Henry Milne	Produced 1951, 1953
NMLI0319	Deadwood	791	25165	1/11/1895	Gallinas Mining and Smelting Co.	
NMLI0048	Summit	606A	18722	10/19/1891	John Thompson and William Spence	
NMLI0708	Summit mill site	606B	16690	10/20/1890		Mill patent
NMLI0712	Conqueror No. 3	2152	1136175	8/13/1952	Allied Chemical and Dye Corp	
NMLI0315	Conqueror No. 4	2152	1136175	8/13/1952	Allied Chemical and Dye Corp	
NMLI0314	Hilltop	2152	1136175	8/13/1952	Allied Chemical and Dye Corp	
NMLI0710	Eagle Nest No. 2	2152	1136175	8/13/1952	Allied Chemical and Dye Corp	
NMLI0014	Eagle Nest No. 1	2152	1136175	8/13/1952	Allied Chemical and Dye Corp	
NMLI0709	Eagle Nest	2152	1136175	8/13/1952	Allied Chemical and Dye Corp	
NMLI0724, NMLI0711	Old Crow No. 2	2152	1136175	8/13/1952	Allied Chemical and Dye Corp	
NMLI0009	Bottleneck	2152	1136175	8/13/1952	Allied Chemical and Dye Corp	
NMLI0040	Red Cloud	790	25164	1/11/1895	Gallinas Mining and Smelting Co.	

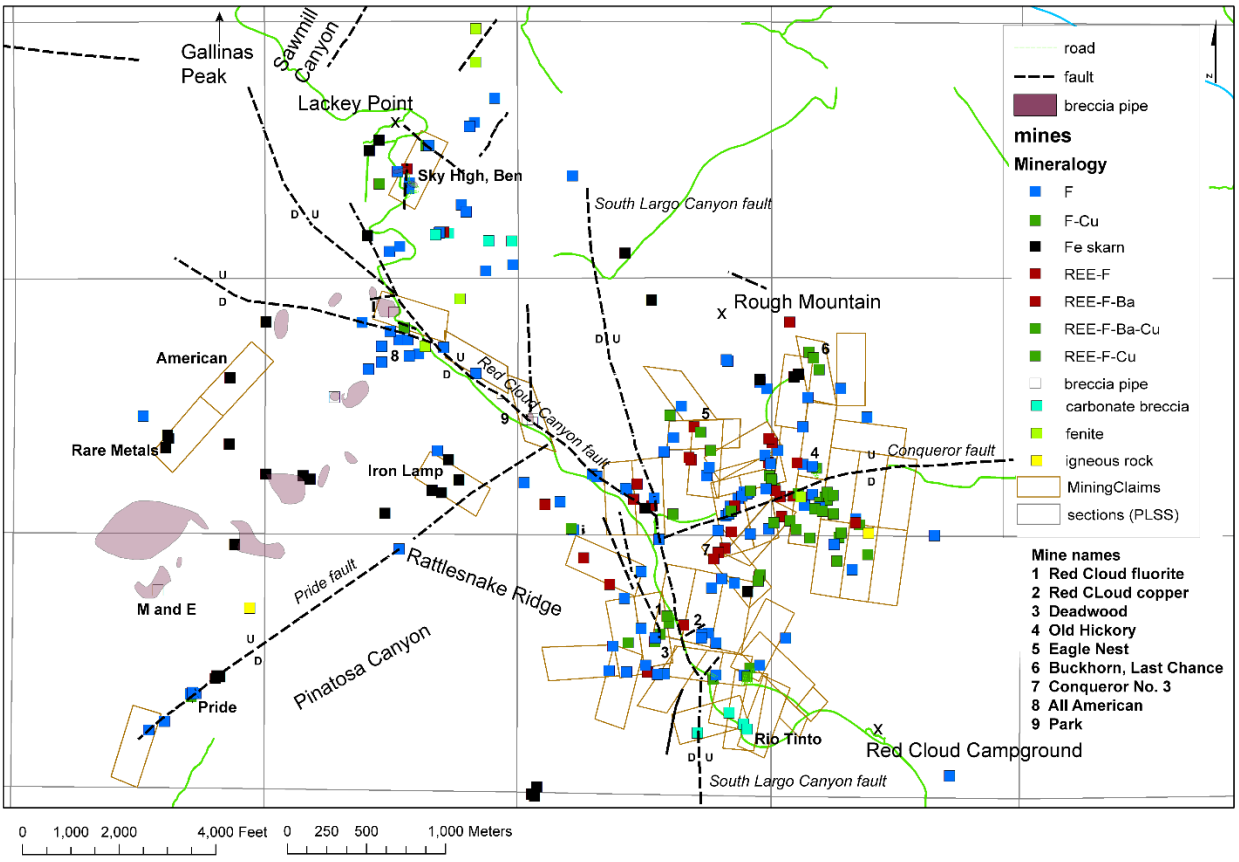

FIGURE 6. Mines, prospects, mining claims, major faults, and geographic localities in the Gallinas Mountains. U-D indicates up thrown and downthrown blocks. Location and summary of information on each mine are in Appendix 3 and the New Mexico Mines Database.

TABLE 2. Reported and estimated base and precious metals production in the Gallinas Mountains district by year. Gold (oz) includes placer and lode gold production. From USGS (1902-1927), USBM (1927-1990), Griswold (1959), NMBGMR production records.

Year	Ore (short tons)	Copper (lbs)	Gold (oz)	Silver (oz)	Lead (lbs)	Zinc (lbs)	Total value ($)	Location of production
1885	unknown	unknown			unknown			
1909	14	361		42	7,907		$409	
1911	8	555		70	6,620		$404	
1912	131	8,337		879	103,911		$6,593	Red Cloud, Deadwood
1913	157	7,068	0.18	895	94,010		$5,777	Red Cloud, Deadwood
1914	82	15,068	3.44	649	10,641		$2,849	Red Cloud, Deadwood
1915	46	5,091	0.11	243	13,277		$1,640	Red Cloud, Deadwood

Year	Ore (short tons)	Copper (lbs)	Gold (oz)	Silver (oz)	Lead (lbs)	Zinc (lbs)	Total value ($)	Location of production
1920	363	11,386		1,345	171,925		$17,315	Red Cloud, Deadwood to El Paso
1921	378	49,240		2,552	155,222		$15,889	Red Cloud, Deadwood to El Paso
1922	1,893	213,072		11,015	700,072		$78,284	Red Cloud, Deadwood to El Paso
1923	578	38,966		3,065	232,657		$24,527	Red Cloud, Deadwood
1924	121	8,596		409	26,912		$3,553	Red Cloud, Deadwood
1927	60	3,382		381	21,683		$2,025	Red Cloud, Deadwood
1928	18	667		77	7,000		$547	Red Cloud, Deadwood
1930	23	700	0.19	151	12,000		$753	Red Cloud, Deadwood
1932	24	1,000	0.58	103	11,500		$449	Red Cloud
1933	42	1,000	0.39	123	14,000		$633	Red Cloud
1934	30	4,400	0.29	221	13,850		$1,017	Red Cloud, Deadwood
1935	61	2,000	0.40	185	17,300		$1,005	Red Cloud, Deadwood
1948	1,015	10,000		854	74,000	16,000	$18,317	Red Cloud
1949	Production not reported							
1951	11			31	4,000	369	$720	Little Wonder
1953	39	4,529		183	14,351	1,344	$3,466	Red Cloud, Little Wonder
1954	23			45	6,000		$863	
1955	250		1.00	205	7,900		$1,398	
1956	300	unknown			unknown			Conqueror No. 10 by NM Copper Corp.
Reported total 1902-1955	5,367	385,418	7	23,723	1,726,738	17,713	188,433	

TABLE 3. Summary of production by commodity from the Gallinas Mountains district. From USGS (1902-1927), USBM (1927-1990), Griswold (1959), NMBGMR production records.

Mineral Produced	Mine name	Years of production	Amount (short tons)	Grade %	Reference
Copper	various	1909-1953	192.7		McLemore (1991a, b)
Gold	various	1913-1955	7 ounces		McLemore (1991a, b)
Silver	various	1909-1955	23,723 ounces		McLemore (1991a, b)
Lead	various	1909-1055	863.4		McLemore (1991a, b)
Zinc	various	1948-1953	8.7		McLemore (1991a, b)
Iron ore	American	1942-1943	3,944	55.7	Kelley (1949)
	Gallinas	1942	6,410	48.7	Kelley (1949)
	Other mines		3,326		Kelley (1949)
Total iron ore		1942-1943	11, 540		Kelley (1949)
Fluorite	All American	1951-1954	129		Griswold (1959), McAnulty (1978)
	Conqueror (Rio Tinto)	1951-1954	300		Griswold (1959), McAnulty (1978)
	Red Cloud	1951-1954	1,000		Griswold (1959), McAnulty (1978)
Total fluorite		1951-1954	1,608		
Bastnäsite	Conqueror No. 9	1954-1955	60		Griswold (1959)
	Conqueror No. 10	1956	11		Griswold (1959)
	Red Cloud (dumps)	1980	600		4935mf
Total bastnäsite		1954-1980	671		

Fluorite was discovered in the Gallinas Mountains before the 1930s (Johnson, 1928; Perhac, 1970). Around 1943–1944, the USBM and the USGS examined some of the deposits in the Gallinas Mountains to assist owners in the evaluation of fluorite and iron for the war effort (Soulé, 1943, 1946; Kelley et al. 1946; Rothrock et al., 1946). Between 1951–1954, fluorite was produced from the Red Cloud fluorite (NMLI0330) and Conqueror mines (Table 2). Bastnäsite was discovered in the area about 1943 (Glass and Smalley, 1945; Dean, 1944; Soulé, 1943, 1946) and approximately 142,000 lbs of bastnäsite was produced from the Red Cloud fluorite mine in the 1950s (Zandra et al., 1952). A bastnäsite mill was established at Gallinas Siding along the railroad about 1950 (Perhac, 1961). Between 1954 and 1956, the New Mexico Copper Corp. operated a small mill facility at Carrizozo, New Mexico and produced 55,000 lbs of bastnäsite. Williams (1966) and McAnulty (1978) further described the fluorite deposits. In 1980, American Resources Company shipped an additional 800 short tons of bastnäsite from Red Cloud mine to Texas for processing and exportation to Germany (NMBGMR mining archive file 4935_mf).

Numerous geologists and mineral collectors have worked in the district since 1960. Minerals identified from the Gallinas Mountains are in Table 4. Various mineral species were identified by DeMark (1980), Modreski (1983), and Vance (2013). Some of the recent work examined the geochemistry and paragenesis of selected deposits in the Gallinas Mountains (Williams-Jones et al., 2000; Gagnon et al., 2003; Gagnon, 2006; Salvi et al., 2005; Samson and

Wood, 2005). McLemore (1991b, 2010a) further summarized the history, geology, geochemistry, and mineral deposits of the district and described a district mineral zonation. Vance (2013) and Robison (2017) conducted M.S. thesis research in the area, improving the understanding of the geochemistry and geochronology of selected deposits and intrusions. Currently, other areas of active research are being conducted as part of two M.S. theses at New Mexico Tech, include vein mineralogy, textural relationships, mineral paragenesis, and mineral chemistry, as well as bulk rock lithogeochemical vectors (Owen et al., 2021) and detailed investigation of the magmatic breccia pipes (in progress).

Several companies have explored in the Gallinas Mountains district since the end of major production. In 1959, Doza-Bur explored for fluorite (Levine and Evans, 1991). Phelps Dodge drilled a 162-m deep hole at the Rio Tinto mine in 1980. Molycorp, Inc. conducted a more extensive exploration program in 1980–1981, which included a geochemical survey, geophysical survey, and the drilling of two holes on a magnetic high anomaly (NMBGMR mining archives; Schreiner, 1993). A summary of available drill hole information is in Appendix 9. None of the core or cuttings were available for study during this project. Other companies examined the area in 1989–1992, including Canyon Resources (1989), Hecla Mining Co. (1991–1992), Doza-Bur (1991–1996), American Copper and Nickel, Inc. (1991), and Romana Resources (1992). Woodward and Fulp (1991) reported gold assays as high as 183 ppb in brecciated trachyte/syenite sills that intruded Yeso Formation sandstone and limestone in the Sawmill Canyon area. The USBM conducted extensive mine mapping and sampling of the REE deposits in 1991-1992 (Schreiner, 1993). In 1993, many of the workings were reclaimed by the New Mexico Abandoned Mine Lands Bureau (NMAMLB). The USGS conducted a mineral-resource assessment of central New Mexico, including the Gallinas Mountains and concluded a high potential for REE (Bartsch-Winkler and Donatich, 1995). Strategic Resources, Inc. staked claims in 2009 and began exploration activities, including the drilling of six shallow holes (summarized in Appendix 9; Strategic Resources, 2012). Hardscrabble Minerals LLC also staked claims around 2010. Recent abstracts and presentations resulting from this study include Owen et al. (2021), McLemore et al. (2021), and McLemore and Diegel (2021).

TABLE 4. Minerals found in the Gallinas Mountains (Kelley et al., 1946; Perhac, 1970; Modreski, 1979, 1983; DeMark, 1980; Schreiner, 1993; Modreski and Schreiner, 1993; DeMark and Hlava, 1993; Northrop, 1996; McLemore, 2010a; Vance, 2013; Robison, 2017; mindat.org; this study). EM=electron microprobe. XRD=X-ray diffraction. New XRD scans are in Appendix 6.

Mineral	Formula	Occurrence
Common to all types of mineral deposits		
aragonite	$CaCO_3$	
barite	$BaSO_4$	White bladed crystals
calcite	$CaCO_3$	White most common, yellow calcite found in some skarns
fluorite	CaF_2	Massive, purple to clear, cementing breccias, 2–3 stages
gypsum	$CaSO_4 \cdot 2H_2O$	
pyrite	FeS_2	Mostly as pseudomorphs in fluorite matrix, replaced by goethite and hematite
quartz	SiO_2	Cement, crystals
Iron skarn deposits		

Mineral	Formula	Occurrence
aegirine-augite	$(Na_aCa_bFe^{2+}{}_cMg_d)(Fe^{3+}{}_eAl_fFe^{2+}{}_gMg_h)Si_2O_6$	XRD this report
anhydrite	$CaSO_4$	
biotite	$K(Mg,Fe)_3AlSi_3O_{10}(OH)_2$	Yellow to brown fine plates
cordierite	$(Mg,Fe)_2Al_3(AlSi_5O_{18})$	
chrysotile	$Mg_3(Si_2O_5)(OH)_4$	
diopside	$CaMgSi_2O_6$	Blue green fibrous, XRD this report
dolomite	$CaMg(CO_3)_2$	
epidote	$\{Ca_2\}\{Al_2Fe^{3+}\}(Si_2O_7)(SiO_4)O(OH)$	
fluoro-edenite	$NaCa_2Mg_5Si_7AlO_{22}(F,OH)_2$	XRD this report
fluorophlogopite	$KMg_3(Si_3Al)O_{10}F_2$	
fluorannite	$KFe^{2+}{}_3(Si_3Al)O_{10}F_2$	
fluoro-richterite	$Na(CaNa)Mg_5[Si_8O_{22}]F_2$	XRD this report
hematite	Fe_2O_3	Disseminated in veins, miarolitic cavities.
magnetite	Fe_3O_4	Major
magnesio-riebeckite	$Na_2(Mg_3Fe^{3+}{}_2)Si_8O_{22}(OH)_2$	Blue gray, XRD this report
muscovite	$KAl_2(AlSi_3O_{10})(OH)_2$	Clear, prismatic to acicular, sericitization. (alteration mineral?)
tremolite	$Ca_2Mg_5(Si_8O_{22})(OH)_2$	Blue green fibrous, XRD this report
Hydrothermal breccia and vein deposits		
acanthite	Ag_2S	Buckhorn mine
adamite	$Zn_2(AsO_4)(OH)$	Buckhorn mine
agardite	$(Ce,Ca,La)Cu_6(AsO_4)_3(OH)_6 \cdot 3H_2O$	Fluorite matrix, acicular crystals, Red Cloud
allanite	$\{A1^{2+}REE^{3+}\}\{M^{3+}{}_2M3^{2+}\}(Si_2O_7)(SiO_4)O(OH)$	
anglesite	$PbSO_4$	Trace
apatite	$Ca_5(PO_4)_3(Cl,F,OH)$	XRD this report
argentite	Ag_2S	Buckhorn mine
arsentsumebite	$Pb_2Cu(AsO_4)(SO_4)(OH)$	Buckhorn mine
austinite	$CaZn(AsO_4)(OH)$	Buckhorn mine
azurite	$Cu_2(CO_3)_2\,(OH)_2$	Trace to minor
bastnäsite	$(Ce,La)(CO_3)F$	Yellow hexagonal crystals, inclusions in fluorite
bornite	Cu_5FeS_4	Trace
brochantite	$Cu_4(SO_4)(OH)_6$	Buckhorn mine
celestine	$SrSO_4$	Blue crystals
cerussite	$PbCO_3$	Gray crystals associated with chrysocolla and mimetite, Red Cloud and Buckhorn mines
chalcocite	Cu_2S	Trace
chalcopyrite	$CuFeS_2$	Trace
chrysocolla	$CuSiO_3 \cdot H_2O$	Botryoidal crusts and vein fillings
conichalcite	$CaCu^{+2}(AsO_4)(OH)$	Rounded and botryoidal crusts and coatings in brecciated sandstones
cornubite	$Cu_5(AsO_4)_2(OH)_4$	Buckhorn mine
covellite	CuS	Buckhorn mine
cyanotrichite	$Cu_4Al_2(SO_4)(OH)_{12} \cdot 2H_2O$	Buckhorn mine
descloizite	$PbZn(VO_4)(OH)$	Trace

Mineral	Formula	Occurrence
digenite	Cu_9S_5	Buckhorn mine
duftite	$PbCu(AsO_4)(OH)$	Buckhorn mine
fluorapatite	$Ca_5(PO_4)_3F$	XRD this report
freibergite	$(Ag,Cu,Fe)_{12}(Sb,As)_4S_{13}$	Buckhorn mine
galena	PbS	Trace
hemimorphite	$Zn_4Si_2O_7(OH)_2 \cdot H_2O$	
iodargyrite	AgI	Buckhorn mine
linarite	$PbCu(SO_4)(OH)_2$	Buckhorn mine
malachite	$Cu_2(CO_3)(OH)_2$	Trace to minor
melanterite	$Fe^{2+}(H_2O)_6SO_4 \cdot H_2O$	
mimetite	$Pb_5(AsO_4)_3Cl$	Trace as prisms with chrysocolla
monazite	$REE(PO_4)$	Confirmed by EM
mottramite	$PbCu(VO_4)(OH)$	Small black crystals
olivenite	$Cu_2(AsO_4)(OH)$	Buckhorn mine
parisite	$Ca(REE)_2(CO_3)_3F_2$	
proustite	Ag_3AsS_3	Buckhorn mine
pyromorphite	$Pb_5(PO_4)_3Cl$	Trace
rostite	$Al(SO_4)(OH,F) \cdot 5H_2O$	Rio Tinto
shattuckite	$Cu_5(SiO_3)_4(OH)_2$	Buckhorn mine
spangolite	$Cu_6Al(SO_4)(OH)_{12}Cl \cdot 3H_2O$	Buckhorn mine
sphalerite	(Zn,Fe)S	Trace
smithsonite	$ZnCO_3$	Trace
strontianite	$SrCO_3$	EM, this report
tennantite	$Cu_6(Cu_4Fe_2)As_4S_{12}S$	Buckhorn mine
tenorite	CuO	Trace
titanite	$CaTiSiO_5$	XRD this report, also in miarolitic cavities
vanadinite	$Pb_5(VO_4)_3Cl$	Prisms typically associated with mottramite
wulfenite	$Pb(MoO_4)$	Fracture coatings and small orange tabular crystals
xenotime	$Y(PO_4)$	
zircon	$Zr(SiO_4)$	
Alteration minerals		
crocidolite	$Na_2Fe^{2+}{}_3Fe^{3+}{}_2(Si_8O_{22})(OH)_2$	
K-feldspar	$K(AlSi_3O_8)$	Potassic fenitization
dickite	$Al_2(Si_2O_5)(OH)_4$	Miarolitic cavities
villiaumite	NaF	Miarolitic cavities

STRATIGRAPHY AND DESCRIPTION OF LITHOLOGIC UNITS

Organization of this section is generally arranged from oldest (Proterozoic) to youngest (Quaternary). The map symbols from Plate 1 are in parentheses. The oldest rocks in the Gallinas Mountains are altered Proterozoic granite and granitic gneiss (exposed in Red Cloud Canyon) overlain by Permian arkosic and quartz sandstones, siltstones, shales, and limestones of the Abo, Yeso, and Glorieta formations. Dikes, sills, and laccoliths of varying compositions, ages, and dimensions intruded the Proterozoic and Permian rocks. Quaternary surficial deposits are found along drainages and slopes in the Gallinas Mountains. A simplified geologic map is in Figure 7 and a correlation chart is shown in Figure 8. Locations of samples and photographs are in the SQL database.

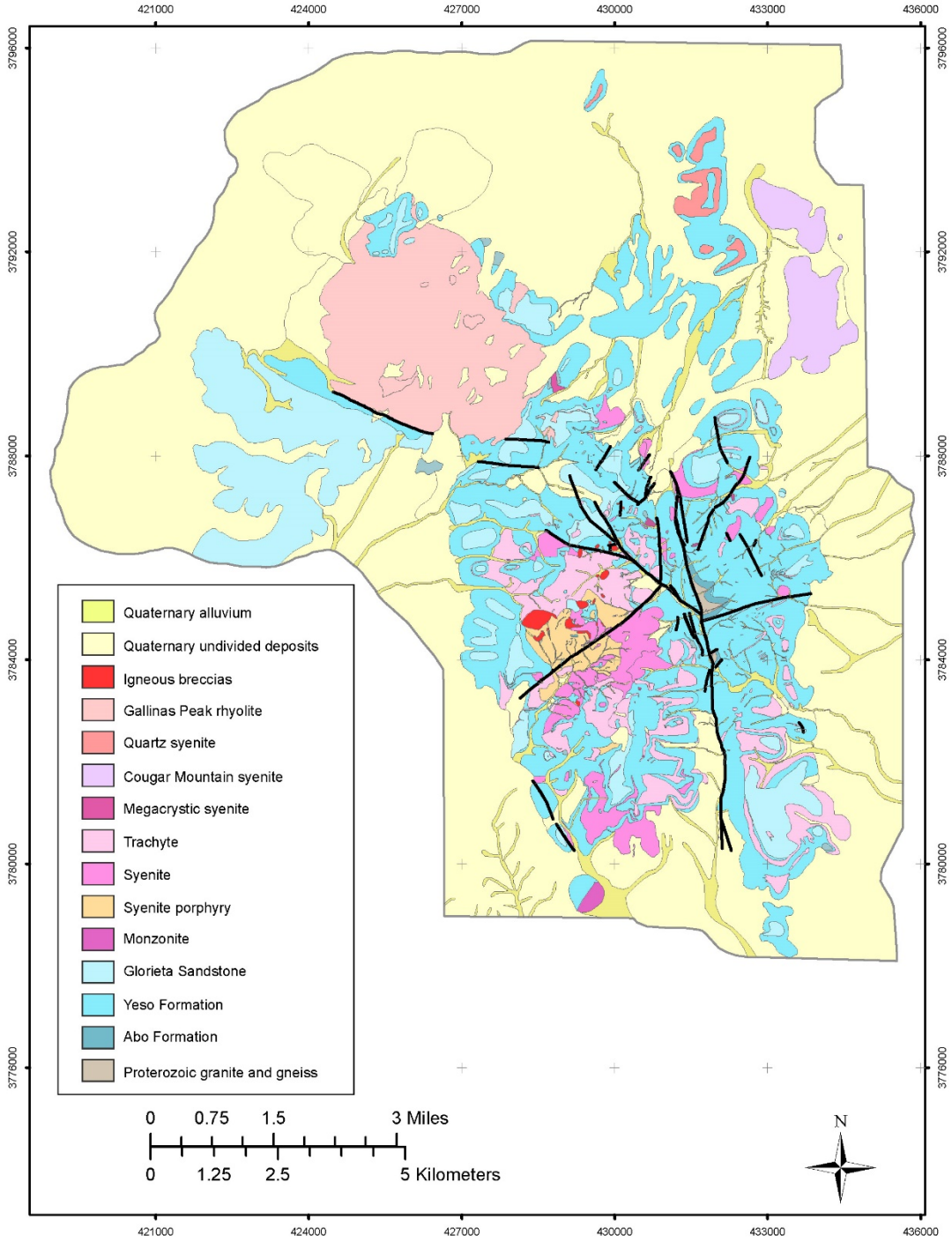

FIGURE 7. Geologic map of the Gallinas Mountains, Lincoln and Torrance Counties, New Mexico based upon new mapping for this study (Plate 1) with incorporation of published maps (Kelley et al., 1946; Kelley, 1949, 1971; Perhac, 1961, 1970; Woodward and Fulp, 1991;

Schreiner, 1993). The thick black lines are major faults. The numbers along the edge are UTM units, zone 13, NAD83.

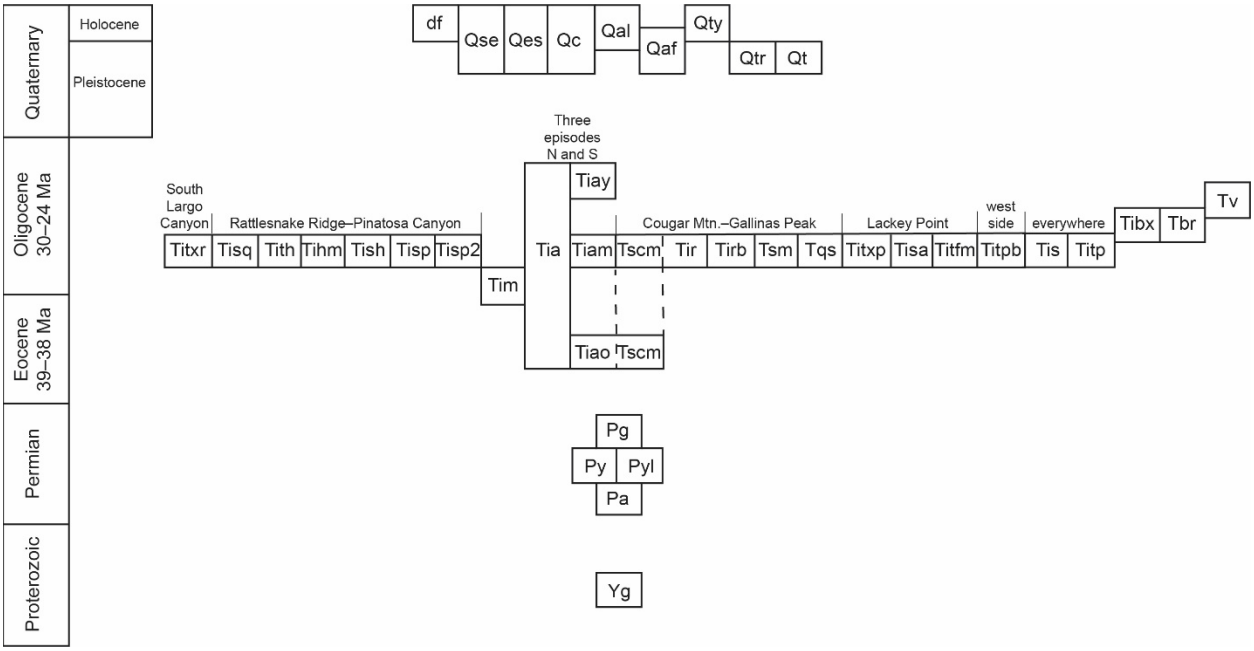

FIGURE 8. Correlation chart for rock units exposed in the Gallinas Mountains (Plate 1). The general geographic location of the intrusive rock units within the Gallinas Mountains is indicated on the chart and is keyed to Figure 6.

Proterozoic rocks (Yg)

Altered Proterozoic rocks (Yg; granite and granitic gneiss) are exposed by faulting in three places in Red Cloud Canyon in the Gallinas Mountains (Fig. 9). The Proterozoic granite, exposed in all three localities is light gray to pink, slightly foliated, fine- to medium-grained, equigranular, and consists of quartz, microcline, oligoclase, biotite, trace hornblende, zircon, titanite, and apatite. The granite is brecciated, fractured and altered to secondary epidote, hematite, mica (sericite), and clay (Perhac, 1961, 1970; Schreiner, 1993; this study). The granitic gneiss is found in two areas, the fault block north of the All American mine (NMLI0002) and east of the Helen S mine (NMLI0742). The granitic gneiss is gray, foliated (Fig. 8), medium- to coarse-grained, and consists of bands of plagioclase, orthoclase, quartz, biotite, magnetite, trace zircon, titanite, and apatite. The granitic gneiss is locally altered to secondary epidote, hematite, mica (sericite), and clay. Proterozoic quartz diorite was found in drill core by Molycorp, Inc. (Schreiner, 1993) and is fine- to medium-grained, consisting of plagioclase, microcline, hornblende, and trace quartz, biotite, titanite, rutile, pyrite, chalcopyrite, magnetite, and apatite. The granite and gneissic granite in the fault block north of the All American mine is locally fenitized (Schreiner, 1993).

Chemically, the Proterozoic granitic samples plot as granite and syenite, are relatively low in REE, lack an Eu anomaly and have relatively light REE-enriched patterns (Fig. 10). The granitic fenites are higher in REE than the unaltered granites and plot in the quartz monzonite field (Fig. 11). A sample from the Pino Hills (Gal97), northeast of the Gallinas Mountains is

similar in composition to the Gallinas granites except the Pino Hills granite has a negative Eu anomaly.

FIGURE 9. Left—Proterozoic granite (Gal245a, V.T. McLemore, photograph). Right—Foliated Proterozoic gneissic granite (Gal6100gr2, V.T. McLemore photograph).

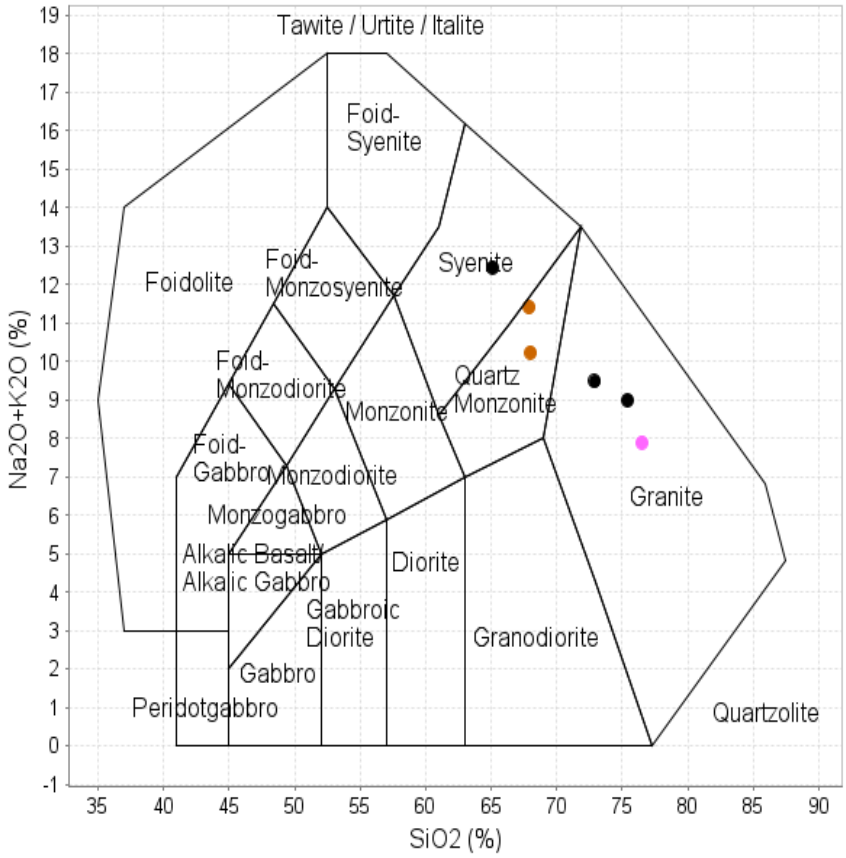

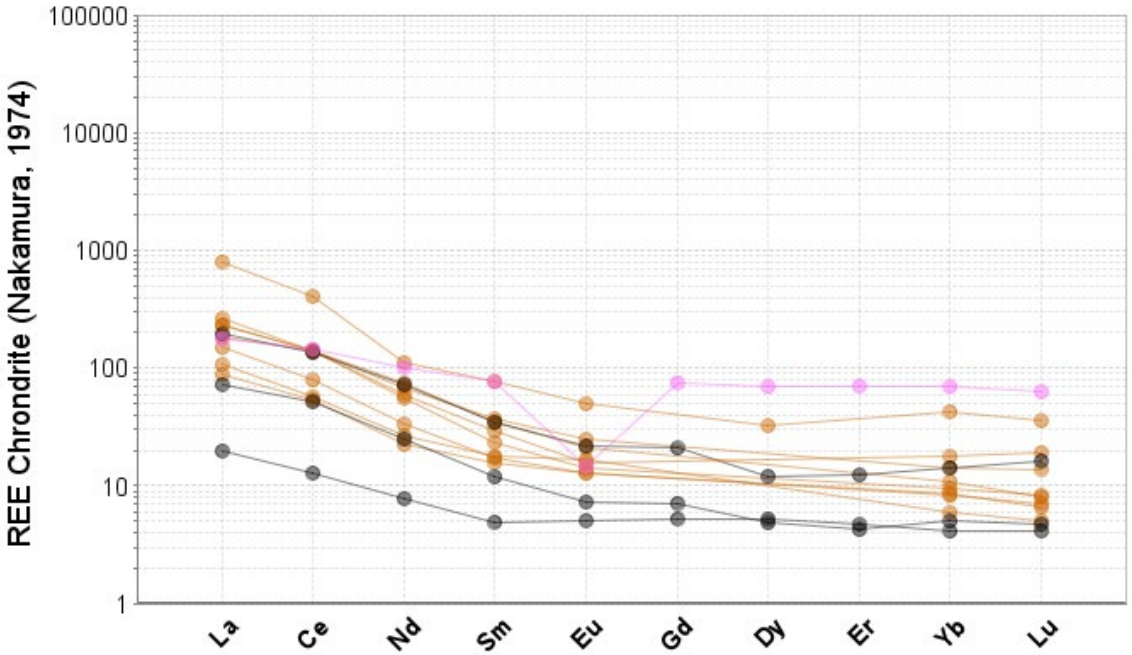

FIGURE 10. TAS plot (Middlemost, 1994) and chondrite-normalized REE plot (Nakamura, 1974) of Proterozoic granite samples (black), granite fenites (brown) from the Gallinas Mountains and a granite sample from the Pino Hills, east of the Gallinas Mountains (pink, Gal97). Chemical data are in Appendix 3.

Permian sedimentary rocks

Abo Formation (Pa)

Permian Abo Formation (Pa) consists of red to dark red, basal, white quartz pebble to arkosic conglomerate, a middle arkosic sandstone, siltstone, and shale sequence, and an upper shale unit (Fig. 11). In the Gallinas Mountains, the Abo Formation ranges in thickness from 10 to 60 m and unconformably overlies the Proterozoic rocks in Red Cloud Canyon (Table 5). Rocks of the Abo Formation also are exposed in a canyon north of the Buckhorn mine (NMLI0811) and in Pinatosa Canyon in the southern Gallinas Mountains. The conglomerates and sandstones are poorly sorted, and consist of subrounded to angular grains of quartz, feldspar, rock fragments of granite, mica schist, quartzite, and minor accessory minerals. Basal conglomerates typically contain white, rounded quartz pebbles (Fig. 11). The upper, gradational contact with the Yeso Formation is arbitrarily defined by the uppermost conglomerate and red sandstone.

FIGURE 11. Left—Contact between Proterozoic granite (pink) and Abo conglomerate with subrounded quartz pebbles (photograph no. YgrPacontactReDCloudCany, V.T. McLemore photograph). Right—Abo conglomerate (Gal291, V.T. McLemore photograph).

TABLE 5. Measured thickness between top of Proterozoic rocks and base of Glorieta Sandstone. *bottom of arroyo at fault (Precambrian not exposed)

Location	Top of Proterozoic (m)	Thickness of Abo (m)	Base of Glorieta or highest hill (m)	Thickness of Yeso Formation (m)	Comments
NMLI0859 (Conqueror No. 9)-Pg	2288	10	2395	107	Includes thick sill
NMLI0741 (Eagle Nest No. 1)-Py near Walsh claim	2330	60	2440	110	
Gal249-Pg	2220	12	2512	126	Includes thin sill
NMLI0928 (unknown)-NMLI0312 (unknown)*	2363	Not exposed	2498	135	Includes thick sill or dike

Yeso Formation (Py, Pyl)

The Yeso Formation (Py, Pyl) gradationally overlies the Abo Formation in Red Cloud Canyon and is found throughout the Gallinas Mountains. Only the upper Joyita Member is exposed in the Gallinas Mountains; the lower Cañas and Torres members found elsewhere in central New Mexico are absent. The total thickness of the Yeso Formation is difficult to estimate because sills intruded the unit increasing the apparent thickness, and thinning of the unit as a result of dissolution and associated collapse of limestone and gypsum units (Table 5). Regionally, the Yeso Formation is as much as 430 m thick (Kelley, 1949), but it is only 109 m thick in the Tecolote Hills to the southeast of the Gallinas Mountains (Rawson, 1957). In the Jones Camp area of Socorro County, ~55 km southwest of the Gallinas Mountains, the Joyita Member is 32-46 m thick (Nogueira, 1971; Bickford, 1980; Gibbons, 1981).

The Yeso Formation in the Gallinas Mountains consists of tan to orange to yellow, thin- to thick-bedded sandstone, laminated to massive siltstone, shale, and gray to dark gray to olive gray limestone and dolomite (Fig. 12). The sandstones are fine- to medium-grained, poor- to moderately-sorted, and consist of subrounded to angular grains of quartz, plagioclase, K-

feldspar, chert, fragments of granite and quartzite, and minor accessory minerals (magnetite, pyrite, hematite) (Table 6). Most sandstone beds average 0.5–1.5 m in thickness, with local beds up to 3 m thick. Most sandstones are silica cemented, but calcite also cements the rocks locally. Towards the upper gradational contact with the Glorieta Sandstone, quartz content and sorting of the sandstone beds increases. Locally in the Gallinas Mountains, upper Yeso sandstones consist of light gray to tan, thin, locally cross bedded quartz sandstones, similar to the Glorieta Sandstone, but much thinner and interbedded with thin shales. Shales are poorly exposed, thinly bedded and gray to tan to reddish brown. The contact between the Yeso Formation and Glorieta Sandstone is defined in this study as the first major, gray to tan, massive, cross bedded, quartz sandstone with well-rounded and coarser sand grains.

FIGURE 12. Left—Yeso Formation sandstone overlain by brecciated limestone (Gal6128; V.T. McLemore photograph). Right—Dipping Yeso Formation sandstone (Gal1093, M. Zimmerer photograph).

TABLE 6. Modal analyses of Yeso sandstone (Perhac, 1961).

Mineral	**6, T1S, R12E**	**1, T1S, R11E**	**25, T1N, R11E**	**14, T1S, R11E**	**26, T1S, R11E**	**5, T2S, R11E**	**13, T1S, R10E**	**3, T2S, R12E**
quartz	72.8	79.4	90.7	75.0	82.9	72.0	75.0	85.2
microcline	0.7	0.6	1.0		5.9	10.7	4.5	
plagioclase	1.4	0.8			2.5	1.8	1.4	
altered feldspar	16.7	11.4	5.0	16.7				8.7
chert	0.8	5.9	0.3	0.6	5.6	1.0		0.8
magnetite				0.8				
hematite							19.1	
matrix	7.3	1.9	3.0	6.9	3.1	14.5		5.2
other	0.3	tr	tr	tr	tr	tr	tr	0.1
Total	100	100	100	100	100	100	100	100

Yeso Formation limestone and dolomite (Pyl) are gray to brownish gray, thin- to medium-bedded, fine-grained, and consists of calcite with local dolomite. In places, the

limestone has a sandy component. In many locations, the limestones are brecciated and locally show extensive dissolution and recrystallization. Calcite veins are common and extend into the adjacent sandstone. Thin quartz crystals locally are found along fractures in the limestones. The limestone beds are, in general, 1 to 2 m thick, but can vary between 0.25 m to as much as 3 m thick. The limestone beds are commonly discontinuous and only mappable for a few tens of meters. Toward the north near Lackey Point, the limestone beds are more continuous than elsewhere in the Gallinas Mountains and are concentrated near the top of the Yeso Formation. The limestones are more weather resistant compared to the sandstones and locally crop out on weathered slopes. The limestone typically is not fossiliferous; in-place oncolites were observed at only one locality at the southern end of the Gallinas Mountains. Iron skarns, described below, are found in limestone and locally sandstone along or near the contract with syenite and trachyte sills.

The gypsum facies (Cañas Member), commonly found in the Yeso Formation elsewhere in central New Mexico, is mostly absent in the Gallinas Mountains. However, at least two gypsum beds are reported to occur in the Joyita Member. These gypsum beds, when exposed in the Gallinas Mountains, are gray to white, banded to brecciated, less than 1 m thick, and show extensive dissolution. Gypsum interbedded with limestone is found in the vicinity of the Sky High and Gallinas mines and in scattered outcrops in Sawmill Canyon.

The Yeso sandstones in the mineralized portion of the Gallinas Mountains are strongly silicified and well-cemented compared to normal, poorly-cemented, soft to moderately hard sandstones of the Yeso Formation elsewhere in central New Mexico. Furthermore, Yeso sandstone in contact with the Paleogene intrusion is commonly brecciated and cemented by quartz, amorphous silica, calcite, and hematite. See alteration section later in the report for more discussion.

Glorieta Sandstone (Pg)

The resistant Glorieta Sandstone (Pg), which is as much as 76 m thick, overlies the Yeso Formation, and caps many of the mesas and ridges in the Gallinas Mountains and surrounding areas. The quartz sandstone unit is tan to light gray to white, massive, medium-bedded, well- to moderately-sorted, and typically cross-bedded (Fig. 13). Laminated bedding of alternating coarse- and medium-grained sandstone is also common. The quartz sandstone consists predominantly of well-rounded quartz grains with few rock fragments, cemented by silica. Accessory minerals include feldspar, zircon, apatite, muscovite, and magnetite (Table 7; Kelley, 1949; Perhac, 1961, 1970).

Several features distinguish Yeso sandstones from the Glorieta Sandstone in the Gallinas Mountains. The Yeso sandstones are less silicified than the Glorieta Sandstone. Sand grains in the Glorieta Sandstone are more well-sorted and rounded compared to Yeso sandstones. The quartz-rich Glorieta Sandstone contains little or no feldspars and other accessory minerals common to the Yeso sandstone (Table 7). The Glorieta Sandstone erodes into larger boulders and forms prominent ridges on poorly-exposed slopes, whereas Yeso sandstones erode into small cobble- to pebble-sized pieces. Glorieta Sandstone tends to erode and obscure underlying Yeso sandstone float on poorly-exposed slopes.

FIGURE 13. Glorieta Sandstone, showing cross bedding (Gal259, Gal6074, V.T. McLemore photograph).

TABLE 7. Modal analyses of Glorieta Sandstone (Perhac, 1961).

Mineral	7, T1S, R12E	12, T1S, R11E	15, T1S, R11E
quartz	92.3	97.1	91.4
chert	1.6	1.8	1.9
microcline			0.7
plagioclase			0.2
altered feldspar	5.1	1.1	5.8
magnetite	1.0	tr	tr
zircon			
other heavy minerals			
Total	100	100	100

Paleogene Igneous Rocks

The following description of the igneous rocks is organized by age with descriptions of hand samples, thin sections (if available), and geochemical characterization. Additional thin section analysis is underway. The map symbols from Plate 1 are in parenthesis. Geographic locations are in Figure 6 and sample locations are in the SQLS database. A detailed description of the new $^{40}Ar/^{39}Ar$ dating results is provided in a later section. The nomenclature of igneous rocks in this report conforms to the International classification proposed by Le Maitre (1989), where the primary classification of igneous rocks is based upon mineralogy and, if too fine-grained, by the use of whole-rock geochemical analyses using the TAS (total alkali-silica; Le Bas et al. 1986; Le Maitre, 1989; Middlemost, 1994) and R1-R2 (de la Roche et al., 1980) diagrams.

According to the definition of volcanic and plutonic rocks proposed by Le Maitre (1989), many of the igneous rocks in the Gallinas Mountains are subvolcanic (i.e. have an aphanitic matrix), with the coarser-grained syenite considered to be plutonic. Field relationships indicate that these rocks are clearly intrusive. Kelley et al. (1946), Poe (1965), Perhac (1961, 1970), and Schreiner (1993) used the volcanic terminology in their research. Allen and Foord (1991) and Williams-Jones et al. (2000) used the plutonic terminology for these rocks; i.e. syenogabbro,

quartz syenite, syenodiorite, and alkali rhyolite. A combination of the volcanic (i.e. aphanitic matrix; porphyritic texture) and plutonic (i.e. medium- to coarse-grained, equigranular matrix) terminology is used in this report according to the grain size, texture, and abundance of matrix as indicated by Le Maitre (1989), but all igneous rocks exposed in the Gallinas Mountains are intrusive. The igneous rocks are then distinguished by predominant mineralogy and texture.

The major intrusions of the Gallinas Mountains are generally poorly exposed and contacts are poorly exposed or covered. Cougar Mountain, in the northeastern portion of the Gallinas Mountains, consists of a coarse-grained porphyritic syenite intrusion, possibly a laccolith (Fig. 7; previously identified as latite, Kelley et al., 1946; Poe, 1965; Perhac, 1961, 1970; McLemore, 2010a). Exposed in the northern portion of the Gallinas Mountains is a crystal-poor, sparsely porphyritic rhyolite laccolith. The southern portion of the Gallinas Mountains consists of syenite (equigranular texture) to porphyritic trachyte (trachytic texture) dikes and sills. These igneous rocks have pervasively intruded the Permian Yeso and Abo formations.

Poe (1965) determined from thermal states of feldspar that the Cougar Mountain syenite (called latite) is the oldest, followed by the trachyte and syenite, and the youngest is the rhyolite. Poe's hypothesis that the Cougar Mountain syenite is the oldest is partially confirmed by $^{40}Ar/^{39}Ar$ dating conducted in this study, although prior dating by Robison (2017) suggest this unit may be contemporaneous with younger alkaline intrusion. Field relationships are ambiguous and geochronological data are not precise enough to distinguish the ages between the trachytes, syenites, and rhyolites, as discussed below. The age of the igneous rocks is middle to late Paleogene and similar in age to other igneous rocks in the LCPB and GPM districts in New Mexico (Fig. 4).

The Cougar Mountain syenite and the rhyolite laccoliths are mineralogically and chemically distinct from the syenites and trachytes elsewhere in the Gallinas Mountains. The syenites and trachytes in the Gallinas Mountains southeast of Gallinas Peak and south of Cougar Mountain appear to be a series of stacked sills from one or more magma reservoirs (Edmonds et al., 2018), possibly fed by dikes found south of Rough Mountain.

Andesite (Tiao, Tiam, Tiay)

Andesite in this study is a broad field term for intermediate- to mafic-composition dikes and sills, many of which are altered and poorly exposed (Fig. 14). The andesites are described together because they are volumetrically a relatively minor lithology and not all of the andesites have been dated. The andesites were originally mapped as one unit. However, dating of the andesites, along with field relationships (based on an andesite dike cutting a breccia with abundant trachyte clasts and, in another place, syenite cutting andesite), suggests three pulses of andesitic magmatism (Tiao - old; Tiam - middle; and Tiay - young). Dating of several andesites (Robison, 2017; this study) indicates that some andesites are the oldest and the youngest igneous events. These samples plot as trachybasalt to basaltic-trachyandesite, and trachyte/trachydacite on a TAS diagram and have relatively flat, low chondrite-normalized REE patterns (Fig. 15).

FIGURE 14. Top left photograph—Andesite dike in road cut near Sky High mine, Gallinas Mountains intruding Yeso Formation (photo Gal43b, V.T. McLemore photograph). Top right photograph —Andesite dike intruding a reddish-brown volcanic breccia unit in Pinatosa Canyon (Gal609, S. Kelley photograph). Bottom photograph—close-up of andesite (Gal609).

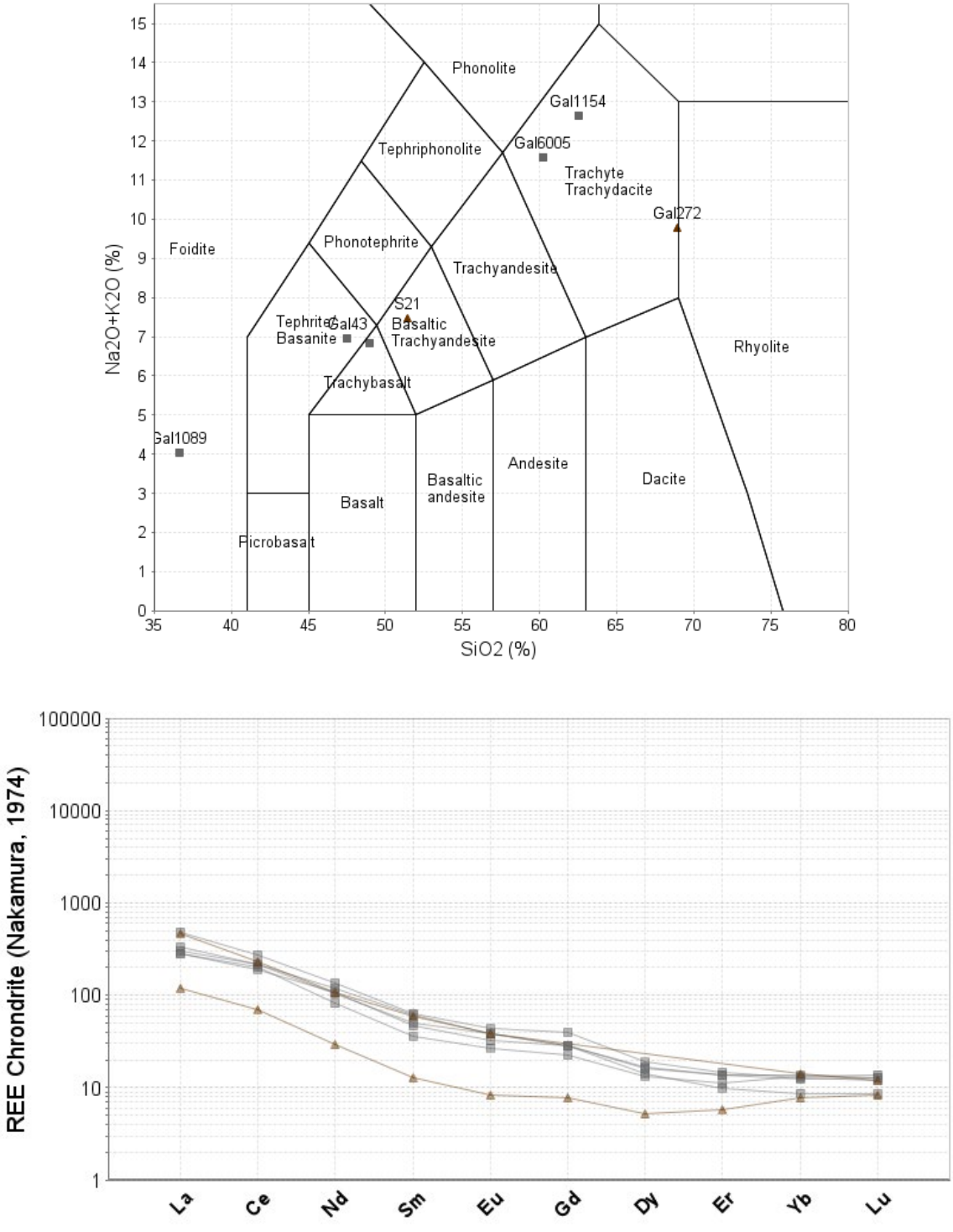

FIGURE 15. TAS plot and chondrite-normalized REE plot (Nakamura, 1974) of andesite samples (black) and andesite fenites (brown) from the Gallinas Mountains. Note that the silicified fenite (GAL272, brown) has the lowest REE concentrations. Chemical data are in Appendix 3.

Many outcrops of andesite can be viewed along the Red Cloud Canyon Forest Service Road, on ridges near Lackey Point, in arroyo bottoms throughout Pinatosa Canyon, and northeast of Gallinas Peak (Fig. 16). The outcrops on Lackey Point are fresh and have datable minerals. The andesite outcrops in Pinatosa Canyon are generally deeply weathered and have a greenish hue due to alteration (Fig. 17). The dikes and sills in Pinatosa Canyon contain <1% plagioclase (<2 mm long) and altered hornblende (also <2 mm) in a gray aphanitic matrix. A single andesite dike of limited extent that contains aegirine megacrysts and up to 10 cm angular inclusions of rhyolite and trachyte cross cuts the Gallinas Peak rhyolite. Altered andesite dikes (Fig. 14, 17) and sills intruded the Yeso Formation as dikes and a sill near the Sky High mine.

The andesite is generally greenish gray to dark gray to dark brown, holocrystalline porphyritic with a holocrystalline groundmass, and consists of hornblende, pyroxene, plagioclase, K-feldspar, and trace amounts of sericite, calcite, apatite, and biotite (Table 8). Locally in Gallinas Mountains, minor quartz has replaced feldspars. One sample (Gal272) is high in SiO_2 because it is silicified by hydrothermal fluids. Chemically, the andesites are alkaline, metaluminous to peraluminous, and have a relatively low, light-REE enriched chondrite-normalized REE pattern without a Eu anomaly (Fig. 15).

TABLE 8. Modal analyses of the andesite in the Gallinas Mountains. 1=Robison (2017).

Mineral	**1**
hornblende	47
plagioclase	41
Ca-pyroxene	8
K-feldspar	4
Total	100

FIGURE 16. Andesite sill intruding the Abo siltstone in Pinatosa Canyon (429061E 3784346N, NAD83, S. Kelley photograph).

FIGURE 17. Example of andesite dike from Pinatosa Canyon (Gal609, S. Cherotich photograph).

Cougar Mountain syenite (Tscm)

The Cougar Mountain syenite (Tscm) is located in the northeastern Gallinas Mountains. The syenite is light to medium gray, and displays porphyritic to local trachytic textures, is crystal to matrix supported, and many crystals are poikilitic (Fig. 18, 19). The porphyritic textures are defined by < 1 to ~2.5 cm phenocrysts of plagioclase, K-feldspar, and hornblende. Some megacrysts appear to show alternating zones of plagioclase and K-feldspar. The medium- to fine-grained matrix consists of plagioclase, orthoclase, hornblende, titanite (sphene), apatite, magnetite, and quartz (Table 9; Poe, 1965; Perhac, 1961, 1970). The nearby Yeso Formation sedimentary rocks are dipping 10-20 degrees to the west, suggesting that the syenite may have a laccolithic geometry. Mafic enclaves (monzonite; Fig. 20) that vary in size from 3 to 30 cm in diameter are sparsely found throughout the intrusion, but are up to 30% of the intrusion in some locations.

Chemically, the Cougar Mountain syenite plots as syenite to quartz syenite to quartz monzonite and has relatively flat chondrite-normalized REE patterns, with slight enrichment in light REE (Fig. 21). Previous workers called the Cougar Mountain syenite either a latite or trachyte (Poe, 1965; Perhac, 1961, 1970; McLemore, 2010a; Robison, 2017), but the classification of a syenite was chosen here to reflect the coarse-grained intrusive texture.

TABLE 9. Modal analyses of Cougar Mountain syenite in weight percent. 1 is from Perhac (1970), 2 is from Poe (1966), other samples are from this report. Tr=trace amounts.

Mineral	1	2	Gal1017
oligoclase	47.6		20
plagioclase		35-40	16
orthoclase	43.5	20-25	3
hornblende	6.0	25-30	10
quartz	2.1	<5	
magnetite	0.8	<5	
apatite		<5	
titanite (sphene)		<5	
accessory minerals	tr		tr
aegerine			6
hematite			5
sillimanite			2
white phyllosilicate			7
kaolinite			30
fluorite			1
Total	100	100	100

FIGURE 18. Upper left photograph of the Cougar Mountain syenite showing the plagioclase and K-feldspar megacrysts that define the distinctive porphyritic texture (sample GM10-6, V.T. McLemore photograph). Upper right photograph showing a mafic enclave within the Cougar Mountain syenite (Gal131c, V.T. McLemore field photograph). Bottom photograph shows porphyritic texture (S. Cherotich slab photograph).

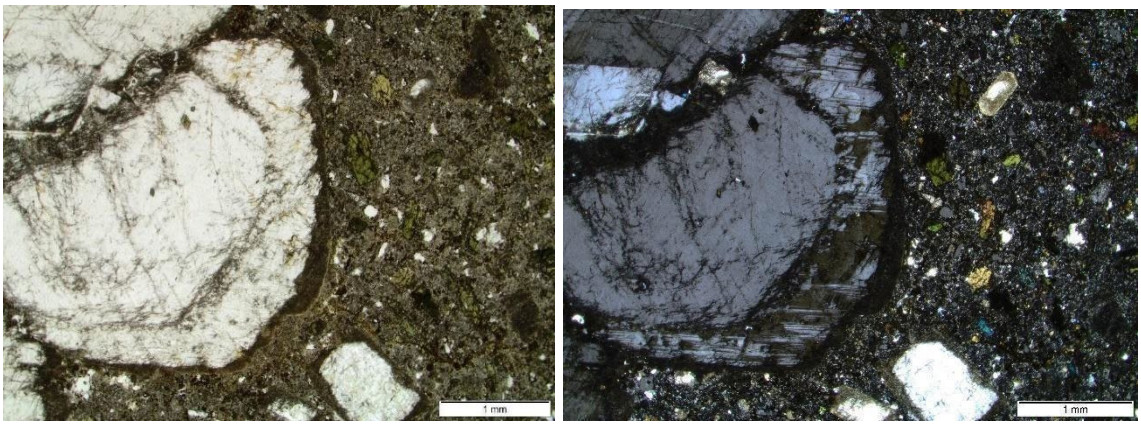

FIGURE 19. Top photograph showing Cougar Mountain syenite (M. Zimmerer photograph). Bottom photomicrographs show plagioclase rimming perthitic feldspar in Cougar Mountain syenite forming rapakivi texture (Gal1017, E.B. Haft photograph). Left is plane polarized light and right is crossed polarized light.

FIGURE 20. Cougar Mountain syenite (Tscm) with mafic enclave and rapakivi texture (Gal1018, M. Zimmerer photograph).

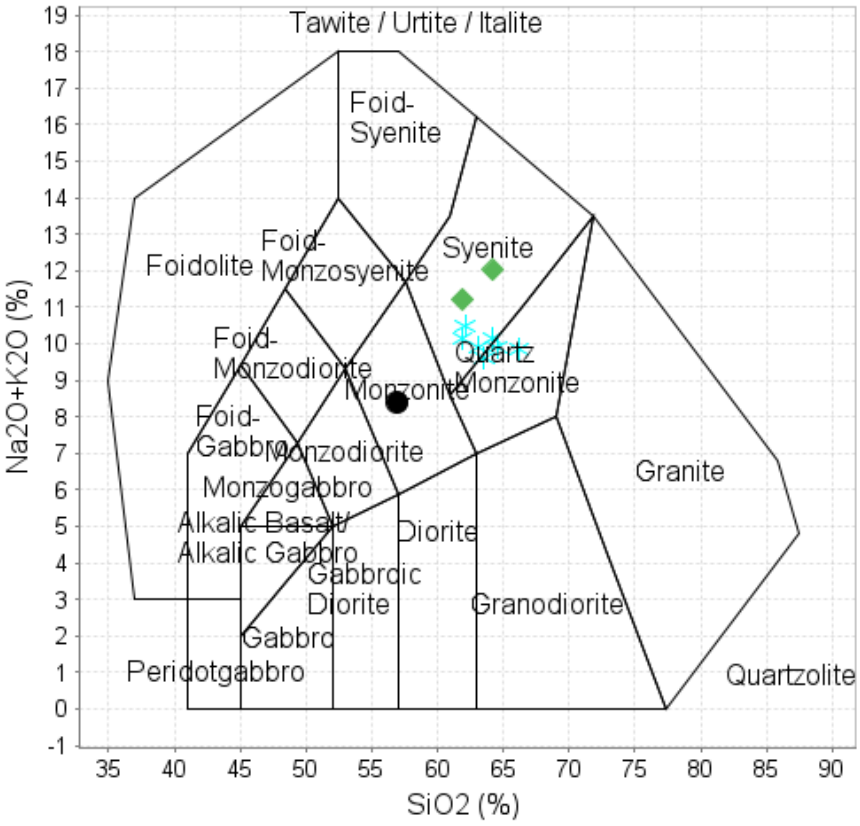

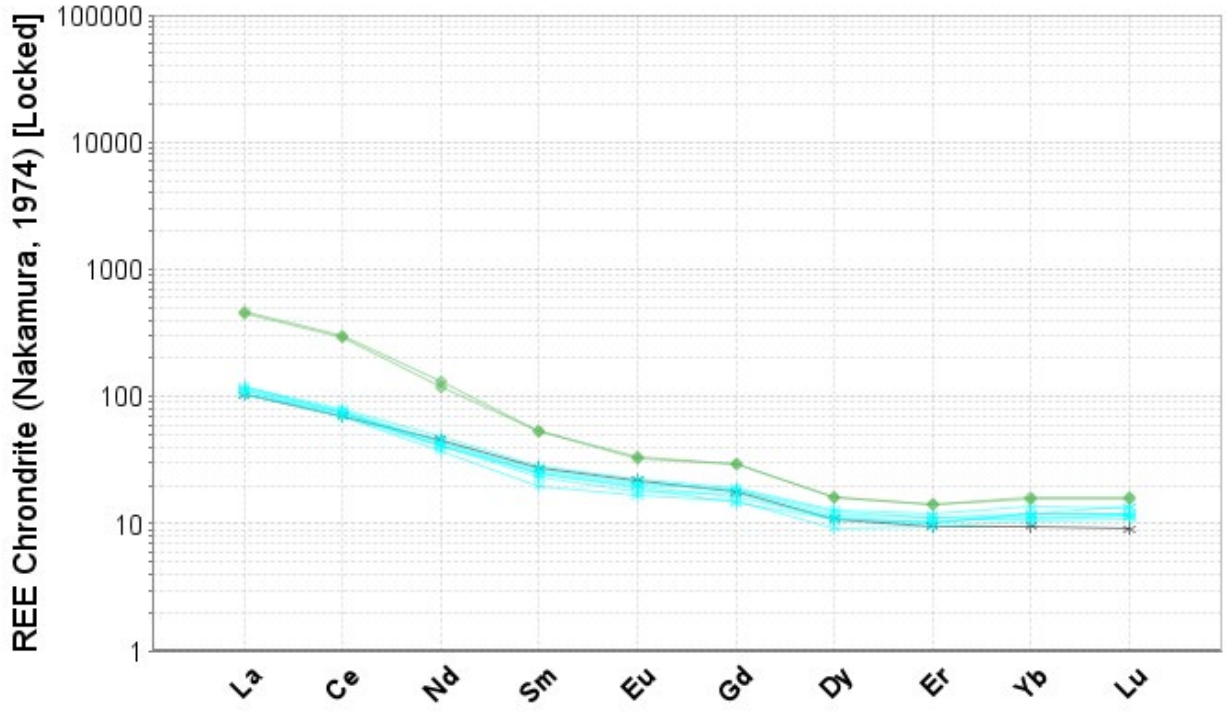

FIGURE 21. TAS plot (Middlemost, 1994) and chondrite-normalized REE plot (Nakamura, 1974) of Cougar Mountain syenites (Tscm; turquoise) and mafic enclave (black), and quartz-

bearing syenites (Tqs) from the hills west of Cougar Mountain (green) from the Gallinas Mountains. Chemical data results are in Appendix 3.

Quartz-bearing syenites in hills west of Cougar Mountain (Tqs)

Sills and a single dike of a quartz-bearing syenite (Tqs) are exposed east of the Gallinas Peak intrusive rhyolite and west of Cougar Mountain in a series of low-relief hills. The unit is light brown on the weathered surface, and light brown to gray to dark gray on fresh surfaces. The unit is fine-grained equigranular with very sparse quartz and altered feldspar phenocrysts (Fig. 22). The groundmass is composed of predominantly feldspar with lower modal amounts of quartz and iron oxides. It contains few mafic enclaves (observed only in the sills). The thickness of the sills is 30 to 45 m and the dike is ~80 m thick. Silicification of the surrounding country rock is common. No additional associated alteration or mineralization is present. Round miarolitic cavities ranging from 1 to 5 mm are present and often partially filled with hematite. Chemically, the quartz-bearing syenite plots as syenite and has a relatively flat chondrite-normalized REE pattern, with slight enrichment in light REE and no Eu anomaly (Fig. 22).

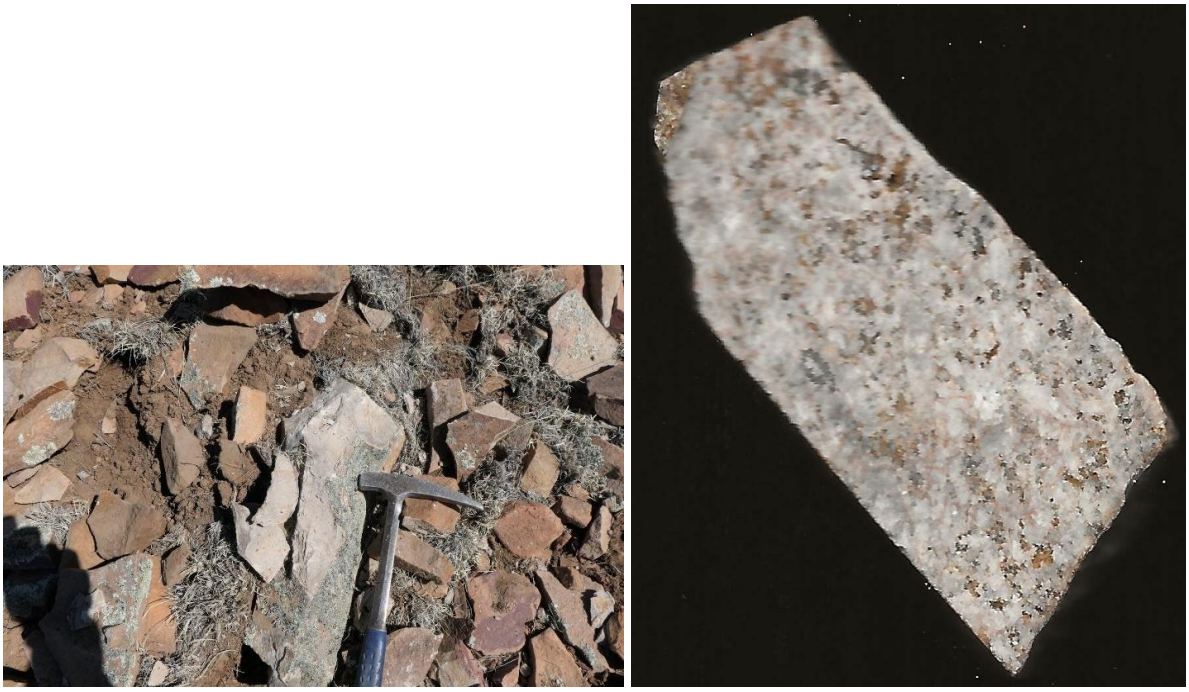

FIGURE 22. Quartz syenite (Tqs) in the hills west of Cougar Mountain, slab is approximately 5 cm wide (Gal130a, V.T. McLemore field photograph; S. Cherotich slab photograph).

Monzonite (Tim)

A monzonite intrusion (Tim, Gal6038, Gal1182), located south-southwest of the Gallinas Mountains, is exposed in contact with Permian sedimentary rocks. The unit is dark gray on weathered surfaces and light to medium gray on fresh surfaces (Fig. 23). The intrusion is fine- to medium-grained consisting primarily of plagioclase, biotite, and pyroxene, with lesser amounts of K-feldspar and hornblende. Sparse megacrysts of biotite 2 to 5 mm in diameter are also present. Chemically the sample plots as a monzonite on the TAS diagram.

FIGURE 23. Monzonite (Gal6038, V.T. McLemore field photograph, S. Cherotich slab photograph).

Syenite and Trachyte Dikes and Sills

The predominant lithologies in the Gallinas Mountains south of Gallinas Peak are numerous varieties of syenite and trachyte dikes and sills. These units are distinguished by textures, feldspar types (i.e. rapakivi, white/grey feldspars, etc.), and the presence or absence of hornblende and/or biotite. Modal analyses are in Table 10, but unfortunately the samples analyzed by Perhac (1961) are not yet keyed to the map units developed during this study. More detailed descriptions of the various textural varieties follow for each subvolcanic unit. A summary of the characteristics of the different syenite and trachyte textural varieties can be found in Table 11.

In general, the syenite is gray to pinkish gray and characterized by a porphyritic-holocrystalline texture, typically with an equigranular matrix. Some varieties are fine-grained with phenocrysts <1 mm in size, whereas coarser varieties have phenocrysts larger than 1 cm. Most of the contacts between the trachyte and syenite are concealed. However, locally the contacts are sharp and in places, the contacts between the trachyte/syenite sills and the Yeso sandstones are interfingering. Brecciated country rock (Tbr) is common adjacent to dikes and sills and intrusive material fills the fractures.

Trachyte in general is found in the southern Gallinas Mountains (Fig. 7) and some textural varieties are associated with the mineral deposits. Trachytes consist of tan to buff to light gray to white holocrystalline-porphyritic texture, locally with a finer-grained trachytic texture. Most of the contacts are concealed. Most trachytes in the Gallinas Mountains are overprinted by hematization and sericitization.

Trachyte porphyry is a subvolcanic rock that contains a higher modal abundance of large feldspar phenocrysts, which are generally twinned and/or form a rapakivi texture of K-feldspar rimmed by plagioclase. The groundmass also is fine-grained and partly aphanitic but more crystalline in comparison to the aphanitic groundmass observed in trachytes including their porphyritic varieties.

TABLE 10. Modal analyses of trachyte and syenite. 1-11, trachyte and 12-16 are from Perhac (1961). Locations of samples in Perhac (1961). Tr=trace amounts.

Mineral	**1**	**2**	**3**	**4**	**5**	**6**	**7**	**8**	**9**	**10**	**11**
oligoclase	74.2	61.0	69.3	62.4	59.2	64.2	75.5	58.4	73.7	66.1	83.0
albite	20.4	29.7	28.1	29.9	35.0	26.5	23.4	26.7	23.4	26.7	14.1
orthoclase											
hornblende	tr	0.3	1.9	5.0	2.7	7.1	0.9	13.1	2.4	5.30	2.9
quartz	0.5	7.8	0.3	2.1	2.5				0.1	1.0	
magnetite	4.3	1.2	0.3	0.6	0.5	2.2	0.2	1.8	0.4	0.9	tr
apatite	tr	tr	tr	tr	tr	tr	tr	tr	tr	tr	tr
accessory minerals	tr	tr	tr	tr	tr	tr	tr	tr	tr	tr	tr
Total	99.4	100	99.9	100	99.9	100	100	100	100	100	100

Mineral	**12**	**13**	**14**	**15**	**16**
oligoclase	74.2	64.5	66.8	76.0	68.5
albite	13.2	22.6	21.3	14.7	21.3
aegirine	10.9				
aegirine-augite		2.1	5.7	3.1	1.4
biotite			4.7		6.0
hornblende			tr	2.7	tr
magnetite	0.7	1.8	1.1	2.7	2.0
quartz		6.7	tr	tr	tr
accessory minerals	1.0	2.3	0.3	0.8	0.7
Total	100	100	99.9	100	99.9

TABLE 11. Summary of the characteristics of the different syenite and trachyte textural varieties.

Rock type	Unit symbol	Location	Textural variety	Color	Modal composition (phenocrysts)	Mineralogy (matrix)
Syenite	Tisa	Lackey Point	Amphibole-rich syenite	gray to pink	5 – 10 % amphibole	K-feldspar, plagioclase
	Tish	Rattlesnake Ridge	Amphibole-rich syenite	gray to pink	5 – 15 % hornblende	K-feldspar, plagioclase
	Tisp	Pinatosa Canyon	Porphyritic syenite	pink	20 – 30% feldspar	K-feldspar, plagioclase, hornblende, magnetite, (biotite)
	Tisp2	Pinatosa Canyon trick tank; north Pinatosa Canyon	Porphyritic syenite	Pink-gray	20 – 30% feldspar	K-feldspar, plagioclase, hornblende, magnetite, (biotite, quartz)
	Tisq	Northeastern side of Rattlesnake Ridge	Quartz syenite	gray to light gray, pink	5 – 10% feldspar, <1% hornblende, trace quartz	K-feldspar, plagioclase, hornblende
	Tis	Pinatosa Canyon	Equigranular syenite	white to gray, pink-gray	N/A	K-feldspar, plagioclase, magnetite, (pyroxene)
	Tsm	East of Gallinas Peak	Megacrystic syenite	light grey	20 – 40% feldspar	plagioclase, K-feldspar, biotite, hornblende, (quartz)
Trachyte	Titp	Widespread over Gallinas Mountains	Porphyryitic trachyte	tan to buff to light gray	5 – 15% feldspar, <1% hornblende or magnetite	K-feldspar, plagioclase
	Titfm	Sawmill Canyon south to American mine	Megacrystic porphyritic trachyte	white to gray	3 – 10% feldspar phenocrysts that are 1 to 2 cm long in an aphanitic matrix	K-feldspar, plagioclase, (hornblende)
	Titxp	South Largo Canyon, Sawmill Canyon	Crystal-poor trachyte	white to gray	1 – 10% feldspar	K-feldspar, plagioclase
	Tith	East side of Pinatosa Canyon	Hornblende trachyte porphyry	greenish-gray	25 – 30% hornblende needles	K-feldspar, plagioclase, hornblende
	Tihm	East side of Pinatosa Canyon	Xenocrystic trachyte	white-gray	5 – 10% feldspar and <5% hornblende less than 3 mm long; contains megacrysts of amphibole 1 – 5 cm across	K-feldspar, plagioclase
	Titxr	South Largo Canyon	Crystal-rich trachyte porphyry	light gray to gray to buff to pink	25 – 30% feldspar phenocrysts	K-feldspar, plagioclase

TABLE 11. continued

Rock type	Unit symbol	Distinguishing feature	Geometry	Handsample	Chemistry sample
Syenite	Tisa	Coarse-grained	3 – 4 m thick sills	Gal549	Gal458,461,463,464
	Tish	Fine to medium-grained	sills (tens of meters)	Gal 645	Gal6037,6038,Tts-2
	Tisp	White/pink feldspar phenocrysts; medium to fine-grained matrix	thick sills or plug	Gal616	Gal344avg,6006,S88
	Tisp2	Zoned feldspar with gray cores and white rims, medium to fine-grained matrix	meter-sized sill or involved in magma mixing	Gal580	
	Tisq	Quartz, equigranular matrix	meter-sized dikes	Gal1052	
	Tis	Equigranular, xenoliths present	sills (tens of meters) or plug	Gal631	Gal103,195,257,280,281,3042,6008,6023,6030,82,RM14,16,17,S23
	Tsm	1 – 3 cm feldspar megacrysts	small plug	Gal1066	Gal1066
Trachyte	Titp	<10 mm feldspar phenocrysts, fine-grained aphanitic matrix	Sills <1 – 3 m thick, associated with hydrothermal breccia near mines	Gal2009	Gal101,106,107,139,150,164,171,2000,2001,2003,2004,2005,2006,2009,2010,215,224,268,3000,3021,3029,317,471,471,74,75,79, TtAM, GM10-8, GM10-9, RM15,27,S217,22,252,253,258,26,27,28,54
	Titfm	Zoned feldspar megacrysts up to 2.5 cm long with rapakivi texture	Thin sills/dikes 1 – 2 m thick		Gal6012,3028
	Titxp	Relative lack of phenocrysts	Sills 1 – 3 m thick	Gal552	Gal274,276,278,279
	Tith	Hornblende needles up to 10 – 20 mm long, greenish-gray aphanitic matrix	occurs as fragments in Tisp2 as xenoliths, thin dikes crosscutting Yeso sandstone	Gal3029, 640, 661	Gal2014
	Tihm	Presence of xenocrysts and megacrysts of orthoclase and hornblende	porphyritic sills, contains xenoliths, thin syenite veins cut it	Gal614	
	Titxr	feldspar with rapakivi texture and complex twinning (diamonds and stars), higher modal abundance of feldspar phenocrysts than Titfm	~30 m thick sills	Gal555	

Syenite (Tisa or Tish, Tisp, Tisp2, Tsm, Tisq, Tis)

The amphibole-rich syenite (Tisa or Tish) has a gray to pink fine- to coarse-grained equigranular matrix composed of K-feldspar and plagioclase with 5-10% amphibole (usually hornblende) phenocrysts. The two largest exposures are located just northeast of Lackey Point (Tisa) and at the southern end of Rattlesnake Ridge (Tish). The amphibole-rich syenite (Tisa) is a coarse-grained syenite with <1-2 mm amphibole phenocrysts. The amphibole identified (XRD analysis, Appendix 6) is fluoro-edenite/fluoro-richterite. The sill is 3 to 4 m thick. The second variety of the amphibole-rich syenite (Tish) is a fine- to medium-grained syenite with 5-15% hornblende needles up to 8 mm long. The exposed thickness of this intrusion, which is a discontinuously exposed thick to thin sill intruding the Yeso Formation, is 60 meters.

The porphyritic syenite (Tisp) has a pink matrix with 20-30% white feldspar phenocrysts up to 6 mm across in a fine- to medium-grained equigranular matrix (Fig. 24, 25). The porphyritic syenite in Pinatosa Canyon has feldspars that are white to pink. Hornblende and magnetite also are present in the matrix, with minor biotite. Tisp seems to have the form of a thick sill with a maximum thickness of 50 m.

FIGURE 24. An example of porphyritic syenite (Tisp), which is the most common unit in the Pinatosa Canyon area. Note that the feldspars are white, in contrast to other textural varieties (Gal616, S. Cherotich photograph).

A second type of porphyritic syenite (Tisp2) is found southwest of Pinatosa trick tank and has feldspars that either have gray-colored cores with white to pink rims or white feldspars that can make up to 50% of the phenocrysts (Fig. 25). Hornblende and magnetite are present, and

biotite is sparse. The matrix is equigranular and pink to gray (Fig. 34). The Pinatosa trick-tank exposure of Tisp2 is a sill that is at most 40 m thick. A slightly different variety of Tisp 2 is gray and is found in northern Pinatosa Canyon. This porphyritic syenite contains 20-30% gray feldspar, commonly zoned with a white rim; hornblende and magnetite are common. Sparse quartz occurs in some areas. The matrix is medium- to fine-equigranular and is gray to pink (Fig. 26). In northern Pinatosa Canyon, Tisp and gray Tisp2 show evidence of magma mixing. The contact between the units is sharp to diffuse and the gray Tisp2 appears to be younger (Fig. 27, 28). The gray Tisp2 intrusions are about 1–3 m thick.

FIGURE 25. Example of porphyritic syenite (Tisp2) in southern Pinatosa Canyon. The porphyritic syenite in this area has feldspars with gray-colored cores and white feldspar rims (Tisp2, S. Cherotich photograph).

FIGURE 26. Example of the gray porphyritic syenite (Tisp2) (sample Gal580, S. Cherotich photograph).

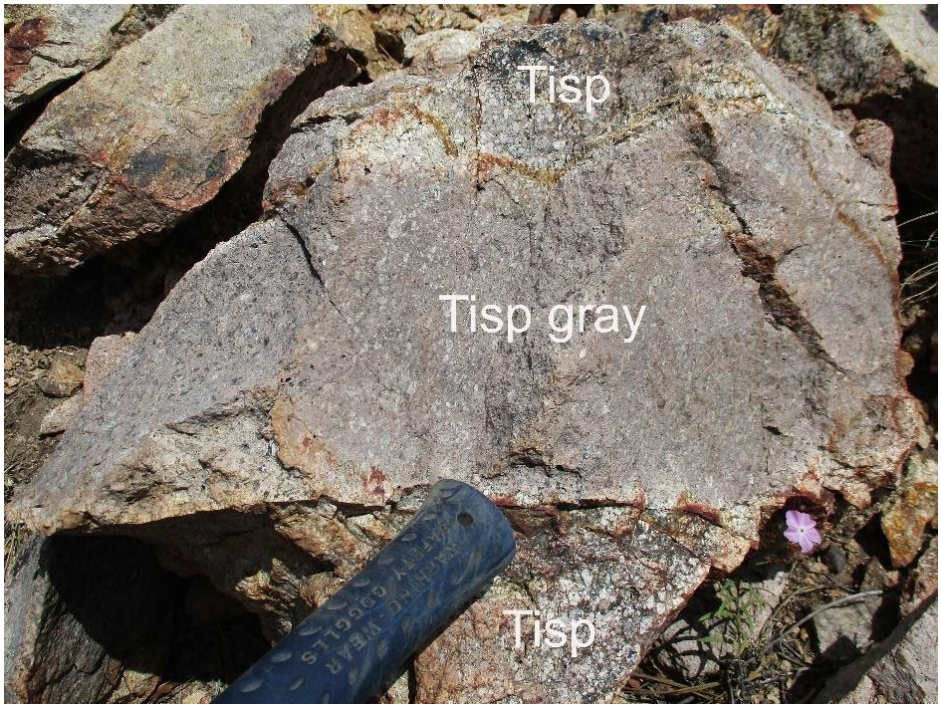

FIGURE 27. Outcrop showing the contact between different Tisp porphyritic syenites; Tisp gray is Tisp2 (S. Kelley photograph).

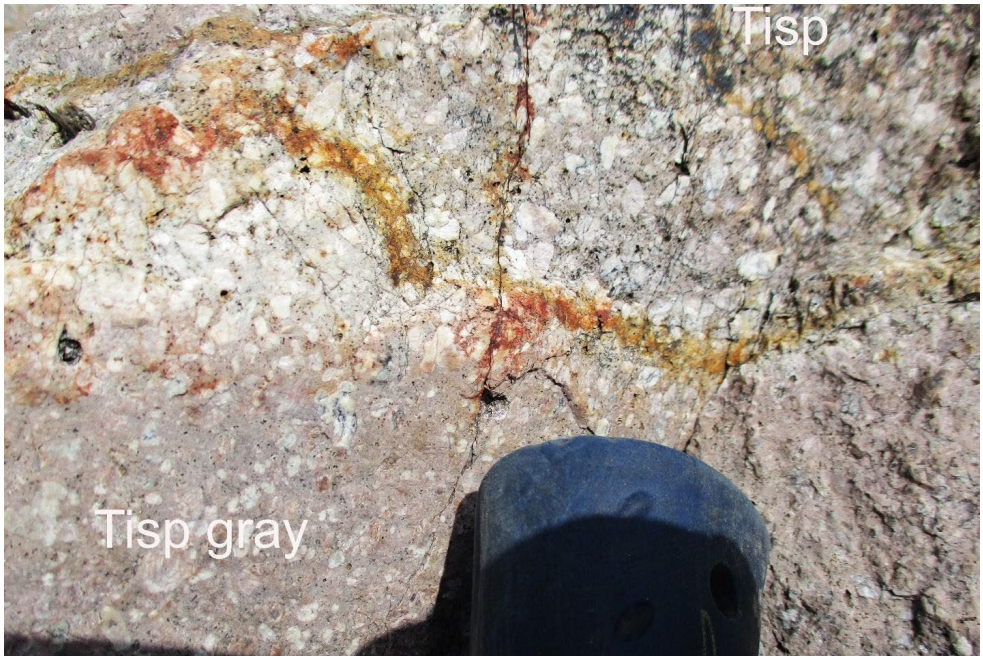

FIGURE 28. Diffuse contact between Tisp and Tisp2 gray porphyritic syenites. Note the white feldspar phenocrysts in Tisp vs. the gray cores rimmed with white feldspar occurring in Tisp2 gray porphyritic syenite (S. Kelley photograph).

The quartz syenite (Tisq) is gray to light gray to pink equigranular matrix with 5-10% K-feldspar and <1% hornblende. Quartz is present, but may be secondary. This unit grades into a Tis unit with gray-colored feldspar and very little quartz. This unit is exposed along the northern and northeastern side of Rattlesnake Ridge. The maximum exposed thickness is 60 meters.

The equigranular syenite (Tis) is white to gray to pinkish gray, holocrystalline to equigranular, and locally porphyritic, and has a medium-grained matrix with K-feldspar, plagioclase, magnetite, and sparse pyroxene visible with a hand lens (Fig. 29, 30). Other minerals include albite, orthoclase, aegirine-augite, local biotite and accessory magnetite, apatite, rutile, quartz, zircon, and riebeckite. Phenocrysts are typically <5 mm. Syenite is found as sills throughout the southern Gallinas Mountains. This unit is well exposed near Pinatosa Canyon trick tank and is a widespread unit on both sides of the canyon. Large numbers of xenoliths are present in this unit along the east side of the canyon near contacts with other units and many of the igneous breccias have formed along the Tis contact (Plate 1). The exposed thickness of this unit is 50–60 meters; the geometry is likely that of a plug.

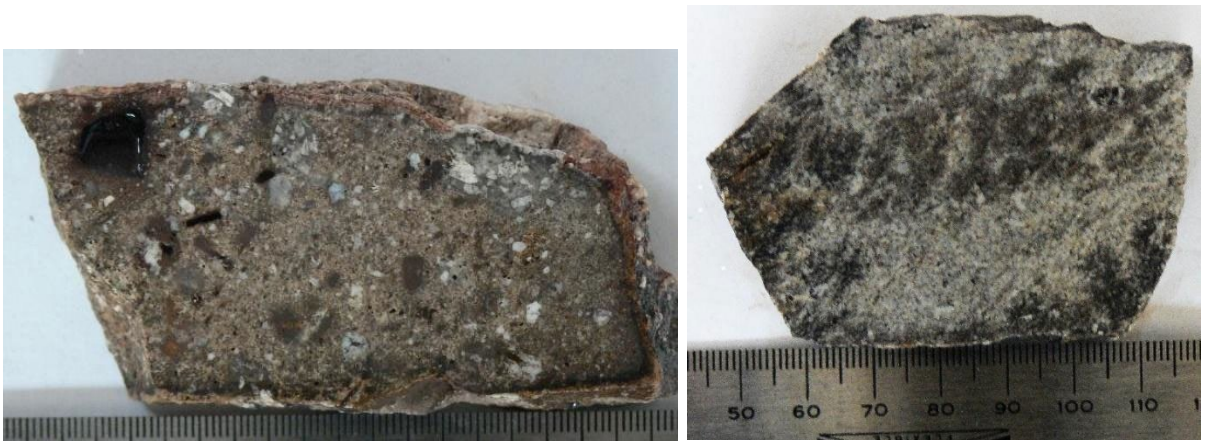

FIGURE 29. Left photograph—Equigranular syenite from outcrop near Pinatosa Canyon trick tank (Gal631, S. Kelley photograph). The black is pervasive hematite alteration in this particular outcrop. Right photograph—Equigranular syenite with abundant xenoliths (sample Gal598; S. Kelley photograph).

FIGURE 30. Equigranular syenite with abundant xenoliths (Gal601, S. Cherotich photograph).

Megacrystic syenite (Tsm) is an intrusion of limited extent located east of the Gallinas Peak intrusive rhyolite. Outcrop geometry suggests a small plug. The intrusion is light gray to reddish brown on fresh and weathered surfaces. Unit displays a distinct porphyritic texture defined by 1 to 3 cm feldspars (Fig. 31). Many megacrysts have a rapakivi texture with pinkish cores of K-feldspar and white, opaque rims of plagioclase. Some megacrysts display multiple zonation bands. Mineral inclusions within the megacrysts are also common. The groundmass is fine- to medium-grained and includes plagioclase, K-feldspar, highly altered mafics (possibly biotite and hornblende), and abundant oxides. Very sparse quartz is also present, but appears irregularly dispersed within the groundmass.

FIGURE 31. Feldspar with rapakivi texture in megacrystic syenite (Tsm) from the closed road SE of Gallinas Peak (Gal1066_5, M. Zimmerer photograph). Twinned feldspar in megacrystic syenite (Gal1066_6, M. Zimmerer photograph).

Trachyte varieties (Titp, Titxp, Titfm, Tith, Tihm, Titxr, Titpb)

The porphyritic trachyte (Titp) consists of tan to buff to light gray holocrystalline - porphyritic trachyte with trachytic texture (Fig. 32, 23). It has a fine-grained to aphanitic matrix with 5–15% albite and K-feldspar phenocrysts that are typically <10 mm across, <1-2% hornblende, and magnetite phenocrysts. It has an aphanitic groundmass consisting of albite, K-feldspar, biotite or hornblende (now altered to hematite and limonite) and trace amounts of apatite, quartz, and zircon. This is the most prevalent intrusive unit in the area, and is found throughout the Gallinas Mountains, displaying a wide variety of feldspar crystal contents over short distances. The chilled margins of the sills are relatively crystal poor and usually have larger feldspar phenocrysts. Sills typically range from <1 to 3 m in thickness, although the sills in South Largo Canyon are 30 m thick. Most of the hydrothermal breccia and fissure vein deposits are associated with the porphyritic trachyte.

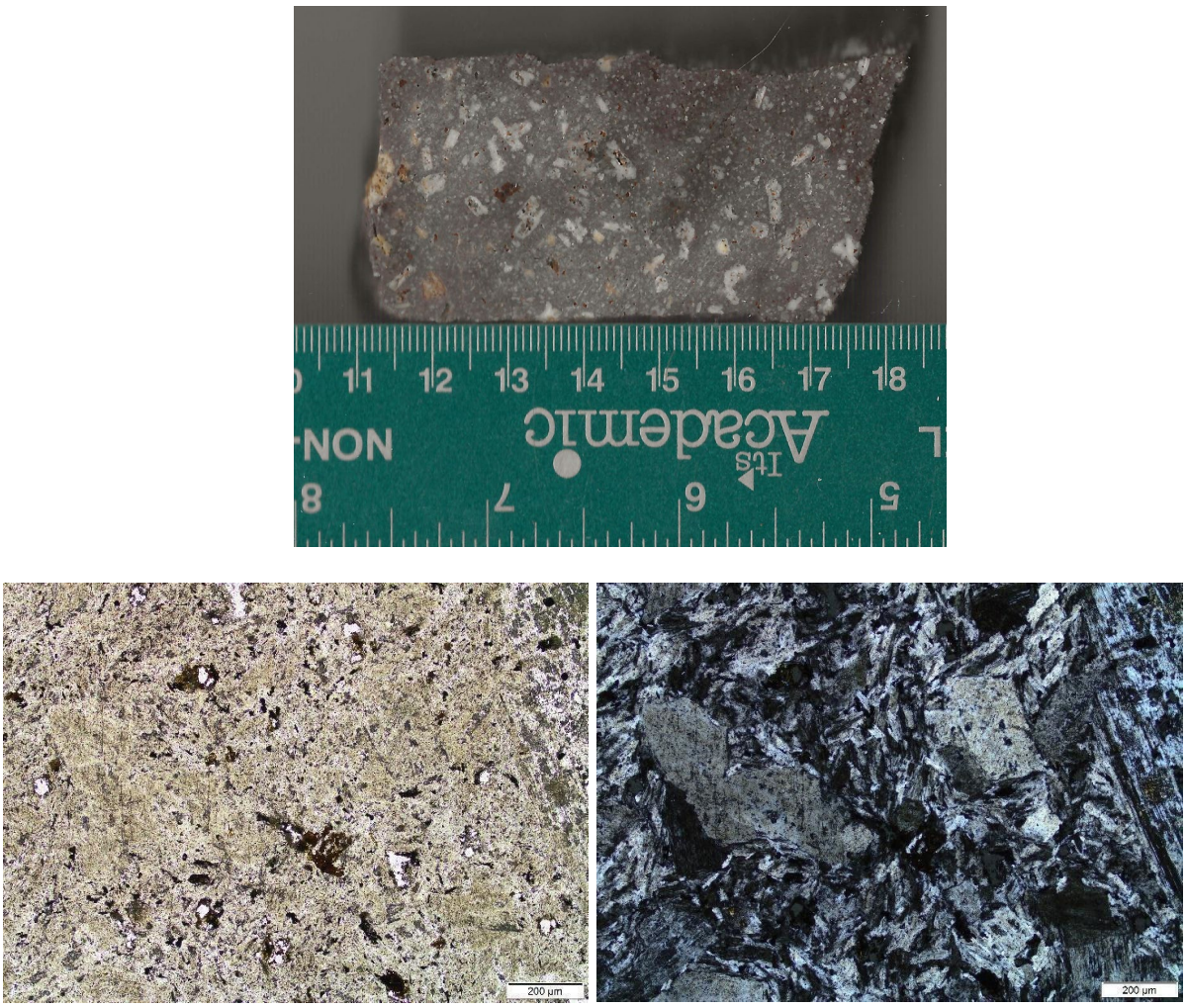

FIGURE 32. Photomicrographs of porphyritic trachyte (Titp). Upper photograph is close-up of Gal2009 (S. Cherotich photograph). Bottom left is plane polarized light and bottom right is crossed polarized light (Gal2009, E.B. Haft photograph).

FIGURE 33. Photograph of the porphyritic trachyte (Titp) (sample GM10-9, V.T. McLemore photograph).

The megacrystic porphyritic trachyte (Titfm) with local rapakivi texture consists of K-feldspar phenocrysts rimmed by plagioclase, in an aphanitic to fine-grained gray matrix. The K-feldspar laths are up to 2.5 cm long. It typically occurs as thin sills and dikes, 1-2 m thick, and 2 m thick, respectively. These rocks are found mostly between Sawmill Canyon and southward to the ridge north of the American mine (NMLI0003).

The crystal-poor trachyte (Titxp) is white to gray, with an aphanitic matrix containing 1–10% feldspar phenocrysts, usually less than <10 mm across. Mafic minerals are not obvious. It occurs as stacked sills on a hill west of and within Sawmill Canyon and as the lowest exposed sill in a stack of sills in South Largo Canyon. Sills are 1 to 3 m thick.

The hornblende trachyte porphyry (Tith) forms an extensive body on the east side of Pinatosa Canyon that contains 25-30% hornblende needles up to 20 mm long (most are 10 mm long) in a greenish-gray aphanitic matrix (Fig. 34). Pieces of the hornblende trachyte porphyry are present in gray porphyritic syenite (Tisp2); they may be xenoliths or thin intrusions. Tith is geographically associated with Tish, but the contact between the two units is obscured by colluvium. Tish could be a finer grained phase of Tish, based on exposures at the southern tip of Rattlesnake Ridge. Hornblende trachyte porphyry dikes (Tith) intruded Yeso Formation sandstone in South Largo Canyon.

FIGURE 34. Field photo of altered hornblende needles in hornblende trachyte porphyry (Tith) (S. Kelley photograph).

The xenocrystic trachyte (Tihm) forms a sill on the east side of Pinatosa Canyon. This unit is porphyritic and characterized by the presence of xenocrysts and megacrysts of equant pink orthoclase (<12 mm) and hornblende (up to 5-6 cm). The matrix is composed of 10% white and gray feldspar set in a pink to gray aphanitic matrix (Fig. 35). Monzonite xenoliths were found along the west edge of the unit.

FIGURE 35. Left photograph—Field photo of hornblende(?) megacrysts in a xenocrystic trachyte sill (Tihm) (S. Kelley photograph). Right photograph—Megacrystic sill (Tihm) with orthoclase megacryst (Sample Gal614, S. Cherotich photograph).

The crystal-rich trachyte porphyry (Titxr) consists of 10 to 35% twinned and untwinned feldspar phenocrysts up to 12 mm across (Fig 36, 37, 38). The feldspar phenocrysts commonly have rapakivi textures and range in color from white, gray, pink, and occasionally green. This unit can be distinguished from the megacrystic porphyritic trachyte (Titfm) by the higher modal abundance of feldspar phenocrysts (10 to 35%), the presence of complexly twinned (star- or diamond-shaped) feldspar and aphanitic gray groundmass. Hornblende can be recognized in the matrix and magnetite is also commonly present. This unit forms thick sills (~30 m) on both sides of South Largo Canyon.

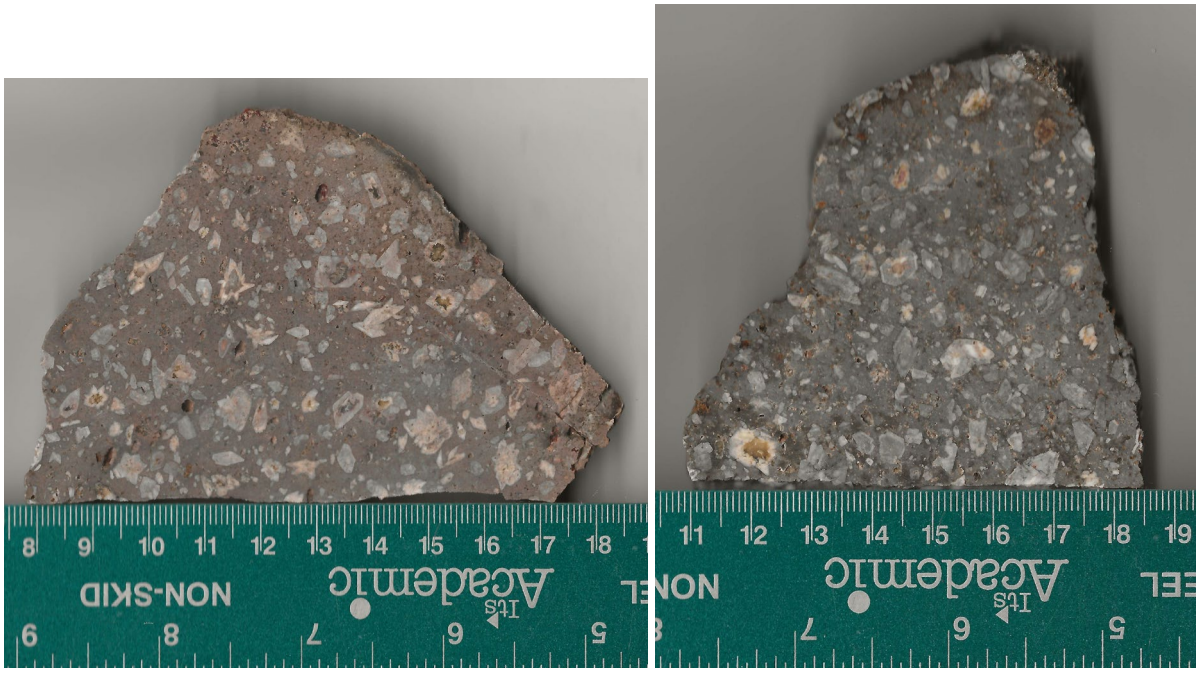

FIGURE 36. Crystal-rich trachyte porphyry (Titxr) in South Largo Canyon (Gal555, 554, S. Cherotich photograph).

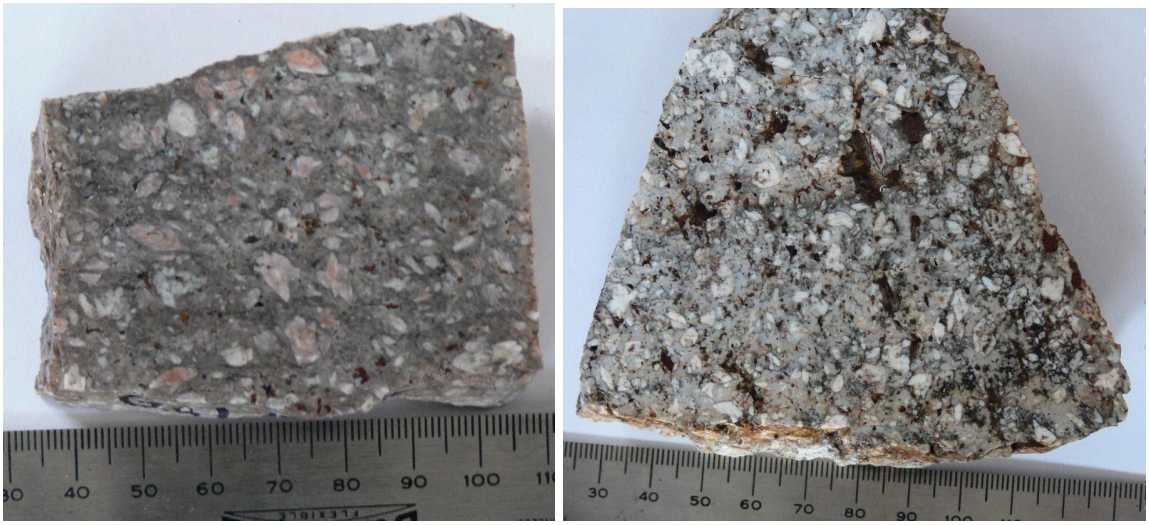

FIGURE 37. Crystal-rich trachyte porphyry (Titxr) in South Largo Canyon (Gal565, 584, S. Kelley photograph).

FIGURE 38. Crystal-rich trachyte porphyry (Titxr) in South Largo Canyon (Gal582, S. Cherotich).

The porphyritic trachyte with a bimodal population (Titpb; Gal 648)) of white plagioclase with green alteration, pink orthoclase with plagioclase rims, and 1% pyroxene is found on the west side of the study area south of Gallinas Peak. The orthoclase phenocrysts are up to 1.5 cm long (Gal 648). The matrix is pink, aphanitic, and contains abundant magnetite. Some secondary quartz is present.

Chemistry of syenites and trachytes

Most syenites and trachytes in the Gallinas Mountains are altered. Altered samples were classified as fenites on the basis of (1) secondary feldspars and other potassic and sodic alteration minerals, (2) Na_2O or K_2O >8%, (3) high CaO (carbonate replacement), (4) high Fe_2O_3T (hemitization), and (5) the use of an alteration plot (Fig. 39). Chemically, the syenites and trachytes in the Gallinas Mountains are similar regardless of texture, excluding the syenites in the Cougar Mountains and quartz-bearing syenites hills west of Cougar Mountain. Most syenites identified in the field plot in the syenite to quartz monzonite field on the TAS diagram (Fig. 40). Two samples (Gal3038 and Tts-2) plot as monzonite and one sample (Gal103) plots as foid-monzosyenite. Most trachytes sampled plot within the trachyte and trachydacite fields (Fig. 39). Two samples are trachyandesite (Gal317 and Gal3029) and one sample is phonolite (Gal471). The trachytes and syenites are alkaline, ferroan, metaluminous to peraluminous, and plot as A-type granites. The sampled syenites and trachytes exhibit relatively flat chondrite-normalized REE patterns, with slight enrichment in light REE and no Eu anomaly (Fig. 41).

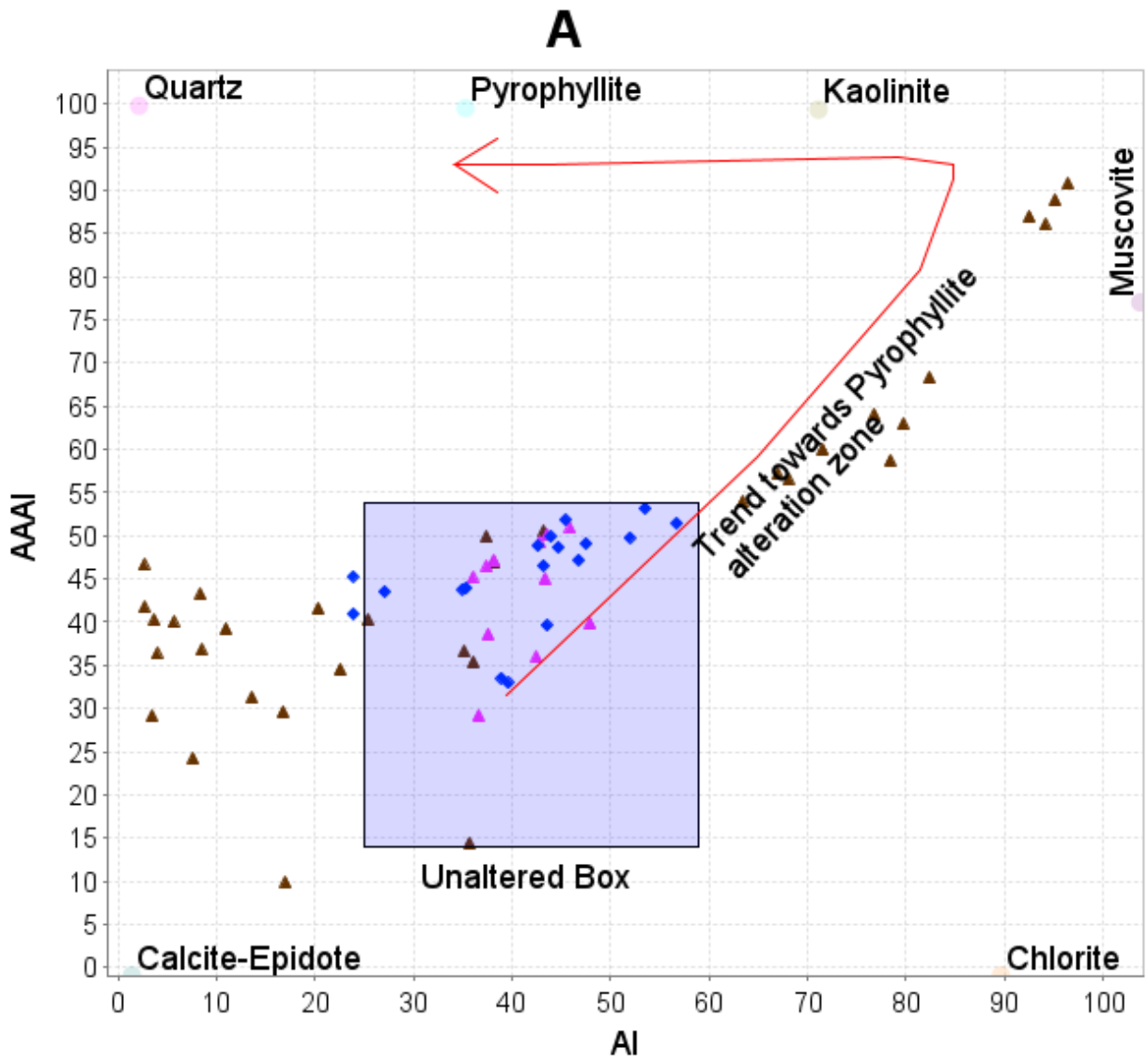

FIGURE 39. This alteration plot is used to distinguish altered samples from fresh igneous rocks. Gallinas trachyte (blue diamonds), syenites (pink triangles) and trachyte/syenite fenites (brown triangles) plotted on an alteration box diagram. The trachyte and syenite samples exhibit little chemical alteration on this plot. More discussion on the alteration (fenites) below. AI=Ishikawa Alteration Index. AAAI=Advanced Argillic Alteration Index. The red arrow indicates the trend from unaltered samples (blue box) toward pyrophyllite alteration. After Williams et al. (2004) and Large (2001). The use of this diagram is only to aid in distinguishing between unaltered and altered samples; it does not imply that there is an advanced argillic alteration in this system. Further work could characterize an alteration diagram for fenitization.

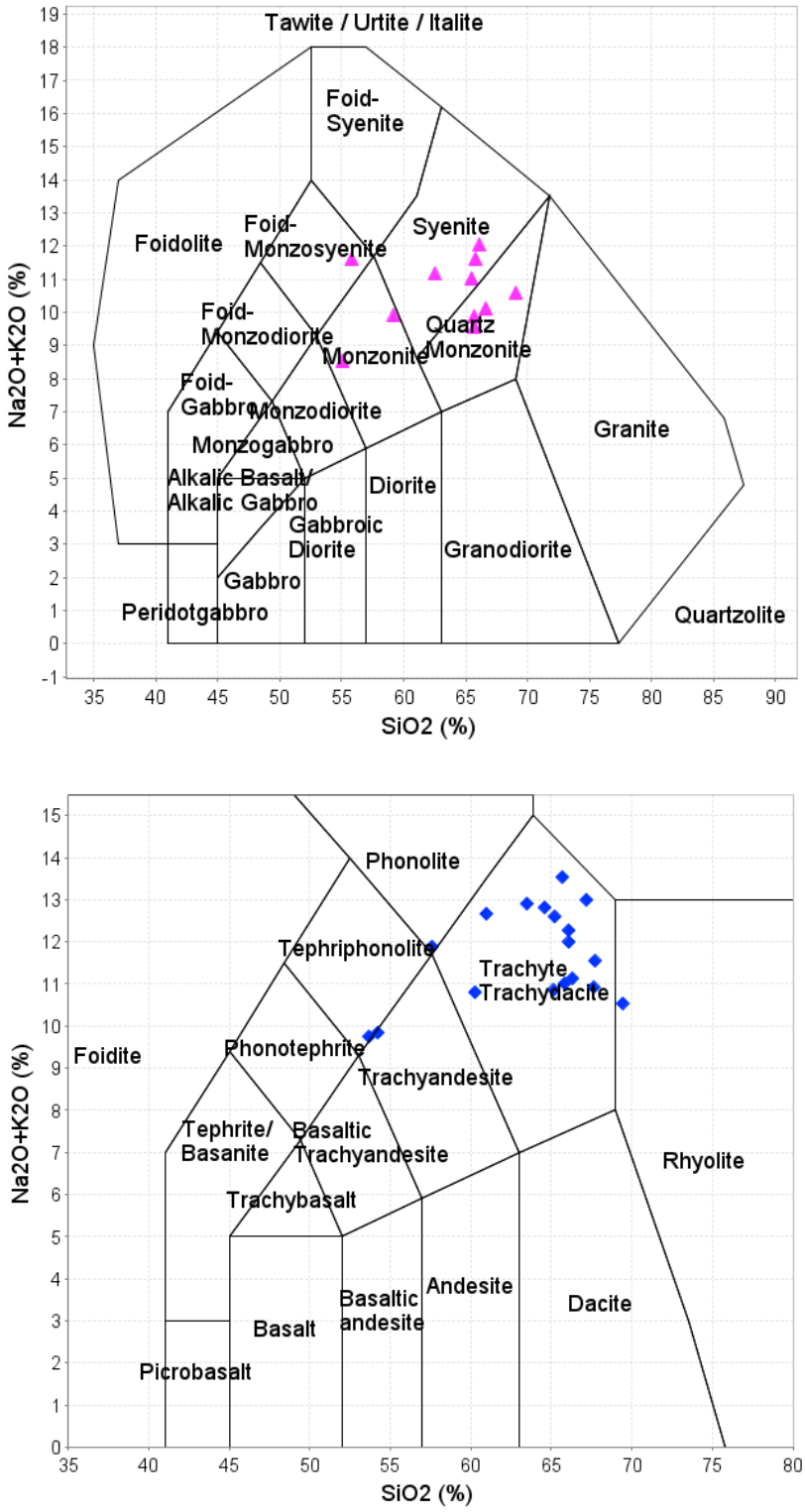

FIGURE 40. TAS diagram of syenites (pink) and trachytes (blue) from the Gallinas Mountains. Left plot is from Le Bas et al. (1986) and Le Maitre (1989) for volcanic rocks; the right plot is

Middlemost (1994) for plutonic rocks. Note that the syenites and trachytes samples overlap in both diagrams, indicating similar chemical compositions.

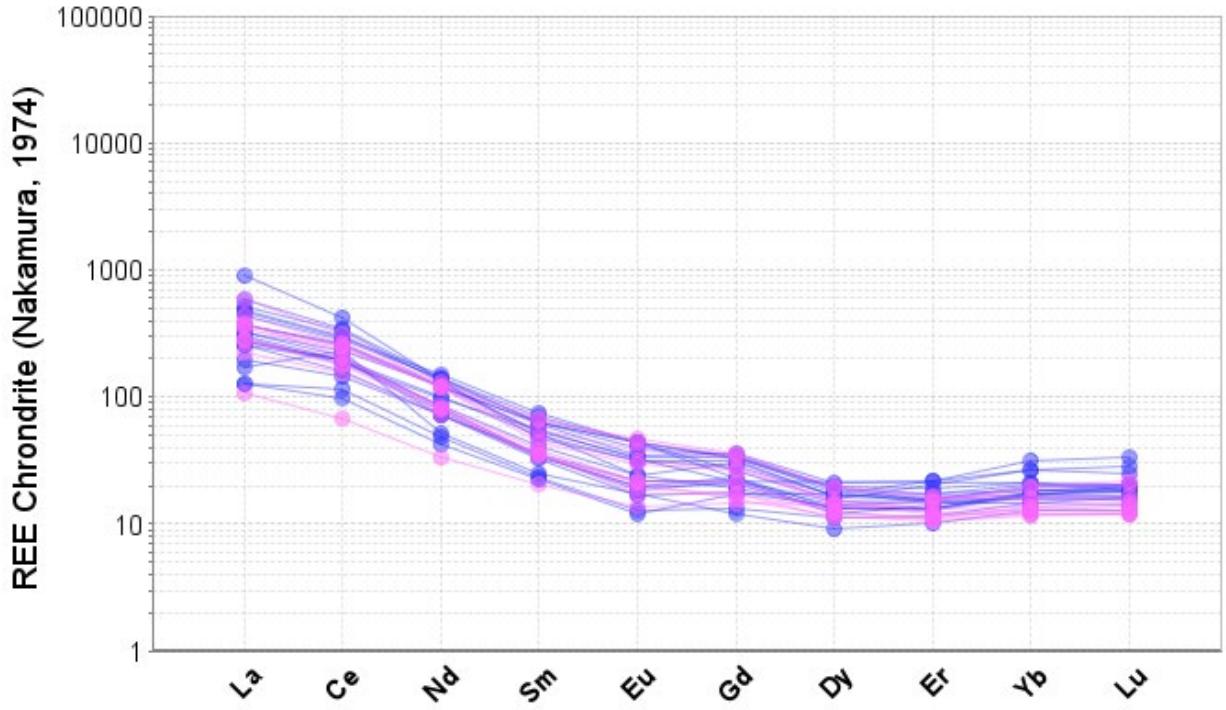

FIGURE 41. Chondrite-normalized REE plot (Nakamura, 1974) of trachytes (blue) and syenites (pink) from the Gallinas Mountains.

Gallinas Peak Rhyolite (Tir, Tirb)

The Gallinas Peak rhyolite (Tir, Tirb) is exposed in the northwestern Gallinas Mountains (Fig. 7) and was first described in detail by Perhac (1961, 1968). The intrusive unit is approximately 366 m thick at Gallinas Peak without an exposed base. The rhyolite is tan to pinkish gray to white, fine-grained aphanitic to sparsely porphyritic (Fig. 42, 43) with phenocrysts of quartz, orthoclase, and albite. The biotite rhyolite (Tirb) has distinctive biotite phenocrysts. Some K-feldspar phenocrysts display adularescence similar to volcanic sanidine. Robison (2017) also reports fluorite phenocrysts; as much as 4800 ppm F is found in some rhyolite samples (Appendix 3). Phenocryst sizes range from 0.3-2 mm and range in concentration from <1 to 10%. The groundmass consists of orthoclase, quartz, albite, and trace biotite, aegirine-augite, apatite, titanite, magnetite, ilmenite, zircon, fluorite, and muscovite (Robison, 2017). Alteration minerals include kaolinite, hematite, sericite, and leucoxene. Locally, the rhyolite is flow banded. The rhyolite commonly contains small miarolitic cavities, up to 4 cm in diameter (Fig. 42) containing small crystals of quartz, titanite, K-feldspar, dickite, villiaumite (a sodium fluoride), and hematite (Robison, 2017; this study). The abundance of miarolitic cavities increases near the top of the exposed intrusion at Gallinas Peak. Modal analyses are in Table 12. The Permian sedimentary roof rocks along the northern and eastern flanks of Gallinas Peak dip away from the intrusion, suggesting a laccolith geometry.

A biotite-rich rhyolite (Tirb) forms an irregular zone within the Gallinas Peak intrusive rhyolite, exposed north and west of Gallinas Peak. It is light brown on both weathered and fresh surfaces to reddish brown where oxidation is abundant. The unit is fine-grained, equigranular to slightly porphyritic, containing ~5 to 7%, 1-3 mm, euhedral, pristine biotite. Groundmass contains feldspar, quartz, and minor oxides. Maximum exposed thickness is ~120 m.

The rhyolite (Tir, Tirb) is alkaline to subalkaline, ferroan (Frost and Frost, 2008), slightly peraluminous (Frost and Frost, 2008), and plots within the A-type granite field (Whalen et al., 1987). They are classified as rhyolite using the TAS diagram or alkali rhyolite using the R1-R2 diagram (Fig. 44). The biotite-rich rhyolite (Tirb) is similar in chemistry to the rhyolite (Tir), but is more alkaline than the rhyolite (Tir) due to increase in K_2O (Fig. 45, 46). The rhyolite is a high silica, non-topaz bearing rhyolite with low MgO, CaO, Zr, and high K_2O, Rb, Th, and U. The Gallinas rhyolites have relatively flat chondrite-normalized REE patterns, with slight enrichment in light REE (Fig. 44).

Rhyolite is rare in the North American Cordilleran alkaline-igneous belt (McLemore, 2018). Another rhyolite locality is found at Round Top Mountain at Sierra Blanca, Texas, where Texas Rare Earth Resources Corp. has identified an estimated 231.0 Mt of REE measured resources with an average grade of 0.06 wt% total REE (Standard Silver Corporation, 2008). Major element chemical analyses of Round Top rhyolites are similar to those of the rhyolites found in the Gallinas Mountains (Fig. 44, 45; Elliott et al., 2017), but Round Top rhyolites are more enriched in heavy REE (Fig. 46), Y, Rb, Zr, and depleted in Ni and Ba. The rhyolites from the Gallinas Mountains do not have a negative Eu anomaly suggesting no or limited plagioclase fractional crystallization. In contrast, the rhyolites from Round Top have a negative Eu anomaly indicating plagioclase fractional crystallization from a more mafic source.

TABLE 12. Modal analyses of rhyolite in weight percent. 1-11 are from Perhac (1961). Locations are in Perhac (1961). 12 is from Poe (1966). Tr=trace amounts.

Mineral	**1**	**2**	**3**	**4**	**5**	**6**	**7**	**8**	**9**	**10**	**11**	**12**
orthoclase	59.9	56.3	75.7	73.8	81.1	73.2	74.4	74.0	80.8	77.8	79.7	50-70
albite	20.8	26.3	10.3	14.9	5.9	6.2	4.4	9.6	7.5	10.7	4.4	10-15
quartz	17.2	14.4	13.4	10.4	12.0	19.4	20.8	15.2	10.2	8.0	14.1	10-15
magnetite	2.0	2.9	0.7	1.0	0.7	1.2	0.4	1.5	1.0	1.8	1.3	<5
biotite									2.5		3.0	<5
apatite												<5
sphene												<5
accessory minerals	tr	tr	tr	tr		tr	tr	tr	tr	tr	tr	
Total	99.9	99.9	100	100	99.9	100	100	100	100	100	100	100

FIGURE 42. Left photograph—Quartz crystals in miarolitic cavities in rhyolite from the Gallinas Mountains (sample Gal1148; M. Zimmerer photograph). Right—photograph of massive rhyolite in the Gallinas Mountains (sample GM10-7; V.T. McLemore photograph).

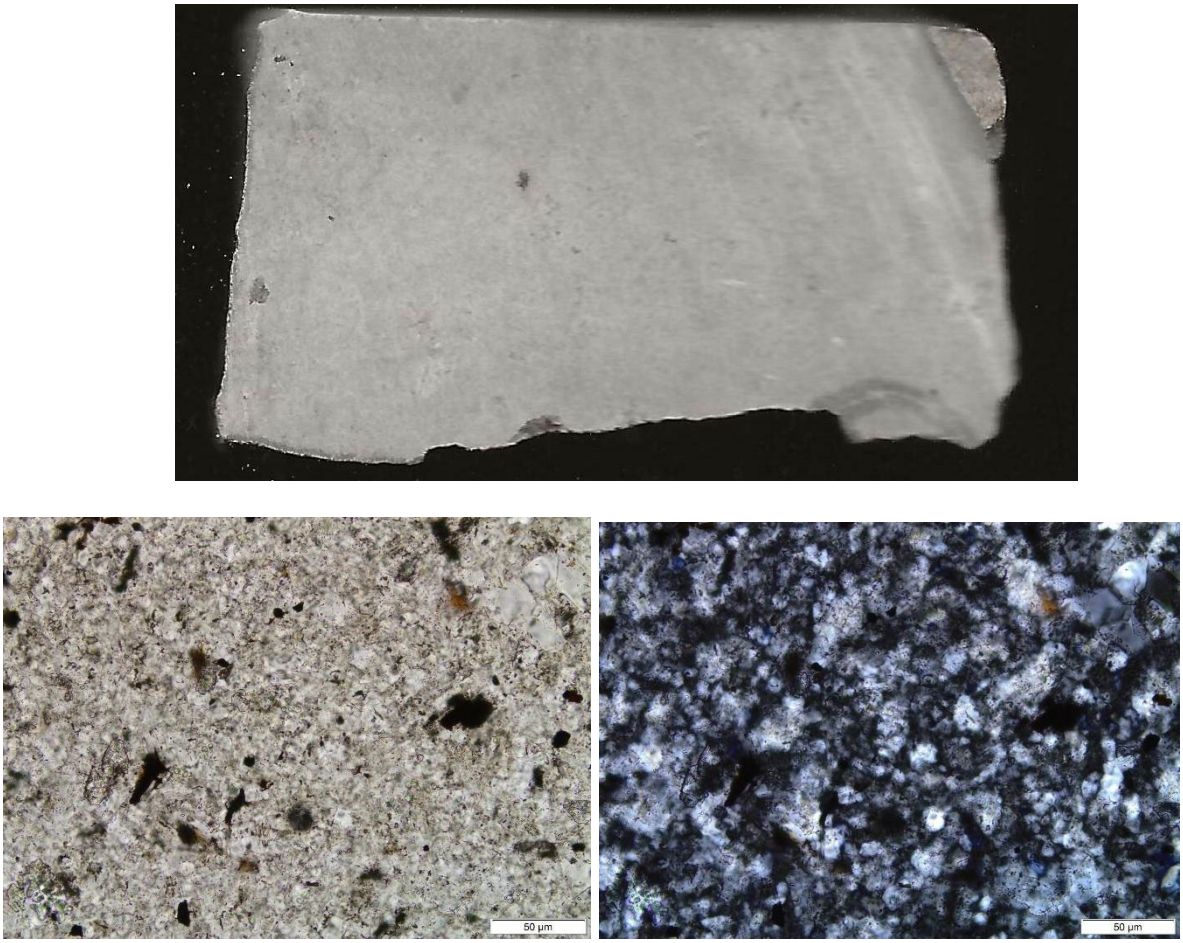

FIGURE 43. Top photograph is the thin section billet. Bottom photographs are thin sections of rhyolite in plane polarized (left) and crossed polarized light (right) (Gal1032, E.B. Haft photograph).

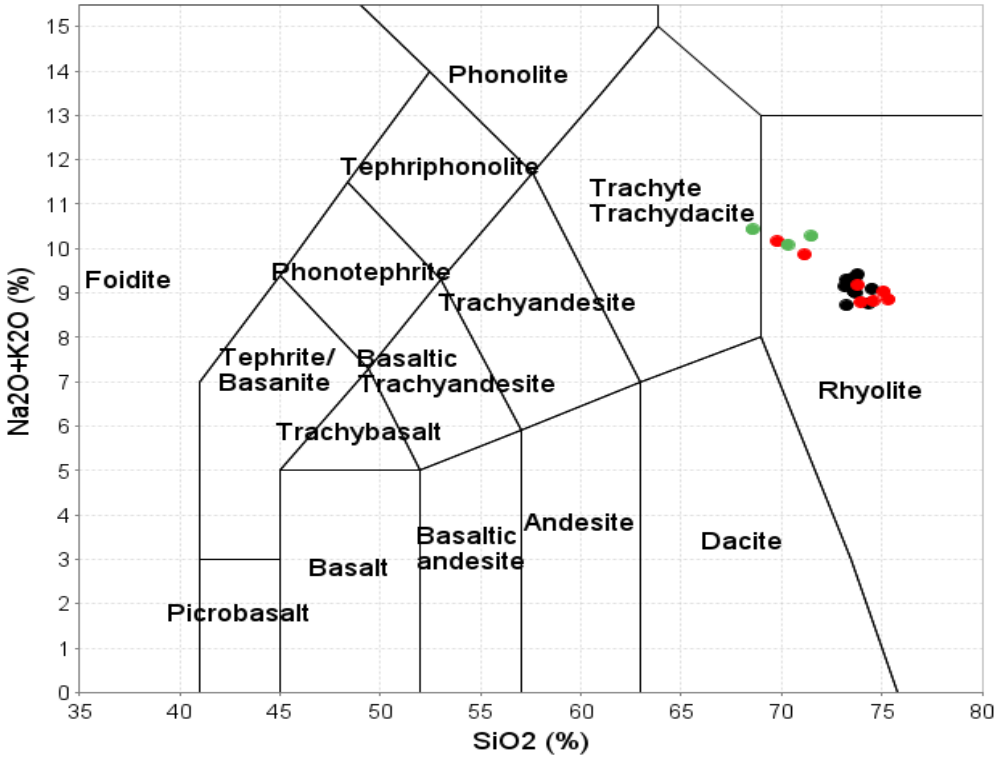

FIGURE 44. TAS (total alkali silica) plot (Le Bas et al., 1986; Le Maitre, 1989) of rhyolites from the Gallinas Mountains (red circles=rhyolite, green circles=biotite rhyolite) Round Top, Sierra Blanca, Texas (black circles). Chemical analyses are in Appendix 3 and Elliott et al. (2017).

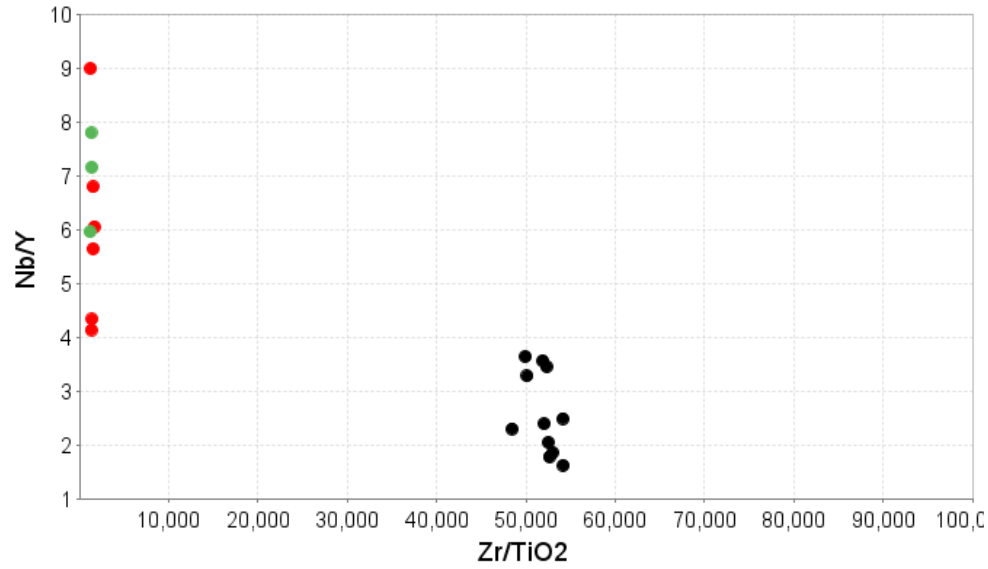

FIGURE 45. Right—Nb/Y vs Zr/TiO_2 plot showing trace element differences in the Gallinas Mountains (red circles=rhyolite, green circles=biotite rhyolite) Round Top, Sierra Blanca, Texas

(black circles), probably as a result of differences in magmatic differentiation of the two areas. Chemical analyses are in Appendix 3 and Elliott et al. (2017).

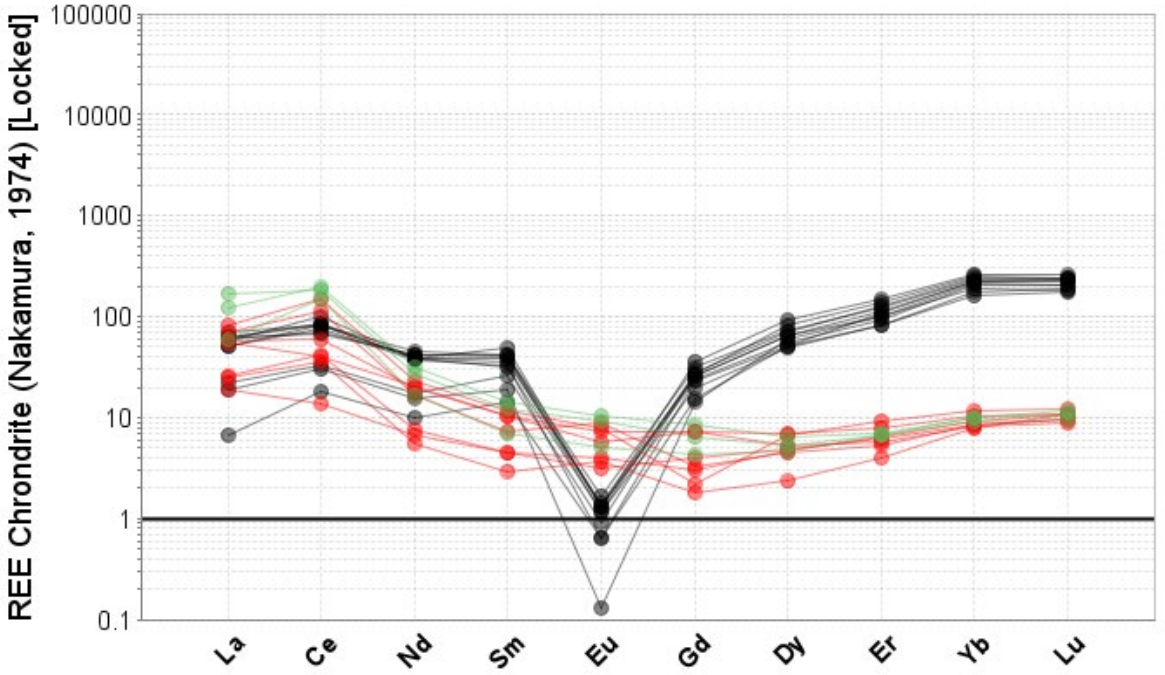

FIGURE 46. Chondrite-normalized REE plot (Nakamura, 1974) of rhyolites from the Gallinas Mountains (red circles=rhyolite, green circles=biotite rhyolite), Round Top Mountain, Sierra Blanca, Texas (black circles). Chemical analyses are in Appendix 3 and Elliott et al. (2017). Note the enriched heavy-REE pattern of the sample from Round Top Mountain.

Magmatic Intrusive Breccia Pipes (Tibx)

More than 20 exposed magmatic intrusive breccia pipes (Tibx) intrude the Yeso Formation, Glorieta Sandstone, trachyte, and syenite units, forming a northeast-trending belt, approximately 3–5 kilometers long in a fault block northwest of the Pride fault (Figs. 6, 7). The contacts are mostly concealed, but the pipes appear to be roughly elliptical to circular in geometry. Previous authors called these features intrusive breccia pipes (Perhac, 1961, 1970; Schreiner, 1993; McLemore, 2010a) or monzonite breccia (Kelley at al., 1946). Intrusive breccias are formed directly from the subsurface movement of magmas (Sillitoe, 1985). Magmatic-hydrothermal breccias are formed by the release of hydrothermal fluids from the magma chamber and can include magmatic, meteoric, connate, or ocean waters (Sillitoe, 1985). In the Gallinas Mountains intrusive breccia pipes, the breccia groundmass consists of fine-grained, anhedral to subhedral feldspars, locally with a igneous trachytic or porphyritic texture. Hornblende phenocrysts are surrounded by a feldspar matrix. Therefore, magmatic intrusive breccia pipe is the preferred term (Sillitoe, 1985).

Magmatic intrusive breccia pipes are gray to brown and consist of angular to subrounded fragments of granite, granitic gneiss, sandstone, shale, limestone, trachyte, and syenite that are as much as 1 m in diameter (Fig. 47, 48). Most of the intrusive breccia pipes are matrix-supported with a groundmass of feldspar and quartz, along with small crystals of other minerals and rock

fragments. Two intrusive breccia pipes, the M and E and Sky High pipes, are partially clast-supported. Most of the breccia pipes are altered and weathered, consisting of secondary hematite and locally calcite, quartz, and fluorite. Some rock fragments are silicified around their edges and other fragments are surrounded and cut by fluorite veins (see below under description of mineral deposits). Fragments of magnetite-hematite ore are found in several magmatic intrusive breccia pipes. Fenitization of mineralized breccia pipes was described by Schreiner (1993) and is shown in Figure 49. Only a few breccia pipes are mineralized at the surface (see below).

There is no obvious structure control of the breccia pipes, although Perhac (1961) and Schreiner (1993) suggest the breccia pipes intruded along concealed faults. The Yeso and Glorieta Sandstone and trachyte are brecciated and cemented by silica cement at the contact with the intrusive breccia. Many of the igneous breccia pipes in Pinatosa Canyon and along Rattlesnake Ridge were emplaced along the margins of syenite intrusions, suggesting a connection between fluids associated with that intrusion and breccia pipe formation. The Sky High breccia pipe intrudes along the contact of a trachyte dike.

In Pinatosa Canyon, several exposures of previously unrecognized crystal-poor intrusive breccias (Tixb) are found (Fig. 50, 51). One variety is a green breccia with an aphanitic matrix that fills spaces between feldspar fragments and rock fragments that are 1-2 mm in diameter. Larger clasts in the green breccia are porphyritic trachyte or medium-coarse syenite with feldspar and hornblende. Some of the clasts in the green breccia are more mafic in composition with plagioclase and hornblende in a dark gray matrix. Another variety of breccia is a reddish brown breccia that contains clasts of sparsely porphyritic andesite with plagioclase ± hornblende that are rounded, embayed, broken or stretched into wispy forms set in a matrix of angular, broken white to pink feldspar.

Chemically, the magmatic intrusive breccia pipes are alkaline to subalkaline, ferroan (Frost and Frost, 2008), and slightly peraluminous (Frost and Frost, 2008). Most magmatic intrusive breccia pipes plot within the trachyte and trachydacite field (Fig. 52). They exhibit light REE-enriched chondrite-normalized patterns (Fig. 52). Samples with high F also have high REE and some have high Au concentrations.

FIGURE 47. Left—Magmatic intrusive breccia pipes (Tibx) on Rattlesnake Ridge (left Gal228c, right Gal231a, V.T. McLemore photograph). Note the different breccia fragments.

FIGURE 48. Magmatic intrusive breccia pipes (Tibx), with mostly Glorieta fragments (V.T. McLemore photograph).

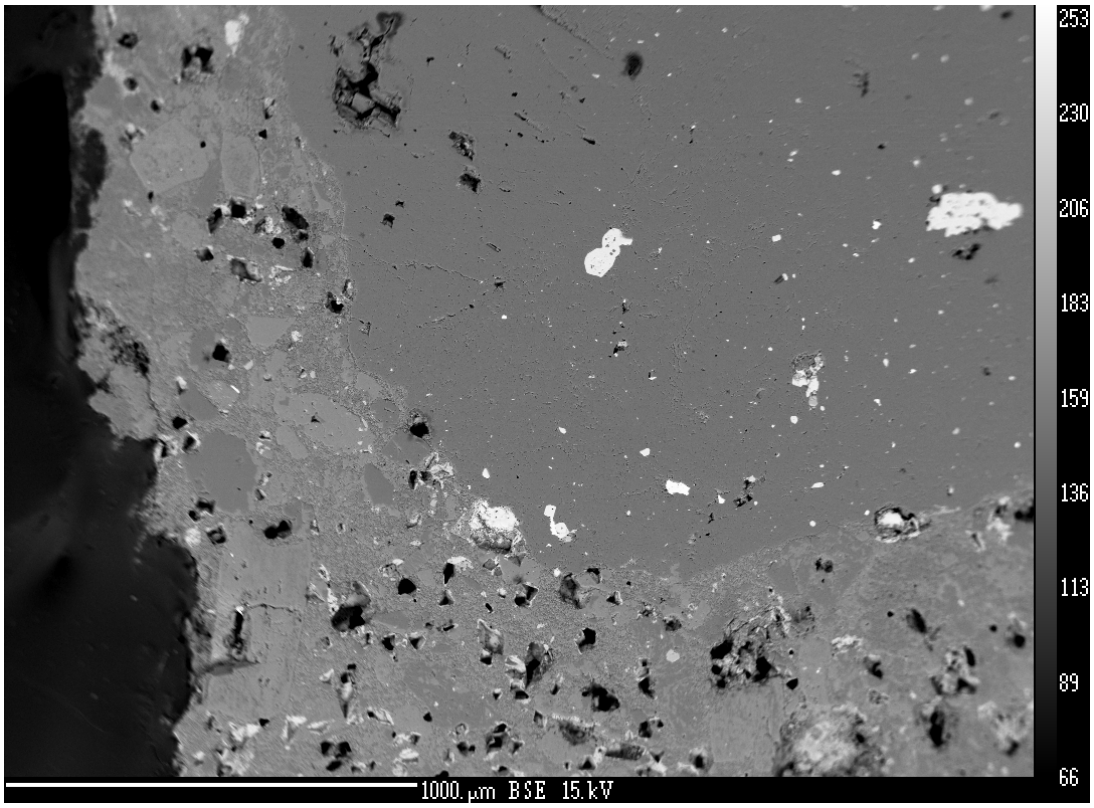

FIGURE 49. Backscattered electron photomicrograph of a typical matrix from a magmatic intrusive breccia pipe showing secondary K-feldspar replacing albite (K-fenitization). The fine-grained matrix consists of primary, magmatic albite (Gal252-01).

FIGURE 50. Igneous breccia (Tixb) with heterogeneous fragments of trachyte and syenite, feldspar phenocrysts and a green aphanitic groundmass (Gal597, S. Cherotich photograph).

FIGURE 51. Field photo of reddish-brown trachyte breccia (Tixb) (Gal619, S. Kelley photograph). Note the flattened nature of some of the clasts above the pen.

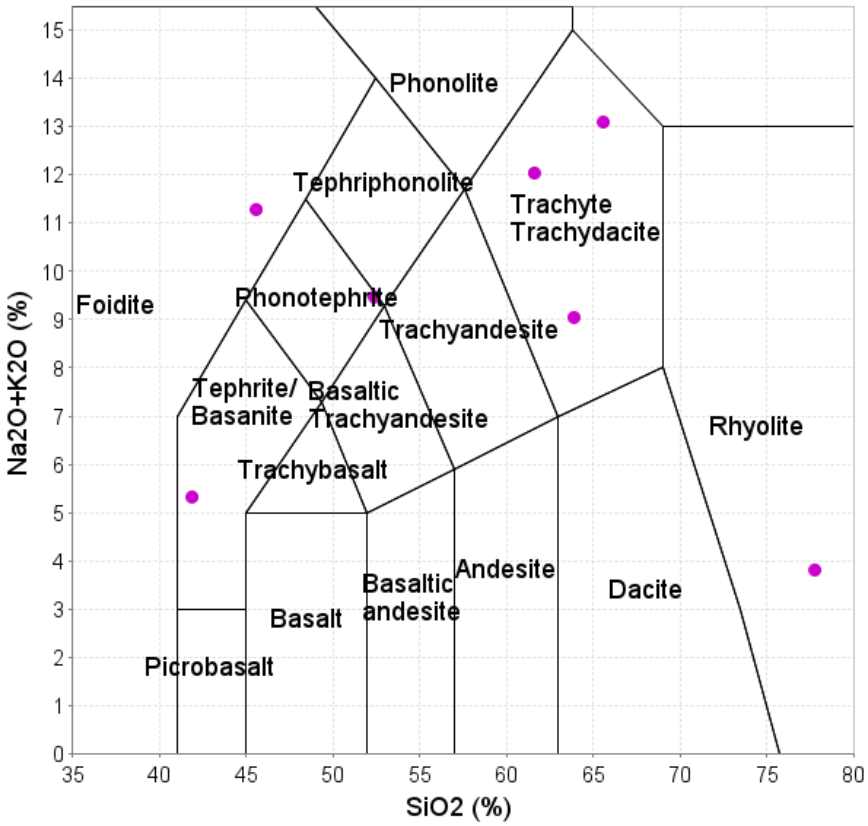
Phonolite
Tephriphonolite
Trachyte
Trachydacite
Foidite
Phonotephrite
Trachyandesite
Tephrite/
Basanite
Basaltic
Trachyandesite
Rhyolite
Trachybasalt
Andesite
Basaltic
andesite
Dacite
Basalt
Picrobasalt
Na2O+K2O (%)
SiO2 (%)

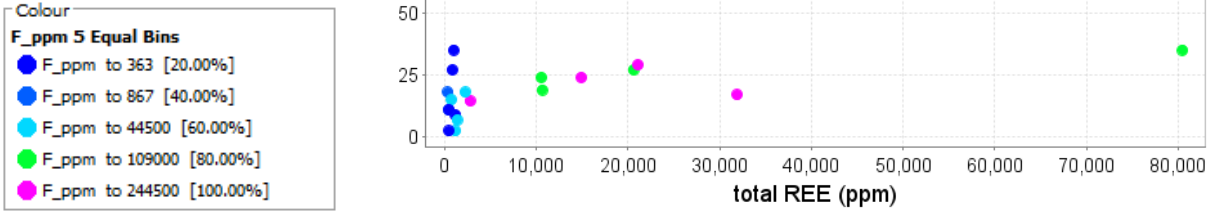
Colour
F_ppm 5 Equal Bins
F_ppm to 363 [20.00%]
F_ppm to 867 [40.00%]
F_ppm to 44500 [60.00%]
F_ppm to 109000 [80.00%]
F_ppm to 244500 [100.00%]
Au (ppb)
total REE (ppm)

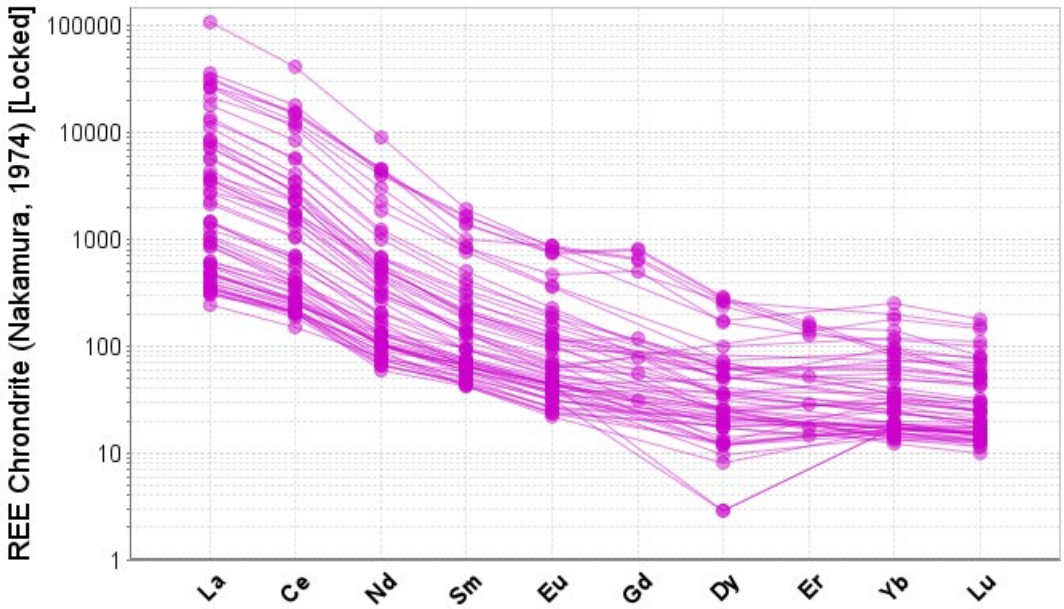

FIGURE 52. TAS plot (Le Bas et al., 1986), Au vs total REE, and chondrite-normalized REE plot (Nakamura, 1974) of magmatic intrusive breccia pipes from the Gallinas Mountains. Chemical data are in Appendix 3. The Au vs total REE plot also shows concentration of F (ppm) in different colored symbols. Samples with high F also have high REE and some have high Au concentrations.

Quaternary units

Spring deposits (Qtr)

Travertines (Qtr) are found throughout the Gallinas Mountains, mostly located near limestone beds, but often coating fractures in Yeso Formation sandstone and in trachytes or syenites. The travertines were likely deposited during climatic periods of abundant rainfall. The travertines are typically white to cream colored, fibrous to banded (Fig. 53). The extent of the deposits are only a few tens of meters in diameter.

FIGURE 53. Left—Travertine (Qtr) overprinting limestone near Iron Lamp skarn (Gal345; V.T. McLemore photograph). Right—Banded travertine (V.T. McLemore photograph).

Talus, block streams, block slopes and rock glacier deposits (Qt)

Talus, block streams, block slopes and rock glacier deposits were mapped by Blagbrough (2005); he interpreted these deposits to represent periglacial mass movement of predominantly rhyolite during Late Wisconsinan (11-20 k.y.B.P.) climate characterized by numerous freeze-thaw cycles. Talus deposits mapped during this study (Plate 1) in the southern Gallinas Mountains are dominated by clasts of Glorieta Sandstone. Only the largest talus fields were mapped in this study, and in many cases talus deposits were included in the bedrock polygons to show the original intrusive geometries. Similar deposits are found in the Capitan Mountains, Sierra Blanca, and Carrizo Mountain (Blagbrough, 1984, 1991, 1994, 1999).

Fan-shaped alluvial deposits (Qaf)

Fan deposits are composed of poorly sorted sandy gravel, cobbles, and boulders. The fans formed at the mouths of larger canyons draining Gallinas Peak and Rattlesnake Ridge. These fans are stabilized by vegetation and appear to be no longer active. Thickness is up to 3–4 meters.

Terrace deposits (Qty)

Unconsolidated gravel, sand, and silt with treads more than 2 m above modern grade. These deposits are only preserved in the wide drainages within the mountains. Thickness is <3 m.

Eolian-slopewash deposits (Qes)

Silt-dominated deposits carried by the wind into local depressions that are later modified by sheetwash. These deposits are found on the west side of the study area (Plate 1) and are 1-2 m thick.

Slopewash-eolian deposits (Qse)

Sand, gravel, and silt deposits on the flat plains surrounding the Gallinas Mountains that are largely modified by sheetwash during storm events, with only modest reworking by wind. Arroyos incised into these deposits indicate the units are at least 3 m thick.

Colluvium (Qc)

Unconsolidated angular boulders, cobbles, and gravel cover the hillslopes between the ridgelines and the valley bottoms. These units were only mapped in areas where the colluvium obscures important contact relationships. The deposits are 1 to 3 m thick.

Stream deposits (Qal)

Unconsolidated sand, gravel, and silt in both active channels and historic overbank deposits. Qal is mostly Holocene in age; maximum thickness of various alluvium deposits is typically thin (less than two meters).

Disturbed artificial fill (df)

Large area of roadbed fill along the forest road that leads to Red Cloud Campground. 3 m thick.

STRUCTURE

Brecciation

Brecciation is extensive in the Gallinas Mountains and is found in a variety of forms. Although a commonly accepted classification of breccias remains elusive, breccias are generally defined by either genetic criteria, descriptive criteria, or a combination of both (Sillitoe, 1985). The accepted classification of breccia pipes is primarily based upon the mechanism of brecciation and the involvement of water, magma, or tectonics (Sillitoe, 1985). A combination of genetic and descriptive criteria is used in this report.

Four predominant types of breccias are found in the Gallinas Mountains:

- Magmatic intrusive breccia pipes (Tibx) (described under igneous rocks)
- Tectonic fault breccia (Tfbx)
- Brecciated country rock adjacent to dikes, sills, and magmatic intrusive breccia pipes (described under regional silicification)
- Brecciated mineralized deposits (discussed under description of mineral deposits below)

The tectonic fault breccia (Tfbx, Plate 1) are clast supported with multiple lithologies and large blocks of host lithologies (meter in diameter) with a matrix of rock flour. They are structurally controlled and found along major faults (i.e. Red Cloud Canyon and South Largo Canyon faults). There is no mineralization except minor calcite or quartz and no fluorite or fenitization present. Slickensides are common.

Faulting

The structure of the Gallinas Mountains has been described as one (Kelly et al., 1946) or two domes (Perhac, 1961, 1970) and our mapping supports that doming has occurred (Plate 1). The absence of outcrops suitable for measurements makes interpretation difficult. However, the few measurements of bedding (Plate 1) in the Gallinas Mountains is consistent with doming resulting from a concealed, subsurface intrusion. Doming also is caused by the intrusion of sills, and laccoliths (Cougar Mountain syenite, Gallinas Peak rhyolite, and trachyte/syenite in the central portion of the mountain range). The dikes trend predominantly northwest and northeast (Plate 1). Sills are more common than dikes and subparallel bedding of the host rocks.

Major faults (strike length longer than a couple of meters and displacement of adjacent host rocks and mineralized breccias and veins), include the Red Cloud Canyon, South Largo Canyon, Pride and Conqueror faults, and several, additional unnamed faults in the area and trend northwest, north, and northeast and are steeply dipping (Plate 1, Fig. 6). Some east-west faults are present. Additional faults have been mapped in this study throughout the Gallinas Mountains. Several smaller faults are parallel or subparallel to the Red Cloud Canyon and South Largo Canyon faults, and these two faults are best considered fault zones. All of the faults appear to show normal displacement, although slickensides along the Red Cloud Canyon fault suggest some late strike slip movement. Furthermore, the majority of slickenlines along the South Largo fault north of Red Cloud Canyon are subhorizontal, again indicating that the last movement along this fault was strike-slip.

The Pride and Conqueror faults are normal faults that trend northeast and east-northeast, respectively (Fig. 6). Both faults have sections that are mineralized, although none of these deposits have any production. The Pride fault forms the southern contact of the Iron Lamp skarn. The Conqueror fault may be a continuation of the Pride fault; this fault has several prospect pits exposing hydrothermal breccia and fissure vein deposits (see description of the Pride mine).

South of the Conqueror fault, the trachyte dikes are more predominant than elsewhere in the district and they trend northeast. The veins in this area also typically trend northeast. North of the Conqueror fault, the veins trend northwest and mostly sills are exposed. Therefore, some rotation has occurred during the evolution of the Conqueror fault.

The Red Cloud Canyon fault offsets the Pride and Conqueror faults, is younger than the Pride and Conqueror faults, and has several splays (Fig. 6). The northern portion of the Red Cloud Canyon fault splits into three northwest-trending splays. The north-trending South Largo Canyon fault appears to be the youngest fault since it offsets the Red Cloud Canyon and Conqueror faults (Fig. 6). In several places, two or more subparallel faults are found, suggesting a major fault zone.

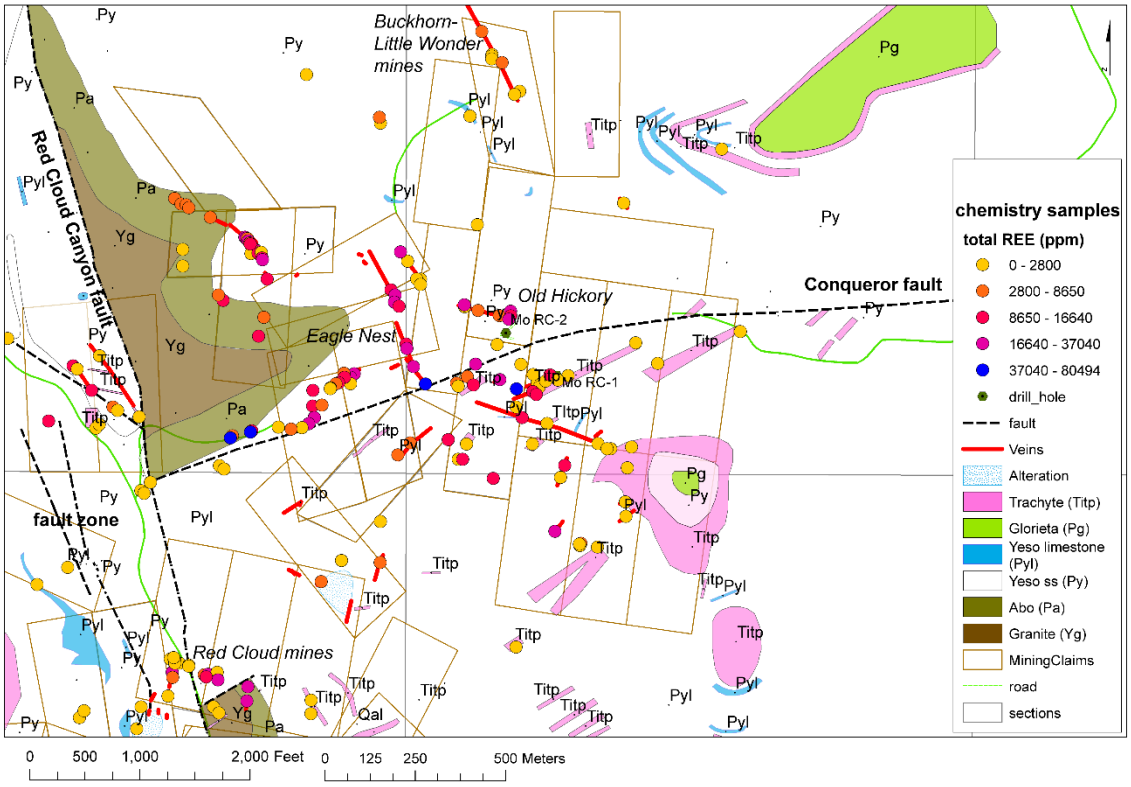

FIGURE 54. Geologic map of the Conqueror and Red Cloud Canyon faults. Veins (red) are found along small length and small displacement fracture and fault zones. North of the Conqueror fault, the veins trend northwest and mostly sills are exposed. South of the Conqueror fault, the trachyte dikes trend northeast. Some rotation has occurred during the evolution of the Conqueror fault. The Red Cloud fault consists of several parallel faults and is a fault zone. Note that many veins north of the Conqueror fault have higher concentrations of REE (blue, red circles) than veins south of the fault.

Tectonic, non-mineralized fault breccias (Tfbx) formed along the Red Cloud Canyon and South Largo Canyon faults (Fig. 55). These fault breccias consist of rock fragments of Proterozoic granite, Yeso Formation sandstone, limestone, and siltstone, Abo conglomerate and sandstone, Glorieta Sandstone, andesite, trachyte, syenite and rock flour. The tectonic breccias are cemented by silica, locally by carbonate, and are cut by calcite veins. Fluorite is absent.

Therefore, the major faults are younger than the intrusions. This point is also illustrated by the fact that the South Largo fault cuts syenite in many places north of Red Cloud Canyon.

Major faults are not mineralized with the exception of the Pride, Conqueror (Fig. 54) and Buckhorn faults. Mineral deposits are mostly along minor faults and fracture zones with small displacements and short lengths (Fig. 54). Numerous small faults of short length (typically less than a couple of meters long) with small displacement host much of the mineralization. These faults are likely the first episode of faulting, since they are found in fault blocks and offset by younger faults. Most of these faults are mapped as veins (Tv) on Plate 1 or as short faults. These faults are normal faults with minor displacement. These faults could be a result of doming by a concealed intrusion.

FIGURE 55. Tectonic breccia along Red Cloud Canyon fault (Gal44c, V.T. McLemore, photograph). White veins are calcite. Purple-red fragments are Abo sandstone. Yellow fragments are Yeso sandstone.

GEOPHYSICAL INTERPRETATIONS

The regional aeromagnetic data indicates multiple magnetic anomalies in the subsurface of the Gallinas Mountains and surrounding areas (Fig. 56; Kucks et al., 2001; McLemore, 2010a; Li, 2017). Li (2017) modeled the data and the blue in the center of the Gallinas Mountains is a magnetic low anomaly. Li (2017) suggested that the magnetic low anomaly centered in the middle of Gallinas Mountain is a result of underlying body enriched in one of four mineralogical models including (1) bastnäsite, (2) mixture of bastnäsite and iron oxides, (3) iron oxides (magnetite and hematite), or (4) magnetite. The mineralized area of the Gallinas Mountains lies just south of and within this magnetic low surrounded by magnetic high anomalies (Fig. 56). Alkaline complexes associated with mineral deposits worldwide can have similar magnetic anomalies (Woolley, 1987). Two magnetic high anomalies are also shown in Figure 56. The anomaly to the northeast displays a sharp gradient suggesting a shallow intrusion, perhaps a continuation of the Cougar Mountain syenite. In contrast, the high anomaly to the southwest of the Gallinas Mountains displays a diffuse gradient and may represent a deeper intrusion of the Lincoln Country Porphyry Belt.

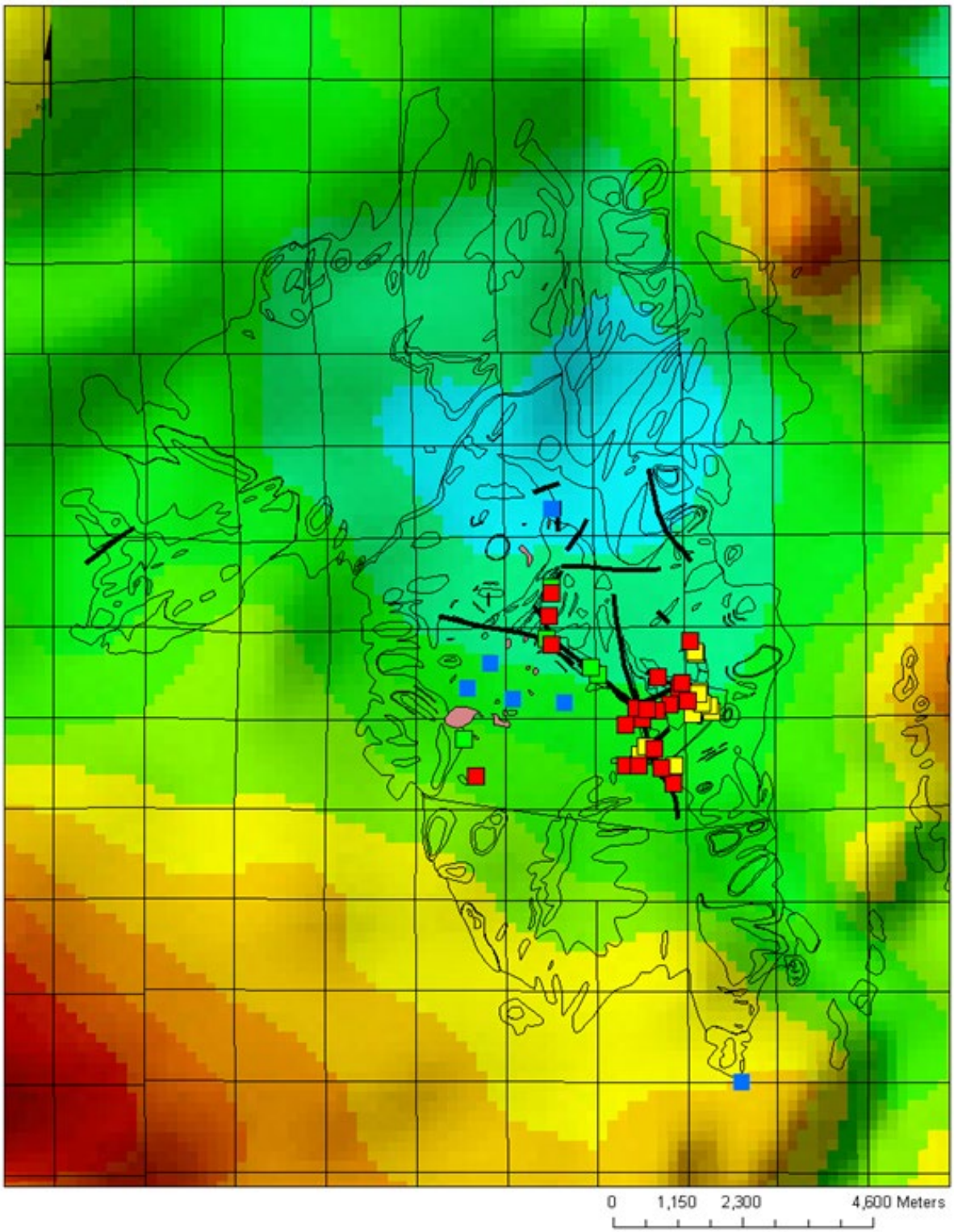

FIGURE 56. Aeromagnetic map of the Gallinas Mountains area, from Kucks et al. (2001). Thin black lines are contacts between units. Dark lines are faults. See Figure 7 for the simplified geologic map.

ALTERATION

Early regional silicification

Regional mapping in the Gallinas Mountains has identified an early regional silicification of the sandstones. The Yeso sandstones in the mineralized portion of the Gallinas Mountains are erosionally resistant, strongly silicified, and well-cemented. However, typical Yeso sandstones elsewhere in central New Mexico are susceptible to erosion, poorly-cemented, and soft to moderately hard sandstones. This silicification is likely the first hydrothermal alteration of the sandstones prior to deposition of the fluorite-bearing hydrothermal breccias and fissure veins and is characterized by formation of reprecipitated quartz, amorphous silica, and/or new silica cement. The silica is derived from leaching of the host sandstones where the fluids are circulating. Sandstones vary in major element composition according to the mineralogical composition. The Glorieta Sandstones are predominantly quartz sandstones (Table 7) and are high in SiO_2. However, the Yeso sandstones are heterogeneous in mineral composition (Table 7) and have varying concentrations of SiO_2. In the Gallinas Mountains, Yeso and Glorieta sandstones are brecciated and recemented by silica cement adjacent to the igneous dikes, sills, and intrusive breccia deposits (Fig. 57). Description of the Phelps Dodge drill hole at the Rio Tinto mine (NMLI0755) documents brecciated and silicified sandstones above the trachyte/syenite sills (see descriptive log below). Quartz overgrowths described by William-Jones et al. (2000, fig. 4) could be representative of this early stage of regional silicification.

In a Glorieta Sandstone breccia near a magmatic intrusive breccia pipe, the sandstone has overgrowth of quartz and amorphous silica (Fig. 58). The fragments are irregular in shape and cemented by quartz, amorphous silica, and hematite. Later veins of fine calcite and hematite busticate the original cement of the host rock.

FIGURE 57. Brecciated Glorieta Sandstone (Gal1088, M. Zimmerer photograph).

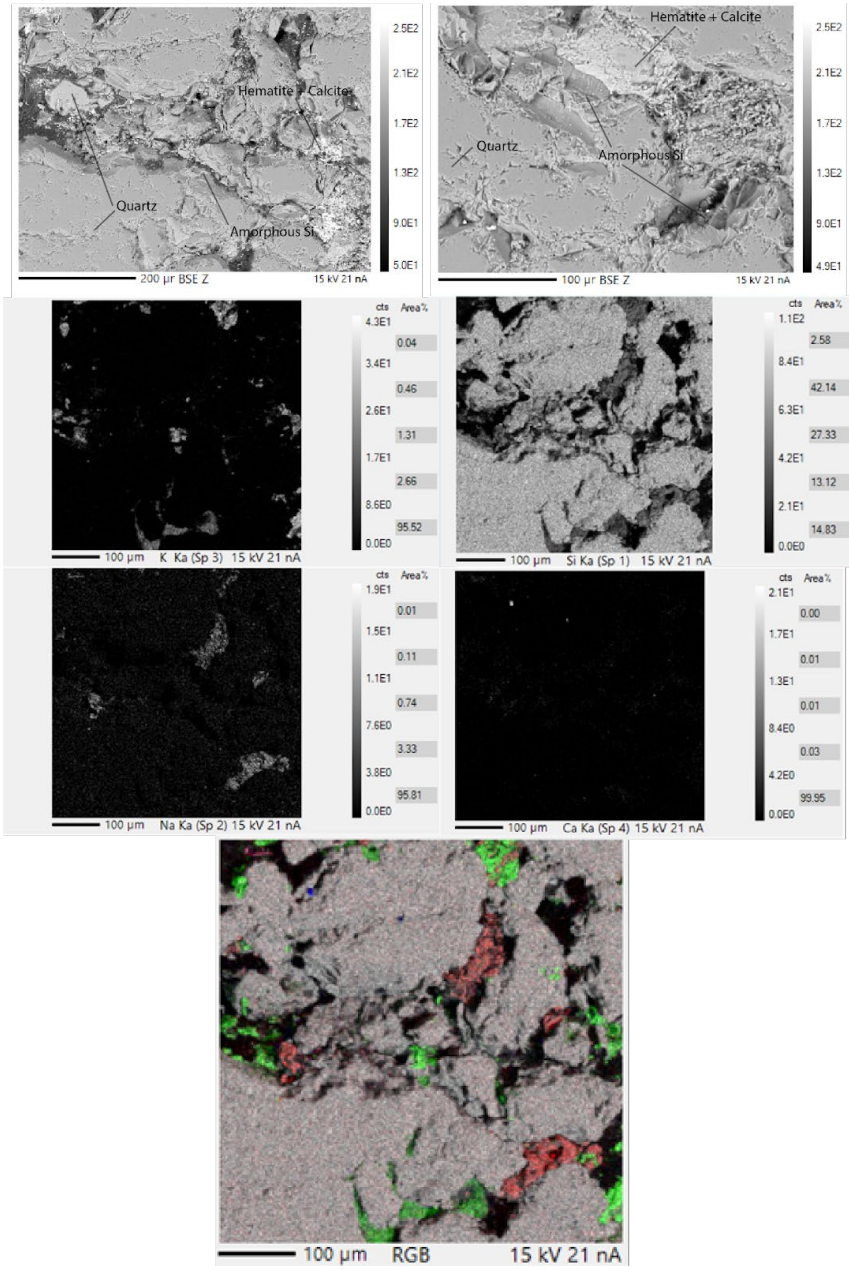

FIGURE 58. Brecciation of Glorieta sandstone adjacent to the intrusive breccia pipes (Gal6086). The upper two photomicrographs are backscattered electron images showing brecciated and recemented quartz grains, busticated amorphous silica, and late hematite-calcite veins. The bottom 5 figures are WDS electron microprobe scans (K, Si, Na, Ca maps). The false color map is a composite of the K, Si, and Na maps (gray = Si, green = K, red = Na).

Hemitization and sericitization

Sericite is not a mineral but a descriptive term used to describe the replacement of primary minerals or matrix with very fine, ragged grains and aggregates of white to colorless phyllosilicate (typically muscovite, illite, or paragonite) forming a turbid appearance of the original mineral grains (typically feldspars). It is a characteristic alteration in epithermal vein and porphyry copper deposits and occurs with fenitization in some areas (William-Jones et al., 2000). Sericitization forms over a wide temperature range and is characterized by replacement of feldspars primarily by fine-grained phyllosilicate mineral, typically mica, with local quartz, hematite, chlorite, and pyrite. The metasomatic process of altering a mineral or rock to sericite is seritization. This term is used in this report to describe a well-known alteration process and texture. In the Gallinas Mountains, sericite commonly replaces feldspars and matrix and accompanies hemitization and fenitization.

Hemitization creates a reddish color to the rocks and in many areas produces bands or rings of red to brown colors, called liesegang banding. Liesegang bands or rings cut across bedding and igneous textures and locally, appear to parallel or subparallel bedding planes and cross bedding (Fig. 59). Liesegang bands are common in altered areas and near the intrusive contacts in the Gallinas Mountains, but also are common diagenetic features in many sedimentary environments. In the Gallinas Mountains, liesegang banding is likely indicative of oxidation caused by fluid movements related to the igneous intrusions, alteration, and mineralization in the area.

A younger period of hemitization is also characterized at the vein scale in the Gallinas Mountains as halos surrounding the dikes, sills, and hydrothermal breccia and vein deposits. These halos overprint the older regional alteration and range in width from centimeters to meters. Reddening of feldspar and alteration of biotite to chlorite is common adjacent to the dikes, sills, and hydrothermal breccia and fissure vein deposits and is accompanied by overprinting of the feldspars with very fine, ragged grains and aggregates of white to colorless phyllosilicate typical of sericitic alteration.

FIGURE 59. Liesegang banding in Yeso sandstone (Gal6032c).

Metasomatic alteration (fenitization) related to the intrusions

Areas of intense alteration, primarily metasomatic alteration, are shown Plate 1 as separate areas shown as red cross-hachured patterns. Additional interpretation and analysis is underway. A summary of current interpretations follows.

Fenitization is the alkali-metasomatism associated with carbonatites and alkaline igneous activity (Le Bas, 2008). Some authors prefer to restrict the term fenitization to the metasomatic alteration associated with only carbonatites (Vance, 2013; Robison, 2017). However, most authors recognize that fenitization is associated with both carbonatites and alkaline igneous rock complexes, many without the presence of carbonatites (Morogan, 1994; Sindern and Kramm, 2000; Le Bas, 2008; Verplanck et al., 2014; Kozlov and Arzamastev, 2015; Menshikov et al., 2015; Wang et al., 2020). Therefore, we will continue to use fenitization in this report as metasomatism related to alkaline igneous rocks but not always associated with carbonatites. Using the whole rock Na_2O/K_2O ratios, fenite can be classified into sodic-, intermediate- and potassic-types (Vartiainen and Woolley, 1976). Fenites also can be divided as vein-, aureole- or contact fenite based upon the spatial relationship with source rocks (Kresten, 1988; Kresten and Morgan, 1986). Chemically, fenitization typically removes Si (quartz) and increases Na, K, Mg and Fe (feldspars, amphiboles, and pyroxenes) in the metasomatized protolith. Close relationships between fenites and alkaline igneous rocks, carbonatites, and REE mineralization has been established in many districts, e.g. Rodeo de Los Molles deposit, Argentina (Lira and Ripley, 1992), Sierra de Sumampa, Argentina (Franchini et al., 2005), Strange Lake, Canada (Gysi and Williams-Jones, 2013), Lemitar carbonatites, New Mexico (McLemore, 1987; McLemore, and Modreski, 1990), and Bayan Obo, China (Liu et al., 2018).

In the Gallinas Mountains both sodic (Na) and potassic (K) fenitization of sandstone (adjacent to trachyte or syenite), syenite, trachyte, and magmatic intrusive breccia pipes are present. Fenitized rocks are typically red from hematite replacement and locally characterized by liesegang banding. Fenitization is distinguished from hematitzation by the growth of new metasomatic red albite or K-feldspar. Early Na fenitization replaced magmatic feldspars with albite and sericite (Fig. 60, 61). K fenitization followed with the replacement of both magmatic and metasomatic albite and magmatic K-feldspar with K-feldspar. Many albites locally have K-feldspar rims. Sericitization in the Gallinas Mountains generally overprints the fenitization (William-Jones et al., 2000) and is characterized by sericite replacing the metasomatic albite and K-feldspar. Most Gallinas fenites are contact or vein type alteration.

Although the AAAI vs AI (alteration box) diagram (Fig. 39) is used in characterizing alteration in volcanic epithermal and volcanic massive sulfide deposits, it is useful in describing the alteration in the Gallinas Mountains. An increase in AAAI represents SiO_2 enrichment and decrease in chlorite, carbonate, and feldspar. An increase in AI reflects chlorite and sericite and a decrease in CaO and Na_2O (feldspar replacement). Three chemical groups of trachyte/syenite fenites are shown in the alteration plot (Fig. 39). The fenite samples (RM16,15, 17, 27, Gal2001, 2000, 2009, 224, 139, 6006, 281, 276, 279, 2004) on the left of the unaltered box show an increase in SiO_2, Na_2O and calcite. A second group of samples, to the right of the unaltered box, show an increase in muscovite (or sericite) alteration (i.e. K_2O; Gal323, 257, 82, 6023, 6012, 1066, 3021, 171). A third group, in the upper right corner, plots in the muscovite (or sericite) field, due to increased K_2O (Gal74, 2010, 75, GM10-8). Two samples plot below the unaltered box (Gal3042, 461), suggesting calcite-epidote alteration. Four samples plot in the unaltered box, although mineralogy and chemical composition indicate they are fenites (Gal215, 463, 344, 2003).

In Gallinas feldspars, fenitization is typically characterized by the intergrowth of plagioclase and K-feldspar phases. Plagioclase alteration rims and exsolution lamellae within altered K-feldspar crystals indicate sodic fenitization (Fig. 61). In one sample (Gal578), at least three different intergrown feldspar phases are observed: microcline (K-rich), albite (Na-rich), and oligoclase (major Na, minor Ca; Fig. 58). In coarse phenocrysts of fenitized feldspar, rims of secondary feldspar surrounding primary feldspars are commonly present. Intergrowth of plagioclase and K-feldspars is generally so fine it is only visible with a microscope. WDS-maps show compositionally distinct feldspar phases, which are more intergrown with increasing alteration or fenitization (Fig. 62).

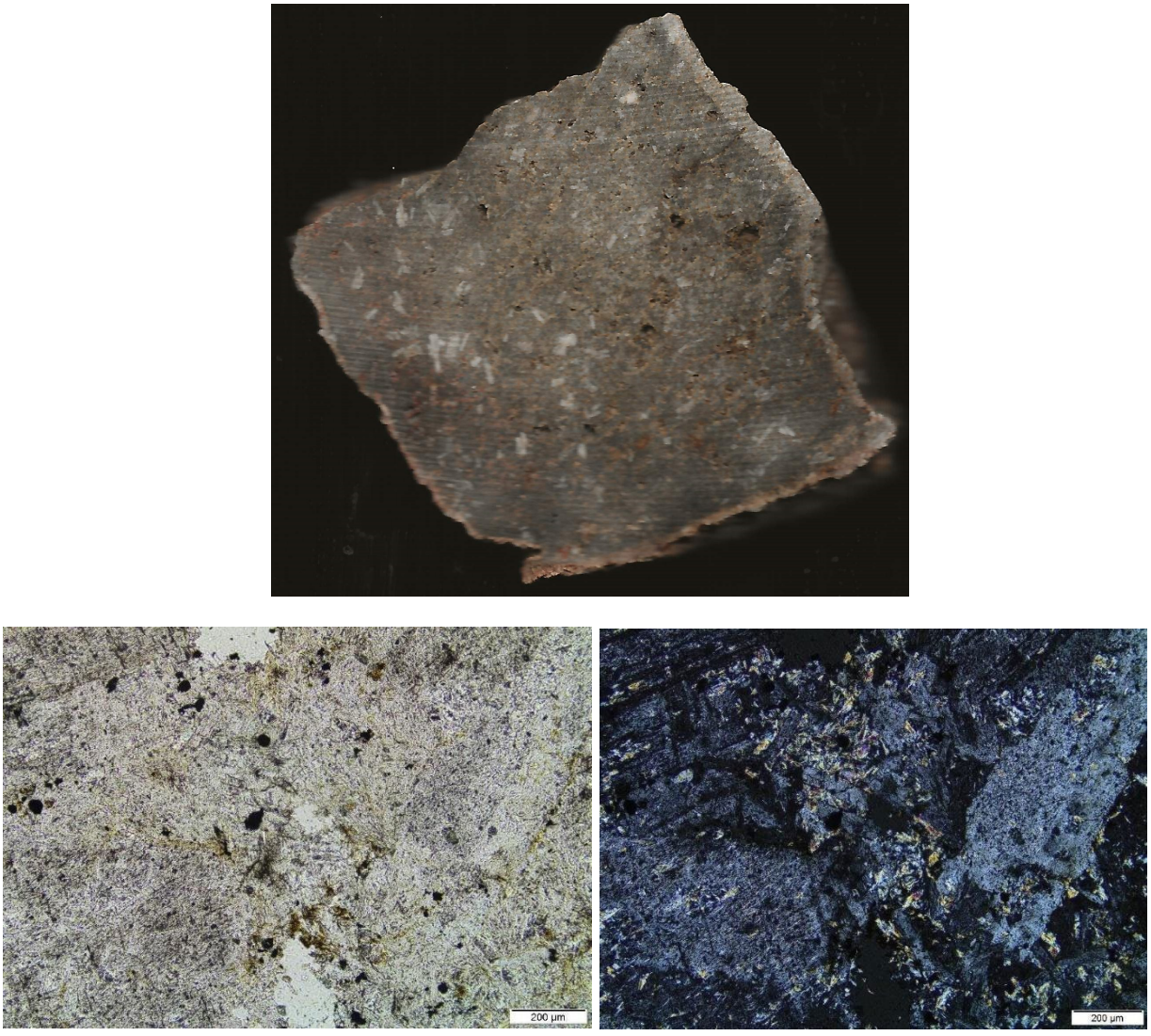

FIGURE 60. Incipient sericite (white phyllosilicate) alteration in trachyte. Top is rock slab. Bottom left is plane polarized light and right is crossed polarized light (Gal531, E.B. Haft photograph).

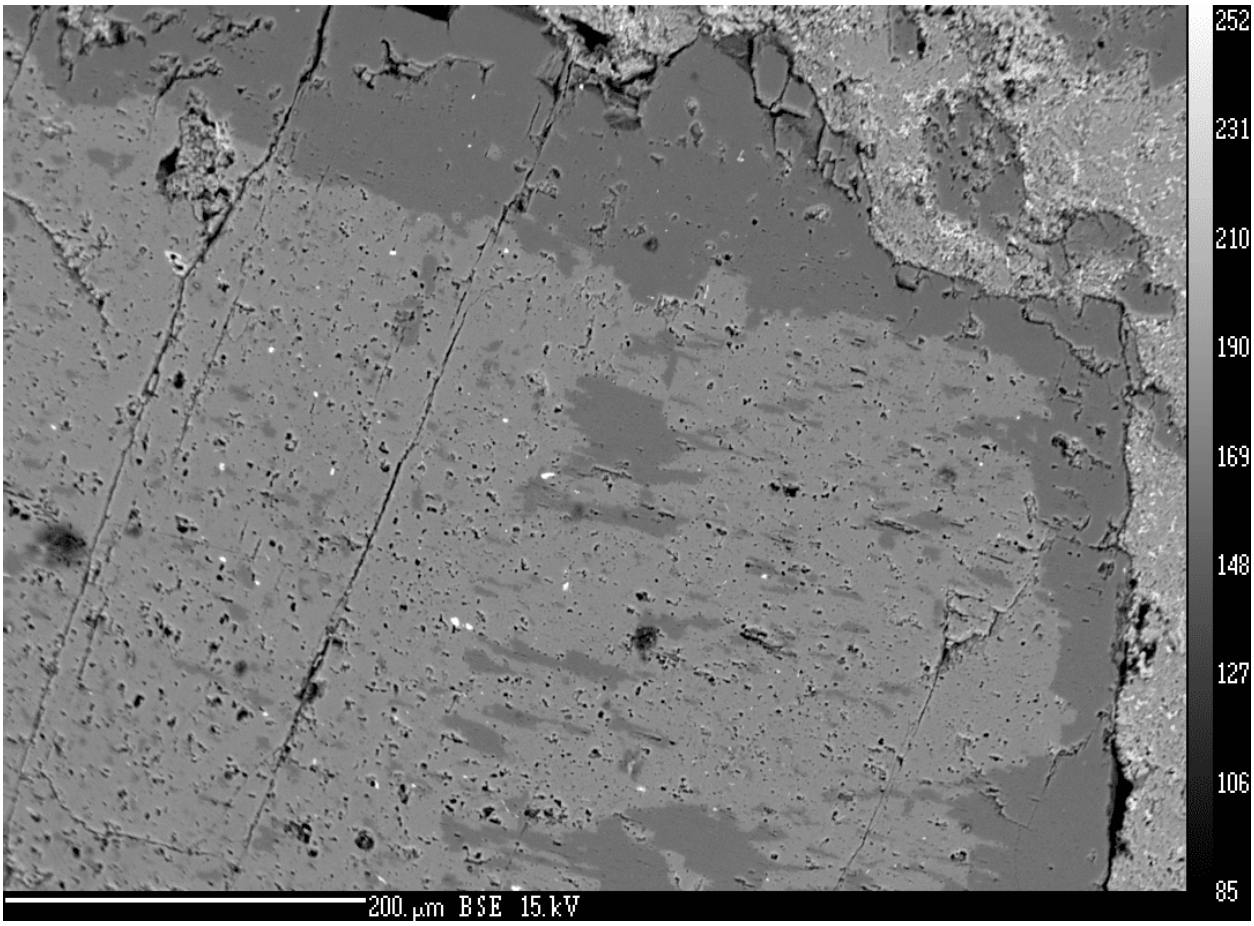

FIGURE 61. Electron microprobe back-scattered image of K-feldspar rimmed by albite (Gal17).

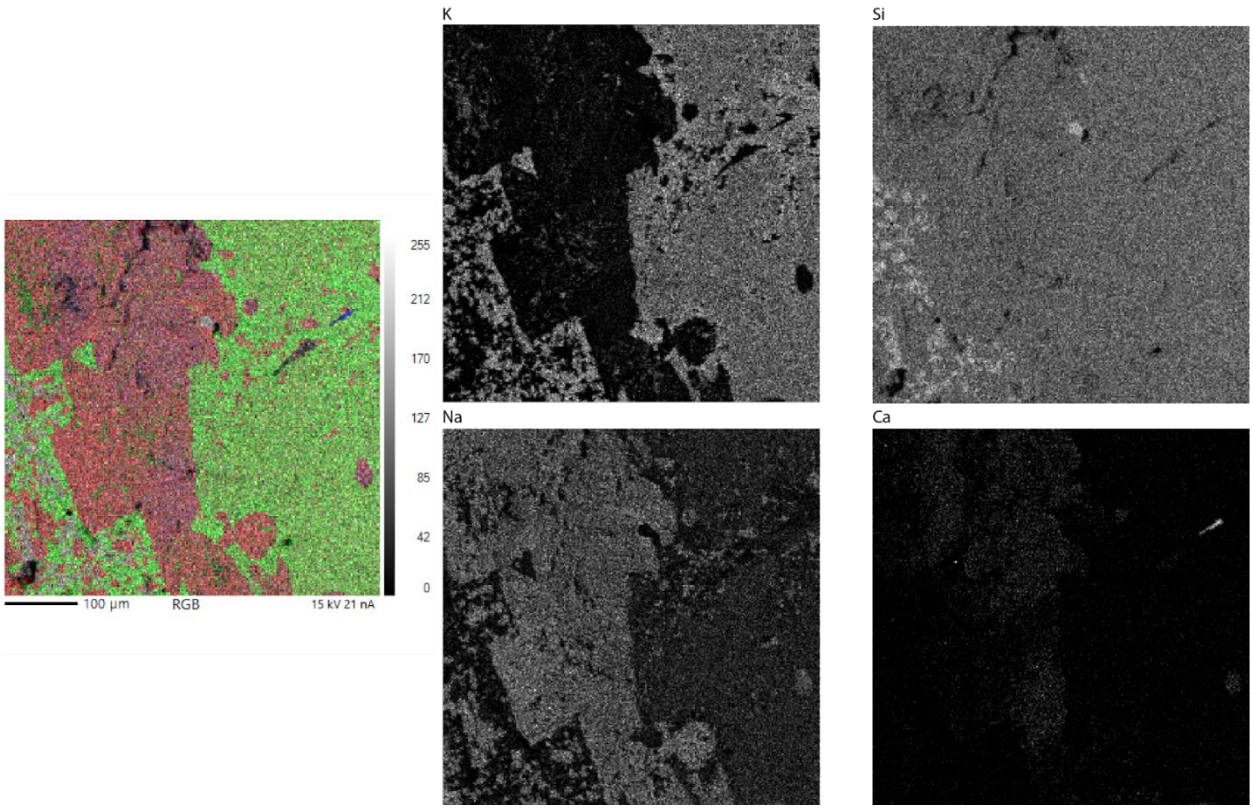

FIGURE 62. Electron microprobe wavelength-dispersive spectroscopy (WDS) maps (K, Si, Na, Ca) showing feldspars in a fenitized porphyritic syenite (Gal578). The false color map is a composite of the Si, Na, K, and Ca images (gray = Si, red = Na, green = K, and blue = Ca).

Alteration related to the skarns

Exoskarn (sedimentary protolith) and endoskarn (igneous protolith) are present in the Gallinas Mountains associated with the iron skarns and contact metasomatic deposits. Alteration associated with both types of skarn are characterized by hematite, sericite, calcite, tremolite, actinolite, and secondary K-feldspars replacing primary minerals in the host rock surrounding the Fe skarn. Other minerals found in altered host rocks adjacent to some skarns include quartz, fluorite, K-feldspar, pyrite, fluorite, phlogopite, and locally bastnäsite. At the American mine, K-feldspar veins cut the trachyte and iron skarn, indicating that fenitization is associated with the skarn (Fig. 63).

FIGURE 63. K-feldspar veins (brown) in the trachyte at the American mine (NMLI0003; AmFeadularia, photograph by V.T. McLemore).

DESCRIPTION OF MINERAL DEPOSITS

Classification of mineral deposits in the Gallinas Mountains

Seven types of mineral deposits are distinguished in the Gallinas Mountains according to the mineralogy, chemistry, form of the deposit, and host rock and are described in order of perceived age, oldest to youngest. Major faults are not mineralized with the exception of the Pride and Buckhorn faults. Types of mineral deposits found in the Gallinas Mountains are listed in Table 13. Locations of samples and photographs are in the SQL database.

TABLE 13. Types of mineral deposits found in the Gallinas Mountains, New Mexico.

Type of Mineral Deposit or Alteration	Mineralogy	Form	Host rocks	Comments
Iron (Fe) skarn and contact-metasomatic deposits (including iron veins)	Hematite, magnetite, calcite, with local fluorite, amphiboles, K-feldspar, and bastnäsite	Replacement bodies and hematite veins near the contact with trachyte or syenite sills and laccoliths	limestone, sandstone, syenite, trachyte, rhyolite	Accounts for all of the iron production. Locally contains elevated REE
Hydrothermal breccia and fissure veins	Purple fluorite and pink to white barite with numerous additional minerals, including local bastnäsite	Purple breccia veins with granite, sandstone, limestone, syenite, and trachyte clasts. Along fractures and minor faults, with thin (<1 cm wide) banded veins or veinlets	Sandstone, limestone, trachyte, syenite, granite	Fluorite cements the breccia, with local fissure veins along fractures and cutting the breccia. Accounts for all of the Cu, Ag,

Type of Mineral Deposit or Alteration	Mineralogy	Form	Host rocks	Comments
		cutting the breccia. Entire mineralized zone can be up to 18 m wide		Pb, Zn, F, and REE production
Fluorite replacements/ disseminations	Fluorite	Disseminated, replacements, and thin veinlets (<mm wide) of fluorite, with few additional minerals	Sandstone, trachyte, syenite, granite	Many are near hydrothermal breccia and fissure veins, and trachyte dikes
Intrusive breccia pipes (Au-rich, hydrothermal breccia pipes vs non-mineralized pipes)	Local disseminated fluorite and veins of REE-F, F and Au in magmatic breccia.	Elliptical pipe-like magmatic, intrusive bodies in a NE-trending belt (approximately 2 km long)	Intruded sandstone and trachyte	Matrix-supported and consist of angular to subrounded fragments
Carbonate breccias and veins (high REE and low REE)	Calcite breccias and veins with additional minerals	Near trachyte and syenite intrusive contacts with limestone, gypsum and limey sandstone. Many contain F, local Au, and variable REE	Limestone, gypsum, limey sandstone	Some carbonate breccias are overprinted by travertine (i.e. spring) deposits
Hypogene oxidation	Oxidation of primary minerals, generally sulfides			Primarily late stage oxidation of late hydrothermal fluids
Supergene oxidation	Oxidation of primary minerals, generally sulfides			Primarily weathering of the mineral deposits

Fe skarn-contact metasomatic replacement deposits

Fe skarn and contact metasomatic replacement deposits are found scattered throughout the Gallinas Mountains (Kelley et al., 1946; Kelley, 1949; Harrer and Kelly, 1963). The Fe skarn deposits consist of magnetite-hematite bodies and hematite veins in trachyte, limestone, and sandstone near or at the intrusive contact with trachyte or syenite sills and laccoliths (Fig. 64). These deposits account for all of the iron production from the Gallinas Mountains. The Permian sedimentary rocks in contact with the intrusive dikes and sills are brecciated, cut by Fe veins, skarns or contact metasomatism. These deposits typically consist of magnetite, hematite, limonite, and martite in a gangue of calcite, quartz, fluorite, tremolite, actinolite, K-feldspar, pyrite, fluorite, phlogopite, and locally bastnäsite. Iron veins cut the host rock (Fig. 64). The iron ore grade is typically less than 50%; higher grade deposits were mined out. Minor Fe-skarn deposits (locally less than a few square meters) are located along the contact with intrusive rhyolite and Yeso Formation limestone (Fig. 65). The iron skarns are probably related to the hydrothermal breccia and fissure vein deposits because they locally contain bastnäsite and fluorite and are similar in trace element geochemistry (Fig. 66; McLemore, 201a).

Chondrite-normalized REE plot (Nakamura, 1974) shows elevated REE and enriched light-REE patterns (Fig. 66). Samples with high REE also have high Ba and some have high F concentrations (Fig. 66). These plots show the similarity in chemical composition between the Fe skarn and contact metasomatic deposits and the hydrothermal breccia and vein deposits (below).

FIGURE 64. Left—Iron skarn at the American mine (NMLI0003; V.T. McLemore photograph). Right—Iron vein cutting trachyte at the American mine (Gal102c; V.T. McLemore photograph).

FIGURE 65. Iron skarn at Iron Box mine (NMLI0311; V.T. McLemore photograph).

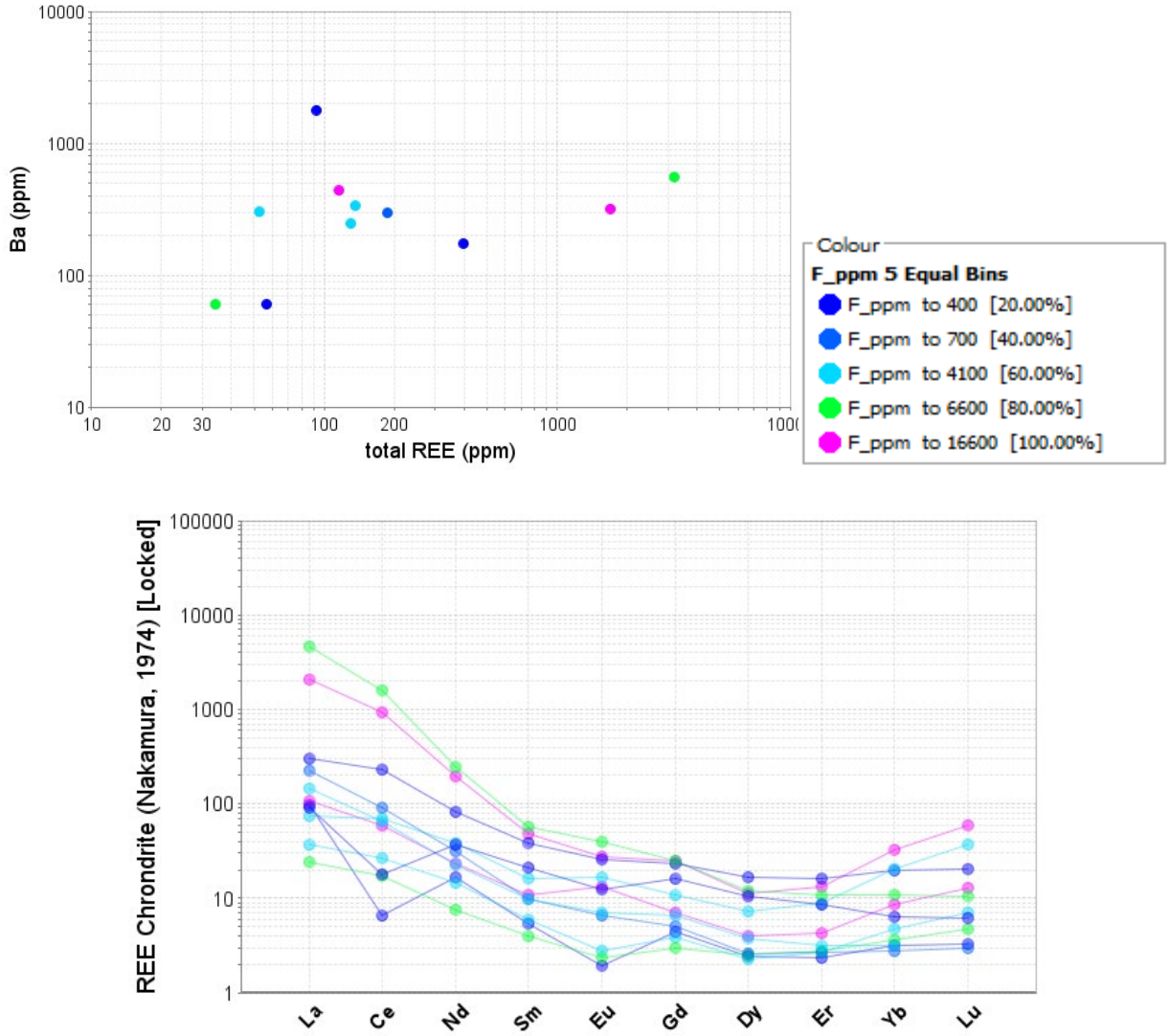

FIGURE 66. Chemical plots of Fe skarn and contact metasomatic deposits from the Gallinas Mountains. The Ba vs total REE plot also shows concentration of F (ppm) in different colored symbols. Samples with high REE also have high Ba and some have high F concentrations. Chondrite-normalized REE (Nakamura, 1974) plot shows elevated REE and enriched light-REE patterns. Chemical data are in Appendix 3. These plots show the similarity in chemical composition between the Fe skarn and contact metasomatic deposits and the hydrothermal breccia and vein deposits.

Hydrothermal breccia and fissure vein deposits (Tv)

The hydrothermal breccia and fissure vein deposits (Tv) locally are vein-like purple breccias and thin (<cm wide), banded veins, or veinlets in sandstone, limestone, syenite, and trachyte controlled by minor faults, fractures, and bedding planes. Fluorite, barite, and quartz are the major minerals in these deposits. Local fissure veins cut the hydrothermal breccia, which is cemented by fluorite (Fig. 67). Barite, early fluorite, and early bastnäsite are typically brecciated, broken and partially replaced by other minerals (Fig. 68, 69). Many hydrothermal breccias

contain fenitized rock fragments of the country rocks (Schreiner, 1993). They are mapped as veins or veinlets on Plate 1 (Tv; Fig. 54).

The hydrothermal breccia deposits account for all of the Cu, Pb, Zn, Ag, Au, fluorite, and bastnäsite production in the Gallinas Mountains (Tables 2, 3). Very few Pb minerals remain at the Red Cloud and other mines, where significant Pb production occurred (Table 4). Hydrothermal breccia and fissure vein deposits containing Cu and Pb minerals (REE-F-Cu and F-Ba-Cu, Table 13, 14) were first developed and mined in the Gallinas Mountains for Cu, Pb, Zn, Ag, and Au. Later the Red Cloud copper and Conqueror mines were mined for fluorite and bastnäsite. Fluorite, barite, and quartz (Fig. 69) are major minerals along with many Cu and Pb minerals (Table 6). Fluorite is intergrown with strontianite (Fig. 70). Later, the REE-F hydrothermal breccia and fissure vein deposits were also developed and mined for fluorite.

Hydrothermal breccia and fissure vein deposits are further subdivided according to mineral and chemistry (Table 14). F-Cu with local Pb hydrothermal breccia and fissure vein deposits are found in three major areas in the Gallinas Mountains (Fig. 6): (1) the largest in area and production, the Red Cloud Canyon-Rough Mountain area (Fig. 54), (2) the northern Sky High-Big Ben area, and (3) the western Pride No. 2 vein; however, F and F-REE veins are found throughout the southern Gallinas Mountains (see Plate 1). On a Eu/Eu* vs La/Gd plot; hydrothermal breccia and fissure vein deposits from the Gallinas Mountains partially overlap the carbonatite field (Castor and Hedrick, 2006).

The main ore control is brecciation, locally at the intersections of minor faults and fracture zones. Although most hydrothermal breccia and fissure vein deposits are linear, vein-like along fracture or fault zones with small displacements and short lengths (Fig. 54; see descriptions of mines and geologic maps below), the breccia vein deposits at the Red Cloud copper, Red Cloud fluorite, Rio Tinto, Old Hickory, and All American deposits appear to be circular or elliptical in plan view and chimney-like or pipe-like in cross section, similar in shape to the magmatic intrusive breccia pipes (see descriptions of mines below).

TABLE 14. Mineralogical-chemical types of hydrothermal breccia and fissure veins in the Gallinas Mountains. Varying amounts of quartz and local calcite and hematite are found in most hydrothermal breccia and fissure veins.

Mineralogy Deposit Type	Predominant mineralogy	Chemistry
F	Mostly fluorite of varying amounts with little or no other hydrothermal minerals	Presence of fluorite
F-Ba	Predominantly fluorite and barite, locally significant calcite	>1000 ppm Ba
F-Ba-Cu	Predominantly fluorite with significant barite and copper oxides, other sulfide and carbonate minerals may be present	>1000 ppm Ba, >1000 ppm Cu
F-Cu	Predominantly fluorite with significant copper minerals	>1000 ppm Cu
REE-F	Predominantly fluorite with REE minerals	>1000 ppm total REE
REE-F-Ba	Predominantly fluorite with REE minerals and barite	>1000 ppm Ba, >1000 ppm total REE
REE-F-Ba-Cu	Predominantly fluorite with REE minerals and barite and copper minerals	>1000 ppm Ba, >1000 ppm Cu, >1000 ppm total REE
REE-F-Cu	Predominantly fluorite with REE minerals and copper minerals, other sulfide and carbonate minerals may be present	>1000 ppm Cu, >1000 ppm total REE

Chondrite-normalized REE plot (Nakamura, 1974) shows elevated REE and enriched light-REE patterns (Fig. 72). Samples with high REE have high Ba, F, and Sr concentrations (Fig. 72). The chemical composition of the hydrothermal breccia and vein deposits is consistent with the subclassification in Table 14. These plots show the similarity in chemical composition between the Fe skarn and contact metasomatic deposits and the hydrothermal breccia and vein deposits.

FIGURE 67. Fluorite-calcite veins in bleached Abo sandstone outcrop (Gal54; V.T. McLemore photograph).

FIGURE 68. Yellow bastnäsite in purple fluorite breccia from the Red Cloud copper mine (NMLI0040, length is ~8 mm in left photo, V.T. McLemore photograph). Bastnäsite is the most common REE mineral mined in the world today.

FIGURE 69. Copper minerals along fractures and bedding planes (Gal6126c).

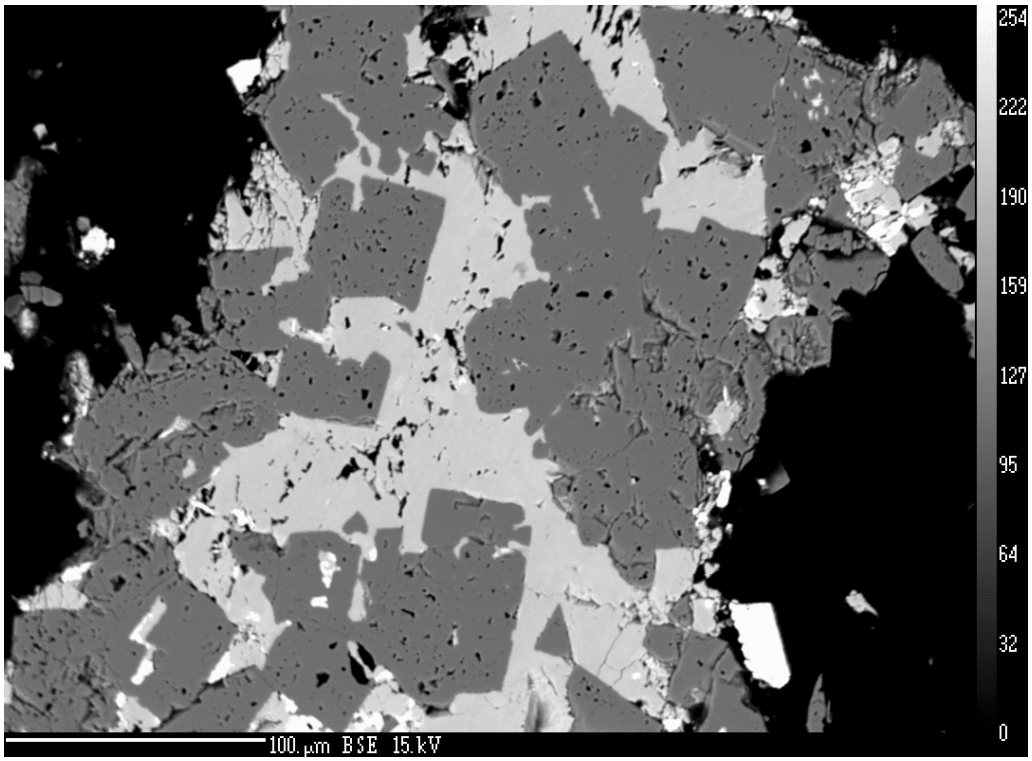

FIGURE 70. Fluorite (gray cubes) intergrown with strontianite (white). Bright white rectangles are bastnäsite (Gal7).

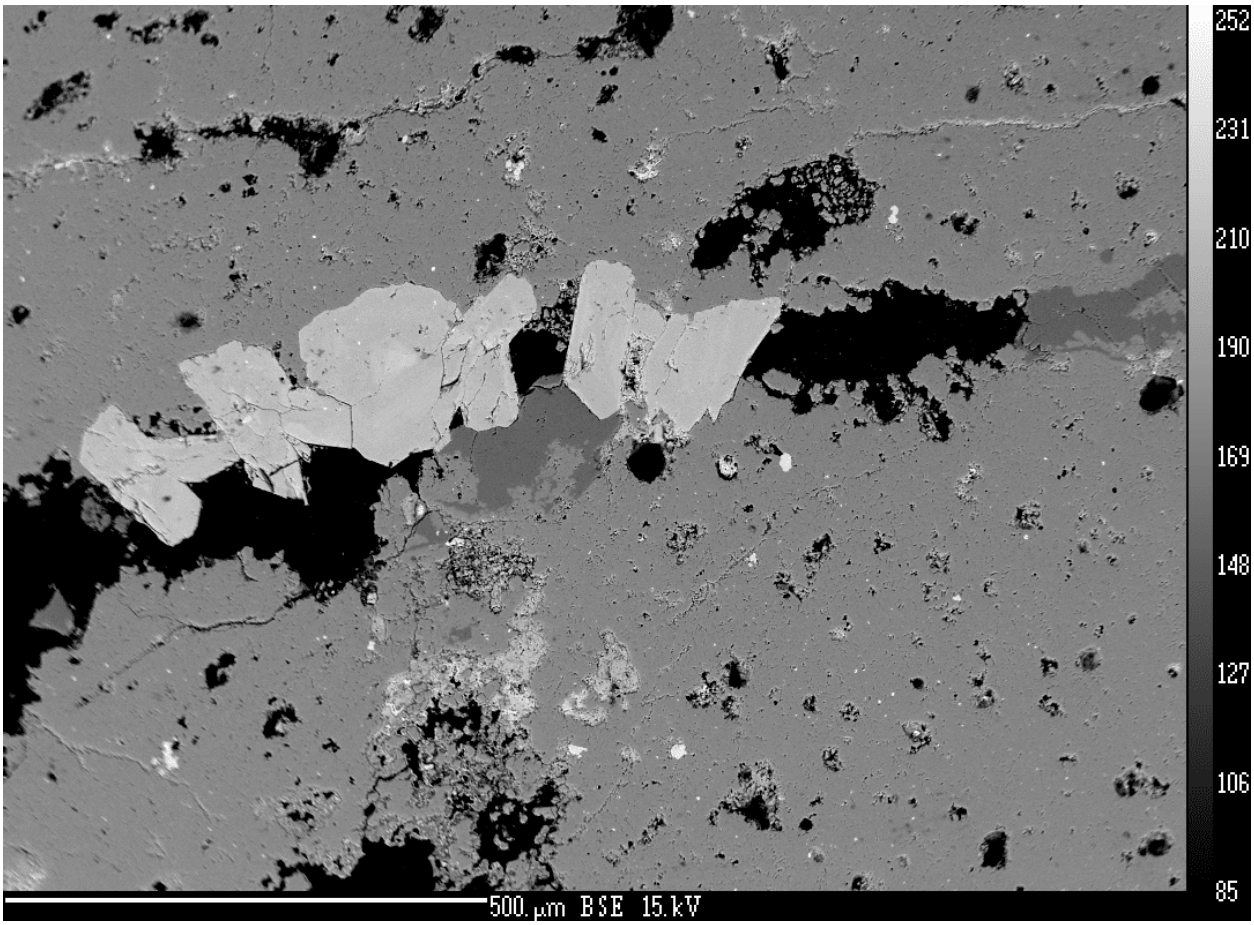

FIGURE 71. Quartz vein with euhedral crystals of Sr-Al-P phase (svanbergite $SrAl_3(PO_4)(SO_4)(OH)_6$). Tiny bright white crystals are rutile (Gal75).

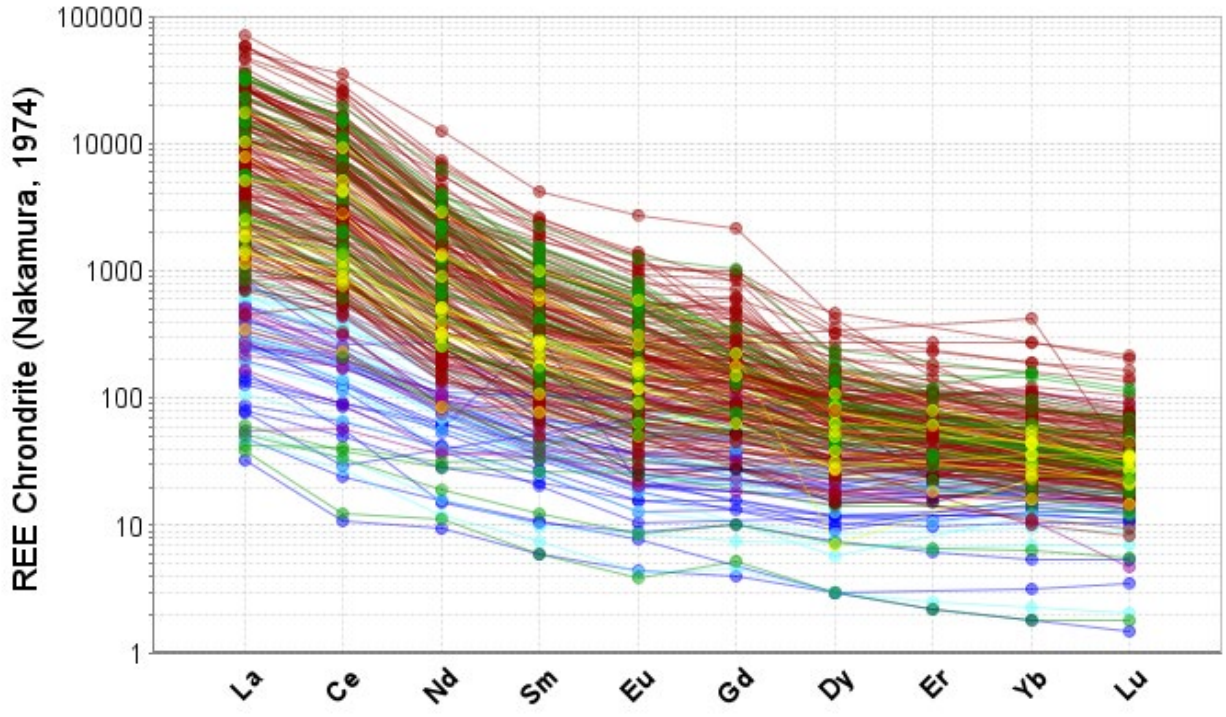
REE Chrondrite (Nakamura, 1974)
100000
10000
1000
100
10
1
La
Ce
Nd
Sm
Eu
Gd
Dy
Er
Yb
Lu

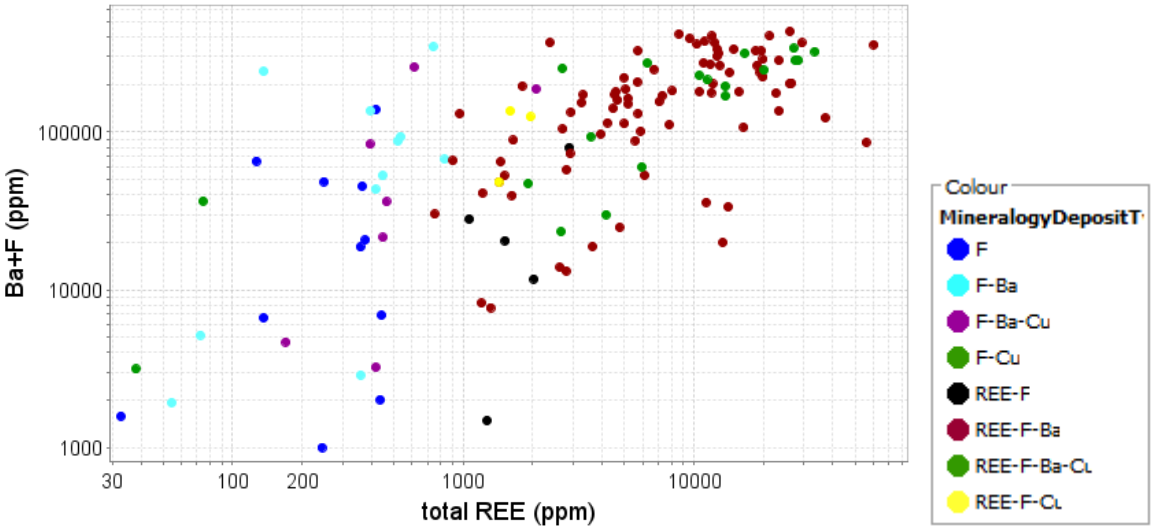
Ba+F (ppm)
100000
10000
1000
30
100
200
1000
10000
total REE (ppm)
Colour
MineralogyDepositT
F
F-Ba
F-Ba-Cu
F-Cu
REE-F
REE-F-Ba
REE-F-Ba-Cu
REE-F-Cu

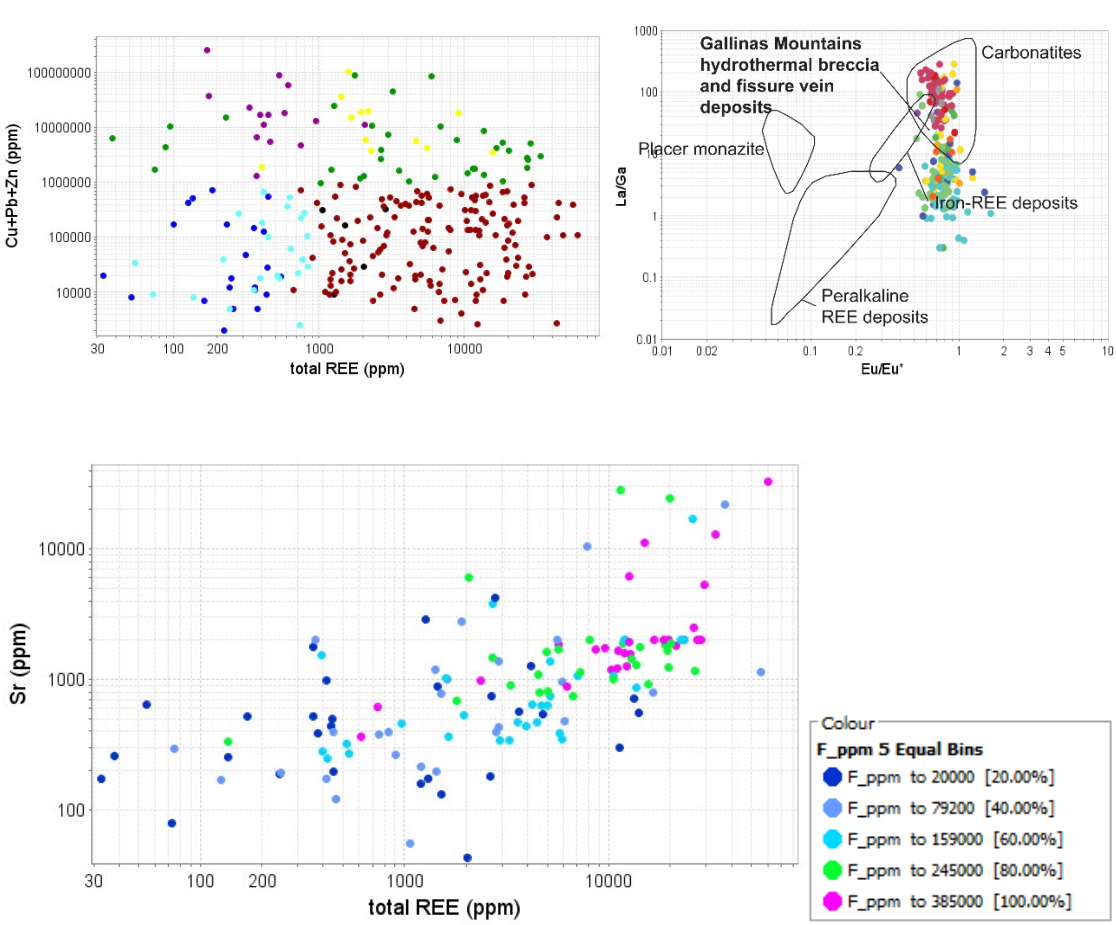

FIGURE 72. Chemical plots of hydrothermal breccia and fissure vein deposits (Tv). Chondrite-normalized REE (Nakamura, 1974), Ba+F vs REE, and Cu+Pb+Zn vs REE are color coded by mineral deposit type (Table 14). On a Eu/Eu* vs La/Gd plot; hydrothermal breccia and fissure vein deposits from the Gallinas Mountains partially overlap the carbonatite field (Castor and Hedrick, 2006). The REE vs Sr plot shows concentration of F (ppm) in different colored symbols. Samples with high REE have high Ba, F, and Sr concentrations. Chemical analyses are in Appendix 3.

Fluorite replacements/disseminations

Fluorite replacements and disseminations are locally found in host rocks adjacent to the hydrothermal breccia and vein deposits. These zones are generally centimeters in width but locally are as much as a meter wide along some veins. Fluorite mineralization includes replacement and disseminated fluorite crystals and thin veinlets (<mm) within granite, sandstone, syenite, and trachyte (Fig. 73, 74) usually found near hydrothermal breccias, fissure veins, and dikes. Fluorite commonly replaces feldspar phenocrysts in trachyte and quartz cement in the sandstones. Thin veinlets cut the host rock along fractures.

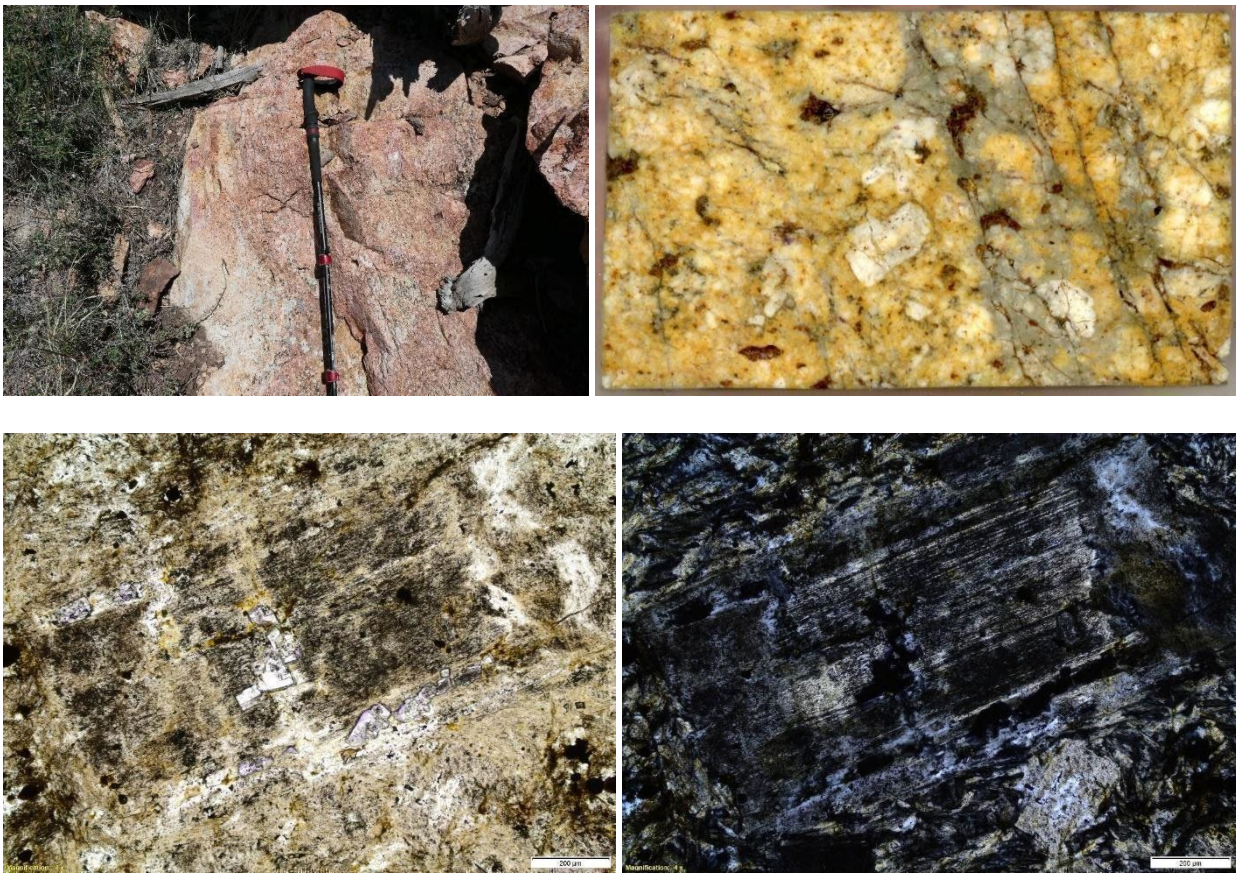

FIGURE 73. Altered trachyte dike exhibiting incipient purple fluorite replacement of feldspar phenocrysts (upper left view of outcrop, upper right view of thin section billet, lower left is plane polarized light and right is crossed polarized light) (sample Gal3023/3021/200, V.T. McLemore, field photographs; E. Owen billet photograph and photomicrographs).

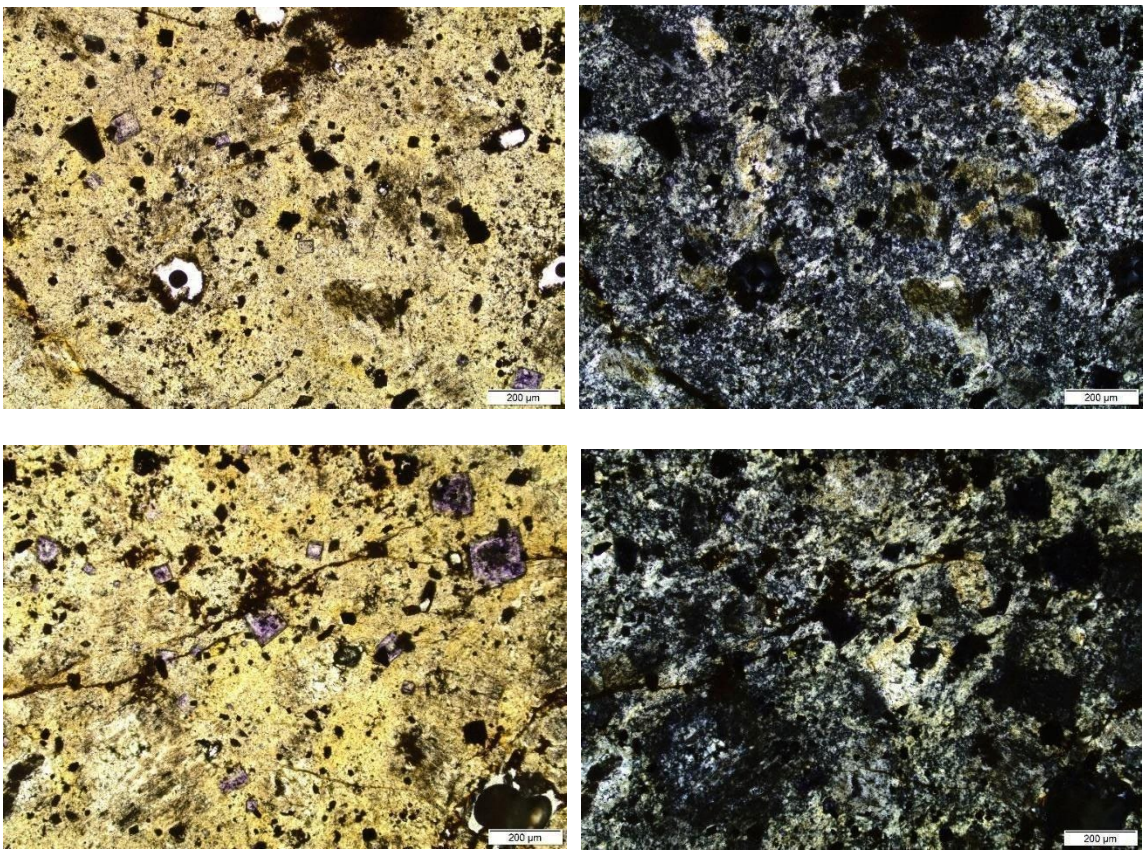

FIGURE 74. Purple fluorite associated with hematite disseminated along fractures in altered trachyte dike at the Eureka mine (Gal170). Upper photo are field photographs. Left photographs are plane light. Right photos are plane polarized light. (V.T. McLemore, field photographs; E.B. Haft photomicrographs).

Magmatic intrusive breccia pipes (Tibx)

Magmatic intrusive breccia pipe deposits (Tibx) were described above under Stratigraphy and Description of Lithologic Units. However, several intrusive breccia pipes are mineralized and described in more detail here. Breccia pipes are important exploration targets because they generally are porous and fractured and provide excellent hosts for subsequent magmatic-hydrothermal and hydrothermal mineralization. There has been no reported production from the magmatic intrusive breccia deposits, although Strategic Resources, Inc. conducted exploration drilling north of the M and E breccia pipe (Appendix 9).

Only a few breccia pipes locally are mineralized. Local hydrothermal fluorite and/or calcite veins are found along intrusive contacts and cutting the intrusive breccia pipes. The Sky High, Big Ben, M and E (Fig. 75), and Park intrusive breccia pipes contain high REE in magmatic-hydrothermal breccia veins that are similar in appearance and composition to the magmatic-hydrothermal and fissure veins (Tv). Some of the mineralized zones cutting the breccia pipes appear to be zoned. Locally calcite overprints the fluorite and REE minerals, suggesting an early magmatic-hydrothermal calcite mineralization. Most intrusive breccia pipes have samples containing >1000 ppm Ba. Prospect pits (NMLI0312, NMLI085, NMLI0824) adjacent to the Gal377 breccia pipe on Rattlesnake Ridge have exposed small hematite veins. Samples from the pits and interior of the Gal377 breccia pipe contain >1000 ppm Ba and >500

ppm total REE. Samples from M and E, the pipe north of the All American mine, Big Ben, and Sky High intrusive breccia pipes all contain >100 ppb Au. The other pipes in the area are not mineralized at the surface.

Samples have elevated REE and a light-REE chondrite normalized enriched pattern (Fig. 77), similar to the same REE plots for Fe skarn (Fig. 62) and hydrothermal breccia and fissure vein deposits (Fig. 72). Samples with high REE have high Ba, F, and Sr concentrations.

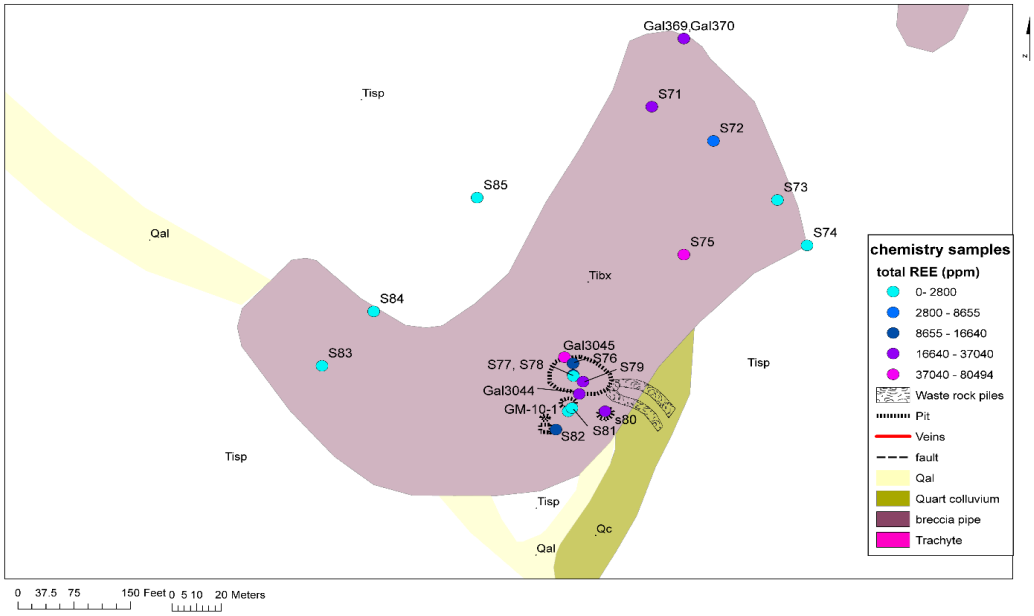

FIGURE 75. Geologic map of the M and E intrusive breccia pipe, showing distribution of samples, coded by total REE concentrations. Sample Gal3045 contained >8% total REE. See Figure 6 for location of M and E prospect.

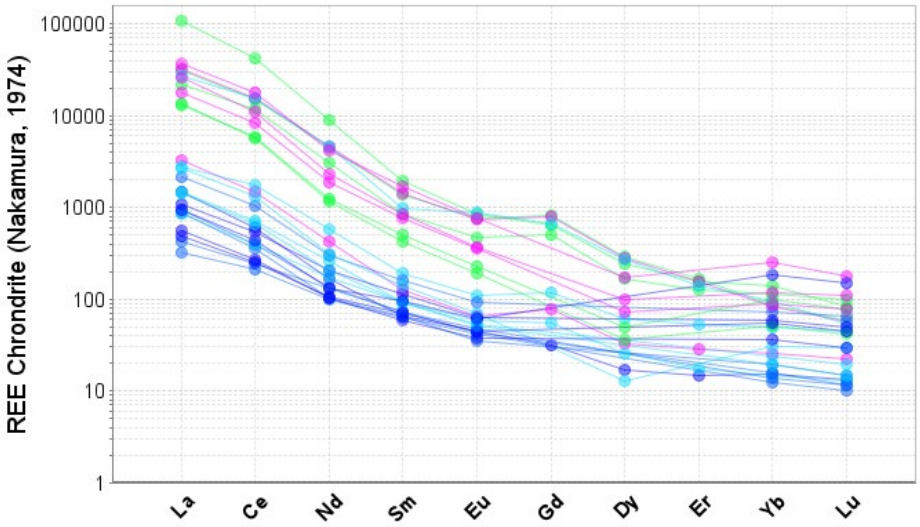

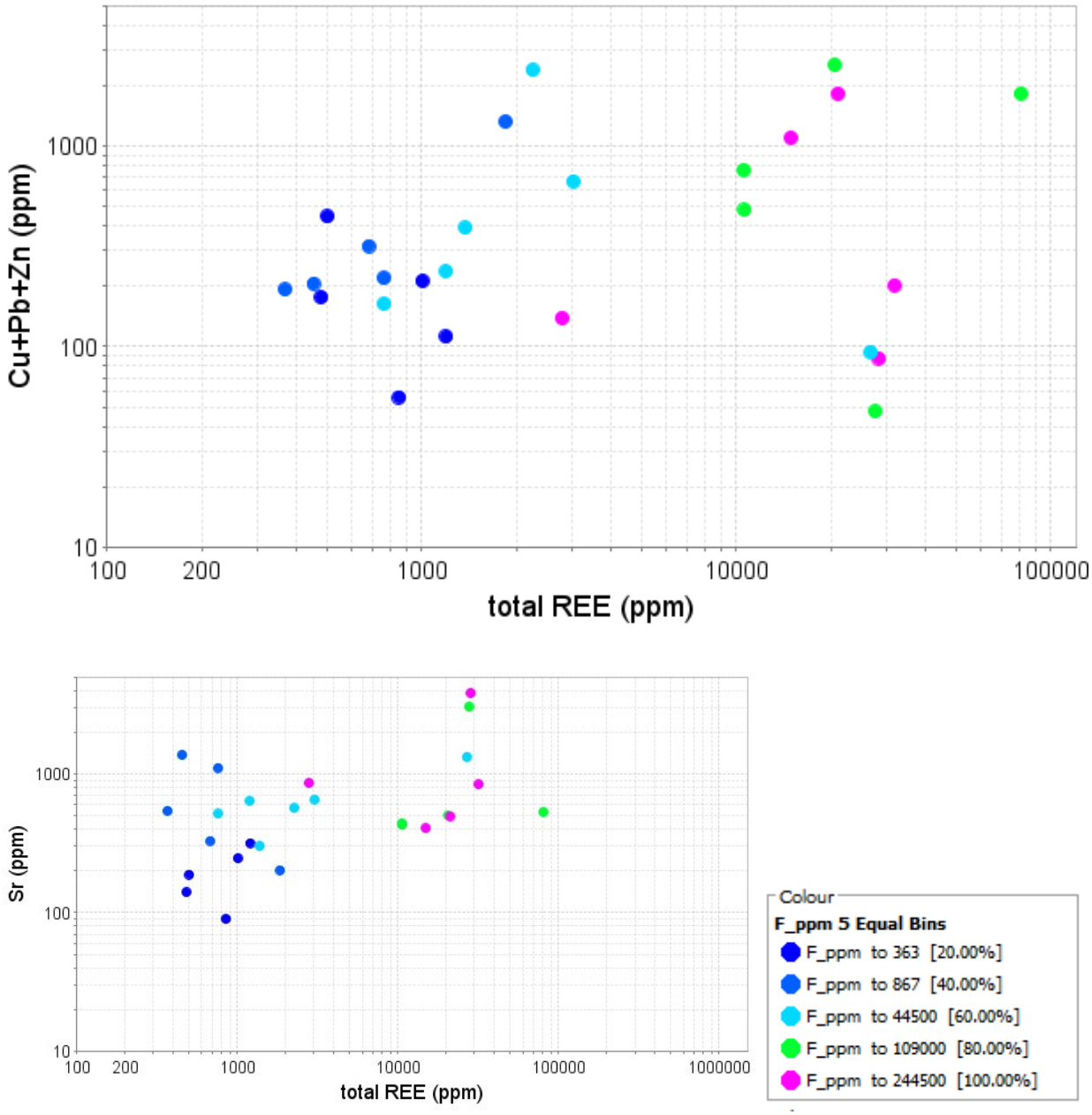

FIGURE 76. Chemical plots of magmatic intrusive breccia deposits. Chondrite-normalized REE (Nakamura, 1974), Cu+Pb+Zn vs REE, and REE vs Sr are color coded by concentration of F (ppm) in different colored symbols. Samples with high REE also have high Sr and high F concentrations and some have high Cu, P, and Zn. Chemical analyses are in Appendix 3.

Carbonate veins and breccias

Carbonate breccias and veins are composed mostly of calcite with local fluorite, barite, bastnäsite, malachite, and chrysocolla and cut limestones, gypsum, and limey sandstones near hydrothermal breccia vein deposits and intrusions (Fig. 77, 78). The mineralized limestones are

gray, fine-grained, brecciated, recrystallized, and locally cut by veins. Gypsum outcrops are rare, brecciated, and exhibit dissolution textures. Some carbonate breccias are overprinted by younger travertine (i.e. spring) deposits. There is no reported production from the carbonate breccia deposits.

Chondrite-normalized REE plot (Nakamura, 1974) shows elevated REE and enriched light-REE patterns (Fig. 79), similar to same REE plots for Fe skarn (Fig. 62), hydrothermal breccia and fissure vein deposits (Fig. 72), and magmatic intrusive breccia deposits (Fig. 76). Samples with high REE have high Ba, Sr and F concentrations.

FIGURE 77. Veins along the road cut near Sky High at Gal363, containing calcite, fluorite, barite, bastnäsite and 22,037 ppm total REE (Gal80d; V.T. McLemore photograph).

FIGURE 78. Left-Veins in limestones containing 4540 ppm Cu and 129 ppm total REE (Gal265; V.T. McLemore photograph), containing calcite, fluorite, and chrysocolla. Right- Fissure vein in limestone containing 11,317 ppm total REE (NMLI0731b, V.T. McLemore).

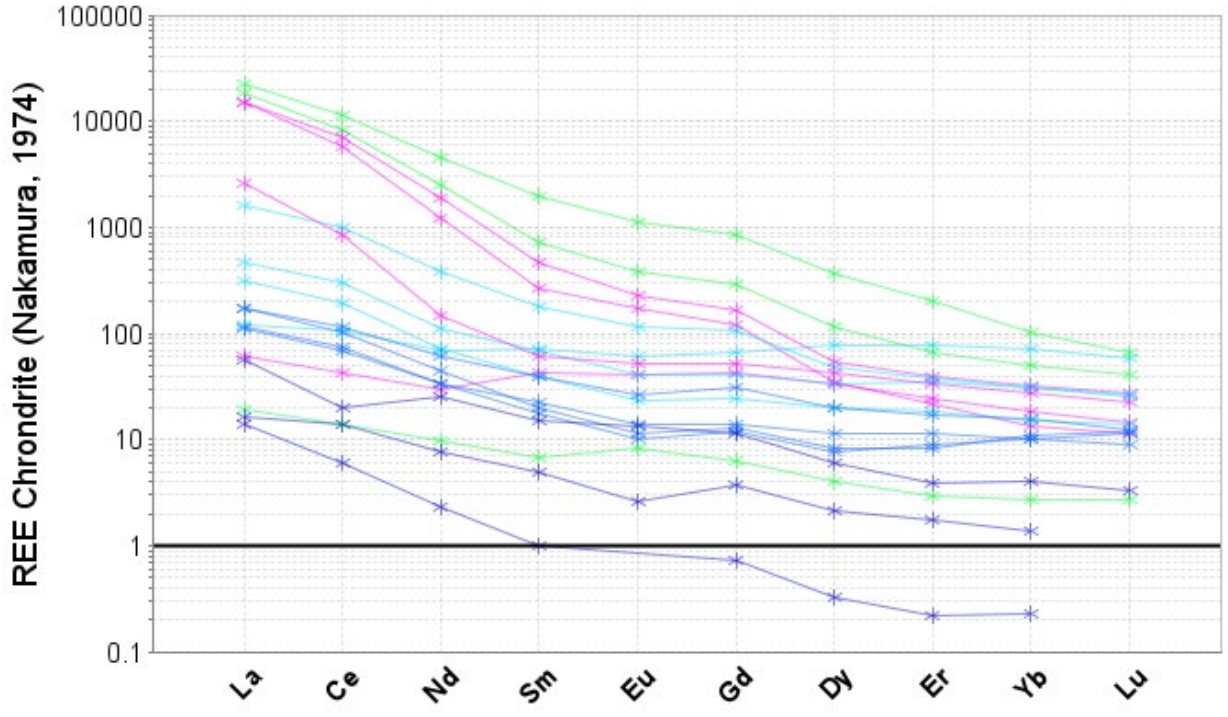
REE Chrondrite (Nakamura, 1974)
100000
10000
1000
100
10
1
0.1
La
Ce
Nd
Sm
Eu
Gd
Dy
Er
Yb
Lu

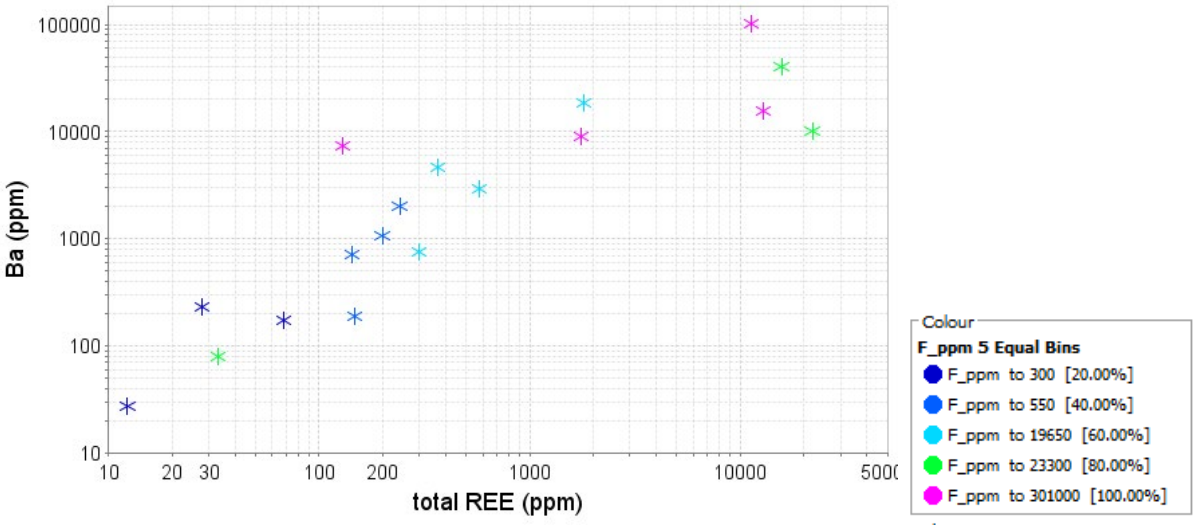
Ba (ppm)
100000
10000
1000
100
10
10
20
30
100
200
1000
10000
5000
total REE (ppm)
Colour
F_ppm 5 Equal Bins
F_ppm to 300 [20.00%]
F_ppm to 550 [40.00%]
F_ppm to 19650 [60.00%]
F_ppm to 23300 [80.00%]
F_ppm to 301000 [100.00%]

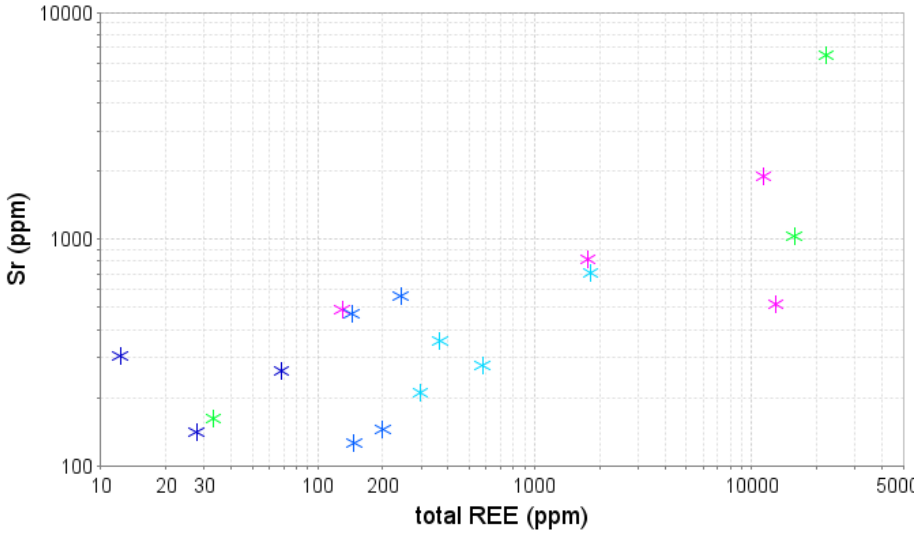

FIGURE 79. Chemical plots of carbonate breccia deposits. Chondrite-normalized REE (Nakamura, 1974), REE vs Ba, and REE vs Sr are color coded by concentration of F (ppm) in different colored symbols. Samples with high REE also have high Ba, Sr and F concentrations. Chemical analyses are in Appendix 3.

Hypogene oxidation (including late calcite veins)

Hypogene oxidation are those processes that occur late in the mineralizing system at depth. In the Gallinas Mountains, hypogene oxidation is characterized by the oxidation of pyrite to goethite and hematite, chalcocite and chalcopyrite to malachite and chrysocolla, and galena to cerussite (Mellen and Olson, 1921; Vance, 2013; this report). Oxidation extends at least 60 m deep at the Red Cloud copper mine (NMLI0040; Mellen and Olson, 1921). Late calcite veins cut the trachyte dikes in the Rough Mountain area, M and E breccia pipe, and tectonic breccias along the major faults. Calcite veins also cut the sandstones near trachyte dikes and veins in the Rough Mountain area. Vance (2013) suggests that agardite and rostite are hypogene minerals.

Supergene oxidation

Supergene oxidation are those processes that occur relatively near the surface, at low temperatures and by meteoric waters as opposed to deep hypogene processes; weathering is one type of supergene oxidation. In some types of ore deposit systems, supergene oxidation can actually reconcentrate the ore minerals into an economic mineral deposit (for example, copper porphyry deposits). In the Gallinas Mountains, supergene oxidation is characterized by the formation of hematite, copper oxides and carbonates, cerussite, anglesite, and arsenates (Vance, 2013). Supergene enrichment did not occur in the Gallinas Mountains.

DESCRIPTION OF MINES

There are numerous shafts, adits, pits, and shallow cuts exposing the mineral deposits throughout the Gallinas Mountains and different names have been used to identify them. In this report, most mine features were named according to the original patented or unpatented mining claim, unless the mine feature was otherwise identified by Perhac (1961) or Kelley et al. (1946). Many of the mine features, therefore, can have one or more aliases because of confusion by other

geologists as to which mine feature was being referenced. Thus, a unique mine identification number in the New Mexico Mines Database is used in this report to differentiate between the different mine workings. Locations of mines by mine id are in Appendix 2 with a summary of other information on the mine. Unknown is given to unnamed mines and prospects where there is no known name. Locations of samples and photographs are in the SQL database. The descriptions below are taken mostly from field descriptions, sampling, and mapping, and incorporate descriptions by Rothrock et al. (1946), Kelley (1949), Perhac (1968), Schreiner (1993), Vance (2013), NMBGMR mine production records, and other reports as cited. Some of the older names used in newspaper articles and older reports cannot be located in the area.

Iron skarn and contact-metasomatic replacement deposits

American mine

The American (Iron Hammer, NMLI0003) mine (Fig. 80, 81) was mined by the Lincoln Ore and Metals Co. in 1942. In 1943, the mine was leased to A.F. Denison who mined approximately 806 short tons. In 1943, another company, the Mineral Materials Co., continued strip mining. Total production from the mine in 1942–1943 is 3,944 short tons of 54.5–56.2% Fe (Kelley, 1949). The deposit was approximately 122 m long and 1.5 m wide and contained magnetite, hematite, epidote, diopside, allanite, and tremolite (Kelley, 1949; Schreiner, 1993). Iron mineralization extended only to the 16 m crosscut, approximately 11 m below the main bench. Ore shipments averaged 55.7% Fe and 0.033% P (Kelley, 1949). Sample no. S58 contained 34.2% Fe and 1090 ppm REE; the REE mineral is allanite (Appendix 3; Schreiner, 1993). Magnetite and hematite replaced limestone and sandstone along the contact with the trachyte in a roof pendant on top of the trachyte or a xenolith within the trachyte. The sandstone has been metamorphosed to clay, muscovite, and chlorite aggregate cut by K-feldspar veins (Fig. 58). The hematite-magnetite skarn consists of quartz, calcite, tremolite and diopside, with local phlogopite. Silicified limestone consists of tremolite and diopside at the contact with syenite and Yeso Formation. Iron veins cut the trachyte and sandstone (Fig. 64).

FIGURE 80. Left photograph—American mine looking south. Right photograph—Close-up of iron skarn (dark brown) at the American mine (NMLI0003).

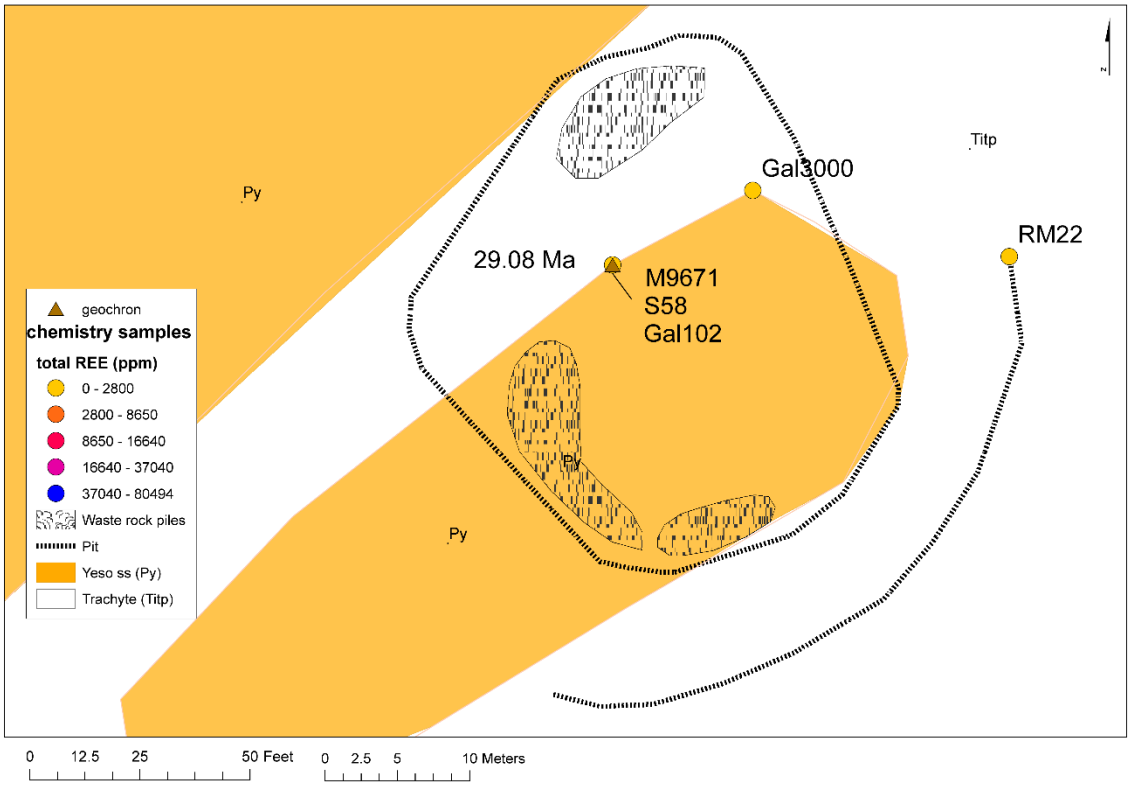

FIGURE 81. Geologic map of the American mine (NMLI0003). See Figure 6 for location of the American mine.

Rare Metals mine

The Rare Metals mine (Little Marie, NMLI0039) was prospected by the Lincoln Ore and Metals Co. and the USBM in 1943, but there was no reported production (Kelley, 1949). The deposit is developed by a 3 m adit and several pits and trenches. Iron minerals replaced limestone adjacent to a syenite sill, and the altered rocks consist of magnetite, hematite, fluorite, galena, epidote, tremolite, and phlogopite. Two separate deposits are approximately 107 m long and 3–5 m thick and average 40–50% Fe. Sample S59 contained 47.1% Fe and 209 ppm REE (Appendix 3; Schreiner, 1993) and is slightly radioactive due to U and Th (McLemore, 1983). The iron mineralization replaced either a roof pendant on top of the trachyte/syenite or a xenolith within the trachyte/syenite.

Gallinas mine

The Gallinas mine (Red Cliff, Corona, NMLI0299) was mined by open pit by Dudley Cornell, Paul Teas and Vincent Moore in 1942 (Fig. 82). Total production from the mine in 1942 was 6,410 short tons of 48.7% Fe (Kelley, 1949). The deposit was approximately 38 m long, 2–3 m thick, consist of magnetite, hematite, and gypsum, and replaced flat-lying limestone and sandstone beds (Fig. 83). Sample S260 contained 44.8% Fe and 216 ppm REE (Appendix 2; Schreiner, 1993).

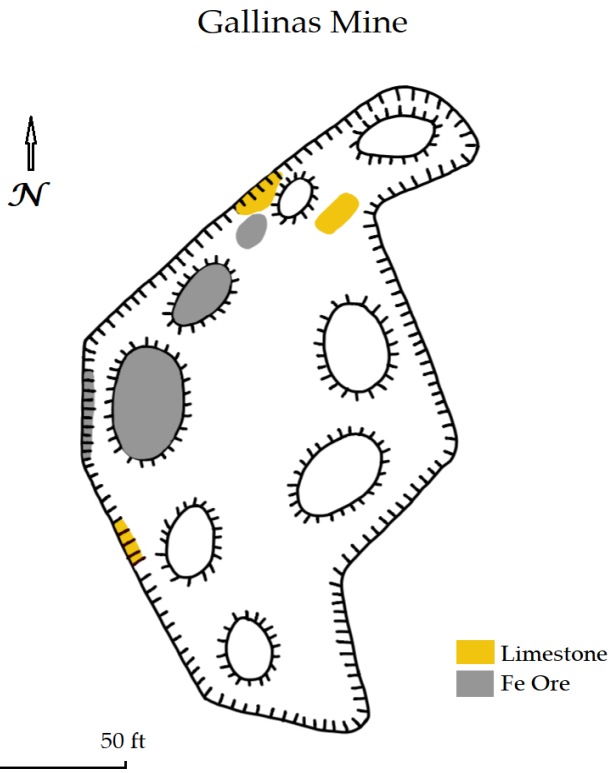

FIGURE 82. Geologic map of the Gallinas mine (NMLI0299). See Figure 6 for location of Gallinas mine.

FIGURE 83. Iron skarn on the northwest wall of the Gallinas mine (NMLI0299; GalMine; V.T. McLemore photograph). Students are masked as a safety protocol for COVID.

Iron Lamp mine

The Iron Lamp deposit (NMLI0313) was developed by a 7-m-deep shaft and trenches, and contained magnetite, hematite, limonite, and calcite (Kelley, 1949; Schreiner, 1993). The deposit is 30 m long and ~1 m thick (Kelley, 1949). Sample no. S96 contains 50.3% Fe and 125 ppm REE (Appendix 2; Schreiner, 1993). The iron minerals replaced limestone in either a roof pendant on top of the trachyte/syenite or in a xenolith within the trachyte/syenite. There is no reported production.

Iron Box mine

The Iron Box deposit (NMLI0311) is 1–2 m thick and 30 m long (Sheridan, 1947). The deposit is in limestone and sandstone and overlain by a trachyte/syenite sill.

Unknown

A small skarn (unknown, NMLI0312) is found in Yeso Formation limestone in section 23, T1S, R11E and contains magnetite, hematite, diopside, and tremolite (Schreiner, 1993). Sample S61 contain 627 ppm REE (Appendix 2; Schreiner, 1993).

Hydrothermal breccia and vein deposits

Red Cloud copper mine

The Red Cloud mine (Corona Queen, Conqueror, NMLI0040) is on the Red Cloud patented mining claim, patented in 1889 (Table 1; Fig. 6, 84). To distinguish it from the Red Cloud fluorite mine (NMLI0330) across the canyon on the Conqueror mining claim, it has been sometimes referred to informally as the Red Cloud copper mine. The Red Cloud copper mine should be called the Red Cloud lead mine, because production records suggest that more lead was produced than copper (Table 2). The open shaft is fenced and is at least 60 m deep with drifts on the 60 m level (Fig. 85). The mine is in purple hydrothermal breccias and along faults in the Yeso sandstone, siltstone, and limestone (Fig. 85). Most of the metals production reported from the Gallinas district in Table 2 is from this mine and the nearby Deadwood mine (NMLI0319, Fig. 84), but very little historical or geologic information on these two mines is known. A third mine feature (NMLI0834) is north of the Red Cloud copper mine and is now collapsed and filled.

Newspaper articles suggest that the Red Cloud copper mine was worked sporadically from 1885 to 1956. In 1919, Corona Lead and Silver Mining Co. leased the mine. In 1926, the mine was 60 m deep. Approximately 200 short tons of fluorite were produced in 1953–1954 and in 1960. In 1954–1955, New Mexico Copper Corp. produced 300 short tons of Cu-Pb-fluorite ore.

The mapped vein is classified as a REE-F-Ba-Cu based upon some samples and known production. The veins are no longer exposed at the surface, except in a few localities. Much of this detailed description is from historical reports. In 1921, three types of ore were described from the Red Cloud copper mine in at least six separate veins (Fig. 84; Mellen and Olson, 1921). The predominant, highest grade ores were a massive, purple, crystalline lead carbonate, massive galena, and a copper carbonate ore that was found in pockets at the intersection of hydrothermal breccia veins and bedding planes. One carload of ore assayed 38.9% Pb, 3.1% Cu, 9.4% CaO and 6 oz/ton Ag (Mellen and Olson, 1921). The second type of ore consists of soft, lead carbonate ore found in hydrothermal breccia veins and thin fissure veins along bedding. The ore

averaged 10–30% Pb, 2 oz/short ton Ag and no copper. The third type of ore is silicified, purple fluorite hydrothermal breccia veins along bedding with galena and lead sulfate that averaged 1–15% Pb. Sulfide minerals typically were found below the 33 m level (Mellen and Olson, 1921). Assays from smelter records are in Table 15. The geologic map is in Figure 84 and a plan and cross section of the mine in 1926 is in Figure 85. The grade of production from the Red Cloud and Deadwood mines averaged 4.6 oz/ton Ag, 3.9% Cu, and 16.9% Zn (Schreiner, 1993).

Minerals reported from the mine include chrysocolla, malachite, azurite, melanterite, galena, wulfenite, fluorite, pyrite, calcite, barite, and bastnäsite (Table 4). These minerals were found in purple fluorite hydrothermal breccia zones that were up to 36 m long, 0.5–7 m wide, with a northeast trend and near vertical dip. The underground drifts are circular to elliptical in plan view, and in cross section the ore body is chimney-like in shape (Fig. 85).

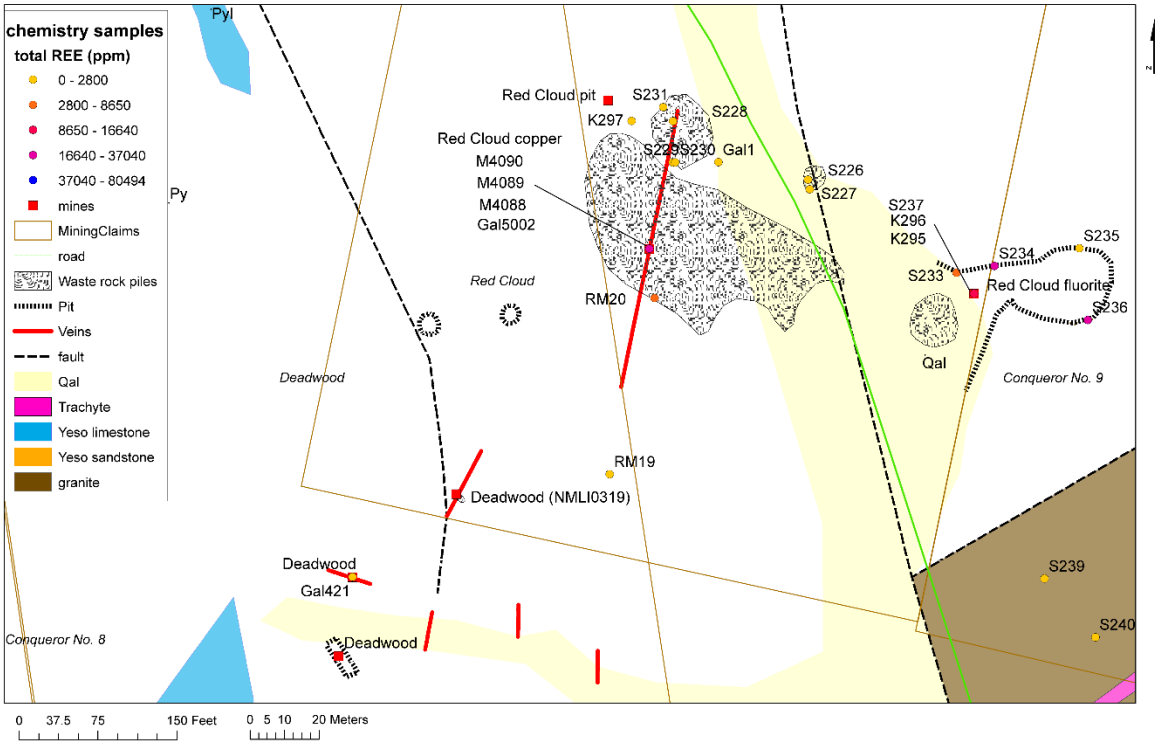

FIGURE 84. Geologic map of surface workings at the Red Cloud copper (NMLI0040), Red Cloud fluorite (NMLI0330), and Deadwood (NMLI0319) mines. Samples are colored according to total REE. See Figure 6 for location of Red Cloud copper, Red Cloud fluorite and Deadwood mines; granite=Proterozoic granite.

TABLE 15. Assays from smelter records, Red Cloud copper mine (NMLI0040), Gallinas Mountains, Lincoln County, New Mexico (NMBGMR file 4933_mf, 1926).

Shipping No.	Date	Dry short tons	Avg. Ag (oz)	Avg. Pb%	Avg. Cu%	Gross value per ton	Smelter charges $	Net Amount $	Relative depth of ore shipments in ft
1-13	6/20-11/20	386.7	3.63	26.9	2.21	36.4	10.66	8,000	90-120
14-42	7/21-4/22	14499.5	6.24	22.7	7.76	27.4	7.13	16,000	120-200
48-52	4/22-6/22	492.6	5.5	20.6	6.9	25.2	7.60	16,000	200-250
53-65	12/22-4/23	669.6	5.33	23.4	5.6	36.5	5.47	20,123.5	250-300
Total		3,048	5.5	23.43	5.95			60,128.5	

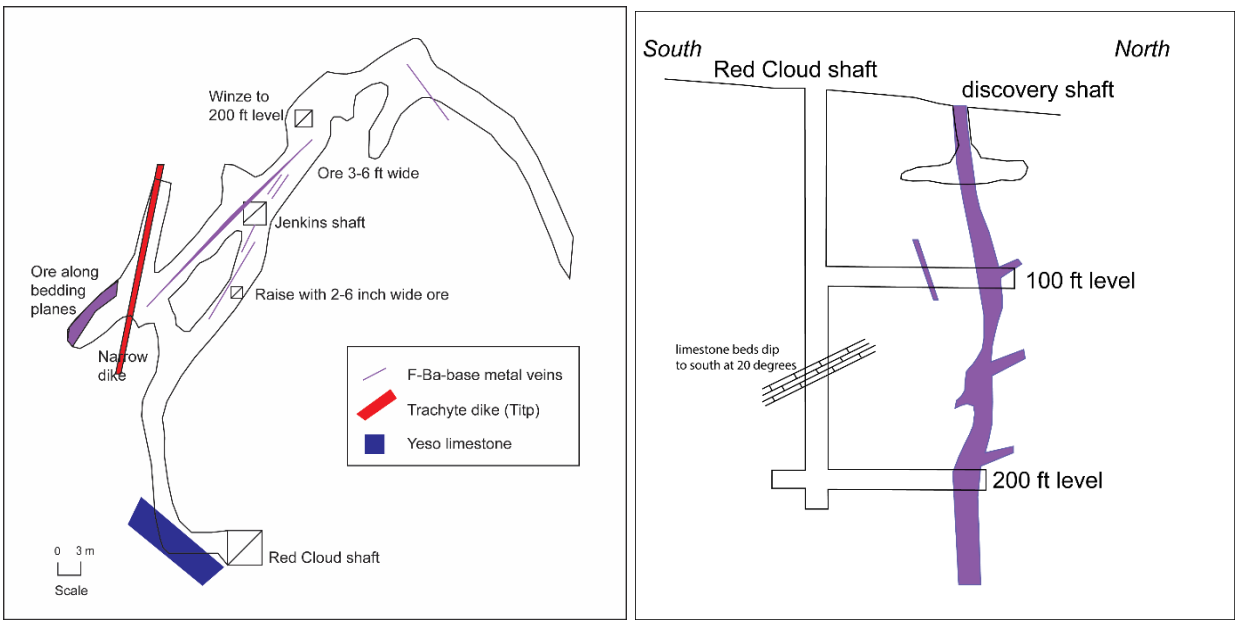

FIGURE 85. Left—plan map of 33 m level of Red Cloud copper mine (NMLI0040) in June 1926 (NMBGMR mine archives 4933_mf and 4931_mf). Right—cross section of the Red Cloud copper mine, Gallinas Mountains, Lincoln County, New Mexico in June 1926 (NMBGMR mine archives 4933_mf and 4931_mf). The entire shaft is in Yeso Formation. Location is on Figure 74 at Red Cloud copper mine.

Deadwood mine

The Deadwood mine (Fig. 84; NMLI0319; McCutcheon) is southwest of the Red Cloud copper mine and is at least 21 m deep with four drifts connecting to open stopes (Fig. 86; Mellen and Olson, 1921). The mapped Deadwood vein is classified as a REE-F-Ba-Cu based upon known production. Not much is known about the history of the Deadwood mine except that it was one of the early mines. Most of the production was probably reported with the production from the Red Cloud copper mine.

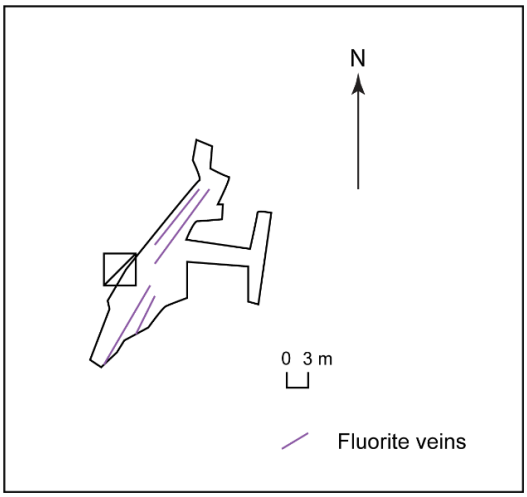

FIGURE 86. Plan map of Deadwood mine (NMLI0319; from (Mellen and Olson, 1921). Location of shaft is on Figure 84 at Deadwood (NMLI0319).

Red Cloud fluorite mine

The Red Cloud fluorite mine (Fig. 84; NMLI0330, Conqueror No. 9, East Ore Body) is across Red Cloud Canyon from the Red Cloud copper mine and was first developed by a shaft and an adit with 85 m of drifts (Fig. 87). Later the deposit was mined by open pit methods, resulting in the current open pit exposure, which is approximately 42 m long, up to 11 m wide, and 15 m high. The elliptical breccia zone is bound by three faults, one of which has a stratigraphic throw of approximately 120 m (Perhac, 1961). The main Red Cloud Canyon fault to the west acts as a boundary separating the Red Cloud fluorite mine from the Red Cloud copper mine (Fig. 84). Fluorite breccia along the faults extend to a depth of 42 m (Perhac, 1961). Some early-stage bastnäsite was replaced by bladed rosettes of Ca bastnäsite (Williams-Jones et al., 2001).

The adjacent rocks are brecciated and altered, and consist of Yeso Formation sandstone, andesite to the west, and Proterozoic granite to the southeast (Fig. 87). The deposit consists of sandstone fragments with quartz, pink barite, yellow-green to honey brown translucent bastnäsite, yellow-green to green agardite, calcite, hematite after pyrite, and clay in a purple fluorite matrix. Although trace amounts of chrysocolla and malachite line small cavities in some samples from the Red Cloud fluorite deposit, the Red Cloud fluorite mine generally lacks copper and lead minerals. Therefore, the Red Cloud fluorite mine has been classified as REE-F.

Perhac and Heinrich (1964) estimated the main ore shoot contained approximately 11,000 short tons of 50% fluorite but only 6,500 short tons were actually produced. Rothrock et al. (1946) reported lower grade material was at depth below the Red Cloud fluorite pit.

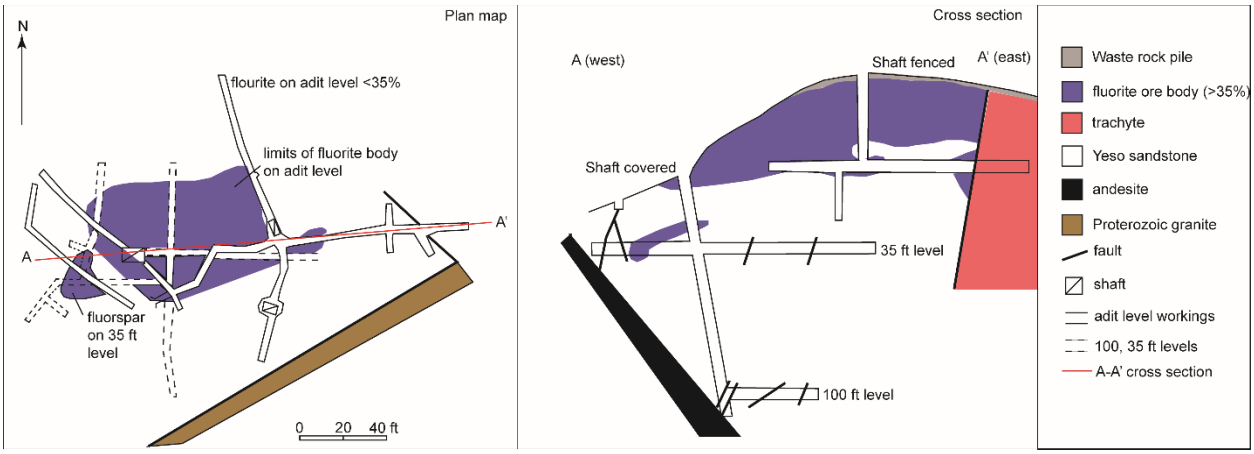

FIGURE 87. Plan map and cross section of the Red Cloud fluorite mine (NMLI0330), Gallinas Mountains, Lincoln County, New Mexico before the deposit was finally mined by open-pit methods (modified from Rothrock et al., 1946; geology by G. Smalley in 1944).

Rio Tinto mine

The Rio Tinto mine (NMLI0042; Conqueror) is on unpatented mining claims, south of the Red Cloud mine, and is the deepest shaft in the district (Fig. 88). Development started in 1940 with a 40 m shaft, which was deepened in 1953–1954 to 70 m (Fig. 88). The 12 m level was extensively developed at that time. The mine is in brecciated and faulted, layered Yeso Formation sandstone, siltstone, and limestone that were intruded by nearby trachyte dikes (Fig. 89, 90). Mineralized brecciated limestone is found on the 41 m level (Fig. 91; Griswold, 1959).

In 1956, 300 short tons of fluorite, copper, and lead ore were shipped to the Carrizozo mill (Williams, 1966). Samples from 39.5m level average 0.8 oz/ton Ag, 2.8% Pb, 1% Cu, 42% CaF_2, some U (0.11% U_3O_8) and Mo (0.58%) (Table 16, Fig. 91; Perhac, 1961). Reserves are estimated as 22,000 short tons 40% fluorite (Perhac, 1961). Samples collected at the surface were as high as 4644 ppm total REE, 170 ppb Au, and 2.3% Cu (Table 17). In 1982, Phelps Dodge Corp. drilled a 162 m hole south of the main shaft (Fig. 88; Table 18).

The predominant mineralogy deposit classification types are F-Ba-Cu and REE-F-Ba-Cu hydrothermal breccias that trend northeast that are up to 7 m thick. At least two periods of brecciation occurred. An early stage of fluorite with barite veins followed by brecciation were deposited first, forming high-grade pods. These pods are cemented by a brecciated matrix containing fluorite, barite, azurite, malachite, chrysocolla, galena, chalcocite, wulfenite, melanterite, and bastnäsite in a gangue of quartz and Fe oxides. The ore is found as: (1) open-space fissure fillings, (2) replacements of linear zones in brecciated sandstone and limestone, (3) purple hydrothermal breccias along fractures in the sandstone, and (4) minor replacement of sandstone a meter from the brecciated zones. Small, discontinuous linear, breccia zones of fluorite, barite and bastnäsite are found at the surface. The mineralized veins and breccias were subsequently oxidized.

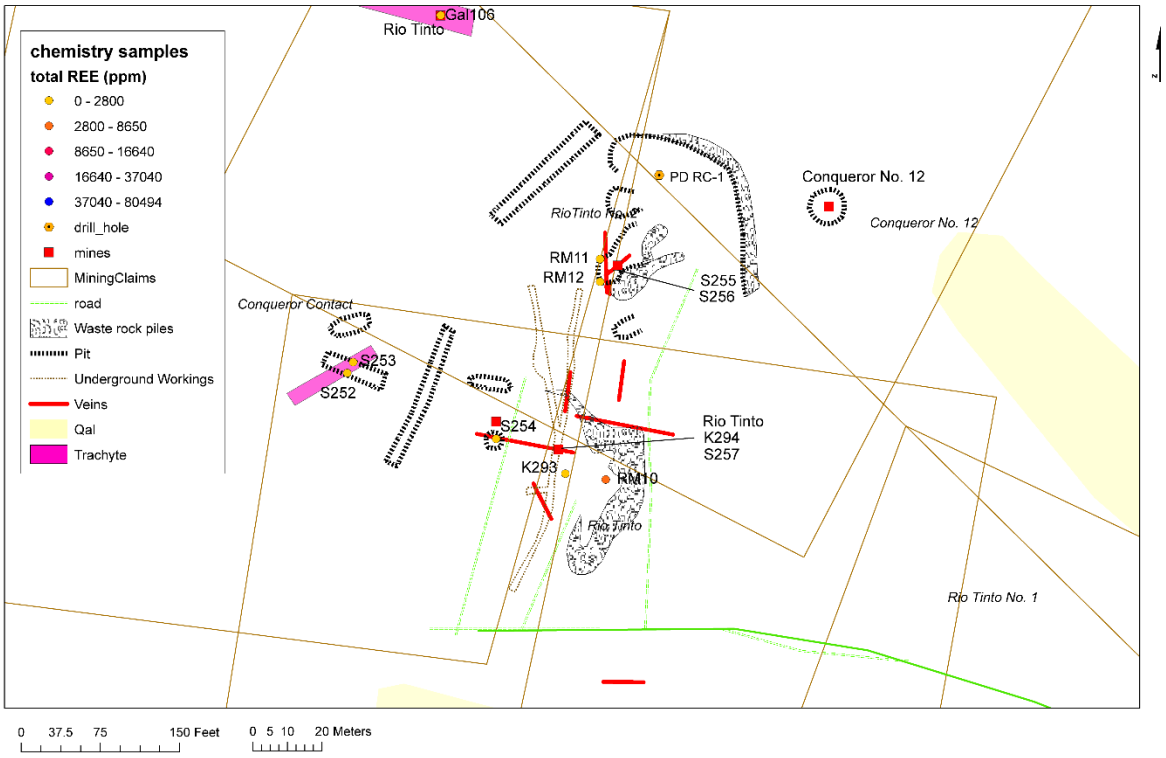

FIGURE 88. Geologic map of workings at the Rio Tinto mine (NMLI0042). The host rocks are part of the Yeso Formation. See Figure 6 for location of Rio Tinto mine.

FIGURE 89. Looking north at Rio Tinto veins in Yeso Formation, location RM11-12 Figure 88 (NMLI0755).

FIGURE 90. Main Rio Tinto shaft (fenced, NMLI0042) with foundations of the headframe in the foreground (location at Rio Tinto on Fig. 88).

TABLE 16. Historic assay data from the Rio Tinto mine (NMLI0042). Samples 1-27 are from the 41 m level (Perhac, 1961, from the New Mexico Copper Corporation). See Figure 91 for location of samples. Samples 12621 and 12622 are from the west and north ends of the shaft at the surface and contain trace gold and no bastnäsite (NMBGMR file data).

Sample No.	Width (m)	Ag (oz/ton)	Pb%	Cu%	Mo%	CaF_2%	U_3O_8%
1	2			0.30		47.40	
2	2			0.30		51.98	
3	2.5			0.60		60.62	
4	2		2.0	0.50		44.2	
5	1.5		18.04	5.09		23.0	
6	2		0.05			60.1	
7	3			0.30		65.46	
8	1.5	1.10	18.30	0.65		58.95	
9	1		1.8	1.6		41.28	0.002
10	2.5		1.0	0.5		62.97	
11	2		4.8	2.50		40.31	
12	3	0.10	0.25			54.50	trace
13	4		4.2	1.4		53	
14	3			1.40		33.91	
15			1.9	0.28		29.0	
16			3.7	4.21		14.6	0.02
17			4.6		0.33	34.53	
18			0.8	1.85	0.68		

Sample No.	Width (m)	Ag (oz/ton)	Pb%	Cu%	Mo%	CaF_2%	U_3O_8%
19	4		1.1	0.4		6	
20	2.5		1.5	1.00		15.71	
21	4.5	6.8	3.4	2.5	0.06	63.94	0.11
22	1.5	1.9	1.4	2.84		28.7	0.07
23	2.5	0.60	5.3	0.55		25.45	0.01
24	3.5	0.05	4.9			49.96	
25	5		2.8	1.90		10.1	
26	2		3.1	2.4		38.21	
27	2		2.8	1.8		37.6	
12621	~1	0.15	0.9	0.55			
12622	~1	.05	0.8	0.90			

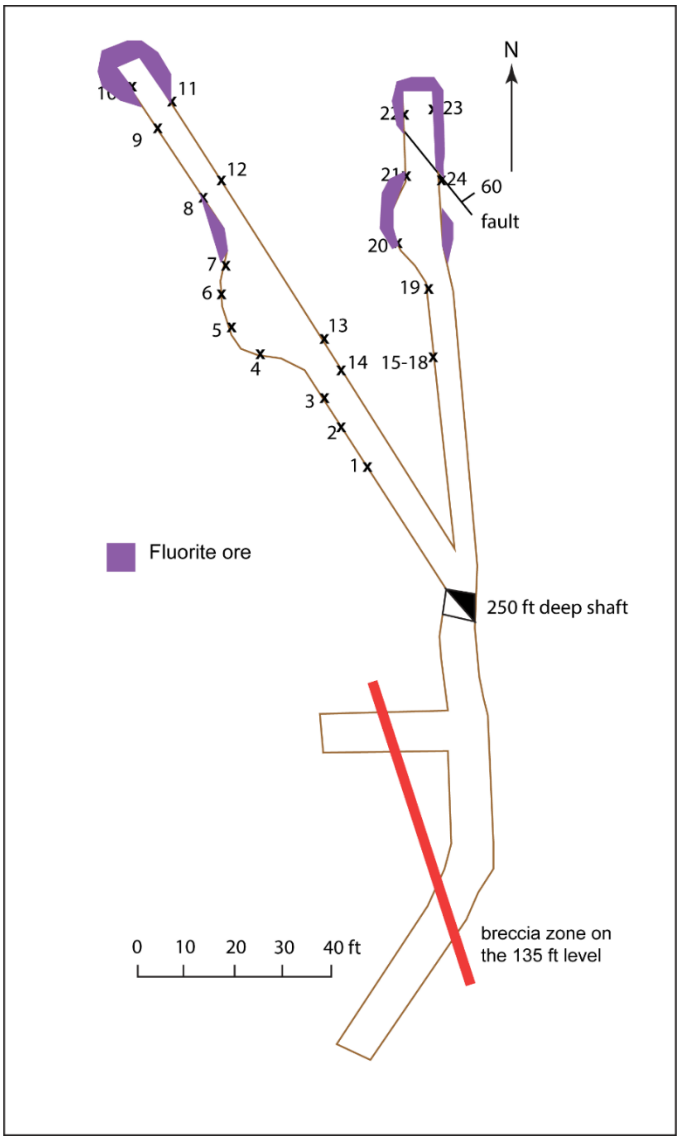

FIGURE 91. Plan view of Rio Tinto (NMLI0042) 40 m level (modified from Griswold, 1959, Perhac, 1961 and the New Mexico Copper Corporation). Local host rock is Yeso sandstone and

limestone. Black x's are sample localities listed in Table 17. Note the curved nature of the underground workings. Location of Rio Tinto is on Figure 88.

TABLE 17. Selected chemical analyses from samples collected at the Rio Tinto mine (NMLI0042). Additional analyses, location, and source of data are in Appendix 3. Samples located in Figure 91.

Sample Id	Mineralogy Deposit Type	F ppm	Au ppb	Ag ppm	As ppm	Ba ppm	Cu ppm	Pb ppm	Sb ppm	U ppm	total REE ppm
Gal106	igneous rock	900	11	2	<5	1840	5	7	0.5	4.47	386.02
Gal107	fenite	300	53	3	<5	1020	<5	33	0.2	6.74	607.75
RM9	fenite	<100	53	2.8	105	1461	140	179	15.4	16.2	1068.9
S252	fenite		17	<0.2	37	830	75	1078	18	16.6	437.22
S253	fenite		8	<0.2	71	400	158	764	13	19	154.85
RM11	F-Ba	41000	150	4.4	630	2168	670	4240	125	12	416.02
S254	F-Ba-Cu		93	21	1571	4500	23200	12900	484	36.4	334.05
S255	F-Ba-Cu		170	13	1270	4100	4727	30000	218	19	750.9
S256	F-Ba-Cu		149	9	1688	1700	1305	9077	304	13.8	371.12
K293	REE-F-Ba		39				1679	331			1215
RM12	REE-F-Ba	96100	154	5.8	820	8465	500	3.04	122	30.1	2704.7
S257	REE-F-Ba		94	3.1	386	5130	903	1987	73.1	7	1399.2
K294	REE-F-Cu		170	8			5786	10000			4644.4
RM10	REE-F-Ba-Cu	86200	135	3.5	432	7443	1610	2740	84	11.5	3567.7

TABLE 18. Inclined drill hole (RC-1, -65°, S25°W, elevation 2274 m) drilled by Phelps Dodge 76 m east-northeast of the Rio Tinto shaft on October 28, 1982 (4928_mf). Location 34.194323°, 105.734154° (NAD27, shown in Fig. 88).

Depth (m)	Thickness (m)	Description (depth in m)	Ag (oz/ton)	Cu (ppm)	Pb (ppm)	Zn (ppm)	F (ppm)	Ce (ppm)	La (ppm)	Y (ppm)
5-15	10	5-10: buff colored sandstone, fluorite, calcite along bedding planes	0.01	196	<20	203	1150	28	18	55
		10-14: breccia								
		14-15: green-gray trachyte porphyry, trace to 1% fluorite, pyrite								
		15-18: buff colored sandstone, fluorite, calcite along bedding planes								

Depth (m)	Thickness (m)	Description (depth in m)	Ag (oz/ton)	Cu (ppm)	Pb (ppm)	Zn (ppm)	F (ppm)	Ce (ppm)	La (ppm)	Y (ppm)
15-21	6	18-22: breccia	0.02	194	45	191	2467	52	22	109
21-29	8	21-29: breccia	0.03	203	617	171	2000			
29-45	16	29-45: bleached trachyte porphyry, veins Fe oxides, fluorite, Cu oxides, pyrite	0.14	502	3260	329	9920			
		44-46: fault gouge								
46-64	18	46-64: sandstone, quartzite (trachyte) breccia, fluorite, quartz, Fe oxide, Cu oxide, pyrite	0.25	113	3438	256	57500			
		cerussite in matrix, veins, pyrite in clasts								
		53-64: Fe oxides, hemimorphite on fractures								
		61, 63: Cu oxides on fractures								
64-79	15	64-78: sandstone, quartzite (trachyte) breccia, fluorite, quartz, Fe oxides, Cu oxides, pyrite	0.51	1572	3567	2826	40833	57	22	59
		cerussite, chalcocite, hemimorphite in matrix, veins pyrite								
79-85	6	78-84: relatively barren sandstone breccia		0.25	1015	697	214			73?
		84-85: trachyte breccia dike/sill								
85-110	25	85-104: sandstone (trachyte) breccia, fluorite	0.14	868	627	233	27750	41	14	63
		86-87: trachyte breccia dike/sill								
		104-105: trachyte breccia dike/sill								
		105-107: trachyte breccia dike/sill								
		107-109: trachyte breccia dike/sill								
110-143	33	110-144: sandstone with locally abundant trachyte breccia, kaolinite, fluorite, sericite, trace pyrite	0.14	1327	186	276	16390	193	42	70

Depth (m)	Thickness (m)	Description (depth in m)	Ag (oz/ton)	Cu (ppm)	Pb (ppm)	Zn (ppm)	F (ppm)	Ce (ppm)	La (ppm)	Y (ppm)
		120-121: trachyte breccia dike/sill								
143-146	3	144-148: fractured trachyte, breccia at base dike/sill	0.07	395	623	273	2500	67	26	52
480-149	3	148-495: sandstone, conglomerate, local breccia with trachyte clasts	0.12	860	343	198	<1000	75	43	33
149-155	6	151-156: conglomerate, pyrite on fractures	0.08	595	1177	133	<1000	63	26	100
155-162	7	156-162: white quartzite, fractured with fragments of monzonite		255	335	141	<1000	30	13	77

Eagle Nest mine

The Eagle Nest mine (NMLI0014) is on unpatented mining claims (Fig. 92) and at least 1000 short tons of fluorite have been produced (Perhac, 1961). The deposit is developed by a 60 m long adit (Fig. 93) and several prospect pits and trenches (Fig. 94, 95). The Eagle Nest vein is one of the best exposed veins in the district. The hydrothermal breccia and fissure veins vary locally from 3-17 m wide and 366 m long and are classified as REE-F-Ba on the basis of chemistry samples. Individual vein deposits are as much as 21 m long and 1 m wide and contain fluorite, barite, bastnäsite, quartz, hematite, chrysocolla, malachite, and calcite (Fig. 96). Locally, galena, chalcocite, and bornite are also found. As much as 755 ppb Au was detected in some samples. The main structure is several subparallel faults, trending approximately N45ºW. Adjacent sandstone is cut and altered by thin veinlets and disseminations of fluorite. Resources were estimated as 37,000 short tons of 56% CaF_2 (NMBGMR mining archive report 4703_mf). Schreiner (1993) estimated resources as 348,000 short tons grading 1.3% total REE and 39% fluorite.

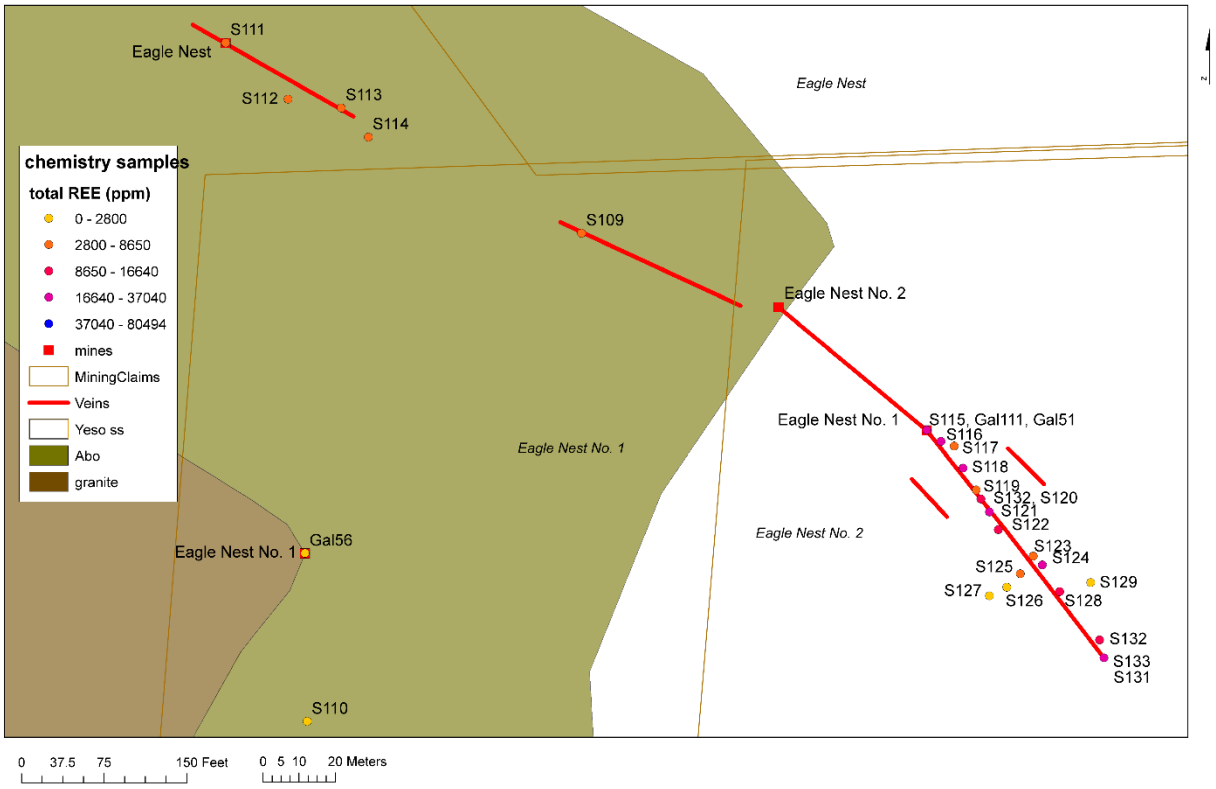

FIGURE 92. Geologic map of workings at the Eagle Nest vein (NMLI0014). See Figure 6 for location of Eagle Nest mines.

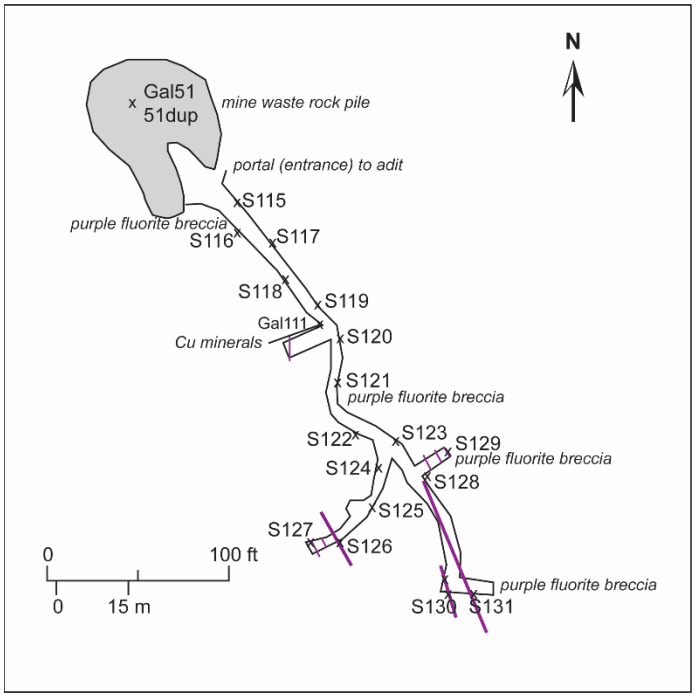

FIGURE 93. Map of Eagle Nest adit (NMLI0014; modified from Schreiner, 1999). Chemical analyses are in Appendix 3.

FIGURE 94. The Eagle Nest adit, looking south (NMLI0014).

FIGURE 95. Hydrothermal fluorite breccia zone at Eagle Nest adit (NMLI0014e, V.T. McLemore photograph).

Old Hickory mine

The Old Hickory mine (NMLI0308) is on a patented mining claim in Yeso Formation sandstone (Fig. 113), and consists of a 60 m shaft with levels at 30 and 70 m (Fig. 96), an adit (15 m below the shaft collar, Fig. 87) and several pits and trenches. The hydrothermal breccia vein is approximately 4 m thick, 55 m long, trends N20ºE, and is classified as a REE-F-Ba hydrothermal breccia and fissure vein deposit. The veins consist of fluorite, barite, calcite, quartz, hematite, bastnäsite, and trace amounts of galena, malachite, chrysocolla, pyrite and dolomite and is cemented by a purple fluorite matrix. Fragments of Yeso Formation sandstone within the mineralized breccia are common. The vein pinches out with depth (Rothrock et al., 1946). A second shaft northeast of the main shaft is <15 m deep and includes an incline. Most of the deeper workings have been backfilled. The Old Hickory mine first produced Pb and Cu, and later during World War 2, it produced fluorite. A fluorite lens is between a trachyte dike and sandstone. The lens is 20–50 m long and 4 m wide, decreasing in width to 3 m at the 30 m level

and to 1 m at the 70 m level (Fig. 87; Kelley et al., 1946); Griswold, 1963). In cross-section, the ore body is chimney-like in shape (Fig. 97).

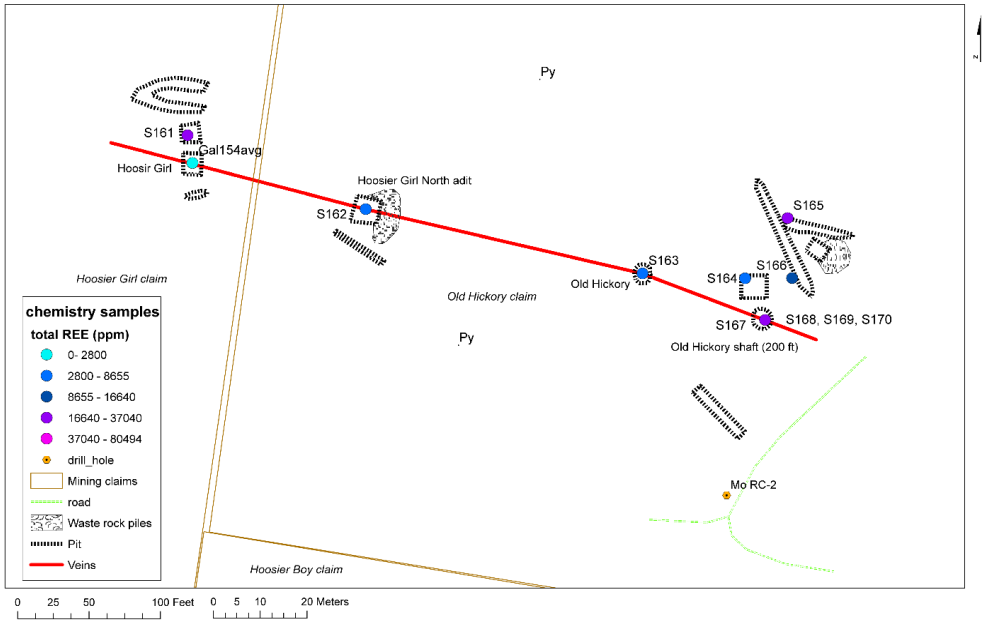

FIGURE 96. Geologic map of the Old Hickory (NMLI0308) and Hoosier Girl claims, showing distribution of samples, coded by total REE concentrations. See Figure 87 for the cross section of Old Hickory shaft. Py=Yeso Formation. See Figure 6 for location of Old Hickory mine.

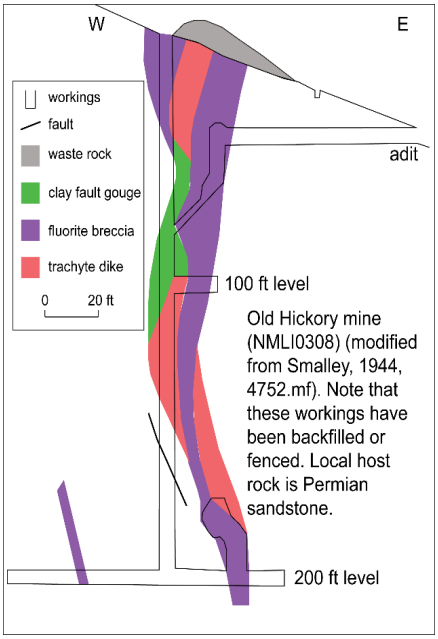

FIGURE 97. Cross section of the Old Hickory shaft (NMLI0308) (modified from 4752_mf). The Old Hickory vein is along a northwest-trending fracture-fault zone (Fig. 86). Note that these workings have been backfilled or fenced. Local host rock is Yeso Formation sandstone (Permian). See Figure 6 for location of mine.

Buckhorn, Little Wonder, and Last Chance mines

The Buckhorn mine (NMLI0727, LA83069), discovered in 1881, is on a patented mining claim that was surveyed in 1884 and patented on 10/2/1902. There were two shafts in 1885. In 1991, the workings consisted of a 10-m adit connecting to a 15-m winze, 7 m and 14 m shafts, and a 5 m adit connecting to a 42 m shaft (Oakes, 1991; Schreiner, 1993). The vein lies along a mineralized fault that strikes 330-335º and is ~1 m wide in Yeso Formation sandstone. The Buckhorn is located on the southeastern part of the same vein as the Little Wonder (NMLI0029) and Last Chance mines (Fig. 98, 99; NMLI0027). The grade of production from the Buckhorn and Little Wonder mines averaged 4.3 oz/ton Ag, 9.4% Cu, 19.2% Pb, and 1.7 % Zn (Schreiner, 1993). Summary of chemical analyses by SEM-EDX of minerals found at the Buckhorn mine (Schreiner, 1993) is in Table 19.

The Buckhorn-Little Wonder-Last Chance vein is classified as F-Ba-Cu and REE-F-Ba-Cu deposits. The vein consisted of fluorite, quartz, barite, bastnäsite, and minor galena, tennantite, freibergite, proustite, xenotime, zircon, calcite, malachite, azurite, chrysocolla, digenite, covellite, shattuckite, actinolite, adamite, cornubite, and hematite-limonite after pyrite (Schreiner, 1993; Modreski and Schreiner, 1993; DeMark and Hlava, 1993). Early reports estimate that assays average 1.91 oz/ton Ag, 1.5–2% Cu and Pb (4935mf). Vance (2013) reports sulfur and oxygen isotopes.

The Little Wonder is on the Buckhorn patented mining claim, north of the Buckhorn mine, along the same structure and consists of veins ~1 m wide and 15 m long with little brecciation. Production was approximately 300 short tons in the 1950s and remaining reserves are estimated as 800 short tons of 3–4% Cu (Perhac, 19610). The vein consists of fluorite, barite, bastnäsite, malachite, azurite, chrysocolla, chalcocite, quartz, with minor calcite, bornite, galena, pyromorphite, anglesite, and hematite-limonite after pyrite (Perhac, 1961; field reconnaissance). Locally in the adit, copper is as high as 15–20% (Perhac, 1961).

The Last Chance mine (NMLI0027, LA83070) consists of an 8 m shaft and an adit, is on unpatented mining claims, and along the Buckhorn-Little Wonder-Last Chance fault. Fluorite, quartz, bastnäsite, barite, pyrite, and minor copper oxide minerals are found at the mine (Perhac, 1961).

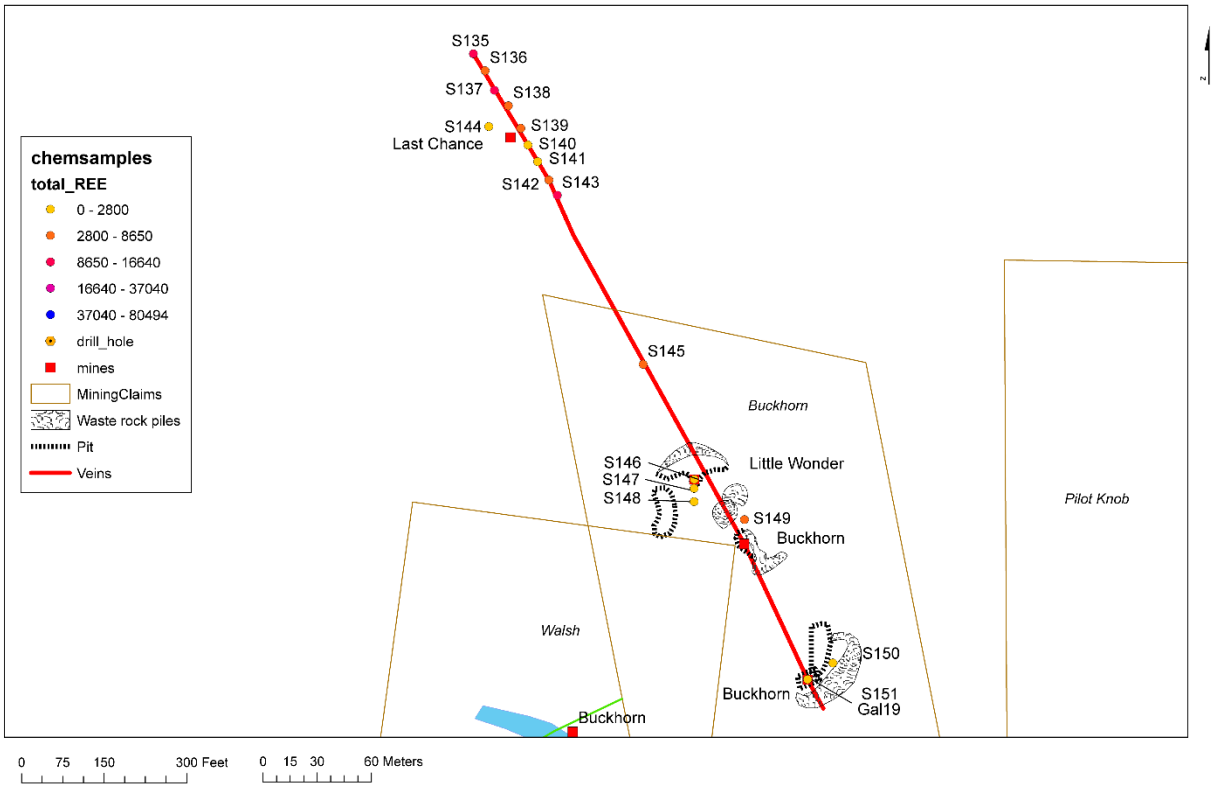

FIGURE 98. Geologic map of workings at the Buckhorn, Little Wonder, and Last Chance mines (NMLI0727, NMLI0029, NMLI0027). The Last Chance mine was not mapped because it was completely backfilled. The host rock is Yeso Formation. See Figure 6 for location of Buckhorn and Last Chance mines. Blue polygon is Yeso Formation limestone (Pyl).

TABLE 19. Chemical analyses by SEM-EDX of minerals found at the Buckhorn mine (NMLI0727; Schreiner, 1993).

mineral	Chemical formula	Ag%	Cu %	As %	Zn%	Sb%	S%
tennantite			45.5-45.3	17.8-19.3	7.8-9.2	0-4.4	24.1-26.8
freibergite		31.7	20.9	17.5	7.2		22.8
proustite		55.0	3.1	15.6	6.2		20.1

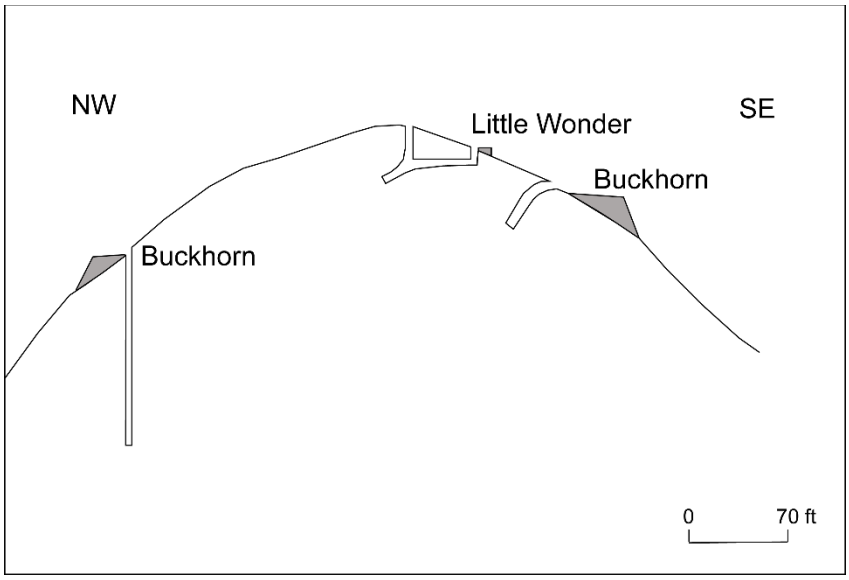

FIGURE 99. Cross section along southern Buckhorn-Last Chance vein, showing the Buckhorn and Little Wonder mines (NMLI0727, NMLI0029) (modified from Johnson, 1980, NMBGMR mining archive file 4935_mf). Note that these workings have been backfilled. Local host rock is Yeso Formation sandstone. See Figure 98 for location.

Sky High-Big Ben mines

The Sky High mine (NMLI0045) consists of a 30 m shaft, 7.5 m shaft, and pits (Fig. 100). Big Ben mine (NMLI0732) consists of a 9 m shaft, pit, trench and collapsed adit (30 m long). The Sky High shaft was covered by a cable netting and the other shafts and adits were backfilled in 1993. The Big Ben prospect consists of a 30 m shaft, adit and pits along brecciated veins of fluorite, barite, quartz, bastnäsite and calcite. The claims were not patented. In 1944, Sky High was owned by the Continental Engineering Co (NMBGMR mining archive report 4723_mf), but by 1961, New Mexico Fluorspar Co. controlled the property (Perhac, 1961). The fault strikes notheast. The vein cuts a magmatic intrusive breccia pipe that intrudes Yeso sandstone and limestone and a trachyte dike. The vein consists of fluorite, quartz intergrown with fluorite, barite, calcite, bastnäsite, chrysocolla, malachite, azurite, wulfenite, mimetite, hematite-limonite after pyrite, manganese-oxides, and late cockscomb quartz (Perhac, 1961; Schreiner, 1993). The intrusive breccia pipe consists of matrix-supported angular to subrounded fragments of sandstone, trachyte, and few granitic clasts. Calcite and fluorite are abundant locally in the breccia pipe.

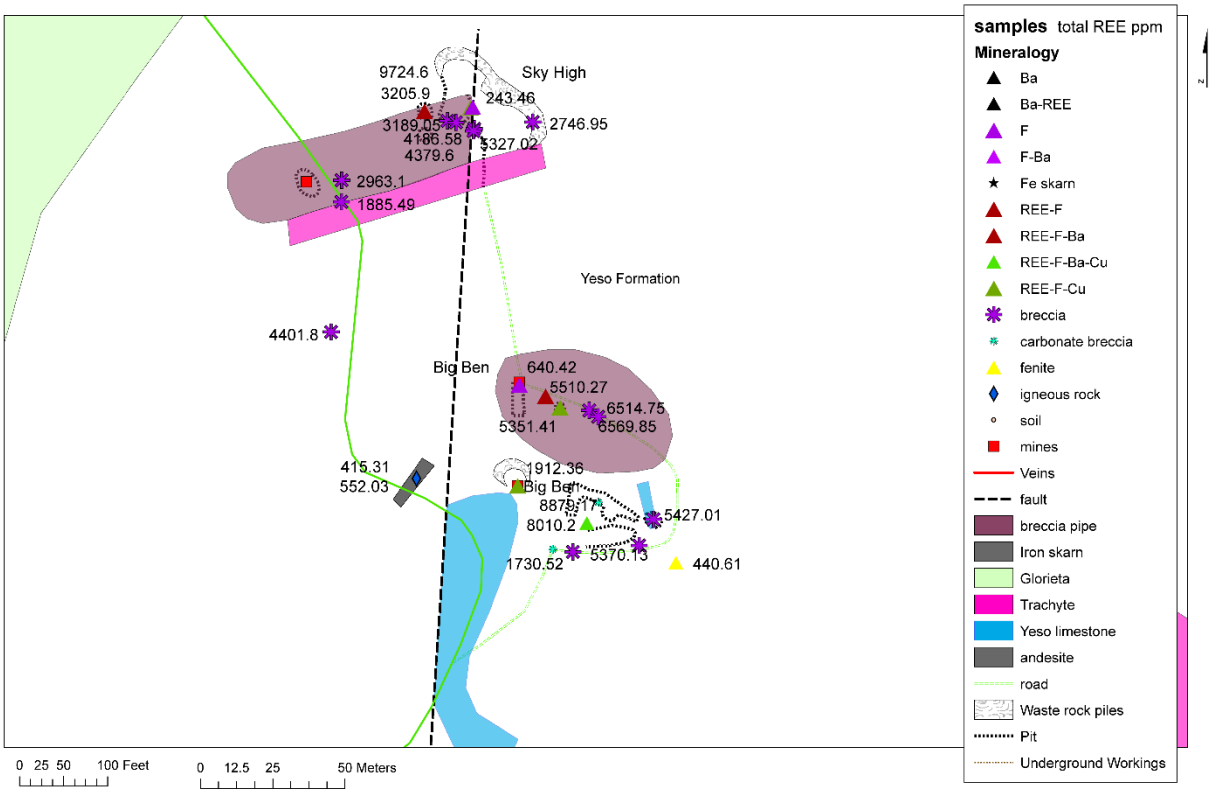

FIGURE 100. Geologic map of workings at the Sky High (NMLI0045) and Big Ben (NMLI0732) mines. See Figure 6 for location of Sky High and Ben mines.

Pride No. 2 mine

The Pride No. 2 mine (NMLI0037) is on an unpatented mining claim and consists of a 70 m trench, prospect pits, and a 6 m shaft (Fig. 101) in hydrothermal breccia along a fault. The fault within the workings is 24 m long, up to 1.5 m wide, and trends N10°E with a vertical dip in syenite porphyry. Fluorite, galena, malachite, and chrysocolla are found in the purple fluorite hydrothermal breccia. Thin (2-8 cm wide) fissure fluorite veins with little brecciation are found along joints in syenite porphyry. Samples contain as much as 2.14% REE, 6.2% Pb, 0.5% Cu, 71 ppb Au and 2.9 ppm Ag (Appendix 3; Schreiner, 1993).

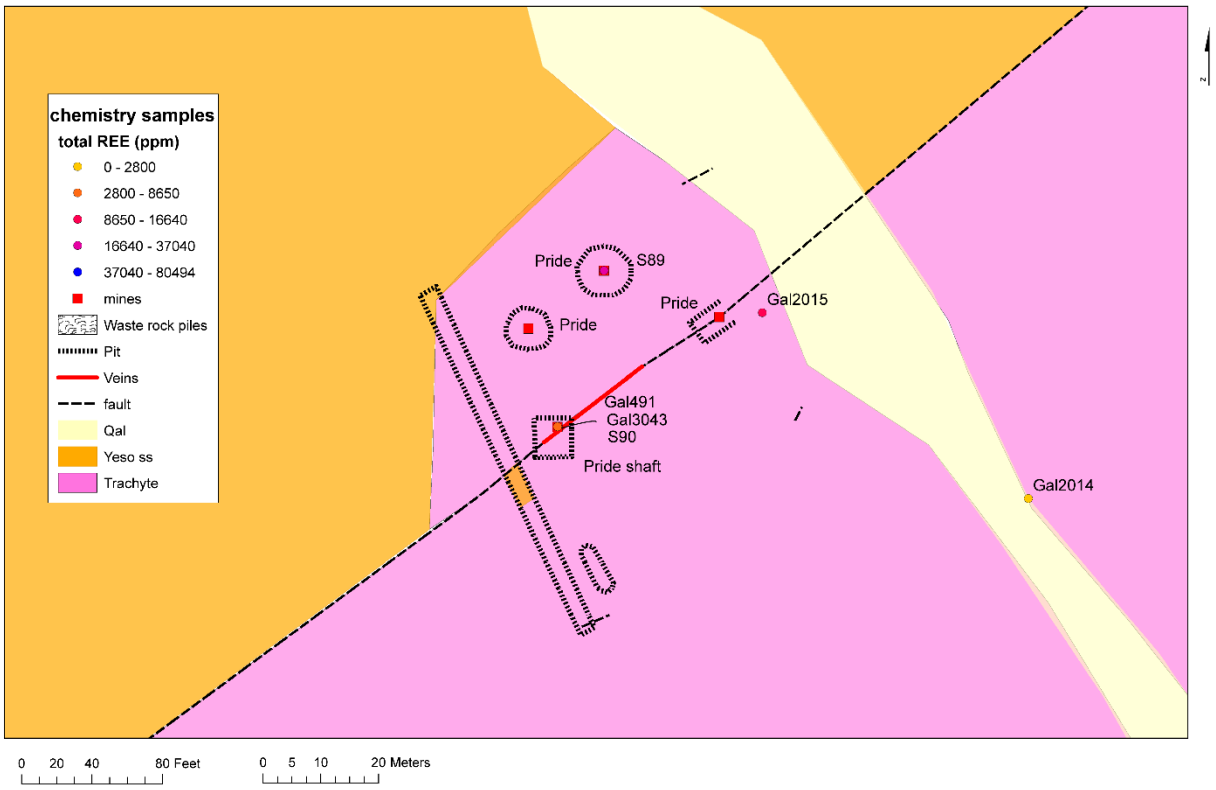

FIGURE 101. Geologic map of workings at the Pride No. 2 mine (NMLI0037). See Figure 6 for location of Pride mine.

All American mine

The All American mine (NMLI0002) consists of a 26 m shaft with a 53 m drift at the 26 m level (Griswold, 1959), 3.5 m shaft, and several pits and trenches (Fig. 102). The shafts have been backfilled. The main deposit is along a trachyte porphyry dike intruding Yeso sandstone between the intersection of three faults striking N30°W, N0°, and N80°W (Kelley, 1946; Perhac, 1961). Most of the purple fluorite hydrothermal breccias are in sandstone, although minor fluorite fissure veinlets are found in the trachyte and limestone. Pods of disseminations of purple to colorless fluorite in the sandstone are locally found several meters from the veins. Fluorite, barite, calcite and trace bastnäsite are found. In the 26 m level of the shaft, copper oxides in limestone and sandstone are reported by Griswold (1959). In 1949–1951, 129 short tons of fluorspar ore was produced (Rothrock et al., 1946; Williams, 1966). Five samples contained 0.03% to 0.33% REE and trace amounts of Au, Ag, and Cu (Appendix 2; Schreiner, 1993). The ore bodies are pipe-like in shape (Rothrock et al., 1946).

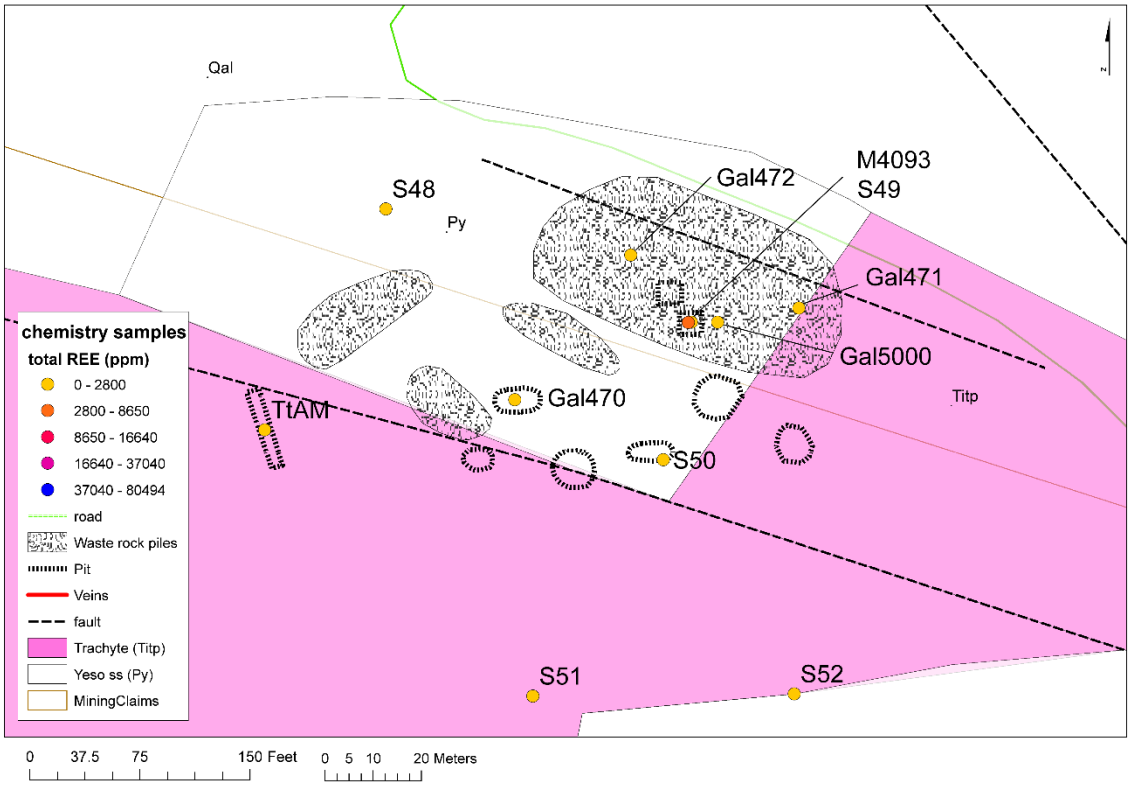

FIGURE 102. Geologic map of the All American mine (NMLI0002). See Figure 6 for location of All American mine.

Conqueror No. 3 and Hilltop mines

The Conqueror No. 3 (Fig. 110; NMLI0762; southwest part of the vein) and Hilltop (Fig. 103; NMLI0314; northeast part of the vein) prospects consist of a 21 m adit (currently the nesting habitat of vultures or crows) and numerous pits and trenches that have exposed fluorite veins and brecciated zones in Yeso sandstone. The zone trends approximately N45ºE and is over 177 m long and 2–8 m wide (Schreiner, 1993). Higher grade deposits are at the intersections of N45ºE, N70ºW, and N15ºW fractures. Brecciated purple and green fluorite zones contain quartz, barite, bastnäsite, hematite after pyrite, and trace amounts of malachite, azurite, and calcite. Sandstone adjacent to the breccia zones is fractured and contains thin veinlets and disseminations of purple fluorite.

The USBM estimated 26,000 short tons of 53% CaF_2 as a resource (4703_mf). Schreiner (1993) estimated an inferred resource of 120,000 short tons grading 1.2% total REE and 38% fluorite.

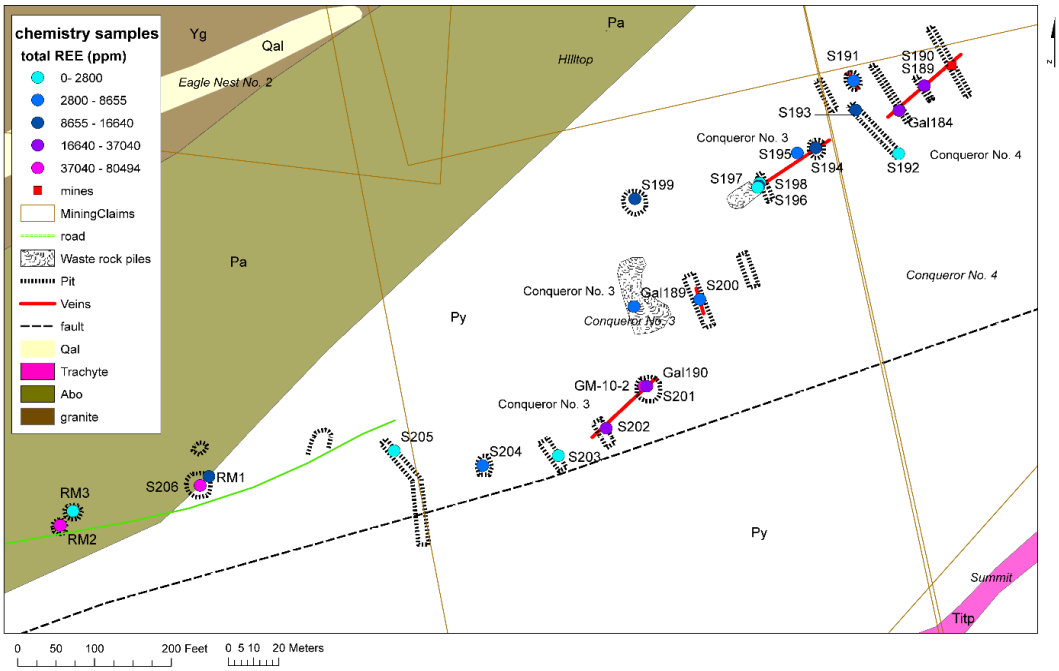

FIGURE 103. Geologic map of the Conqueror No. 3 and 4 claims (west of Hilltop and Hoosier Girl claims, Fig. 104), showing distribution of samples, color coded by total REE concentrations. Py=Yeso Formation, Pa=Abo Formation, Yg=Proterozoic granite. Conqueror No. 3 adit (NMLI0762) is at S197, S198, and S196. See Figure 6 for location of the Conqueror No. 3.

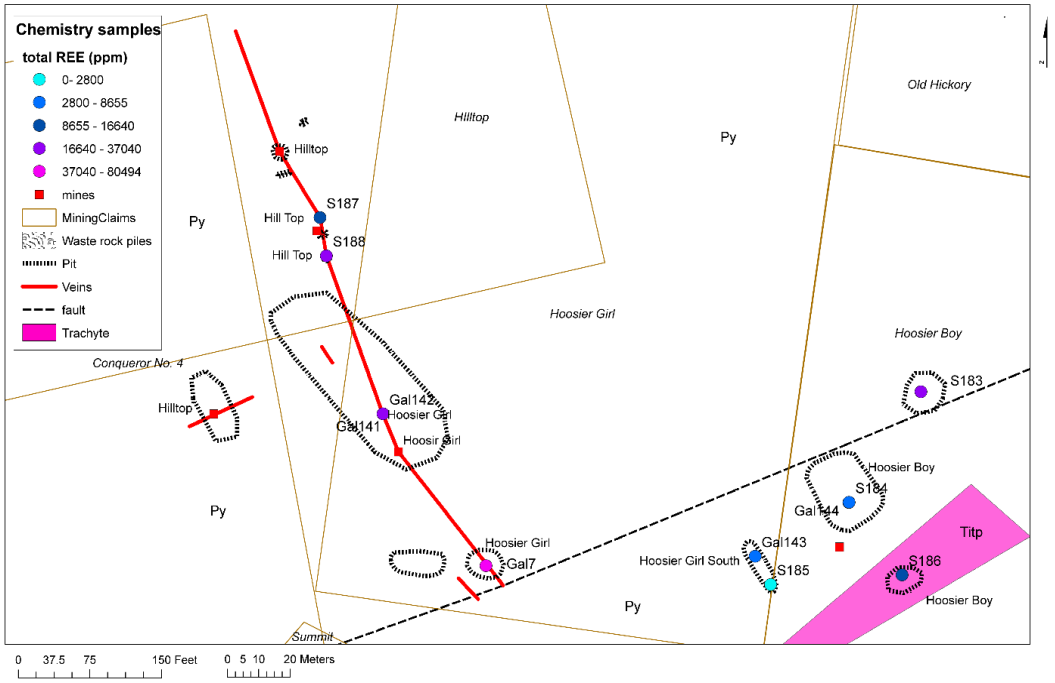

FIGURE 104. Geologic map of the Hilltop and Hoosier Girl claims (east of Conqueror No. 3 and 4 claims, Fig. 103) showing distribution of samples, coded by total REE concentrations. Py=Yeso Formation.

$^{40}Ar/^{39}Ar$ DATING RESULTS

Ages from a prior $^{40}Ar/^{39}Ar$ dating campaign (Table 20; Robison, 2017) are in Table 20 and new $^{40}Ar/^{39}Ar$ ages determined for this study are reported in Table 21. A summary of the new dates from this study, as well as selected dates from Robison (2017), are shown in Figure 105. All samples are in the ArcMap and SQL databases. Appendix 7 contains the associated plots (spectra, inverse isochrons, and ideograms) and full analytical data tables for new dates.

Samples display a variety of complexity related to excess ^{40}Ar, ^{40}Ar loss, and ^{39}Ar recoil. Eight of eleven samples yield robust results that provide meaningful insight into the magmatic history of the Gallinas Mountains. Three samples (Gal628 groundmass concentrate, and Gal1017 K-feldspar and hornblende) yield highly discordant spectra, poor fits to inverse isochron, and/or extremely scatter single-crystal ages. These results are presented for completeness, but their reliability for interpretation is limited.

TABLE 20. Summary of $^{40}Ar/^{39}Ar$ ages from Robison (2017).

Sample	Unit	Material Dated	Age (Ma)	±	2s	MSWD	Method	Comments
F1-1	Alkali Metasomatized rock	K-feldspar	25.8	±	1.20	12.00	Inverse Isochron	Contains excess ^{40}Ar ($^{40}Ar/^{36}Ar$ = 346 ± 2)
Tts-2-2	Syenite	K-feldspar	26.88	±	0.42	2.77	Plateau	
Tts-2-1	Syenite	K-feldspar	27.09	±	0.23	16.13	Inverse Isochron	Contains excess ^{40}Ar ($^{40}Ar/^{36}Ar$ = 317 ± 5)
Tt3-2-2	Trachyte	K-feldspar	27.28	±	0.19	1.54	Inverse Isochron	Contains excess ^{40}Ar ($^{40}Ar/^{36}Ar$ = 302 ± 4)
Tts-1-2	Syenite	K-feldspar	27.68	±	0.17	2.10	Inverse Isochron	Contains excess ^{40}Ar ($^{40}Ar/^{36}Ar$ = 319 ± 3)
T1 HB	Cougar Mtn. Syenite	Hbl	28.13	±	0.05	6.90	Inverse Isochron	Contains excess ^{40}Ar ($^{40}Ar/^{36}Ar$ = 299 ± 1)
Tt3-2-1	Trachyte	K-feldspar	28.14	±	0.20	7.10	Inverse Isochron	Contains excess ^{40}Ar ($^{40}Ar/^{36}Ar$ = 300 ± 2)
F2-2-1	Alkali Metasomatized rock	K-feldspar	28.9	±	0.05	1.19	Inverse Isochron	Contains excess ^{40}Ar ($^{40}Ar/^{36}Ar$ = 431 ± 11)
Tt3-1-2	Trachyte	K-feldspar	29.02	±	0.16	24.01	Inverse Isochron	Contains excess ^{40}Ar ($^{40}Ar/^{36}Ar$ = 301 ± 4)
Afa-1-2	Alkali Metasomatized rock	K-feldspar	29.08	±	0.04	3.23	Inverse Isochron	Contains excess ^{40}Ar ($^{40}Ar/^{36}Ar$ = 299 ± 3)
TA2	Andesite dike	K-feldspar	38.52	±	0.05	3.81	Plateau	

TABLE 21. New $^{40}Ar/^{39}Ar$ ages from the Gallinas Mountains.

Sample	Unit	Latitude	Longitude	Material	Age (Ma)	±	2s	Age determination method	MSWD	N	Comments
Gal628	Tia	34.197649	-105.769386	Groundmass Concentrate	24.41	±	0.02	Integrated age	---	11 of 11	Scatter due to ^{39}Ar recoil
Gal3029	Trachyte	34.209728	-105.723744	Hornblende	28.76	±	0.19	Plateau	1.74	3 of 8	
Gal1148	Tirb	34.35417	-105.78898	Biotite	28.22	±	0.08	Fixed Plateau	7.54	6 of 11	Elevated MSWD
Gal1032	Tir	34.260069	-105.801662	K-feldspar	28.78	±	0.02	Wt. Mean	7.13	15 of 19	Elevated MSWD indicates some excess scatter
Gal1180	Tir	34.247009	-105.787986	K-feldspar	28.81	±	0.02	Wt. Mean	1.74	11 of 20	Some scatter to older ages
Gal464	Tisa	34.230713	-105.75347	K-feldspar	28.81	±	0.02	Wt. Mean	1.01	11 of 20	Some scatter to older ages
Gal575	Richterite vein	34.229597	-105.752487	Richterite	28.96	±	0.10	Plateau	0.55	3 of 12	Possible excess ^{40}Ar in initial steps
Gal31	Tia	34.220231	-105.758425	Hornblende	29.39	±	0.49	Fixed Plateau	6.64	5 of 10	
Gal1182	Tim	34.15515	-105.763115	Biotite	29.96	±	0.09	Inverse Isochron	5.17	7 of 10	$^{40}Ar/^{36}Ar$ intercept of 322 ± 8; contains excess ^{40}Ar
Gal1017	Tscm	34.27415	-105.72598	Hornblende	38.16	±	0.18	Inverse Isochron	9.49	7 of 13	$^{40}Ar/^{36}Ar$ intercept of 535 ± 12; contains excess ^{40}Ar
Gal1017	Tscm	34.27415	-105.72598	K-feldspar	38.44	±	0.31	Wt. Mean	0.22	4 of 37	Youngest population of fusion steps

$^{40}Ar/^{39}Ar$ dating of K-feldspar

K-feldspar analyses yield the highest precision ages for this study (Fig. 105). Ages were determined by calculating a weighted mean of fusion-steps from incremental heating experiments of single crystals. Low-wattage steps typically yield younger ages compared to the distribution of the fusion steps. These initial steps are interpreted to reflect degassing of sites that have experienced ^{40}Ar loss within the feldspar, likely related to the pervasive alteration in the region. In some cases, initial ages are older than the fusion steps indicating excess ^{40}Ar. Ages of initial steps in the incremental heating experiments were not used in the age calculations. Two K-feldspar analyses for the Gallinas Peak intrusive rhyolite yield weighted mean ages of 28.78 ± 0.02 Ma (Gal1032) and 28.81 ± 0.02 Ma (Gal1180). K-feldspar from a syenite sample yields an indistinguishable age of 28.81 ± 0.02 Ma (Gal464). For these three samples, fusion step analyses

with low radiogenic yields, or that scatter to older or younger ages, were omitted from the age calculation. After omitting outlier analyses, MSWD (mean square weighted deviation) values for Gal1180 and Gal464 are approximately 1, indicating a single distribution. The MSWD value for Gal1032 is 7.13, indicating a slightly scattered distribution.

A robust age for K-feldspar in the syenite of Cougar Mountain was not obtained. Fusion steps for 37 single-crystals of feldspar range from ~38 to 64 Ma. Step-heat experiments show a consistent pattern of old initial ages (e.g., > 100 Ma) that decrease during the analysis. Inverse isochron regression have $^{40}Ar/^{36}Ar$ intercepts greater than atmospheric air (295.5; Neir, 1950) indicating excess ^{40}Ar. The youngest population of fusion steps (n=4) yield a weighted mean age of 38.44 ± 0.31 Ma, interpreted to represent a maximum age because of the potential for incomplete degassing of sites with excess ^{40}Ar prior to fusion.

$^{40}Ar/^{39}Ar$ dating of amphibole, biotite, and groundmass

Bulk step-heating of amphibole (n = 4), biotite (n = 2), and groundmass (n = 1) typically provide less precise, but equally important temporal constraints for magmatism exposed in the Gallinas Mountains. Similar to feldspar analyses, dating of these mafic phases display a variety of complexity. Three samples, Gal3029 (hbl), Gal575 (hbl), and Gal1182 (bt) yield a plateau, defined as three or more contiguous steps with ages that are indistinguishable at 2-sigma and compose more than 50% of the gas released (Fleck et al., 1977). Two samples, Gal1148 (bt) and Gal31(hbl) yield an Ar-release profile that did not meet the plateau criteria. For these two samples, a plateau was calculated (i.e., a fixed plateau) even though MSWD values indicated excess scatter. Plateau and fixed plateau ages range from 28.76 ± 0.19 to 30.22 ± 0.02 Ma. All mafic step-heat analyses were plotted on an inverse isochron to evaluate the trapped $^{40}Ar/^{36}Ar$ component. All samples have atmospheric intercepts with the exception of biotite from Gal1182 ($^{40}Ar/^{36}Ar$ intercept = 322 ± 8). For this sample, the inverse isochron of 29.96 ± 0.09 Ma is preferred compared to the older plateau age of 30.22 ± 0.02 Ma. Radiogenic yields are variable from < 20% to >99%. K/Ca values for biotite are ~10, whereas those from amphibole are ~0.1 to 1.0.

One amphibole and the only groundmass concentrate dated in this study yield highly discordant spectra and extraction of useful information from these analyses is difficult. Hornblende from the syenite of Cougar Mountain (Gal1017) yields a "saddle-shaped" spectrum (i.e., old, low-wattage steps that decrease in age during moderate wattages steps then increase in age during the highest-wattage steps typical of excess ^{40}Ar (Kelley, 2002). After removing outliers on the inverse isochron regression, seven steps yield an age of 38.16 ± 0.18 Ma and a $^{40}Ar/^{36}Ar$ intercept of 535.0 ± 11.9 indicating excess ^{40}Ar. Although the MSWD for this sample is 9.49 indicating excess scatter, the age and $^{40}Ar/^{36}Ar$ intercept are relatively insensitive to which points are included in the regression. This age is indistinguishable at 2σ error to the 38.44 ± 0.31 Ma K-feldspar from the same sample. The groundmass concentrate of an andesite sill (Gal628) also yields a discordant spectrum. The near uniform radiogenic yield of the steps for this analysis produces a "cloud" of points on the inverse isochron, and thus no reliable regression can be fit to the data. If discordance is related to ^{39}Ar recoil, the integrated age of 24.41 ± 0.02 Ma is preferred but is not considered extremely robust. Furthermore, given the presence of alteration throughout the region, the integrated age of this andesite sill is probably best considered a minimum age.

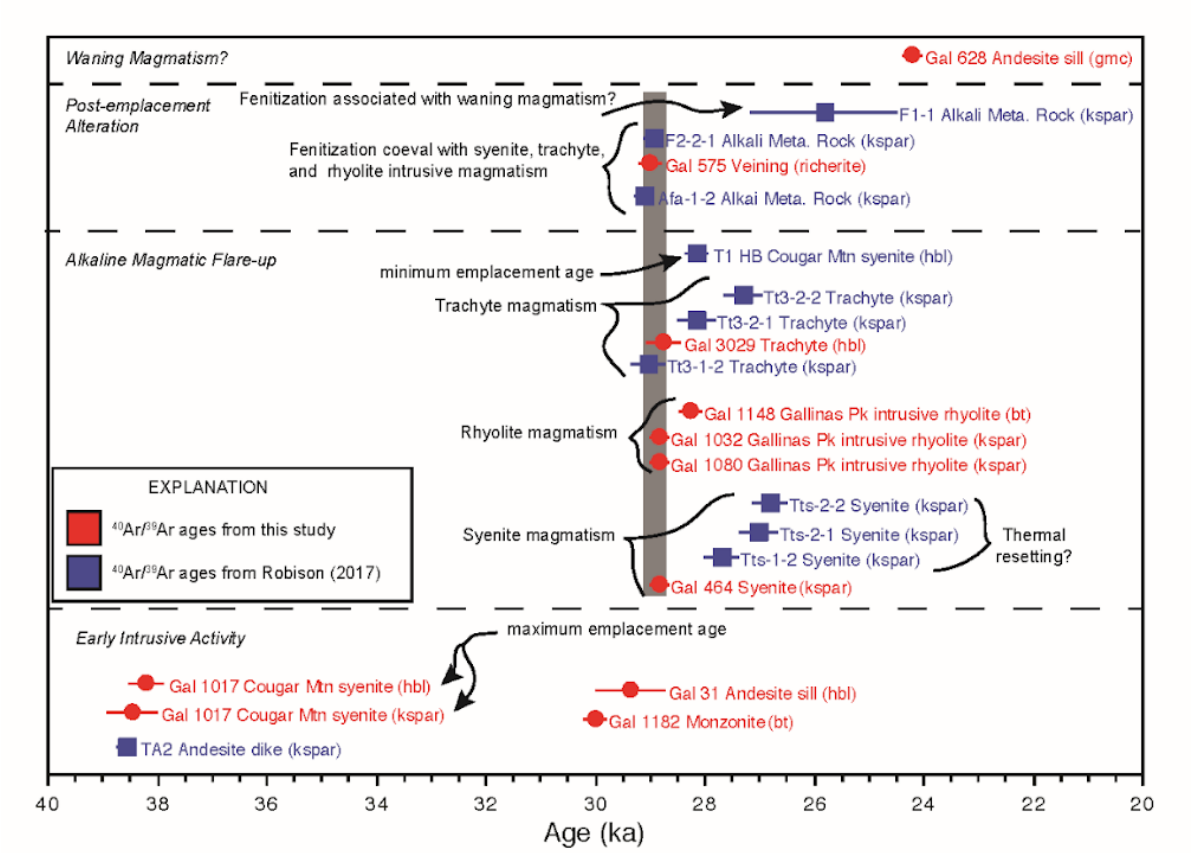

FIGURE 105. Summary of new (red) and published (blue; from Robison 2017) $^{40}Ar/^{39}Ar$ ages. Ages reported with 2 sigma errors. Mineral phases dated are indicated in parentheses. Vertical gray bar highlights the numerous, statistically indistinguishable ages at ~28.8 that suggest a brief period of intrusive activity and related alteration. Younger ages for syenite, rhyolite, and trachyte magmatism could be related to additional intrusive events, slow cooling, or thermal resetting.

ENVIRONMENTAL GEOCHEMISTRY

Acid rock drainage (ARD) is formed when sulfide minerals are exposed to oxidizing conditions such as weathering. Field characteristics of potential ARD in mine waste rock piles include identification of pyrite and/or jarosite and low pH. The rate of sulfide oxidation depends on reactive surface area of sulfide, oxygen concentration and solution pH. ARD can be determined by Acid Base Accounting (ABA) and Net Acid Generation (NAG) tests. The ABA procedure consists of two separate tests; the acid potential (AP) test and the neutralization potential (NP) test. ABA was calculated and plotted (Sobeck et al., 1978) on the ARD classification plot for waste rock pile samples from the various mines. Results of ABA tests are presented in Figure 106 and Table 22. The assumption is that all C in the samples are $CaCO_3$ (no organic carbon) and also the NAG pH equals the measured soil paste pH of the sample. Below are the formula used:

AP (kg $CaCO_3$/tonnes) = 31.25 x S (%)
NP (total C) = 83.3 x C (%)
NNP (net neutralization potential) = NP – AP
NPR (neutralisation potential ratio) = NP/AP.

Most rock samples from mine waste rock piles collected in the Gallinas Mountains exhibit iron-oxide alteration, mostly as pyrite replacements by hematite. Average pH values of the mine rock piles range between 5.85 and 9.3 (Table 22). The pH results indicate moderately alkaline to slightly acidic waste rock piles, making it unlikely that any of the rock piles in the Gallinas Mountains contain acid-generating material.

TABLE 22. Acid-rock chemical criteria for composite samples from Gallinas Mountains rock piles. Definition of parameters are above. Full chemical analyses of samples are in Appendix 3.

Sample	Mine Name	S%	C%	AP (Kg CaCO3)	NP (total C)	NNP	NPR	NAGpH
Gal51	Eagle Nest	0.78	0.18	24.375	14.994	-9.381	0.615	9.2
Gal5000	All American	0.13	2.26	4.0625	188.258	184.2	46.34	8.26
Gal5001	American	0.02	0.22	0.625	18.326	17.7	29.32	8
Gal5002	Red Cloud copper	0.19	1.04	5.9375	86.632	80.69	14.59	5.85
Gal5003	Big Ben	0.2	1.7	6.25	141.61	135.4	22.66	9.3
Gal5004	Sky High	0.01	0.6	0.3125	49.98	49.67	159.9	8.11

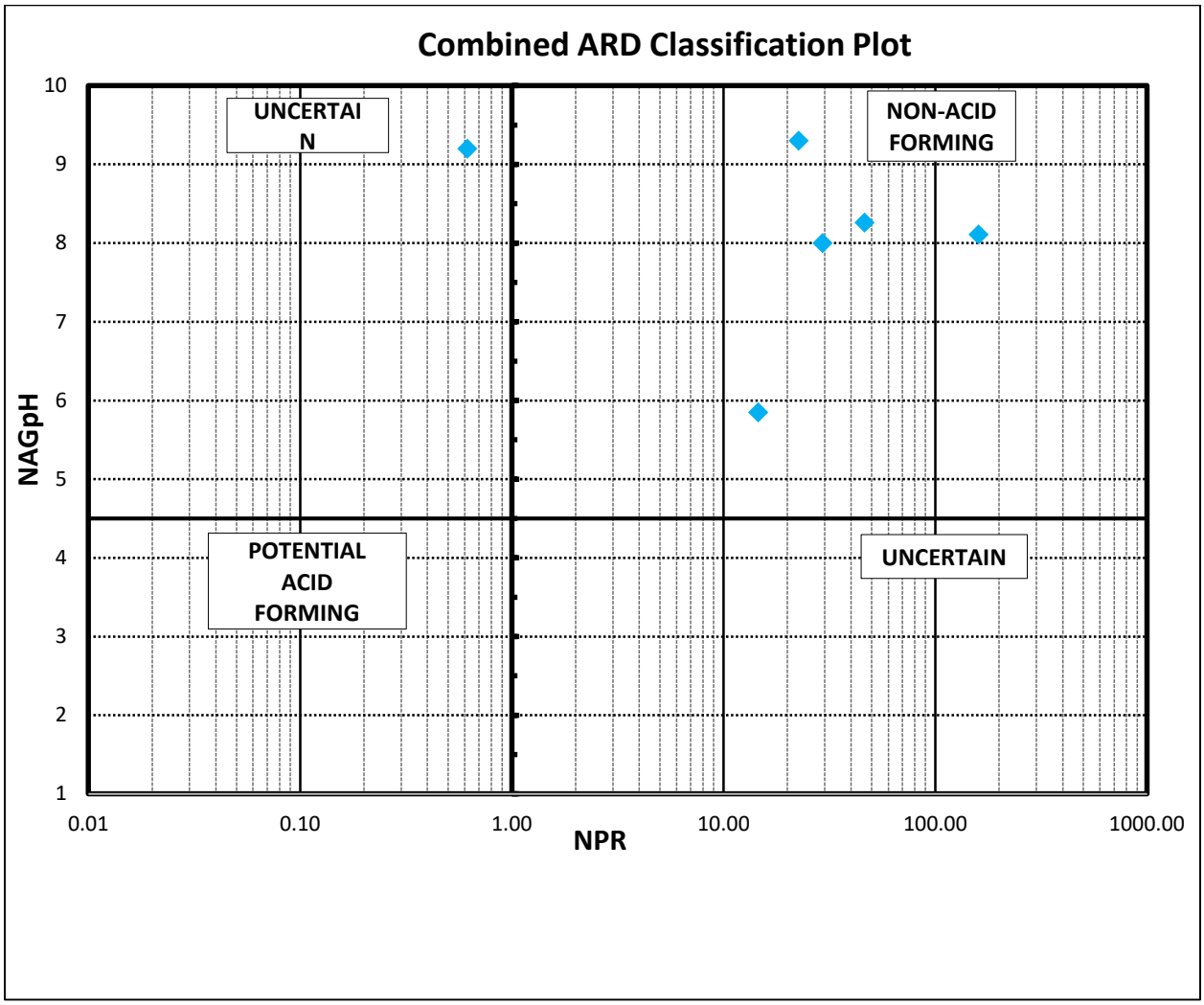

FIGURE 106. Acid Rock Drainage (ARD) plot of waste rock pile at mines.

DISCUSSION

Petrochemistry of the igneous rocks

Gallinas igneous rocks are metaluminous to peraluminous (alumina saturation; Barton and Young, 2002; Frost et al., 2001), alkaline (Na_2O+K_2O vs SiO_2, Irvine and Baragar, 1971) and have chemical compositions similar to A-type granites (A and I-S-M-type Granite Differentiation, Whalen et al., 1987). The identification of A-type granites is based upon both tectonic setting and chemical characteristics. A-type (anorogenic or anhydrous) granites typically are found along rift zones and within stable continental blocks. Many types of ore deposits in the world are associated with A-type granites (Lindgren, 1933; Mutschler et al., 1985, 1991; McLemore, 1996). The trachytes, syenites, rhyolites, and andesites plot as within-plate granites of Pearce et al. (1984; WPG, Fig. 107), whereas the Cougar Mountain syenites plot as volcanic-arc granites (VAG, Fig. 107). These trends may indicate differences in magmatic fractionation or even be related to magma mixing, as evidenced by field textures. The igneous rocks exhibit typical light rare earth elements (REE)-enriched chondrite-normalized REE patterns of alkaline rocks with no Eu anomaly (Fig. 52). The Eu anomaly is where Eu concentration is enriched or depleted relative to a chondrite. A Eu negative anomaly on a chondrite-normalized plot indicates that fractionation of plagioclase is important. The absence of a Eu anomaly indicates no plagioclase fractionation. On a Eu/Eu* vs La/Gd plot (Fig. 108), the igneous rocks from the Gallinas Mountains partially overlap the carbonatite field (Castor and Hedrick, 2006).

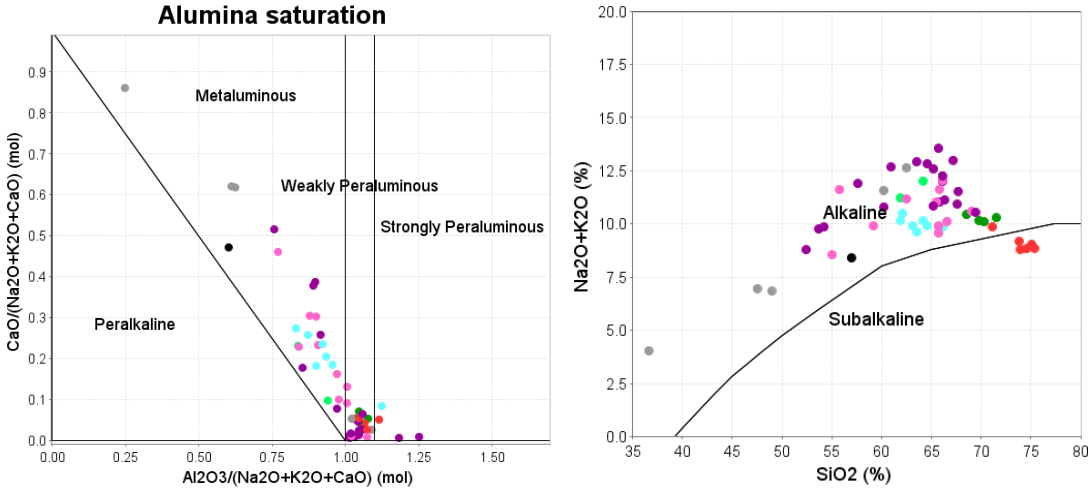

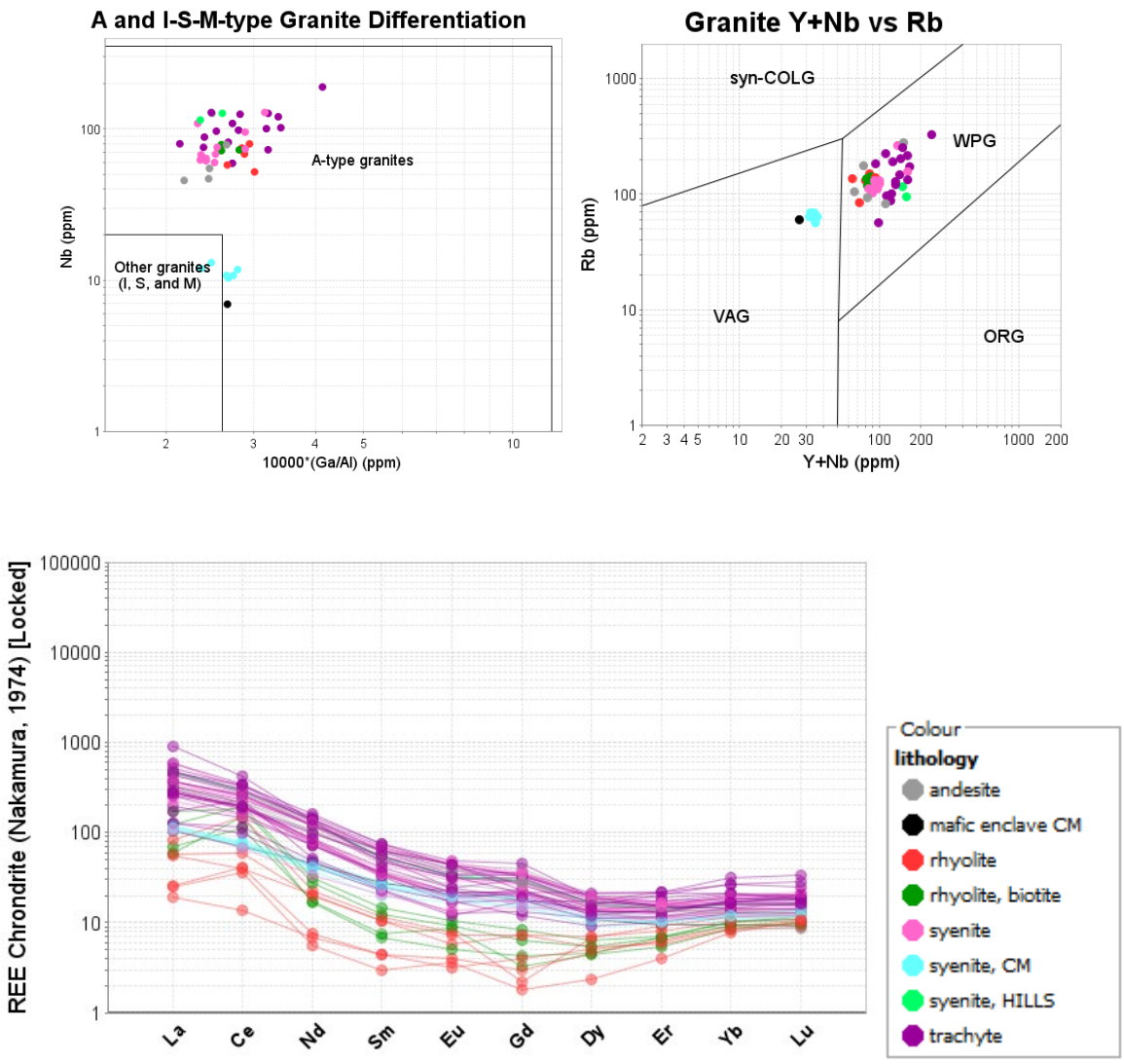

FIGURE 107. Chemical plots of igneous rocks from the Gallinas Mountains. Gallinas igneous rocks are metaluminous to peraluminous (alumina saturation; Barton and Young, 2002; Frost, 2008), alkaline (Na_2O+K_2O vs SiO_2, Irvine and Baragar, 1971) and have chemical compositions similar to A-type granites (A and I-S-M-type Granite Differentiation, Whalen et al., 1987). On the Granite Y+Nb vs Rb plot, the trachytes, syenites, rhyolites, and andesites plot as within-plate granites (WPG) of Pearce et al. (1984), whereas the Cougar Mountain syenites plot as volcanic-arc granites (VAG). The igneous rocks exhibit typical light rare earth elements (REE)-enriched chondrite-normalized REE patterns of alkaline rocks with no Eu anomaly.

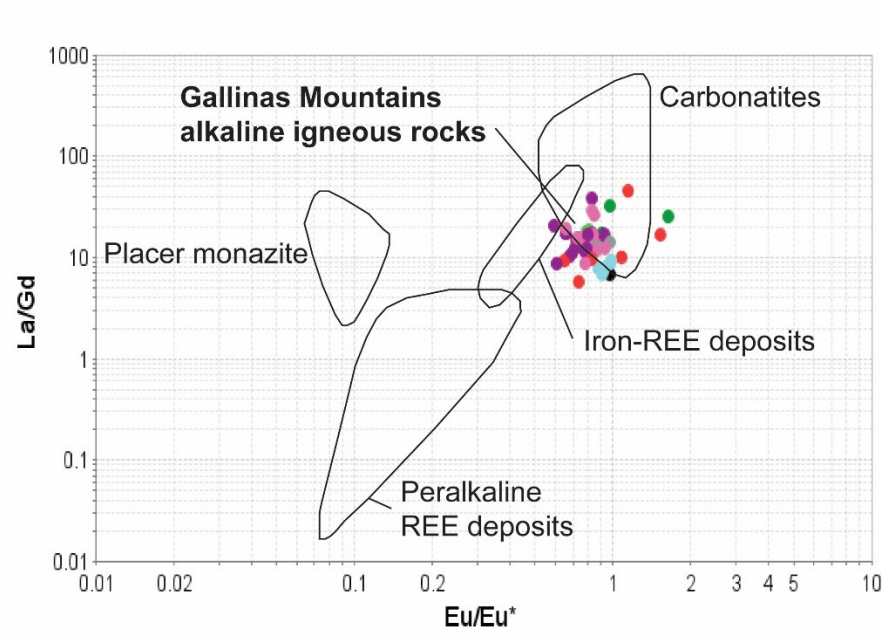

FIGURE 108. On a Eu/Eu* vs La/Gd plot; the igneous rocks from the Gallinas Mountains partially overlap the carbonatite field (Castor and Hedrick, 2006).

Regional geochemistry and geochronology

Mineral and chemical compositions, along with $^{40}Ar/^{39}Ar$ ages, of igneous rocks in areas surrounding the Gallinas Mountains were obtained from numerous reports as cited, unpublished data by the authors, and analyses of samples collected and analyzed for this study (Appendix 4). This data is briefly discussed to provide comparison to new data from Gallinas Mountains samples.

Comparison to intrusions in central New Mexico

Samples were collected from mafic to intermediate dikes from throughout Chupadera Mesa, west of the Gallinas Mountains (Fig. 3), including the Jones Camp district (Gibbons, 1981) and Sierra Larga intrusion (Chamberlin, 2009). The published $^{40}Ar/^{39}Ar$ age Jones Camp dike (MDS-49) is 29.07 ± 0.22 Ma and 28.58 ± 0.60 Ma for a dike (MDS-47) near Bingham (Chamberlin et al., 2009; ages recalculated relative to the interlaboratory FC-2 standard equal to 28.201 Ma; Kuiper et al., 2008). Samples collected from Chupadera Mesa were too altered for dating. These ages are similar to the beginning of the alkaline flare-up in the Gallinas Mountains (Fig. 109, Table 20, 21) and suggest a temporal relationship of regional magmatism.

Samples for dating were collected from Lone Mountain and Baxter Mountain in the White Oaks district, located ~55 km south of the Gallinas Mountains, part of the LCPB (Fig. 3). Three samples from the Lone Mountain pluton (LM6, LM8, LM10) yield $^{40}Ar/^{39}Ar$ ages of 35.28 ± 0.19 Ma, 35.07 ± 0.03 Ma, and 34.54 ± 0.08 (Appendix 8). A sample collected from Baxter Mountain (C-342) was dated using an older generation MAP 215-50 mass spectrometer at NMGRL in 2011 and yields a similar age of 34.75 ± 0.18 Ma. These ages represent a pulse of magmatism not recorded in the Gallinas Mountains, supporting a model for temporal and spatial variable magmatism in the LCPB (Appendix 8).

The Chupadera Mesa samples were called diorite, diabase, and basaltic trachyandesite in the field, but plot as trachybasalt to basaltic-trachyandesite, and trachyte/trachydacite on a TAS diagram (Fig. 109). They are low in REE and exhibit a relatively flat chondrite-normalized REE pattern (Fig. 109). The Lone Mountain samples were called syenites in the field and plot as granite and quartz monzonite.

These rocks are metaluminous (alumina saturation; Barton and Young, 2002; Frost, 2008) and alkaline (Na_2O+K_2O vs SiO_2, Irvine and Baragar, 1971) (Fig. 109). Two samples from Chupadera Mesa and the Lone Mountain samples have chemical compositions similar to A-type granites; the other samples from the Chupadera Mesa area are I and S type granites (A and I-S-M-type Granite Differentiation, Whalen et al., 1987). On the Granite Y+Nb vs Rb plot, the Lone Mountain samples and two samples from Chupadera Mesa plot as within-plate granites (WPG) of Pearce et al. (1984), whereas the other samples plot on the line as WPG and volcanic-arc granites (VAG). The igneous rocks exhibit typical light rare earth elements (REE)-enriched chondrite-normalized REE patterns of alkaline rocks; the Lone Mountain samples have a Eu anomaly. Chemical data are in Appendix 3.

Summary

Gallinas Mountains lie in between the Chupadera Mesa area to the west and the Lone Mountain area to the east. The igneous rocks from the Gallinas Mountains are similar in some chemical aspects to both areas, and differ in other chemical aspects. These results support earlier conclusions that the North American Cordilleran belt, including the LCPB is a complex region of highly fractionated and differentiated magmas. More analysis is underway.

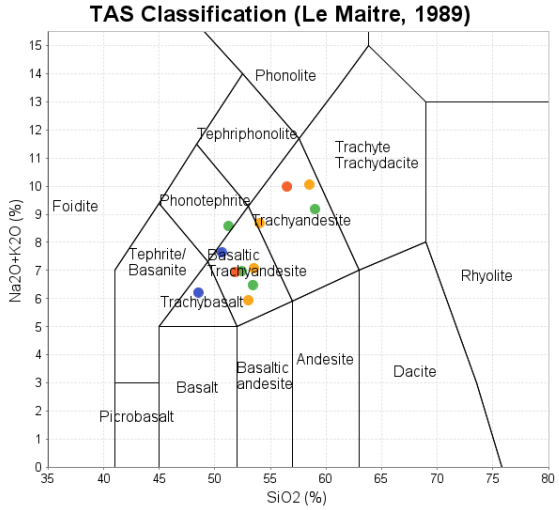

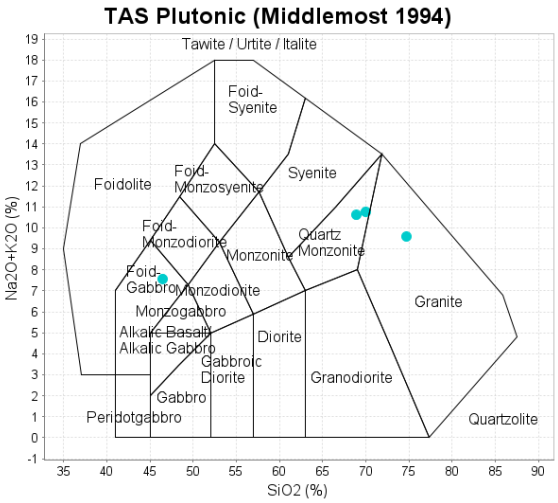

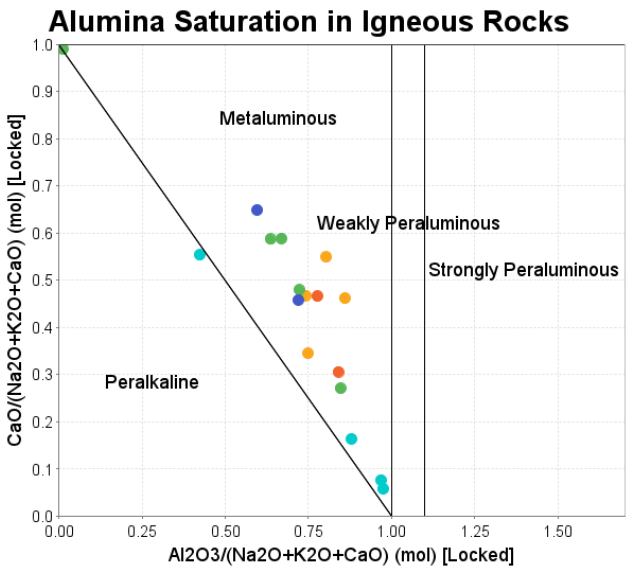
Alumina Saturation in Igneous Rocks
Metaluminous
Weakly Peraluminous
Strongly Peraluminous
Peralkaline
CaO/(Na2O+K2O+CaO) (mol) [Locked]
Al2O3/(Na2O+K2O+CaO) (mol) [Locked]

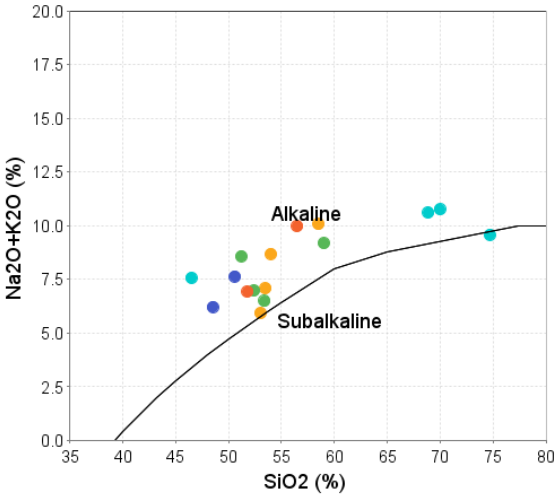
Alkaline
Subalkaline
Na2O+K2O (%)
SiO2 (%)

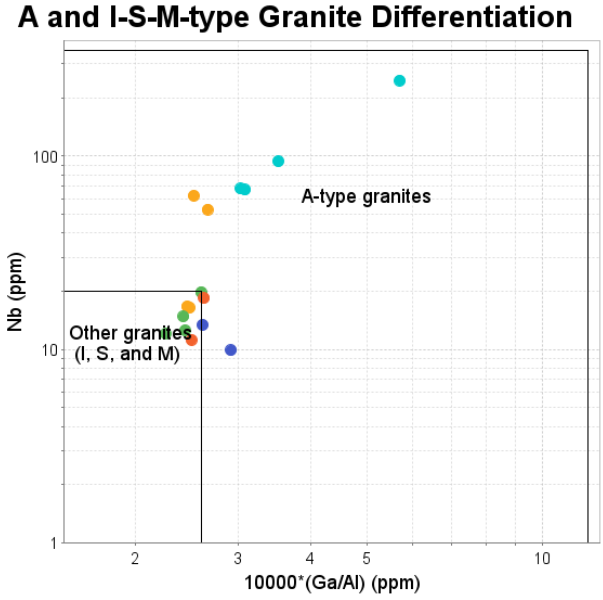
A and I-S-M-type Granite Differentiation
A-type granites
Other granites
(I, S, and M)
Nb (ppm)
10000*(Ga/Al) (ppm)

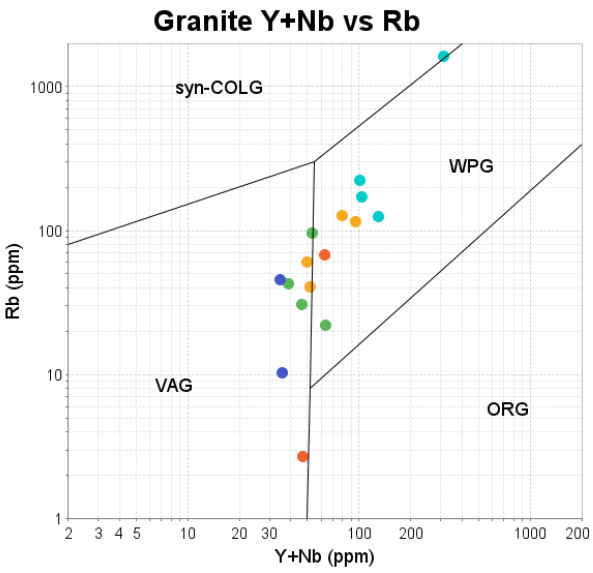
Granite Y+Nb vs Rb
syn-COLG
WPG
VAG
ORG
Rb (ppm)
Y+Nb (ppm)

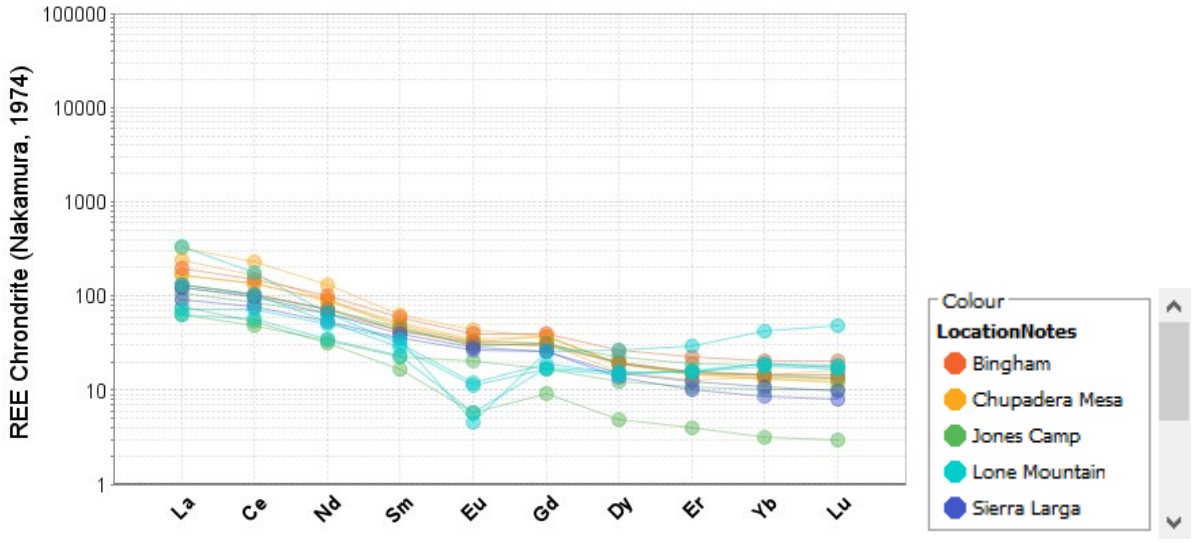

FIGURE 109. Chemical plots of selected igneous rocks from Chupadera Mesa and Lone Mountain in central New Mexico. TAS plot (Na_2O+K_2O vs SiO_2; Le Bas et al., 1986) showing rock classification. These rocks are metaluminous (alumina saturation; Barton and Young, 2002; Frost, 2008), alkaline (Na_2O+K_2O vs SiO_2, Irvine and Baragar, 1971). Two samples from Chupadera Mesa and the Lone Mountain samples have chemical compositions similar to A-type granites; the other samples from the Chupadera Mesa area are I and S type granites (A and I-S-M-type Granite Differentiation, Whalen et al., 1987). On the Granite Y+Nb vs Rb plot, the Lone Mountain samples and two samples from Chupadera Mesa plot as within-plate granites (WPG) of Pearce et al. (1984), whereas the other samples plot on the line as WPG and volcanic-arc granites (VAG). The igneous rocks exhibit typical light rare earth elements (REE)-enriched chondrite-normalized REE patterns of alkaline rocks; the Lone Mountain samples have a Eu anomaly. Chemical data are in Appendix 3.

Temporal Assessment of the Gallinas Mountains Magmatic System

In the absence of U/Pb ages of zircon and titanite, which are typically used to constrain intrusion emplacement (Coleman et al., 2016), $^{40}Ar/^{39}Ar$ ages are used to approximate the timing of magmatic activity for the region. However, the closure temperatures for ^{40}Ar diffusion in K-feldspar, biotite, and amphibole are 150–300°C, 300–350°C, and 500–550°C, respectively (McDougall and Harrison, 1999) — well below crystallization temperatures of ~700–900°C for silicic magmas (Miller et al., 2003). Thus, all $^{40}Ar/^{39}Ar$ ages are considered minimum emplacement ages because slow cooling from magmatic temperatures and reheating events cannot be fully disregarded.

New $^{40}Ar/^{39}Ar$ ages, combined with published $^{40}Ar/^{39}Ar$ ages (Table 20; Robison, 2017) temporarily constrain the lifespan of the Gallinas Mountains magmatism and mineralization. In general, magmatism in the region is divided into two periods: (1) sparse, dominantly mafic, early magmatism from 38.5 to 29.3 Ma and (2) a brief, dominantly silicic, and volumetrically significant pulse at 28.8 Ma that may have extended to 27.0 Ma. Events as young as 26 to 24 Ma are also possible, but are poorly dated. Furthermore, much of the alteration is contemporaneous with syenite, trachyte, and rhyolite magmatism.

Early intrusive activity (38.5 to 29.3 Ma)

The earliest magmatic activity in the Gallinas Mountains includes the emplacement of andesite dikes and a small monzonite plug. The oldest, robust age for rocks of the Gallinas Mountains is an andesite dike (Perhac, 1970) dated at 38.52 ± 0.05 Ma (Robison, 2017) found near the center of the magmatic complex. A nearby andesite sill yields an age of 29.34 ± 0.49 Ma, indicating at least two pulses of early andesitic magmatism. A previously undated pyroxene- and biotite-rich monzonite (unit Tim) located south-southwest of the main mapping area, mapped first by Kelley (1972), yields a biotite age of 29.69 ±0.09 Ma. This age is within error of the younger andesite dike and may suggest a pulse of ~29 Ma magmatism that is poorly exposed within the Gallinas Mountains.

An alkaline intrusive flare-up (28.8 to 28.0 Ma)

The majority of the intrusive rocks exposed in the Gallinas Mountain were emplaced between ~29.0 and 27.0 Ma, the majority of which were during an abbreviated period of activity at approximately 28.8 Ma. K-feldspar from a syenite in the southern Gallinas Mountains dated in this study yields an age of 28.81 ± 0.02 Ma. In contrast, K-feldspar from syenites dated by Robinson (2017) yield ages ranging from 27.68 ± 0.17 Ma to 26.79 ± 0.18, or nearly 1 to 2 Ma younger than the new $^{40}Ar/^{39}Ar$ ages of this study. The difference in age indicates (1) multiple pulses of syenite magmatism, (2) differential cooling of a single intrusion, or (3) reheating by young, non-exposed ~27 Ma intrusions. Alternatively, the younger, irreproducible ages of Robinson (2017) may reflect dating altered grains that have variably lost ^{40}Ar.

Three new ages were determined for the previously undated intrusive rhyolite of Gallinas Peak. Two K-feldspar analyses yield indistinguishable ages of 28.81 ± 0.02 and 28.78 ± 0.02 Ma. Biotite within a newly discovered biotite-bearing phase of the intrusive rhyolite, located North of Gallinas Peak, yields a slightly younger age of 28.22 ± 0.08 Ma. However, the plateau for the biotite is located along a rising spectrum, possibly indicating ^{40}Ar loss, in which case this age is considered a minimum age rather than a distinctively younger event. Thus, the K-feldspar ages are interpreted as the best constraint for the emplacement age. Furthermore, the fine-grained texture of the intrusion rhyolite suggests rapid cooling from magmatic temperatures and slow cooling seems unlikely.

Timing of trachytic magmatism is coeval with syenite and rhyolite magmatism. A new hornblende age of a trachyte intrusion is 28.76 ± 0.19 Ma, which is statically indistinguishable from new K-feldspar ages for the syenite and rhyolite. Prior dating of three K-feldspar grains from a single sample yielded ages of 29.02 ± 0.16, 28.14 ± 0.20, and 27.98 Ma (Robison, 2017). The oldest trachyte age in Robison (2017) is statistically indistinguishable to the new age reported here; however, the irreproducibility of Robison (2017) is not understood at this time. The younger ~28 Ma ages of Robison could reflect slow cooling. If so, the 28.8 Ma hornblende age of this study is preferred because of its higher closure temperature compared to K-feldspar.

The emplacement age of the syenite of Cougar Mountain is poorly understood. Previous work by Robison (2017) suggests an emplacement age of 28.13 ± 0.05 Ma based on an inverse isochron for a hornblende analysis. In contrast, K-feldspar and hornblende in this study yield significantly older ages of 38.44 ± 0.31 (the youngest population of fusion ages from step-heat analyses of single grains) and 38.16 ± 0.18 Ma (a poorly fit isochron regression), respectively. As previously mentioned, the ~38 Ma K-feldspar and hornblende are complicated by the presence of excess ^{40}Ar and a conservative interpretation is that those ages are maximum

emplacement ages. However, the statistical agreement between the K-feldspar and hornblende ages provides some confidence that the Cougar Mountain syenite represent a distinctly older event. Likewise, ~38 Ma magmatism is found elsewhere in the Gallinas Mountains (TA2 - 38.52 ± 0.05 Ma; Robison, 2017). The new ages of the Cougar Mountain syenite are from a sample collected along the northern parts of the intrusion, whereas those of Robison (2017) are from the southern exposures. Therefore, there exists the possibility for two different events. However, that is hard to reconcile with field observations that do not indicate contacts between the two units as well as a near identical mineralogy, chemistry (Fig. 21), and texture (Fig. 18, 19; coarse-grain, porphyritic K-feldspar and hornblende) between the two localities. Future work is necessary to resolve the significant age discrepancy between the two studies.

The age of alteration and fenitization association with intrusive magmatism

Several ages provide insight into the timing of alteration and mineralization in the Gallinas Mountains. Richterite, a sodium-rich amphibole, was discovered in association with syenite. The richterite may be genetically related to a skarn located 700 m to the west. Step-heating of the richterite yields an age 28.96 ± 0.10 Ma. This age only slightly predates the high-precision K-feldspar ages (i.e., ~28.8) from the syenite and intrusive rhyolite and is indistinguishable to hornblende of the trachyte. Likewise, inverse isochron ages K-feldspar in alkali metasomatized rocks are 28.90 ± 0.05 Ma (sample F2-2-1) and 29.08 ± 0.04 Ma (sample Afa-1-2; Robison, 2017). Together, these ages support an interpretation that alteration and fenitization in the Gallinas Mountains is related to an abbreviated pulse of syenite, trachyte, and rhyolite magmatism.

Younger intrusions and fenitization? (25.8 to 24.4 Ma)

Intrusive activity and related alkali metasomatism may have continued following the preceding pulse of alkaline magmatic activity. Robison (2017) reports an inverse isochron age of 25.8 ± 1.3 Ma for K-feldspar (sample F1-1) in an alkali metasomatized rock. Although no intrusive activity of this age has been identified in the Gallinas Mountains, younger intrusions that produced fenitizing fluids were possibly emplaced at a deeper crustal level than is currently exposed. A poorly dated andesite sill with an integrated age of 24.41 ± 0.02 Ma may suggest an even younger magmatic event. However, given the complicated spectrum and likelihood for alteration, a ~24.4 Ma intrusive event is highly speculative.

District mineral zonation

McLemore (2010a) suggested a district mineral zonation based upon predominant mineralogy and chemistry of the known deposits at that time, especially the limited extent of copper-lead mineralization and the occurrence of Fe skarns surrounding the district. However, additional hydrothermal breccia and fissure veins were mapped and sampled during this project, demonstrating that REE mineralization is more extensive than previously thought. Mapping, cross-cutting relationships, mineralogy and chemistry of hydrothermal breccia, and vein deposits no longer supports a district mineral zonation.

Paragenesis of the mineral deposits

The paragenesis as determined from petrographic studies by Schreiner (1993), Williams-Jones et al. (2000) and field observations by the author is summarized in Figure 110. Additional studies are underway.

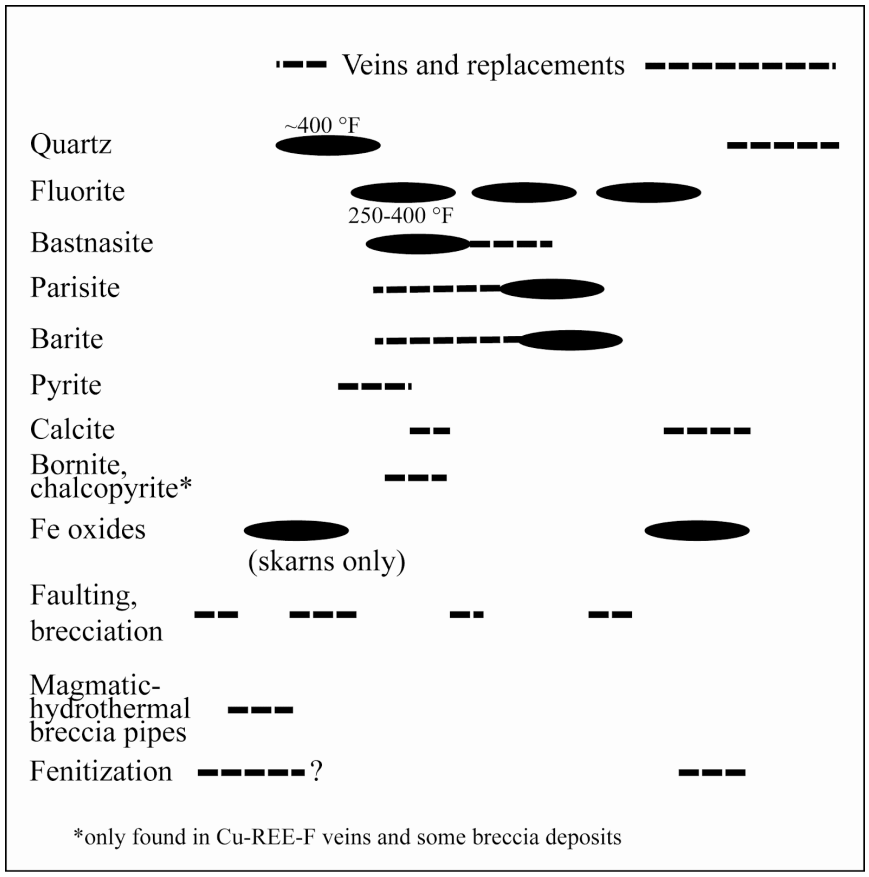

FIGURE 110. Simplified paragenesis of the REE deposits in the Gallinas Mountains (modified from Perhac, 1970, Schreiner, 1993, William-Jones et al., 2000, McLemore, 2010a). Temperature estimates are from Williams-Jones et al. (2000). The early events are to the left.

Source of the intrusions

Sr and Nd isotopes of igneous rocks

Although isotope studies were not employed in this study, previous Sr and Nd isotope results have been reported and provide some insights into the origin of the intrusions. Sr and Nd isotopes of igneous rocks associated with GPM districts in New Mexico are similar, and imply a lower to upper mantle homogeneous source (Table 23, McLemore, 2017). Geochemical analyses from this report are consistent with that previous conclusion for the Gallinas Mountains intrusions (Allen and Foord, 1991; this report). Nd isotopes of GPM deposits (epsilon Nd of −0.3 to −5.5, Table 23) are higher than those of igneous intrusions associated with the Colorado Mineral Belt, where a crustal source is envisioned (epsilon Nd of −7 to −9) (Stein et al., 1990; Anthony, 2005), which is also consistent with a lower to upper mantle, homogeneous source.

TABLE 23. Compilation of Sr and Nd isotopes of some GPM deposits in New Mexico (McLemore, 2017). See McLemore (2017) for reference of the age of the igneous systems. Age of Gallinas Mountains from this report. See Figure 2 for locations of areas. The isotope values from the Gallinas Mountains are comparable to values from other GPM systems and imply a similar, lower to upper mantle, homogeneous source.

District ID	Name	Age	Sr Isotopes	Nd ($CHUR_t$)	Isotope Reference
DIS237	Questa	22–28	0.7076–0.7069		Laughlin et al. (1969)
DIS020	Laughlin Peak	22.8–32.3	0.7044, 0.7039–0.7060		Potter et al. (1991)
DIS019	Elizabethtown-Baldy	29.1	0.70617		Kish et al. (1990)
DIS092	Gallinas Mountains	28.8 to 28.0	0.7061	-2.8	Allen and Foord (1991)
DIS095	Nogal-Bonito	26–33	0.7067	-0.3	Allen and Foord (1991)
DIS091	Capitan Mountains	28.3	0.70801	-5	Allen and Foord (1991)
DIS216	Jones Camp	28.88	0.70715	-5.5	Allen and Foord (1991)
DIS098	Tecolote Iron		0.70490–0.70513		Allen and Foord (1991)
DIS030	Organ Mountains	26–36	0.7085 to 0.7060	-5	Verplank et al. (1995, 1999) Zimmerer and McIntosh (2013)
DIS099	White Oaks	31.7–34.7	0.70673	-3.7	Allen and Foord (1991)
DIS128	Cornudas Mountains	36.3	0.7041		Barker et al. (1977)
DIS093	Jicarilla	39.1–45.6	0.70565–0.70578	-4.8	Allen and Foord (1991)

Source of the mineralization

Stable isotopes and fluid inclusion studies

Although fluid inclusion and stable isotope studies were not employed in this study, previous results are reported. Fluid homogenization temperatures of previous studies indicate that quartz deposition was first (~400°C) followed by bastnäsite (~325°C) with low salinities (~15-19 wt% NaCl eq.; William-Jones et al., 2000; Vance, 2013). Stable isotope studies are consistent with a magmatic source of mineralizing fluids, specifically mixing of magmatic-hydrothermal fluids with formation waters derived from the Yeso Formation (Vance, 2013).

Trace-element compositions of fluorites from the Gallinas Mountains are characterized by relatively flat to LREE-enriched chondrite-normalized REE patterns, with no Eu anomaly (Fig. 111; Gagnon et al., 2003). The earliest generation of fluorite is similar to the composition of the trachyte and syenite. The fluorite samples plot in the hydrothermal and pegmatitic field according to the classification of Möller et al. (1976; Gagnon et al., 2003), which is consistent with a magmatic-hydrothermal origin.

Geochemical analyses, mineralogy, texture and field relationships from this report are consistent with previous conclusions from fluid inclusion and stable isotope studies that the hydrothermal breccia and fissure vein deposits are derived from magmatic-hydrothermal fluids from either a carbonatite or an alkaline magma (trachyte to syenite).

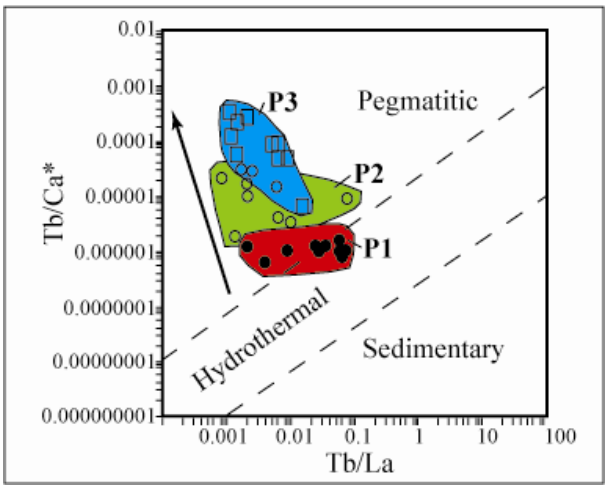

FIGURE 111. Log Tb/Ca verses log Tb/La plot of fluorite samples from the Gallinas Mountains (from Gagnon et al., 2003). Pegmatitic, hydrothermal, and sedimentary fields are from Möller et al. (1976). The arrow indicates the compositional trend from earliest (P1) to latest (P3). See Gagnon et al. (2003) for more detailed discussion.

A synopsis of geologic events in the Gallinas Mountains

The sequence of events in the Gallinas Mountains is summarized in Figure 112. Early igneous activity began approximately 38.5 to 29.3 Ma (Tables 20, 21; Fig. 105) with the emplacement of andesite dikes, a monzonite sill, and possibly the Cougar Mountain syenite. At least one Fe skarn deposit was formed at this time in association with the Cougar Mountain syenite.

The predominant alkaline magmatic flare-up occurred approximately 29 to 27 Ma. Most of the igneous activity occurred at ~28.8 Ma. During this period, syenite, rhyolite, and trachyte magmas were intruded as dikes, sills, stacked sills, and a laccolith. Rapakivi feldspar and magma mingling textures indicate multiple injections of different magma compositions during magma chamber evolution. The final intrusive event in the Gallinas Mountains appears to be a late waning period of magmatism and associated minor fenitization at ~25.8 to 24.4 Ma, although the ages are not robust. More work is needed to assess the termination of igneous activity.

Multiple episodes of alteration and mineralization characterize the Gallinas Mountain geologic history. Regional silicification of the sandstones and local brecciation adjacent to the trachytes, syenites, and magmatic intrusive breccia pipes occurred during or after intrusive activity. Regional heating from the intrusions dissolved silica and iron from the host sandstones. Hematization and sericitization (liesegang banding) of the sandstones and igneous laccoliths, dikes, and sills followed intrusive activity. Fenitization is associated with the intrusions occurring after emplacement of the intrusions, but before emplacement of Fe skarns and intrusion of the magmatic intrusive breccia pipes (29 to 27 Ma; Schreiner, 1993). Na fenitization is characterized by magmatic feldspars replaced by albite. Na fenitization was followed by K fenitization, characterized by replacement of altered albite by K-feldspar or growth of new K-feldspar and replacement by sericite.

The mineralization occurred in stages. Fe skarns (containing local F, REE, Cu, Pb, and S) and contact-metasomatic deposits (including Fe veins) formed during or after intrusions but before the hydrothermal breccia deposits as indicated by fragments of magnetite-hematite ore within the magmatic intrusive breccia pipes and some hydrothermal breccia deposits. Elevated

REE concentrations and other trace element chemistry suggest that the Fe skarns formed from similar fluids as the hydrothermal breccia and vein deposits (McLemore, 2010a). The hydrothermal breccia and fissure veins deposits are the predominant mineralizing event. Fluorite replacements and disseminations in the adjacent host rocks occurred along with the hydrothermal breccia and fissure veins deposits, after faulting and fenitization. Some of the hydrothermal fissure veins formed in recemented carbonate breccias. Hydrothermal breccias and veins also formed in a few of the magmatic intrusive breccia pipes. The origin of the hydrothermal fluids is uncertain but presumed to be the intrusions, although a concealed intrusion (carbonatite? younger alkaline intrusion?) could be the source.

At least three stages of faulting occurred after intrusive activity. Hydrothermal breccia and vein deposits formed along minor faults (short length) after the intrusion emplacement. Although Schreiner (1993) suggested that the faulting occurred before intrusion of the breccia pipes, our new mapping indicates that the Pride and Red Cloud Canyon faults displaced the Park pipe, and the breccia pipe north of the All American mine. Mineralization occurs along the Pride and Conqueror faults, although it is uncertain when these faults were mineralized. The Pride, Conqueror and Red Cloud Canyon faults clearly offset dikes, sills, and hydrothermal breccia and vein deposits, indicating faulting continued after hydrothermal activity. Tectonic breccias along the Red Cloud and South Largo Canyon faults contain sandstone, Proterozoic granite, trachyte, and syenite rock fragments that are cut by calcite veins, also indicating a younger age. Hydrothermal breccia and fissure veins deposits display hypogene oxidation. Carbonatization occurred late during the emplacement of the hydrothermal breccia and fissure veins, as indicated by calcite replacement and overgrowths on fluorite, barite, quartz, and fenite feldspar (Schreiner, 1993). Late quartz deposition occurred in vugs and along fractures in the hydrothermal breccia and fissure vein deposits. Supergene oxidation followed. Dissolution and brecciation of gypsum and limestone occurred, followed by recrystallization and cementation by calcite to form carbonate breccias and veins (high REE and low REE).

Younger dissolution, brecciation of limestone, followed by recrystallization and cementation by calcite to form low REE travertines (i.e. spring deposits?), overprinting the carbonate breccias, occurred possibly during the Late Wisconsinan, when the periglacial mass movement deposits (i.e. rock glaciers) formed (Blagbrough, 2005).

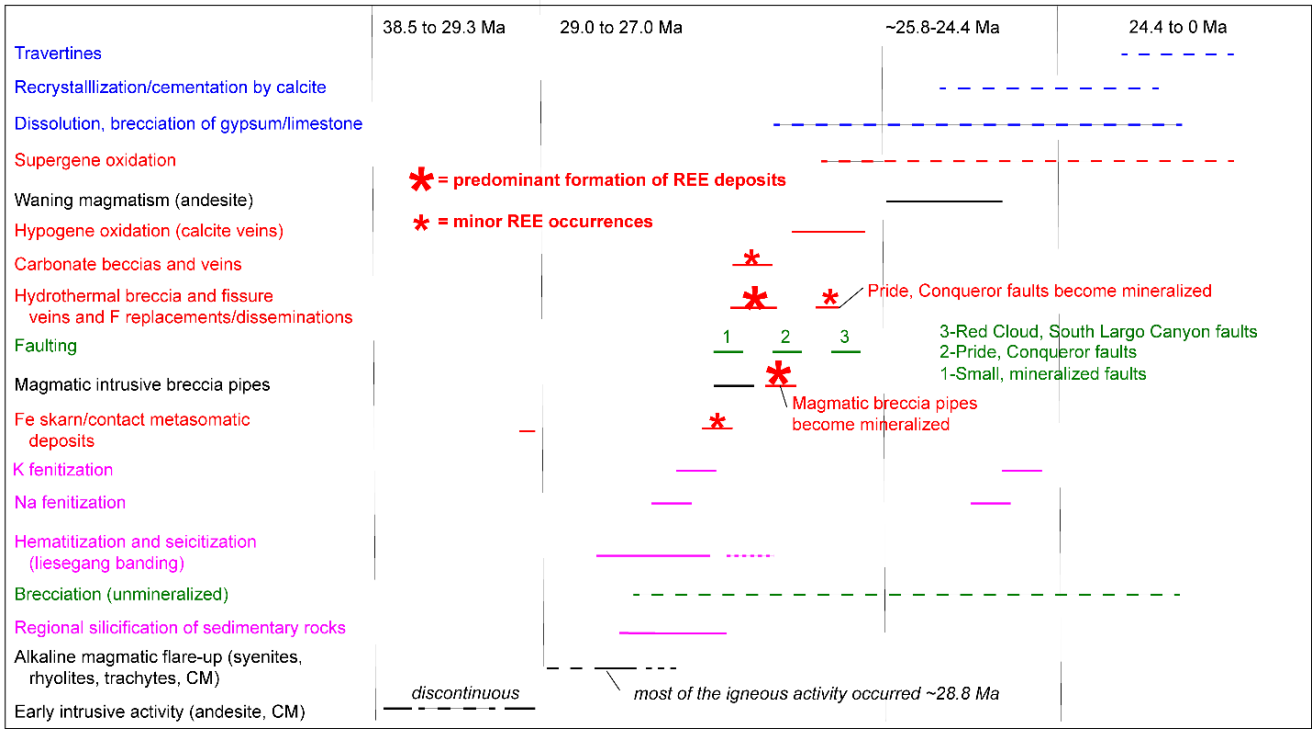

FIGURE 112. Sequence of events in the Gallinas Mountains. See discussion for details. Black=magmatic events, red=mineralizing events, green=faulting, purple=alteration, and blue=dissolution and recrystallization.

Are there carbonatites in the Gallinas Mountains?

Carbonatites are carbonate-rich igneous rocks containing more than 50% primary magmatic carbonate minerals (typically as calcite, dolomite, and ankerite) and less than 20% silica (Le Bas, 1987; Le Maitre, 1989; Verplanck et al., 2014; van Gosen et al., 2019). Many carbonatite intrusions are found in continental shields and continental rift environments within zoned intrusive complexes consisting of alkaline igneous and/or carbonatite stocks, ring dikes, and cone sheets. Carbonatites are quite diverse and are likely derived from multiple magmatic processes (Verplanck et al., 2014). Carbonatites typically contain REE, U, Th, Nb, Ta, Zr, Hf, Fe, Ti, V, Cu, Ba, P, magnetite, and vermiculite (Berger et al., 2009). Fenitization is the predominant alteration associated with carbonatites. However, not all fenitization is associated with carbonatites and also can be associated with alkaline igneous rocks. Carbonatites with bastnäsite and the weathered products of carbonatites are predominant sources of REE production in the world today (Verplanck et al., 2014; van Gosen et al., 2019). Carbonatites are rare in the southern portion of the North American-Cordilleran alkaline igneous belt and found only at Laughlin Peak, New Mexico and Villa Ahumada, Chihuahua Mexico (McLemore, 2017).

There are no carbonatites exposed in the Gallinas Mountains. However, carbonatites are hypothesized to be at depth by the presence of Na and K fenitization (Schreiner, 1993), carbonate breccias and carbonatization of the hydrothermal breccia and fissure vein deposits, presence of bastnäsite (REE) in veins, fluorite mineral chemistry (Fig. 111; Gagnon et al., 2003), geophysical anomalies (Fig. 8; McLemore, 2010a; Li, 2017), fluid inclusion and stable isotope studies (Vance, 2013), geochemistry of igneous rocks and hydrothermal breccia and fissure vein

deposits (Fig. 72, 108), and similarity of the intrusive rocks, alteration, and mineralization to areas with known carbonatites. Drilling is ultimately required to determine if carbonatites are present beneath the Gallinas Mountains.

Mineral-Resource Potential

In general, most exposed outcrops of hydrothermal breccias and fissure veins in the Gallinas Mountains appear small, although samples as high as 8% total REE are found in some hydrothermal breccias, fissure veins, and magmatic intrusive breccia pipes. The hydrothermal breccia and vein deposits in the Gallinas Mountains are too low grade to be economic for Au, U, Th, and Nb in today's market. Further drilling and subsurface sampling is suggested at the Pride vein, M and E breccia pipe, Red Cloud-Deadwood copper veins, Rio Tinto vein, Sky High-Big Ben veins, veins along the road to Rough Mountain, and Park magmatic intrusive breccia pipe to determine the mineral-resource potential in the area.

In 1991-1992, USBM calculated an inferred resource of 537,000 short tons with a grade of 2.95% total REE (not NI 43-101 compliant; Schreiner, 1993). An unclassified resource of 46,000 metric tonnes of 2.96% (1,400 tonnes TREO) was published by Jackson and Christainsen (1993). A grade-tonnage graph showing where Gallinas Mountains plots is in Figure 113.

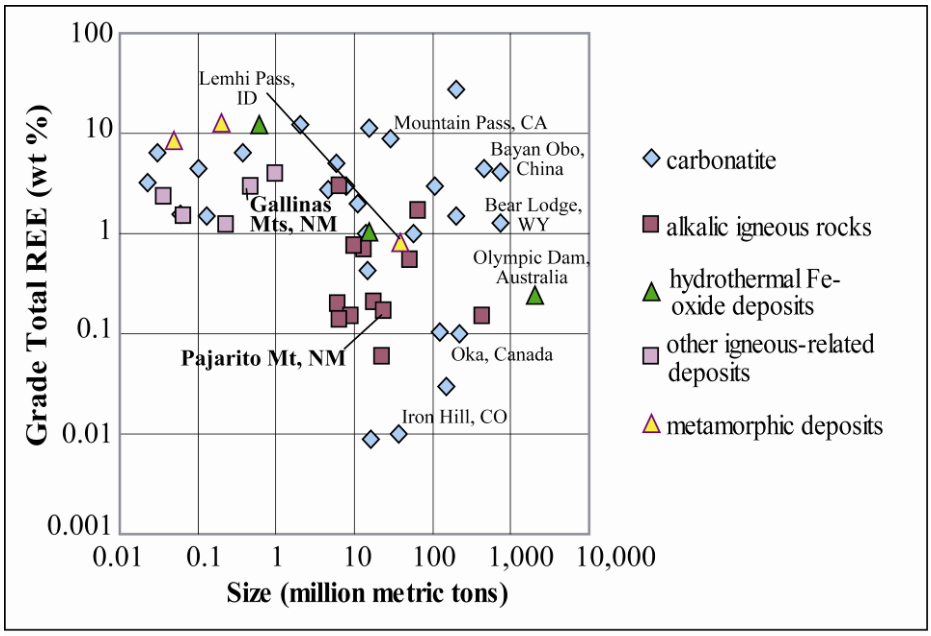

FIGURE 113. Grade and size (tonnage) of selected REE deposits, using data from Oris and Grauch (2002) and resources data from Schreiner (1993) and Jackson and Christiansen (1993) for the Gallinas Mountains. Deposits in bold are located in New Mexico. Further exploration could identify additional resources in most of these areas.

Comparison of the mineral deposits in the Gallinas Mountains to other REE deposits in New Mexico and elsewhere

REE occurrences are common in the North American-Cordilleran alkaline igneous belt (McLemore, 2018). Carbonatite dikes are found in the Laughlin Peak area in northern New Mexico (Fig. 2), where bastnäsite and florencite are the predominant REE minerals. Allanite is the predominant REE mineral in the Capitan Mountains (McLemore and Phillips, 1991;

Campbell et al., 1995). Eudialyte is the predominant REE mineral in the Cornudas Mountains (McLemore et al., 1996). At Round Top Mountain, Sierra Blanca, Texas, the predominant REE minerals are bastnäsite, xenotime, and fluocerite (Pingitore et al., 2014; Elliott et al., 2017). Carbonatites are found at Villa Ahumada, Chihuahua, Mexico (Nandigam, 2000), but the REE mineralogy is not known. These occurrences reflect the complex magmatic and resulting hydrothermal activity in the north American cordilleran belt.

CONCLUSIONS

1. Five types of mineral deposits are present. Economically, hydrothermal breccia and fissure veins are the most significant. Magmatic intrusive breccia pipes could have economic significance. Most precious and base metal sulfide deposits are associated with REE-F-Ba hydrothermal breccia and fissure vein deposits. The origin of the hydrothermal fluids is not constrained, but likely related to the exposed intrusions. However, fluids could be sourced from a non-exposed carbonatite or alkaline intrusion.
2. Detailed mapping coupled with sampling for geochemistry, mineralogy, and geochronology is critical to understand mineralization and alteration field relationships. For example, the updated mapping (Plate 1) reveals that many of the magmatic intrusive breccia pipes in Pinatosa Canyon and along Rattlesnake Ridge were emplaced along the margins of syenite intrusions, suggesting a connection between fluids associated with the intrusions and breccia pipe formation. The Sky High breccia pipe was emplaced along the contact of a trachyte dike. Furthermore, the mineralized hydrothermal breccia deposits at several larger mines (Red Cloud copper, Red Cloud fluorite, Rio Tinto, Old Hickory, and All American) appear to be or elliptical in plan view and chimney-like or pipe-like in cross section (not linear or vein-like), similar to the intrusive breccia pipes. These observations provide a focus for future research into the origin of intrusive breccia pipes in this part of the Gallinas Mountains.
3. Other controls of mineralization include:
    a. Major faults (based on length and displacement) are not mineralized with the exception of the Pride and Buckhorn faults
    b. Some REE hydrothermal breccia and fissure veins are along bedding planes (Fig. 69)
    c. REE breccia and vein deposits are associated with dikes that are south of Rough Mountain
4. $^{40}Ar/^{39}Ar$ geochronology results indicate at least two, possibly three periods of magmatic activity.
    a. Early magmatic activity (38.5 to 29.3 Ma)
    b. Alkaline intrusive flare-up from 29.0 to 27.0 Ma with most activity at 28.8 Ma. Most alteration and mineralization is associated with this phase of intrusive activity.
    c. Alteration and younger intrusions (25.8 to 24.4 Ma)
5. Five predominant types of alteration are described in the Gallinas Mountains related to the intrusions.
    a. Early regional silicification and brecciation (non-mineralized) and silicification of host rocks near intrusions
    b. Hematization and sericitization (liesegang banding)
    c. Dissolution and brecciation of gypsum and limestone that is followed by recrystallization and cementation by calcite to form carbonate breccias and calcite veins, and locally are enriched in REE

d. Metasomatic alteration (i.e. fenitization) characterized by Na fenitization followed by K fenitization that is coeval with the intrusions emplaced during the alkaline flare-up (29 to 27 Ma), but is not significantly enriched in REE and likely includes alteration related to the skarns

6. A combination of detailed mapping, thin section petrography, and whole-rock geochemistry indicates that geochemical reactions with 1 or 2 stages of barite-fluorite-calcite veins may control REE distribution followed by precipitation of later bastnäsite-fluorite veins.

RECOMMENDATIONS FOR FUTURE STUDIES

1. Isotope studies are needed to identify the source of the hydrothermal activity, i.e. a carbonatite or trachyte/syenite magma.
2. Fluid inclusion and isotope studies of the mineral deposits are needed in light of new interpretations and field relationships. Additional mineral chemistry of fluorite is needed to provide insights on evolution and origin of mineralizing fluids. Mineralogy, fluid inclusion and stable isotope detailed study along some of the best exposed veins, such as Eagle Nest and Buckhorn (F-Ba-Cu)-Last Chance (REE-F-Ba) vein.
3. The similarity in mineralogy, chemistry, and pipe-like or chimney-shaped deposits of some of the hydrothermal breccia and fissure vein deposits and the magmatic intrusive breccia pipes requires more detailed study.
4. High resolution geophysical studies are needed to refine the underlying geology and assist in locating drill targets. A carbonatite generally would be represented by a magnetic low and a gravity high (Schreiner, 1993).
5. U/Pb ages of zircon and titanite from the igneous intrusions are needed to better define the age of emplacement. Given the syenite, rhyolite, and trachyte all yield 28.8 Ma $^{40}Ar/^{39}Ar$ cooling ages – is the entire Gallinas Mountain intrusive complex just a single, complex zoned intrusion? Or could the similarity of ages simply reflect near-uniform regional cooling during waning magmatism of the system?
6. The andesites require more study in order to understand their significance and age.
7. Test if durations of intrusive activity have links to mineralization of economic importance at multiple systems throughout New Mexico and elsewhere. This would also require U/Pb zircon ages.
8. Further study of the travertine deposits, including geochemistry, isotopic studies, and geochronology is of interest, both tectonically and from a paleoclimatic point of view, because these particular deposits lie at the transition between the Great Plains, where little work on travertines has been done and the Rio Grande rift, where travertines have been extensively studied.
9. More structure interpretation is needed in order to locate potential drill targets.
10. Drilling is suggested at the Pride vein, M and E breccia pipe, Red Cloud-Deadwood copper veins, Rio Tinto vein, Sky High-Big Ben veins, veins along the road to Rough Mountain and Park magmatic intrusive breccia pipe.

ACKNOWLEDGEMENTS

This work is part of ongoing research of the economic geology of mineral resources in New Mexico at NMBGMR, Nelia Dunbar, Director and State Geologist. This study was partially funded by the U.S. Geological Survey Earth MRI (Mapping Resources Initiative) Cooperative Agreement No. G19AC00258 and student grants from the New Mexico Geological Society, New

Mexico Tech Brightstar Scholarship, and Society of Economic Geology. Without these funds, this project could not have been completed. Previous mapping by Molycorp geologists, Vincent Kelley, and Richard Perhac was helpful in focusing and understanding recent geologic mapping. Geochemical analyses by Molycorp geologists, Strategic Resources geologists, and Brian Alers provided additional analyses for interpretation. This study also utilized earlier thesis and dissertation projects by T. Poe, Ralph Perhac, Alanna Robison, and Zach Vance. Lynne Heizler and Nels Iverson performed the electron microprobe analyses. Virgil Lueth and Kesley McNamara performed the XRD analyses. Nicholas Harrison, Keith Diegel, Gabriel K. Arechederra, and Carmin Vasquez provide technical support. Sarah Bennett maintained organization in the laboratory. I would like to thank Russ Schreiner for his prior work in the area and sharing his insights and information over the years. Finally, James McLemore spent many days in the field camping, driving, mapping, and collecting samples with the senior author. Everyone's assistance is appreciated.

REFERENCES

Adams, J.W., 1965, Rare earths; in Mineral and water resources of New Mexico: New Mexico Bureau of Mines and Mineral Resources, Bulletin 87, p. 234-237.

Alker, J.D. and Cohen, H.A., 2009, The Geoscience Handbook: American Geological Institute data sheets, 4th edition, revised, Alexandria Va., 302 p.

Allen, M.S. and Foord, E.E., 1991, Geological, geochemical and isotopic characteristics of the Lincoln County porphyry belt, New Mexico: implications for regional tectonics and mineral deposits: New Mexico Geological Society, Guidebook 42, p. 97-113.

Anthony, E.Y., 2005**,** Source regions of granites and their links to tectonic environment: Examples from the western United States: Lithos, v. 80, p. 61–74.

Barker, D.S., Long, L.E., Hoops, C.K., and Hodges, F.N., 1977, Petrology and Rb-Sr isotope geochemistry of intrusions in the Diablo Plateau, northern Trans-Pecos magmatic province, Texas and New Mexico: Geol. Soc. Am. Bull., v. 88, p. 1437–1446.

Bartsch-Winkler, S.B. and Donatich, A.J., ed., 1995, Mineral and Energy Resources of the Roswell Resource Area, East-Central New Mexico: U.S. Geological Survey, Bulletin 2063, 145 p.

Berger, V.I., Singer, D.A., and Orris, G.J., 2009, Carbonatites of the world, explored deposits of Nb and REE; database and grade and tonnage models: U.S. Geological Survey Open-File Report 2009-1139, 17 p. and database.

Bickford, D.A., 1980, Economic geology of the Jones Camp iron deposit, Socorro County, New Mexico. [M.S. Thesis]: Socorro, New Mexico Institute of Mining and Technology, 226 p.

Blagbrough, J.W., 1984, Fossil rock glaciers on Carrizo Mountain, Lincoln County, New Mexico: New Mexico Geology, v. 6, no. 4, p. 65-68.

Blagbrough, J.W., 1991, Late Pleistocene rock glaciers in the western part of the Capitan Mountains, Lincoln County, New Mexico—description, age, and climate significance: New Mexico Geological Society, Guidebook 42, p. 333-338.

Blagbrough, J.W., 1994, Late Wisconsin climatic inferences from rock glaciers in south-central and west-central New Mexico and east-central Arizona: New Mexico Geology, v. 16, no. 4, p. 67-71.(not cited)

Blagbrough, J.W., 1999, Rock glaciers of two ages in the Capitan Mountains, Lincoln County, south-central New Mexico: New Mexico Geology, v. 21, no. 3, p. 57-65.

Blagbrough, J.W., 2005, Periglacial mass movement deposits of late Wisconsin age, Gallinas Mountains, Lincoln County, central New Mexico: New Mexico Geology, v. 27, no. 2, p. 31-38.

Bonham, H.F., Jr., 1988, Models for volcanic-hosted epithermal precious metal deposits; *in* Bulk mineable precious metal deposits of the western United States: Geological Society of Nevada, Symposium Proceedings, p. 259-271.

Campbell, A.R., Banks, D.A., Phillips, R.S., and Yardley, B.W.D., 1995, Geochemistry of the Th-U-REE mineralizing fluid, Capitan Mountains, New Mexico, USA: Economic Geology, v. 90, p. 1273-1289.

Carrizozo Outlook, 1915, Red Cloud mine closes: Carrizozo Outlook, August 15, 1915, v. 9, no. 33, p. 1, file no. 0265

Chamberlin, R.M, 2009, Rare-earth geochemical anomaly at Sierra Larga, New Mexico: NURE stream-sediment data suggest a monazite placer deposit in the Permian Gloria Sandstone: New Mexico Geological Society Guidebook 60, p. 71-73.

Chamberlin, R.M, McIntosh, W.C., and Peters, L., 2009, $^{40}Ar/^{39}Ar$ geochronology of the Jones Camp dike, central New Mexico: An eastward projection of the Magdalena radial dike swarm from under the Oligocene Socorro-Magdalena caldera cluster: New Mexico Geological Society Guidebook 60, p. 337-346.

Chapin, C.E.; Wilks, M.; McIntosh, W.C. Space-Time Patterns of Late Cretaceous to Present Magmatism in New Mexico; Comparison with Andean Volcanism and Potential for Future Volcanism; InTectonics, Geochronology and Volcanism in the Southern Rocky Mountains and Rio Grande rift: New Mexico Bureau of Geology and Mineral Resources; Bulletin 160; Socorro, NM, USA, 2004; p. 13–40. Available online: http://geoinfo.nmt.edu/publications/monographs/bulletins/160/downloads/02chapin.pdf (accessed on 20 January 2018).

Clark, K.F., 1989, Metallogenic provinces and epochs in Mexico: 28th International Geological Congress, Abstracts, v. 1, p. 1-300.

Coleman, D.S., Mills, R.D., and Zimmerer, M.J., 2016, The Pace of Plutonism: Elements, v. 12, p. 87-102.

Committee on Critical Mineral Impacts of the U.S. Economy, 2008, Minerals, Critical Minerals, and the U.S. Economy: Committee on Earth Resources, National Research Council, ISBN: 0-309-11283-4, 264 p., http://www.nap.edu/catalog/12034.html

Daily New Mexican, 1882, Mines and Mining: Dailey New Mexican, p. 2, Dec. 15, NMBGMR mining archives report no. 4705_mf

Darton, Nelson H., 1928, Geologic map of New Mexico, U.S. Geological Survey, Atlas

Dean, R.S., 1944, Bastnaesite at Corona, New Mexico: American Mineralogist, v. 29, p. 157.

De la Roche, H., Leterrier, J., Grandclaude, P. and Marchal, M., 1980, A classification of volcanic and plutonic rocks using R1, R2-diagrams and major element analysis—its relationships with current nomenclature: Chemical Geology, v. 29, p. 183-210.

DeMark, R.S., 1980, The Red Cloud mines, Gallinas Mountains, New Mexico: Mineralogical Record, v. 11, no.2, p. 69-72.

DeMark, R.S. and Hlava, P.F., 1993, Spangolite and other secondary minerals from the Buckhorn mine, Lincoln County, New Mexico (abstr.): New Mexico Geology, v. 15, p. 19.

Dunbar, N.W., Campbell, A.R., and Candela, P.A., 1996, Physical, chemical, and mineralogical evidence for magmatic fluid migration within the Capitan pluton, southeastern New Mexico: Geological Society of America Bulletin, v. 108, p. 318-333.

Eaton, G.P., 1980, Geophysical and geological characteristics of the crust of the Basin and Range Province; *in* Burchfield, C., Silver, E., and Oliver, J., eds., Continental tectonics, National Research Council Studies in Geophysics: Washington, D.C., National Academy of Sciences, p. 96-113.

Edmonds, M., Cashman, K.V., Holness, M., and Jackson, M., 2018, Architecture and dynamics of magma reservoirs: Philosophical Transactions Royal Society A, v. A377, 20180298, 29 p.

Elliott, B.A., O'Neill, L.C., and Kyle, J.R., 2017, Mineralogy and crystallization history of a highly differentiated REE-enriched hypabyssal rhyolite: Round Top laccolith, Trans-Pecos, Texas. Miner. Petrol., v. 111, p. 569–592.

Esser, R., McIntosh, W., Heizler, M., and Kyle, P., 1997, Excess argon in melt inclusions in zero-age anorthoclase feldspar from Mt. Erebus, Antarctica, as revealed by the $^{40}Ar/^{39}Ar$ method: Geochimica et Cosmochimica Acta, v. 61, p. 3789–3801, doi: 10.1016/s0016-7037(97)00287-1.

File, L., and Northrop, S.A., 1966, County township, and range locations of New Mexico's mining districts: New Mexico Bureau of Mines and Mineral Resources, Circular 84, 66 p.

Franchini, M., Lira, R., Meinert, L., Rios, F.J., Poklepovic, M.F., Impiccini, A., Millone, H.A., 2005. Na-Fe-Ca alteration and LREE (Th-Nb) mineralization in marble and granitoids of Sierra de Sumampa, Santiago del Estero, Argentina. Econ. Geol. 100, 733–764.

Frost, B.D., Barnes, C.G., Collins, W.J., Arculus, R.J., Ellis, D.J., and Frost, C.D., 2001, A geochemical classification for granitic rocks: Journal of Petrology, v. 42, no. 11, p. 2033-2048.

Frost, B.D. and Frost, C.D., 2008, A geochemical classification for feldspathic igneous rocks. J. Petrol., v. 49, 1955–1969.

Fulp, M.S. and Woodward, L.A., 1991, Mineral deposits of the New Mexico alkalic province (abstr.): Geological Society of America, Abstracts with Programs, v. 23, p. 23.

Gagnon, J.E., 2006, Genesis of hydrothermal highfield strength element mineral deposit: Evidence from laser ablation-inductively coupled plasma spectrometry: PhD dissertation, McGill University, Montreal, 638 p.

Gagnon, J.E., Samson, I.M., Fryer, B.J., and Williams-Jones, A.E., 2003, Compositional heterogeneity in fluorite and the genesis of fluorite deposits: insights from LA-ICP-Ms analysis: Canadian Mineralogist, v. 41, p. 365-382.

Gibbons, T.L., 1981, Geochemical and petrographic investigation of the Jones Camp magnetite ores and associated intrusives, Socorro County, New Mexico (M.S. thesis): Socorro, New Mexico Institute of Mining and Technology, 156 p.

Glass, J.J. and Smalley, R.G., 1945, Bastnaesite {Gallinas Mountains, New Mexico]: American Mineralogist, v. 30, p. 601-615.

Griswold, G.B., 1959, Mineral deposits of Lincoln County, New Mexico: New Mexico Bureau of Mines and Mineral Resources, Bulletin 67, 117 p.

Gysi, A.P., Williams-Jones, A.E., 2013. Hydrothermal mobilization of pegmatite-hosted REE and Zr at Strange Lake, Canada: a reaction path model. Geochim. Cosmochim. Acta 122, 324–352.

Harrison, N., McLemore, V.T., Silva, M., Mojtabai, N., and Asafo-Akowuah, J., 2020, A study of abandoned mine lands in New Mexico: SME Annual Meeting, Preprint 20-37, 6 p., https://geoinfo.nmt.edu/staff/mclemore/documents/20-037.pdf

Harrer, C.M. and Kelly, F.J., 1963, Reconnaissance of iron resources in New Mexico, U.S. Bureau Mines, Information Circular 08190, 112 p.

Irvine, T.N. and Baragar, W.R.A., 1971, A guide to the chemical classification of the common volcanic rocks. Can. J. Earth Sci., v. 8, 523–548.

Jackson, W.D. and Christiansen, G., 1993, International strategic minerals inventory summary report—rare-earth oxides: U.S. Geological Survey, Circular 930-N, 76 p.

Johnson, R.D, 1980, Buckhorn mining project, Gallinas Mountains mining district, Lincoln, County, New Mexico: unpublished report, 20 p., NMBGMR mining archives report no. 4935_mf

Johnston, W.D., Jr., 1928, Fluorspar in New Mexico: New Mexico Bureau of Mines and Mineral Resources, Bulletin 4, 128 p.

Jones, F.A., 1904, New Mexico mines and minerals: Santa Fe, New Mexican Printing Company, 349 p.

Kelley, K.D. and Luddington, S., 2002, Cripple Creek and other alkaline-related gold deposits in the southern Rocky Mountains, USA: influence of regional tectonics: Mineralium Deposita, v. 37, p. 38-60.

Kelley, K.D. and Spry, P.G., 2016, Critical Elements in Alkaline Igneous Rock-Related Epithermal Gold Deposits: Chapter 9 *In* Rare Earth and Critical Elements in Ore Deposits; Verplanck, P.L., Hitzman, M.W., eds.; Society of Economic Geologists, Reviews in Economic Geology 18, Littleton, CO, USA, p. 195–216. (not cited)

Kelley, S, 2002, Excess argon in K-Ar and Ar-Ar geochronology, Chemical Geology, v. 188, p. 1-22.

Kelley, V.C., 1949, Geology and economics of New Mexico iron ore deposits: University of New Mexico, Publications in Geology, no. 2, 246 p.

Kelley, V.C., 1971, Geology of the Pecos country, southeastern New Mexico: New Mexico Bureau Mines Mineral Resources, Memoir 24, 75 p.

Kelley, V.C., 1972, geology of the Fort Sumner sheet, New Mexico: New Mexico Bureau Mines Mineral Resources, Bulletin 98, 55 p.

Kelley, V.C., Rothrock, H.E., and Smalley, R.G., 1946, Geology and mineral deposits of the Gallinas district, Lincoln County, New Mexico: U.S. Geological Survey, Strategic Minerals Investigation Preliminary Map 3-211, scale 1:62,500.

Kelley, V.C. and Thompson, T.B., 1964, Tectonics and general geology of the Ruidoso—Carrizozo region, central New Mexico: New Mexico Geological Society, Guidebook 15, p. 110-121.

Kish, S.A., Ragland, P.C., and Cannon, R.P., 1990, Petrochemistry of the Palisades sheet, Cimarron Pluton, Northern New Mexico: New Mexico Geological Society Guidebook 41, p. 341–347.

Korzeb, S.L., and Kness, R.F., 1992, Mineral resource investigation of the Roswell Resource Area, Chaves, Curry, De Baca, Guadalupe, Lincoln, Quay, and Roosevelt Counties, New Mexico: U. S. Bureau of Mines, Open-file Report MLA 12-92, 220 p.

Kozlov, E.N. and Arzamastev, A.A., 2015, Petrogenesis of metasomatic rocks in the fenitized zones of Ozernaya Varaka alkaline ultrabasic complex, Kola Peninsula: Petrology, v. 23, p. 45-67.

Kresten, P., 1988. The chemistry of fenitization – examples from Fen, Norway. Chem. Geol. 68, 329–349.
Kresten, P. and Morgan, V., 1986, Fenitization at the Fen complex, southern Norway: Lithos, v. 19, p. 27-42.
Kucks, R.P., Hill, P.L., and Heywood, C.E., 2001, New Mexico magnetic and gravity maps and data; a web site for distribution of data: U.S. Geological Survey, Open-file Report 01-0061, https://pubs.usgs.gov/of/2001/ofr-01-0061/ (November 2021).
Kuiper, K. F., Deino, A., Hilgen, F. J., Krijgsman, W., Renne, P. R., and Wijbrans, J. R., 2008, Synchronizing rock clocks of earth history: Science, v. 320, p. 500-504.
Large, R.R. et al., 2001, The alteration box plot: A simple approach to understanding the relationship between alteration mineralogy and lithogeochemistry associated with volcanic-hosted massive sulfide deposits: Economic Geology v.96, pp. 957-972
Laughlin, A.W.; Rehrig, W.A.; and Mauger, R.L., 1969, K-Ar chronology and sulfur and strontium isotope ratios at the Questa mine, New Mexico: Econ. Geol., v. 64, p. 903–909.
Le Bas, M.J., 1987, Nephelinites and carbonatites; *in* J.G. Fitton and B.G.J. Upton, eds., Alkaline igneous rocks: Geological Society, Special Publication No. 3, p. 53-83.
Le Bas, M.J., 2008, Fenites associated with carbonatites: Canadian Mineralogist, v. 46, p. 915-932.
Le Bas, M.J., Le Maitre, R.W., Streckusen, A., and Zanettin, B., 1986, A chemical classification of volcanic rocks based on the total alkali-silica diagram: Journal of Petrology, v. 27, p. 745-750.
Le Maitre, R.W., ed., 1989, A classification of igneous rocks and glossary of terms: Blackwell Scientific Publications, Oxford, Great Britain, 193 p.
Levine, D.F. and Evans, L.G., 1991, An archaeological survey of abandoned mines in the Gallinas mining district near Corona, Lincoln, County, New Mexico: Museum of New Mexico, Archaeology Notes No. 31, 56 p.
Li, M., 2017, Aeromagnetic and spectral expressions of rare earth element deposits in Gallinas Mountains area, central New Mexico, USA: M.S. thesis, Montana Tech, 133., http://digitalcommons.mtech.edu/grad_rsch/133
Lira, R., Ripley, E.M., 1992. Hydrothermal alteration and REE-Th mineralization at the Rodeo-De-Los-Molles Deposit, Las-Chacras-Batholith, Central Argentina. Contrib. Mineral. Petrol. 110, 370–386.
Lincoln County Leader, 1883a, Red Cloud mining district: Lincoln County Leader, June 2, 1883, v. 1, no. 33, p. 1.
Lincoln County Leader, 1883b, Red Cloud sortings: Lincoln County Leader, September 1, 1883, v. 1, no. 36, p. 2.
Lindgren, W., 1915, The igneous history of the Cordilleras and its problems: Yale University, p. 284-286.
Lindgren, W., 1933, Mineral deposits: 4th edition, New York, McGraw-Hill, 930 p.
Lindgren, W., Graton, L.C., and Gordon, C.H., 1910, The ore deposits of New Mexico: U.S. Geological Survey, Professional Paper 68, 361 p.
Liu, S., Fana, H., Yanga, K., Hua, F., Ruskd, B., Liua, X, Lie, X., Yangf, Z., Wang, Q., Wang, K., 2018, Fenitization in the giant Bayan Obo REE-Nb-Fe deposit: Implication for REE mineralization: Ore Geology Reviews, v. 94, p. 290–309

Long, K.R., van Gosen, B.S., Foley, N.K. and Cordier, D., 2010, The principle rare earth elements deposits of the United States—A summary of domestic deposits and a global perspective: U.S. Geological Survey, Scientific Investigations Report 2010-5220, 104 p., http://pubs.usgs.gov/sir/2010/5220/

Mains, J.F., 1901, The White Oaks Country, International Industrial Record, El Paso, Texas, July 20, 1901, p.34.

Mason, G.T., Jr. and Arndt, R.E., 1996, Mineral resources data system (MRDS): U.S. Geological Survey, Digital Data Series DDS-20, CD-ROM.

Maynard, S.R., Martin, K.W., Nelson, C.J., and Schutz, J.L., 1989, Geology and gold mineralization of the Ortiz Mountains, Santa Fe County, New Mexico: Society of Mining Engineers, Preprint No. 89-43, 9 p.

Maynard, S.R., Nelson, C.J., Martin, K.W., and Schutz, J.L., 1990, Geology and gold mineralization of the Ortiz Mountains, Santa Fe County, New Mexico: Mining Engineering, August, p. 1007-1011.

McAnulty, W.N., 1978, Fluorspar in New Mexico: New Mexico Bureau of Mines and Mineral Resources, Memoir 34, 64 p.

McDougall, I., and Harrison, T.M., 1999, Geochronology and thermochronology by the $^{40}Ar/^{39}Ar$ method: New York, Oxford University Press, p. 269.

McLemore, V.T., 1983, Uranium and thorium occurrences in New Mexico—distribution, geology, production, and resources; with selected bibliography: New Mexico Bureau of Mines and Mineral Resources, Open file Report 182, 950 p., also; U.S. Department of Energy Report GJBX11 (83).

McLemore, V.T., 1987, Geology and regional implications of carbonatites in the Lemitar Mountains, central New Mexico: Journal of Geology, v. 95, p. 255-270, http://www.jstor.org/pss/30063811.

McLemore, V.T., 1991a, Base-and precious-metal deposits in Lincoln and Otero Counties, New Mexico: New Mexico Geological Society, Guidebook 42, p. 305-309.

McLemore, V.T., 1991b, Gallinas Mountains mining district, New Mexico: New Mexico Geological Society, Guidebook 42, p. 62-63.

McLemore, V.T., 1996, Great Plains margin (alkaline-related) gold deposits in New Mexico; in Coyner, A.R. and Fahey, P.L., eds, Geology and ore deposits of the American Cordillera, Symposium Proceedings: Geological Society of Nevada, Reno, p. 935-950.

McLemore, V.T., 2001, Silver and gold resources in New Mexico: New Mexico Bureau of Mines and Mineral Resources, Resource Map 21, 60 p.

McLemore, Virginia T., 2010a, Geology and mineral deposits of the Gallinas Mountains, Lincoln and Torrance counties, New Mexico: Preliminary report, New Mexico Bureau of Geology Mineral Resources, Open-file Report, OF-0532.

McLemore, V.T., 2010b, Use of the New Mexico Mines Database and ArcMap in Uranium Reclamation Studies: Society of Mining, Metallurgy and Exploration Annual Convention, Phoenix, Feb 2010, Preprint 10-125.

McLemore, V.T., 2011, Rare earth elements for emerging technologies: New Mexico Earth Matters, summer, 4 p., http://geoinfo.nmt.edu/publications/periodicals/earthmatters/11/EM11n2.pdf

McLemore, V.T., 2015a, Great Plains Margin (alkaline-related) gold deposits in New Mexico: twenty years later: Geological Society of Nevada, New concepts and discoveries, 2015 Symposium volume.

McLemore, V.T., 2015b, Rare Earth Elements (REE) Deposits in New Mexico: Update: New Mexico Geology, v. 37, p. 59-69, http://geoinfo.nmt.edu/publications/periodicals/nmg/current/home.cfml

McLemore, V.T., 2017, Mining districts and prospect areas of New Mexico: New Mexico Bureau of Geology and Mineral Resources, Resource Map 24, 65 p., scale 1:1,000,000.

McLemore, V.T., 2018, Rare Earth Elements (REE) Deposits Associated with Great Plain Margin Deposits (Alkaline-Related), Southwestern United States and Eastern Mexico: *Resources*, *7*(1), 8; 44 p., doi:10.3390/resources7010008; http://www.mdpi.com/2079-9276/7/1/8 link http://www.mdpi.com/2079-9276/7/1/8

McLemore, V.T. and Diegel, K., 2021, Examining Potential Geochemical Indicators of Fenitization in Soil Samples Collected From the Gallinas Mountains, Lincoln County, New Mexico (abstr.): New Mexico Geological Society, Spring Meeting, http://nmgs.nmt.edu/meeting/abstracts/view.cfm?aid=2734 poster https://nmgs.nmt.edu/meeting/abstracts/view.cfm?aid=2734

McLemore, V.T., Donahue, K., Breese, M., Jackson, M.L., Arbuckle, J., and, Jones, G., 2001, Mineral-resource assessment of Luna County, New Mexico: New Mexico Bureau of Mines and Mineral Resources, Open file Report 459, 153 pp., CD-ROM, http://geoinfo.nmt.edu/publications/openfile/downloads/OFR400-499/451-475/471/ofr_471.pdf

McLemore, V.T., Hoffman, G., Smith, M., Mansell, M., and Wilks, M., 2005a, Mining districts of New Mexico: New Mexico Bureau of Geology and Mineral Resources, Open-file Report 494, CD-ROM.

McLemore, V. T., Krueger, C. B., Johnson, P., Raugust, J. S., Jones, G.E., Hoffman, G.K. and Wilks, M., 2005b, New Mexico Mines Database: Society of Mining, Exploration, and Metallurgy, Mining Engineering, February, p. 42-47.

McLemore, V.T., Owen, E. Haff, E., Kelley, S.K., Zimmerer, M. and Gysi, A., 2021, Mineralogical and chemical types of REE mineral deposits in the Gallinas Mountains (Gallinas District), Lincoln County, New Mexico: 57th Industrial Minerals Forum, https://isgswikis.web.illinois.edu/FGIM/index.php/Mineralogical_and_Chemical_Types_of_REE_Mimeral_Deposits_in_the_Gallinas_Mountains_(Gallinas_District),_Lincoln_County,_New_Mexico

McLemore, V.T., North, R.M., and Leppert, S., 1988a, Rare-earth elements (REE), niobium and thorium districts and occurrences in New Mexico: New Mexico Bureau of Mines and Mineral Resources, Open-file Report OF-324, 28 p.

McLemore, V.T., North, R.M., and Leppert, S., 1988b, Rare-earth elements (REE) in New Mexico: New Mexico Geology, v. 10, p. 33-38.

McLemore, V.T., Owen, E. Haff, E., Kelley, S.K., Zimmerer, M. and Gysi, A., 2021, Mineralogical and chemical types of REE mineral deposits in the Gallinas Mountains (Gallinas District), Lincoln County, New Mexico: 57th Industrial Minerals Forum, https://isgswikis.web.illinois.edu/FGIM/index.php/Mineralogical_and_Chemical_Types_of_REE_Mimeral_Deposits_in_the_Gallinas_Mountains_(Gallinas_District),_Lincoln_County,_New_Mexico

McLemore, V.T. and Phillips, R.S., 1991, Geology of mineralization and associated alteration in the Capitan Mountains, Lincoln County, New Mexico: New Mexico Geological Society, Guidebook 42, p. 291-298.

McLemore, V.T., Smith, K.S., Russell, C.C., editors, 2014, Management Technologies for Metal Mining Influenced Water, volume 6: Sampling and monitoring for the mine life cycle: Society for Mining, Metallurgy, and Exploration, Inc., Littleton, CO.

McLemore, V.T. and Zimmerer, M., 2009, Magmatic Activity and Mineralization Along The Capitan, Santa Rita, And Morenci Lineaments In The Chupadera Mesa Area, Central New Mexico: New Mexico Geological Society Guidebook 60, p. 375-386.

McMillan, N.J., 2004, Magmatic record of Laramide subduction and the transition to Tertiary extension: Upper Cretaceous through Eocene igneous rocks of New Mexico, *in* The geology of New Mexico, Mack, Greg H.; Giles, Katherine A., ed(s): New Mexico Geological Society, Special Publication, v. 11, pp. 249-270.

McMillan, N.J.; Dickin, A.P.; and Haag, D., 2000, Evolution of magma source regions in the Rio Grande rift, southern New Mexico. Geol. Soc. Am., v. 112, 1582–1593.

Mellen, R.J. and Olson, F.F., 1921, Concentration of lead ores of the Corona Lead and Silver Mining Company, Corona, New Mexico: B.S. thesis, Massachusetts Institute of Technology, 138 p.

Menshikov, Y.P., Mikhailova, Y.A., Pakhomovsky, Y.A., Yakovenchuk,V.N., and Ivanyuk, G.Y., 2015; Minerals of zirconolite group from fenitized xenoliths in nepheline syenites of Khibiny and Lovozero plutons, Kola Peninsula: Geology of Ore Deposits, v. 57, p. 591-599.

Middlemost, E.A.K., 1994, Naming materials in the magma/igneous rock system; Earth Science Reviews, v. 37, p. 215-224.

Miller, C.F., McDowell, S.M., and Mapes, R.W., 2003, Hot and cold granites?: Implications of zircon saturation temperatures and preservation of inheritance: Geology, v. 31, p. 529-532

Min, K., Mundil, R., Renne, P. L., and Ludwig, K. R., 2000, A test for systematic errors in 40Ar/39Ar geochronology through comparison with U/Pb analysis of a 1.1-Ga rhyolite: Geochimica et Cosmochimica Acta, v. 64, p. 73-98.

Mining World, 1881, Gallinas gold, A visit to the new mining district in Lincoln County: Mining World, November 1, NMBGMR mining archives report no. 4704_mf, p. 71.

Modreski, P.J., 1979, Rare earth elements in agardite and in other minerals from the Red Cloud district, New Mexico (abstr.): New Mexico Minerals Symposium, University of New Mexico, Albuquerque, New Mexico.

Modreski, P.J., 1983, Agardite-(La), a chemically complex rare-earth arsenate from the Gallinas district, Lincoln County, New Mexico (abstr.); in Oxidation mineralogy of base metal deposits: 5th Joint Mineralogical Society of America, Friends of Mineralogy Symposium, Tucson, Arizona.

Modreski, P.J. and Schreiner, R.A., 1993, Silver and copper mineralization at the Buckhorn mine, Gallinas Mountains, New Mexico (abstr.): New Mexico Geology, v. 15, p. 20.

Möller, P., Parekh, P.P. and Schneider, H.J., 1976, The application of Tb/Ca-Tb/La abundance ratios to problems of fluorspar genesis: Mineralium Deposita, v. 11, p. 111-116.

Morogan, V., 1994, Ijolite versus carbonatite as sources of fenitization: Terra Nova, v.6, p. 166-176.

Munroe, E. A., 1999, Geology and geochemistry of waste rock piles in the Hillsboro mining district, Sierra County, New Mexico: M.S. thesis, New Mexico Institute of Mining and Technology, Socorro, 144 p.

Mutschler, F.E., Griffin, M.E., Stevens, D.S., and Shannon, S.S., Jr., 1985, Precious metal deposits related to alkaline rocks in the North American Cordillera-an interpretive review: Transactions Geological Society of South Africa, v. 88, p. 355-377.

Mutschler, F.E., Mooney, T.C., and Johnson, D.C., 1991, Precious metal deposits related to alkaline igneous rocks-a space-time trip through the Cordillera: Mining Engineering, v. 43, p. 304-309.

Nakamura, N., 1974, Determination of REE, Ba, Fe, Mg, Na and K I carbonaceous and ordinary chondrites: Geochimica et Cosmochimica Acta, v. 38, p. 757-775.

Nandigam, R., 2000, Geology and geochemistry of newly discovered Tertiary carbonatite occurrences near Villa Ahumada area, Basin and Range province, Chihuahua, northern Mexico: PhD. Dissertation, University of Texas at El Paso, 377 p.

Neir, A.O., 1950, A redetermination of the relative abundances of the isotopes of carbon, nitrogen, oxygen, argon, and potassium: Physical Reviews, v. 77, p. 789-793.

New Mexico Bureau of Geology and Mineral Resources, 2003, Geologic map of New Mexico: New Mexico Bureau of Geology and Mineral Resources, scale 1:500,000.

New Mexico Bureau of Mines and Mineral Resources, New Mexico State University Southwest Technology Institute, and TRC Mariah Associates, Inc., 1998, Mineral and energy resource assessment of the McGregor Range (Fort Bliss), Otero County, New Mexico: New Mexico Bureau of Mines and Mineral Resources Open-file report 456, 543 p., http://geoinfo.nmt.edu/publications/openfile/downloads/OFR400-499/451-475/456/ofr-456.pdf

New Mexico Miner, 1952, Mining gains momentum in Corona region: July, p. 7.

Noguiera, A.C., 1971, Mineralogy and Geochemistry of Contact Metasomatic Iron Deposits at Jones Camp, Socorro County, New Mexico [M.S. Thesis]: New Mexico Institute of Mining and Technology, 101 p.

North, R.M., and McLemore, V.T., 1986, Silver and gold occurrences in New Mexico: New Mexico Bureau of Mines and Mineral Resources, Resource Map 15, 32 p., scale 1:1,000,000.

North, R.M., and McLemore, V.T., 1988, A classification of the precious metal deposits of New Mexico; *in* Bulk mineable precious metal deposits of the western United States Symposium Volume: Geological Society of Neva, Reno, Symposium proceedings, p. 625-659.

Northrop, S.A., 1996, Minerals of New Mexico: University of New Mexico Press, Albuquerque, New Mexico, 356 p.

Oakes, Jaylene S., 1991, Allochemical and isochemical diagenetic processes in feldpsathic arenites, Pennsylvanian Sandia Formation, Taos Trough, New Mexico, M.S. thesis, University Texas, Dallas, TX, pp. 1-94.

Oris, G.J. and Grauch, R.I., 2002, Rare earth elements mines, deposits, and occurrences: U.S. Geological Survey, Open-file Report 02-189, 174 p.

Owen, E., Gysi, A., and McLemore, V.T., 2021, Lithogeochemical Vectors and Mineral Paragenesis of Hydrothermal REE-Bearing Fluorite Veins and Breccia Deposits in the Gallinas Mountains, New Mexico. SEG 100 Conference: Celebrating a Century of Discovery, Abstract ST. 180.

Pearce, J.A., Harris, N.B.W. and Tindle, A.G., 1984, Trace element discrimination diagrams for the tectonic interpretation of granitic rocks: Journal of Petrology, v. 24, p. 956–983.

Perhac, R.M., 1961, Geology and mineral deposits of the Gallinas Mountains, New Mexico: Unpublished Ph.D. thesis, Ann Arbor, University of Michigan, 224 p.
Perhac, R.M., 1964, Resume of the geology of the Gallinas Mountains, New Mexico, in: Ruidoso Country, Ash, Sidney R.; Davis, Leon V., ed(s), New Mexico Geological Society, Guidebook, 15th Field Conference, pp. 87-91.
Perhac, R.M., 1968, Notes on the mineral deposits of the Gallinas Mountains, New Mexico: New Mexico Geological Society, Guidebook 15, p. 152-154.
Perhac, R.M., 1970, Geology and mineral deposits of the Gallinas Mountains, Lincoln and Torrance Counties, New Mexico: New Mexico Bureau of Mines and Mineral Resources, Bulletin 95, 51 p.
Perhac, R.M., and Heinrich, E.W., 1964, Fluorite-bastnaesite deposits of the Gallinas Mountains, New Mexico and bastnaesite paragenesis: Economic Geology, v. 59, p. 226–239.
Phelps Dodge Corp. 1982, Drill log: unpublished report, 9 p., NMBGMR mining archives report no. 4928mf
Phillips, R.S., 1990, Geochemistry of hydrothermal Th-U-REE quartz/fluorite veins from the Capitan pluton (M.S. thesis): Socorro, New Mexico Institute of Mining and Technology, 202 p.
Phillips, R.S., Campbell, A.R., and McLemore, V.T., 1991, Th-U-REE quartz/fluorite veins, Capitan pluton, New Mexico: evidence for a magmatic/hydrothermal origin: New Mexico Geological Society, Guidebook 42, p. 129-136.
Pingitore, N., Clague, J., and Gorski, D., 2014, Round Top Mountain rhyolite (Texas, USA), a massive Y-bearing-fluorite-hosted heavy rare earth element (HRRE) deposit: Journal of Rare Earths, v. 32, no.1, p. 90-96.
Poe, T.I., III, 1965, The intrusive sequence of igneous rocks in the Gallinas Mountains, New Mexico: M.S. thesis, New Mexico Institute of Mining and Technology, Socorro, 41 p.
Porter, E.W. and Ripley, E.M., 1985, Petrologic and stable isotope study of the gold-bearing breccia pipe at the Golden Sunlight deposit, Montana: Economic Geology, v. 80, p. 1689-1706.
Potter, L.S.; Nordlie, B.; Stormer, J.C., 1991, Evolution of the Chico Hills alkalic sill complex, northeast New Mexico: Chemical, mineralogical and isotopic evidence (abstr.): Geol. Soc. Am. Abstr. Programs, 23, 57.
Prodehl, C. and Lipman, P.W., 1989, Crustal structure of the Rocky Mountain region; *in* Pakiser, L.C. and Mooney, W.D., eds., Geophysical framework of the continental United States: Boulder, Colorado, Geological Society of America Memoir 172, p. 249-284.
Rawson, D.E., 1957, The geology of the Tecolote Hills area, Lincoln County, New Mexico (M.S. thesis): Albuquerque, University of New Mexico, 77 p.
Richards, J.P., 1995, Alkalic-type epithermal gold deposits—a review; *in* Thompson, J.F.H., ed., Magmas, fluids, and ore deposits: Mineralogical Association of Canada, Short Course Series, v. 23, p. 367-400.
Rioux, Matthew; Farmer, G.; Bowring, Samuel; Wooton, Kathleen; Amato, Jeffrey; Coleman, Drew; Verplanck, Philip, 2016, The link between volcanism and plutonism in epizonal magma systems; high?precision U–Pb zircon geochronology from the Organ Mountains caldera and batholith, New Mexico, Contributions to Mineralogy and Petrology, v. 171, no. 2, pp. 1-22.

Robison, A., 2017, $^{40}Ar/^{39}Ar$ Geochronology of Magmatism and Alteration in the Gallinas Mountains with Implications for Rare Earth Mineralization: Master's Thesis, New Mexico Institute of Mining and Technology, Socorro, NM, USA.

Ross, J., 2014, Geochronology of southern McMurdo Sound and development of pychron: a $^{40}Ar/^{39}Ar$ data collection and processing software suite [dissertation]: New Mexico Institute of Mining and Technology.

Rothrock, H.E., Johnson, C.H., and Hahn, A.D., 1946, Fluorspar resources of New Mexico: New Mexico Bureau of Mines and Mineral Resources, Bulletin 21, 245 p.

Salvi, S. and Williams-Jones, A.E., 2005, Alkaline granite-syenite deposits; *in* Linnen, R.L. and Samson, I.M., eds., Rare-element geochemistry and mineral deposits: Geological Association of Canada, GAC Short Course Notes 17, p. 315-341.

Samson, I.M. and Wood, S., 2005, The rare-earth elements: behavior in hydrothermal fluids and concentration in hydrothermal mineral deposits, exclusive of alkaline settings; *in* Linnen, R.L. and Samson, I.M., eds., Rare-element geochemistry and mineral deposits: Geological Association of Canada, GAC Short Course Notes 17, p. 269-297.

Santa Fe New Mexican, 1902, The Red Cloud district: Santa Fe New Mexican, April 2, 1902, v. 32, no. 36, p. 1.

Schandl, E.S.; Gorton, M.P. Application of high field strength elements to discriminate tectonic settings in VMS environments. Econ. Geol. 2002, 97, 629–642

Schreiner, R.A.**,** 1993, Mineral investigation of the rare-earth-element-bearing deposits, Red Cloud Mining district, Gallinas Mountains, Lincoln County, New Mexico: U.S. Bureau of Mines, MLA 99-93, 189 p.

Seagerstrom, K. and Ryberg, G.E.**,** 1974, Geology and placer-gold deposits of the Jicarilla Mountains, Lincoln County, New Mexico: U.S. Geological Survey, Bulletin 1308, 25 p..

Sheridan, M.J., 1947, Lincoln County iron deposits, New Mexico: U.S. Bureau of Mines, Report of Investigation 3988.

Sindern, S. and Kramm, U., 2000, Volume characteristics and element transfer of fenite aureoles: a case study from the Iivaaraa alkaline complex, Finland: Lithos, v. 51, p. 75-93.

Sillitoe, R.H. 1985, Ore-related breccias in volcanoplutonic arcs: Economic Geology, v. 80, p. 1467-1515.

Smith, K.S. 2007. Strategies to predict metal mobility in surficial mining environments, J.V. DeGraff, editor, Understanding and Responding to Hazardous Substances at Mine Sites in the Western United States: Ch. 3. Reviews in Engineering Geology, Vol. 17, Boulder, CO, Geological Society of America. p. 25–45.

Smith, K.S., Ramsey, C.A., and Hageman, P.L., 2000, Statistically-based sampling strategy for sampling the surface material of mine-waste dumps for use in screening and prioritizing historical dumps on abandoned mines lands; *in* ICARD 2000; Proceedings from the 5th international conference on acid rock drainage: Society for Mining, Metallurgy, and Exploration, Inc., Littleton, Colo., p. 1453-1461. http://crustal.usgs.gov/minewaste/minewaste.pubs.html

Sobek, A.A., Schuller, W.A., Freeman, J.R. and Smith, R.M., 1978, Field and laboratory methods applicable to overburdens and minesoils: U.S. EPA 600/2-78-054, Washington, D.C., 203 p.

Soulé, J.H., 1943, Gallinas fluorspar deposits, Lincoln County, New Mexico: U.S. Bureau of Mines, War Minerals Report 125, 14 p.

Soulé, J.H., 1946, Exploration of Gallinas fluorspar deposits, Lincoln County, New Mexico: U.S. Bureau of Mines, Report of Investigations 3854, 25 p.
Standard Silver Corporation, 2008, Round Top Beryllium, Uranium, Rare Earth Project: Unpublished Company Report. Available online: http://www.standardsilvercorp.com/main-sect/uploads/08/round_top_ presentation.pdf (accessed on 3 February 2010).
Stein, H.J. and Crock, J.C., 1990, Late Cretaceous-Tertiary magmatism in the Colorado mineral belt; rare earth element and samarium-neodymium isotopic studies, in the nature and origin of Cordilleran magmatism: Geol. Soc. Am. Mem., v. 174, p. 195–223.
Strategic Resources (2012), Exploration update—Gallinas Mountains REE project: Strategic Resources press release, July 16, 3 p., 7162012
Subcommittee on Critical and Strategic Mineral Supply Chains Committee on Environment, Natural Resources, and Sustainability, 2018, Assessment of critical minerals: Updated application of screening methodology: National Science and Technology Council, 7 p., https://www.whitehouse.gov/wp-content/uploads/2018/02/Assessment-of-Critical-Minerals-Update-2018.pdf
Thompson, T.B., 1968, Hydrothermal alteration and mineralization of the Rialto Stock, Lincoln County, New Mexico: Economic Geology, v. 63, p. 943-949.
Thompson, T.B., 1973, Mineral deposits of Nogal and Bonito mining districts, New Mexico: New Mexico Bureau of Mines and Mineral Resources, Circular 123, 29 p.
Thompson, T.B, 1991a, Genesis of gold associated with alkaline igneous rocks (abstr.): Geological Society of America, Abstracts with Programs, v. 23, p. 99-100.
Thompson, T.B., 1991b, The Bonito-Nogal district, Lincoln County, New Mexico (abstr.): Geological Society of America, Abstracts with Programs, v. 23, p. 99.
Thompson, T.B., 1991c, The Lincoln County porphyry belt, New Mexico (abstr.): Geological Society of America, Abstracts with Programs, v. 23, p. 99.
Thompson, T.B., 1992, Mineral deposits of the Cripple Creek district, Colorado: Mining Engineering, v. 44, p. 135-138.
Thompson, T.B., Trippel, A.D., and Dwelley, P.C., 1985, Mineralized veins and breccias of the Cripple Creek district, Colorado: Economic Geology, v. 80, p. 1669-1688.
U.S. Bureau of Mines, 1927-1990, Mineral yearbook: Washington, D.C., U.S. Government Printing Office, variously paginated.
U.S. Bureau of Mines, 1995, MAS/MILS CD-ROM: U.S. Bureau of Mines, Special Publication 12-95, CD-ROM.
U.S. Executive Order No. 13,817, 2017, Presidential executive order on a federal strategy to ensure secure and reliable supplies of critical minerals: https://www.whitehouse.gov/presidential-actions/presidential-executiveorder-federal-strategy-ensure-secure-reliable-supplies-critical-minerals/.
U.S. Geological Survey, 1902-1927, Mineral resources of the United States (1901-1923): Washington, D.C., U.S. Government Printing Office, variously paginated.
Van Alstine, R.E., 1976, Continental rifts and lineaments associated with major fluorspar districts: Economic Geology, v. 71, p. 977-987.
Vance, Z., 2013, Mineralogy, geochemistry and genesis of the hydrothermal REE fluorite-Ag-Pb-Cu ore deposits of the Gallinas Mountains, New Mexico: Unpublished M.Sc. thesis, Socorro, New Mexico, New Mexico Institute of Mining and Technology, 219 p.

Vartiainen, H., Woolley, A.R., 1976. The petrography, mineralogy and chemistry of the fenites of the Sokli carbonatite intrusion, Finland. Bull. Geol. Sury. Finland, No. 280, p. 1–87.
Verplanck, P.L., Farmer, G.L., McCurry, M., Mertzman, S., and Snee, L.W., 1995, Isotopic evidence on the origin of compositional layering in an epizonal magma body: Earth and Planetary Science Letters, v. 136, p. 31–41, doi: 10.1016/0012-821X(95)00147-6.
Verplanck, P.L., Farmer, G.L., McCurry, M., and Mertzman, S.A., 1999, The chemical and isotopic differentiation of an epizonal magma body: Organ Needle pluton, New Mexico: Journal of Petrology, v. 40, p. 653-678.
Verplanck, P.L.; Van Gosen, B.S.; Seal, R.R.; McCafferty, A.E., 2014, A Deposit Model for Carbonatite and Peralkaline Intrusion-Related Rare Earth Element Deposits: Chapter J in Mineral Deposit Models for Resource Assessment; Scientific Investigations Report 2010-5070-J; U.S. Geological Survey: Reston, VA, USA, 58p.
Wang, Z., Fan, H., Zhou, L., Yang, K., and She, H., 2020, Carbonatite-related REE deposits: An overview: Minerals, v. 10, 26 p., Minerals | Free Full-Text | Carbonatite-Related REE Deposits: An Overview | HTML (mdpi.com)
Whalen, J.B., Currie, K.L., and Chappell, B.W., 1987, A-type granites: geochemical characteristics, discrimination and petrogenesis: Contributions to Mineralogy and Petrology, v. 95, p. 40-418.
Williams-Jones, A.E., Samson, I.M., and Olivo, G.R., 2000, The genesis of hydrothermal fluorite-REE deposits in the Gallinas Mountains, New Mexico: Economic Geology, v. 95, p. 327-342.
Williams, F.E., 1966, Fluorspar deposits of New Mexico: U.S. Bureau of Mines, Information Circular 8307, 143 p.
Williams, N.C., and Davidson, G.J., 2004, Possible submarine advanced argillic alteration at the Basin Lake prospect, Western Tasmania, Australia: Economic Geology v.99, pp. 987-1002
Woodward, L.A. and Fulp, M.S., 1991, Gold mineralization associated with alkali trachyte breccias in the Gallinas mining district, Lincoln County, New Mexico: New Mexico Geological Society, Guidebook 42, p. 323-325.
Woolley, A.R., 1987, Alkaline rocks and carbonatites of the world, Part 1: North and South America: University of Texas Press, Austin.
Zandra, J.B., Engel, A.L., and Shedd, E.S., 1952, Concentration of bastnaesite and other cerium ores, with analytical methods: U.S. Bureau of Mines, Report of Investigations RI-4919, 15 p.
Zimmerer, M.J. and McIntosh, W.C., 2013, Geochronologic evidence of upper-crustal in situ differentiation: Silicic magmatism at the Organ caldera complex, New Mexico: Geosphere, v. 9, p. 155-169.

APPENDIX 1. Chronological synopsis of the Gallinas Mountains mining district, Lincoln County, New Mexico.

Date	Event	Source
1870	A stamp mill was constructed in Gallinas Canyon.	Mellen and Olson (1921)
1881	The Red Cloud shaft was 15 m deep where the copper-silver-lead vein was 1 m wide. Development at the Deadwood and Tenderfoot mines were in progress.	Mining World (1881)
1882	Mining district was declared by the miners and a mining constitution was written and approved.	Daily New Mexico (1883a)
1883	20,000 lbs copper ore from Tenderfoot mine shipped to Hubb's smelter in Albuquerque.	Lincoln County Leader (1883a)
1883	Smith and Keegan smelter begins operation.	Lincoln County Leader (1883b)
1885	Jones Taliaferro produced Pb-Cu ore.	Mains (1901), Griswold (1959)
1885	Ore shipped from Red Cloud, Old Hickory, Tenderfoot, and Deadwood mines and shipped to the Socorro smelter.	Jones (1904)
1902	General store, 2 sawmills, and a population of 159 were in the district. Ore assayed 55% Cu, 28 oz/ton Ag, $8/short ton Au.	Santa Fe New Mexican (1902)
1915	Red Cloud mine closed due to poor ventilation.	Carrizozo Outlook (1915)
1920-1922	Ore shipped from Red Cloud mine to El Paso smelter (see Table 1).	
1932-35	Ore shipped to El Paso smelter.	USBM Mineral Yearbooks (1932-1935)
1942	Fluorite discovered in the district during road construction.	Soulé (1946)
1943	Drilling and trenching by USBM.	Soulé (1946)
1946	USBM identified bastnäsite.	Soulé (1946)
1948	Drunzer and Casner leased Red Cloud claims and shipped ore from dumps and mine.	USBM Mineral Yearbooks (1948)
!948	Forest fire in the Gallinas Mountains burns some infrastructure.	Perhac (1961)
1950	A bastnäsite mill was established at Gallinas Siding along the railroad.	Perhac (1961)
1952	Lindsey Light and Chemical Co. of Chicago bought the bastnäsite mill at Gallinas Siding from W.M. Heim and E.D. French.	New Mexico Miner (1952)
1980	American Resources Co. shipped 800 tons of bastnäsite from the Red Cloud mine.	Johnson (1980)
1980-1982	Molycorp, Inc. mapped, sampled and drilled two holes.	
1981	Phelps Dodge drilled one hole at Rio Tinto.	Phelps Dodge Corp. (1982)

1988	American Copper and Nickel Co. sampled for REE and gold; drilled two winkie holes near Old Hickory mine.	Brian Alers, personal communication (8/7/2020)
1989	Canyon Resources, joint venture with Hecla Mining Co. in 1991, drilled seven RC holes	Brian Alers, personal communication (8/7/2020)
1990	Woodward and Fulp examined Sawmill Canyon for gold.	Woodward and Fulp (1991)
1991	The Office of Archaeological Studies, Museum of New Mexico conducted an archaeological survey.	Levine and Evans (1991)
1991	Doza-Bur explored the district for REE.	Levine and Evans (1991)
1992	USBM mineral resource assessment.	Schreiner (1993)
1993	NMAMLB safeguard project, reclaiming most mines in the district.	Levine and Evans (1991)
2004	Major forest fire in 2004 destroyed the original Red Cloud Campground and many wooden structures at the mines, making access impossible for the next few years.	
2009	USGS examined the area for tellurium potential.	Miles Silberman, personal communication (9/8/2019)
2012	Strategic Resources Inc. drilled four holes.	Strategic Resources (2012)
2015	Strategic Resources Inc. sold the project to Tierra Rara Minerals LLP.	
2019-2022	NMBGMR mapped and sampled the district	This report and Plate 1